Doctoral Dissertation

Catalytic Activity of Lewis Acid Complexes Controlled by Coordination Environment around a Group 13/14 Element Center

Daiki Tanaka

January 2022

Department of Applied Chemistry

Graduate School of Engineering

Osaka University

Preface and Acknowledgements

This thesis has been performed from 2016 to 2022 under the guidance of Prof. Dr. Makoto Yasuda at the Department of Applied Chemistry, Graduate School of Engineering, Osaka University. The thesis describes the design of group 13/14 Lewis acid catalysts with a rigid and bulky organic framework.

First and foremost, I would like to extend my most profound appreciation to Prof. Dr. Makoto Yasuda for his precise guidance and valuable suggestions. He also gave me a lot of chances to have precious experiences. I really appreciate him for teaching me chemistry and an attitude as a scientist.

I would also like to thank Professors Dr. Toshiyuki Kida and Dr. Mamoru Tobisu for their helpful advice and kind assistance in cutting my chemistry in different ways.

I gratefully acknowledge Associate Prof. Dr. Yoshihiro Nishimoto for his intimate guidance, continuous advice, and kind encouragement. He assisted me in pondering each experimental result in my work.

I would like to express my sincere gratitude to Assistant Prof. Dr. Akihito Konishi for his invaluable assistance, helpful suggestion, and stimulating discussion. Daily discussion with him has broadened my horizons, and I have enjoyed learning chemistry from him.

I really wish to make a grateful acknowledgement to specially appointed lecturer Dr. Shuntaro Tsubaki for his kindness in my lab life.

I would like to thank Mr. Hiroshi Moriguchi, Dr. Nobuko Kanehisa, Dr. Kyoko Inoue, Dr. Hiroaki Tanaka, Mr. Kunihiko Kamon, and Mr. Hiromi Ohi for giving me analytic assistance at the analytical instrumentation facility.

I am deeply thankful to Ms. Yoshimi Shinomiya and Ms. Tomoko Shimizu for giving me their grateful support and heartwarming kindness.

Furthermore, I gratefully wish to thank Mr. Yuya Tsutsui for his active discussion and hard work to find new Lewis acid catalysts with exciting properties. I also want to acknowledge all the members of Yasuda laboratories for their hearty encouragement, constant support, and assistance.

Professor Yasuda also gave me a chance to visit Technische Universität Berlin, Germany (1/Aug/2021~31/Oct/2021). I would sincerely like to thank Prof. Dr. Martin Oestreich for allowing me to study his fascinating chemistry even under the COVID-19 pandemic. I am also thankful to all members at Martin lab for their kind supports during my stay.

Finally, I would like to thank respectable parents, Osamu Tanaka and Tomoko Tanaka, for their understanding of my work, constant assistance, and financial support. I would also like to thank my sister, Risa Tanaka, for her energetic conversation to cheer me up.

Daiki Tanaka

Department of Applied Chemistry
Graduate School of Engineering
Osaka University
2-1 Yamadaoka, Suita, Osaka 565-0871, JAPAN
January 2021

List of Publications

1) Synthesis of Cage-shaped Aluminum Aryloxides: Efficient Lewis Acid Catalyst for Stereoselective Glycosylation Driven by Flexible Shift of Four- to Five-Coordination
D. Tanaka, Y. Kadonaga, Y. Manabe, K. Fukase, S. Sasaya, H. Maruyama, S. Nishimura, M. Yanagihara, A. Konishi, M. Yasuda
J. Am. Chem. Soc. **2019**, *141*, 17466–17471.

2) Selective Activation of Aromatic Aldehydes Promoted by Dispersion Interactions: Steric and Electronic Factors of a π-Pocket within Cage-Shaped Borates for Molecular Recognition
D. Tanaka, Y. Tsutsui, A. Konishi, K. Nakaoka, H. Nakajima, A. Baba, K. Chiba, M. Yasuda
Chem. Eur. J. **2020**, *26*, 15023–15034.

3) Synthesis and Catalytic Activity of Atrane-type Hard and Soft Lewis Superacids with a Silyl, Germyl, or Stannyl Cationic Center
D. Tanaka, A. Konishi, M. Yasuda
Chem. Asian J. **2021**, *16*, 3118–3123.

Contents

General Introduction

Lewis acid is one of the most essential reagents utilized for many chemical transformations, including Friedel-Crafts reaction, Diels-Alder reaction, and Mukaiyama aldol reaction.[1] Lewis acid-promoted processes are broadly employed in both academic and industrial fields. It is essential to understand and control the properties of Lewis acids for more precise and effective transformations.

Classical Lewis acids such as $AlCl_3$, $TiCl_4$, $BF_3{\cdot}OEt_2$, or $SnCl_4$ have a strong Lewis acidity to activate various functional groups. Because each metal has its own characteristics, a suitable choice of Lewis acid for each reaction is essential to realize a highly effective transformation. These classical Lewis acids can assist a lot of reactions, although the reactions sometimes proceed with relatively low stereo-, regio-, or chemoselectivity.

For more precise controls of Lewis acids' properties, the design of ligands on the metal center is quite important. Lewis acids with a well-designed ligand show more various reactivities than simple metal salts. Organic ligands give us a variety of tuning factors of Lewis acids, such as an electronic and a steric control, a coordination number, and a noncovalent interaction, thanks to a variety of substitution patterns on the organic ligand framework (Figure 1). Lewis acids with organic ligands have more tuning factors than metal salts. Many Lewis acids with organic ligands have been designed to achieve desired transformation reactions.

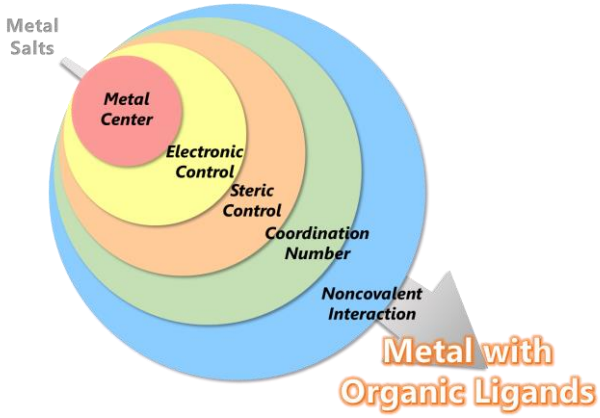

Figure 1. Difference of tuning factors between metal salt and metal with organic ligands.

The difference in a metal center dramatically changes the reactivities of the Lewis acid. Understanding interactions between metal centers and substrates is vital to control original reaction pathways. A Lewis acidity of a metal center, which is frequently related to the hardness/softness of the center, plays an essential role in demonstrating the selectivity of the substrates. Seminal work was represented by Kobayashi's group. They reported the chemoselective reaction between an aldehyde and aldimine, where the selectivity was switched depending on the identity of the metal center (Scheme 1A).[2] The difference in the acid-base interactions between the Lewis acid and the substrate realized the selectivity: Me_3SiOTf selectively activated the aldehyde, whereas $Yb(OTf)_3$ did the aldimine. Interesting regioselectivity driven by the difference in the utilized Lews acid was observed in the cyclization of alkynes.[3][4] When chlorocatecholborane was applied to the cyclization reaction, the 5-*exo* cyclization selectivity occurred. Contrarily, the 6-*endo* cyclization proceeded in the presence of indium(III) iodide (Scheme 1B).

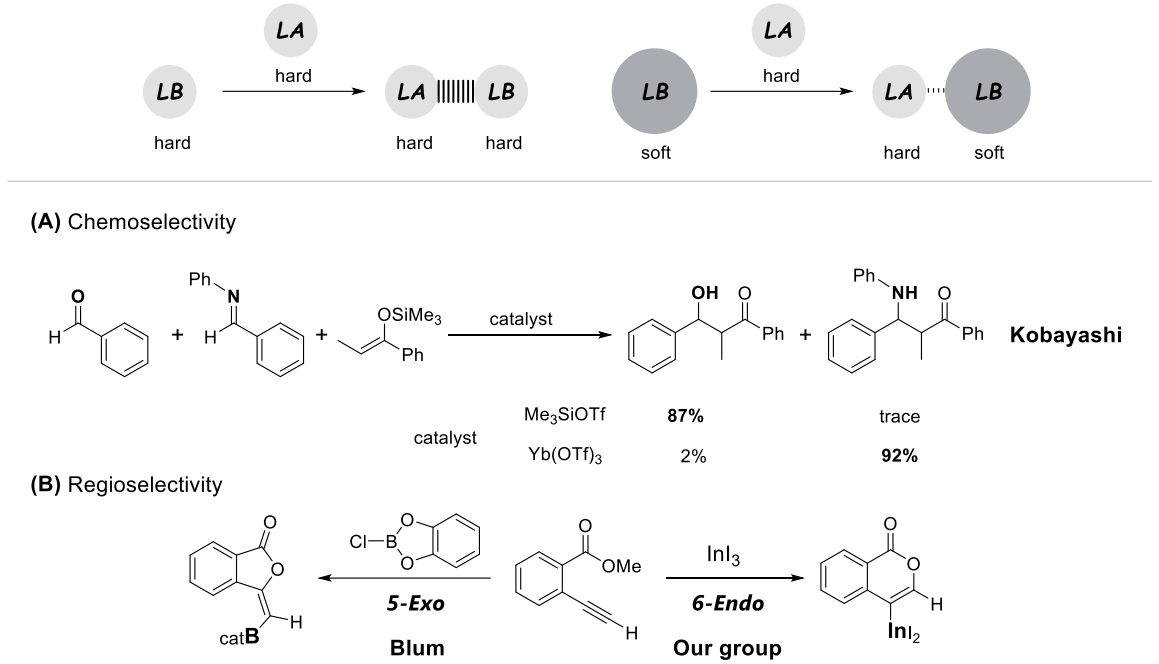

Scheme 1. Metal-controlled selective transformations.

When considering a Lewis acid catalyzed system, Lewis acidity affects not only the activation step of the substrate but also in the regeneration step of the catalyst with the release of the product. Controlling electronic property on the metal center of a Lewis acid is crucial in developing an efficient catalyst system. The introduction of various substituents into the organic frameworks of a Lewis acid can precisely control the electronic property of the metal center. For example, Piers and coworkers reported the allylation of aldehydes, in which $PhB(C_6F_5)_2$ with a lower Lewis acidity more effectively catalyzed the reaction than $B(C_6F_5)_3$ with a higher Lewis acidity (Scheme 2).[5] In the reaction, the lower Lewis acidity should facilitate the release of products and the regeneration of the catalyst in the catalytic cycle.

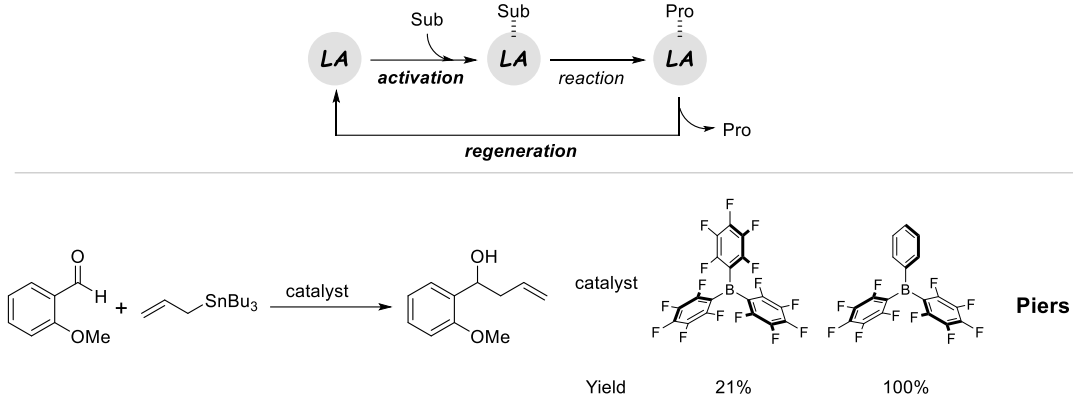

Scheme 2. High catalytic efficiency with a suitable Lewis acidity.

A steric hindrance around a metal center, given by the bulkiness of organic ligands, significantly affects the catalytic cycle. In a reaction catalyzed by a Lewis acid, the deactivation of the Lewis acid through association with the reaction product is often problematic. The bulkiness of the ligand occasionally assists the release of the product from the mental center and the regeneration of the Lewis acid catalyst. Furthermore, the steric factor of the ligand has a significant influence on the control of

regio-, stereo-, and chemoselectivities. The Diels-Alder reaction with the asymmetric boron catalyst is a representative example of stereoselective reactions (Scheme 3A).[6] Recently, much effort has been devoted to developing asymmetric Lewis acid catalysts with organic ligands. Yamamoto and coworkers demonstrated unique chemoselectivity based on the ligand bulkiness. They synthesized the aluminum reagent with bulky ligands to successfully recognize the carbon framework with the same functional group (Scheme 3B).[7] The bulkiness of ligands can provide Lewis acids with other functions, which cannot be achieved by changing the metal center. Moreover, the bulkiness around a metal center offers unconventional acid-base interactions that are never found in typical Lewis acid-base adducts. In the 2000s, the Stephan group has established a novel use of Lewis acids, the combination of the bulky Lewis acid and base, known as a frustrated Lewis pair (FLP) (Scheme 3C).[8] In the FLP, the bulkiness hampered to form the classical Lewis acid-base adduct, realizing unprecedented reactivities such as a heterolytic cleavage of hydrogen gas.

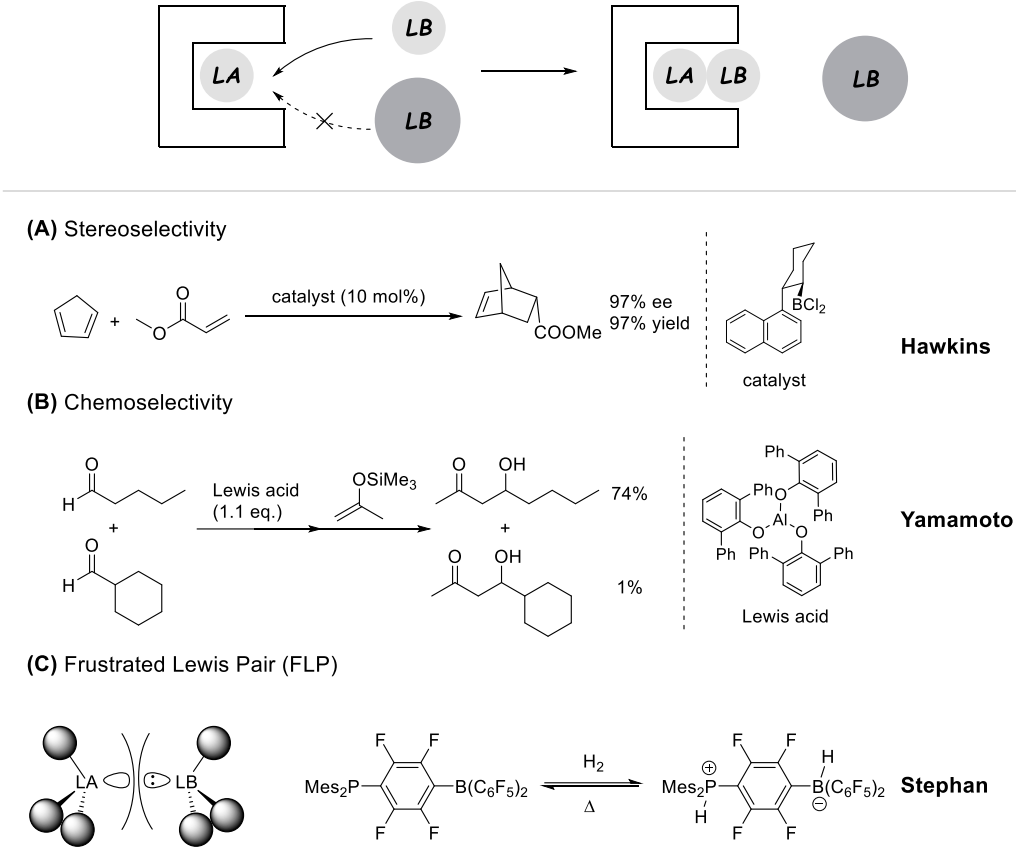

Scheme 3. Steric control of stereo- and chemoselectivities and frustrated Lewis pair (FLP).

A coordination number of a metal center can change not only its Lewis acidity but also its structure. Our group has studied the aluminum catalysts with a pheox or phebox ligand (Scheme 4).[10] The aluminum catalysts with a different coordination number of the aluminum center showed different Lewis acidities and catalytic activities. The coordination number of a metal center is one of the critical tuning factors for the design of Lewis acids.

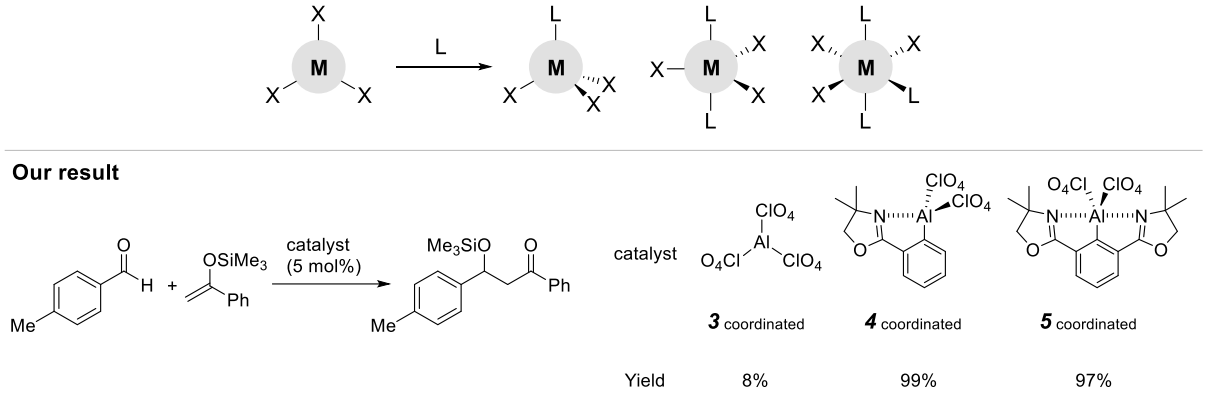

Scheme 4. Effects of a coordination number of the metal center on the catalytic activity.

The biological phenomenon mediated by enzymes proceeds with an excellent substrate specificity in a gigantic and complicated structure. In order to apply such sophisticated designs to the Lewis acid chemistry with small and simple molecules, it is important to understand accurately what factor is dominant for the elaborate selectivity. Noncovalent interactions, such as p-p and CH-p interactions, induced by organic frameworks are useful tools to improve chemoselectivities like biomolecules. Such interactions are quite weak, although they can assist the precise control of reaction pathways when located in the correct position and direction. Schreiner and coworkers reported the stereoselectivity of the carbonyl reduction was improved by the use of noncovalent interactions (Scheme 5).[11]

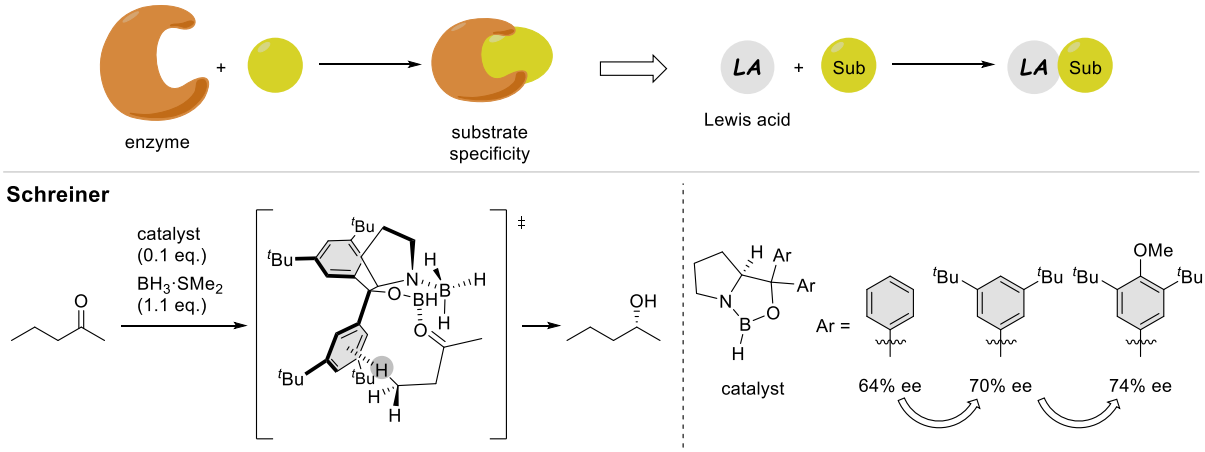

Scheme 5. Improvement of the stereoselectivity with noncovalent interactions.

As shown above, Lewis acids with organic ligands have much potential for precise tunings of their properties. In order to design Lewis acids with desired properties, it is essential to deeply understand each role of a metal center and ligands.

Our group has reported cage-shaped borates with a triphenoxy ligand. The structural change of borate from planar to cage shape enables the borate to work as a Lewis acid catalyst with a moderate Lewis acidity.[12] Moreover, the Lewis acidity can be precisely controlled by the substituents on aryl groups, the size of the tether atom,[13] and the through space interaction between a vacant p orbital on the boron center and the σ* orbital on the tether atom[14] (Figure 2A). Furthermore, the cage-shaped structure shields one side of the vacant p orbital so that substrates can approach only from another side, which makes it much easier to design the coordination environment. With those properties in hand, we found that the introduction of three phenyl groups around the boron center constructs the unique coordination

environment, π-pocket, which can recognize aromatic substrates through π electron interactions.[15] In addition, this rigid framework can be applied to an asymmetric catalysis[16] (Figure 2B).

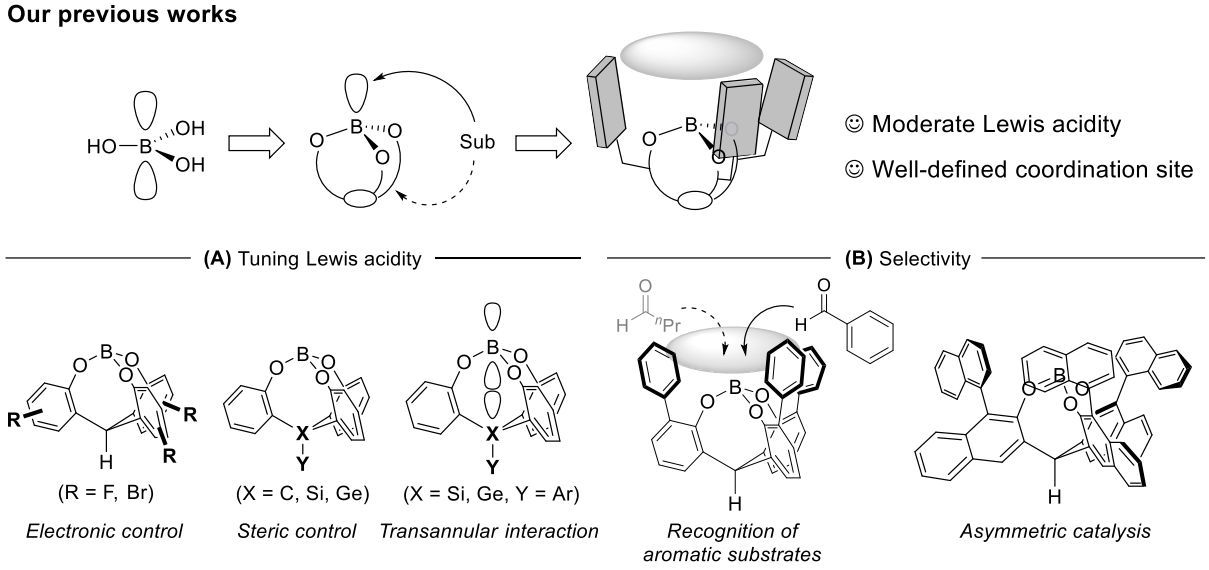

Figure 2. Cage-shaped borate with various tuning factors of Lewis acidity and coordination environment.

The cage-shaped framework has much potential for the fine tuning of not only Lewis acidity but also the coordination environment. In this study, rigid cage-shaped ligands were employed to control the coordination environment and catalytic activities of Lewis acids with a group 13/14 center.

In chapter 1, the mechanistic study of the recognition of aromatic compounds was conducted by experiments and theoretical calculations. Electronic and steric effects on the selectivity were investigated with borate complexes bearing different types of π-pocket. According to the results of the kinetic study and the theoretical calculation, it was clarified that the selectivity is induced by noncovalent interactions between π-pocket and aromatic substrates.

In chapter 2, monomeric cage-shaped aluminum complexes were synthesized without forming multinuclear aluminum complexes. The bulky triphenoxy ligand controlled the Lewis acidity of the aluminum center and enabled the aluminum complex to work as a Lewis acid catalyst with a moderate Lewis acidity. The aluminum complex can activate substrates via a highly coordinated state. The interaction with substrates at the highly coordinated state played an essential role in the β selective glycosylation reaction.

In chapter 3, a rigid atrane structure effectively controlled the coordination number of heavier group 14 elements (E = Si, Ge, Sn). The rigid and bulky ligand stabilized heavier group 14 cations with high reactivities thermodynamically and kinetically and enabled them to work as a hard and soft Lewis superacid (LSA). These cations were applied to many catalytic reactions with hard and soft substrates.

Chapter 1 ***Chapter 2*** ***Chapter 3***

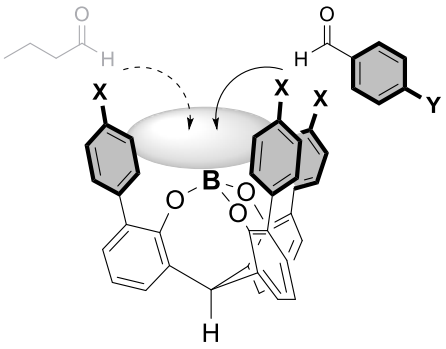

Mechanistic Study for Recognition of Aromatics

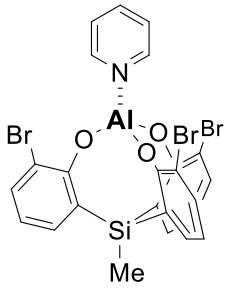

Monomeric Aluminum Complex Stereoselective Glycosylation

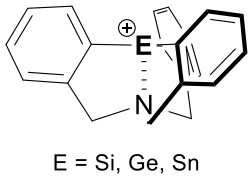

Atrane-type Group 14 Cations Hard and Soft Lewis Superacids

References

[1] H. Yamamoto, Ed. , *Lewis Acids in Organic Synthesis*, Wiley-VCH, Weinheim, **2000**.
[2] S. Kobayashi, S. Nagayama, *J. Am. Chem. Soc.* **1997**, *119*, 10049–10053.
[3] D. J. Faizi, A. Issaian, A. J. Davis, S. A. Blum, *J. Am. Chem. Soc.* **2016**, *138*, 2126–2129.
[4] Y. Kita, T. Yata, Y. Nishimoto, K. Chiba, M. Yasuda, *Chem. Sci.* **2018**, *9*, 6041–6052.
[5] D. J. Morrison, W. E. Piers, *Org. Lett.* **2003**, *5*, 2857–2860.
[6] J. M. Hawkins, S. Loren, *J. Am. Chem. Soc.* **1991**, *113*, 7794–7795.
[7] K. Maruoka, S. Saito, H. Yamamoto, *Synlett* **1994**, *1994*, 439–440.
[8] G. C. Welch, R. R. S. Juan, J. D. Masuda, D. W. Stephan, *Science* **2006**, *314*, 1124–1126.
[9] M. Kira, M. Kobayashi, H. Sakurai, *Tetrahedron Lett.* **1987**, *28*, 4081–4084.
[10] Y. Nishimoto, S. Nakao, S. Machinaka, F. Hidaka, M. Yasuda, *Chem. – A Eur. J.* **2019**, *25*, 10792–10796.
[11] C. Eschmann, L. Song, P. R. Schreiner, *Angew. Chem. Int. Ed.* **2021**, *60*, 4823–4832.
[12] M. Yasuda, S. Yoshioka, S. Yamasaki, T. Somyo, K. Chiba, A. Baba, *Org. Lett.* **2006**, *8*, 761–764.
[13] M. Yasuda, H. Nakajima, R. Takeda, S. Yoshioka, S. Yamasaki, K. Chiba, A. Baba, *Chem. - A Eur. J.* **2011**, *17*, 3856–3867.
[14] A. Konishi, K. Nakaoka, H. Nakajima, K. Chiba, A. Baba, M. Yasuda, *Chem. - A Eur. J.* **2017**, *23*, 5219–5223.
[15] H. Nakajima, M. Yasuda, R. Takeda, A. Baba, *Angew. Chem. Int. Ed.* **2012**, *51*, 3867–3870.
[16] A. Konishi, K. Nakaoka, H. Maruyama, H. Nakajima, T. Eguchi, A. Baba, M. Yasuda, *Chem. - A Eur. J.* **2017**, *23*, 1273–1277.

Chapter 1
Selective Activation of Aromatic Aldehydes Promoted by Dispersion Interactions: Steric and Electronic Factors of a π-Pocket within Cage-Shaped Borates for Molecular Recognition

1-1. Introduction

The development of selective bond-forming reactions has been an important subject in organic synthesis. Use of non-covalent interactions, such as hydrogen bonding,[1–3] halogen bonding,[4–6] π–π,[7–11] and ion/lone pair–π interactions[12–16] is one of the promising approaches for selective transformation of organic molecules.[17],[18] In biological systems, enzymes utilize hydrogen bonding as one of the major catalytic factors that selectively recognize substrates and facilitate chemical transformations. Notably, mimicking geometric and electronic structures of enzymes has provided many small organic molecules that possess potent catalytic activities,[19–22] which realizes the regio-, chemo-, and stereoselective transformations of fine chemicals.[23–25]

Lewis acid–mediated electrophilic reactions of carbonyls are the most fundamental and important reactions for carbon–carbon bond formations that construct many useful molecules.[26] The coordination of carbonyl groups to Lewis acids exerts a dramatic effect on the rates and selectivities of the reactions at the carbonyl center.[27] The Lewis acidity of the metal center and the geometric features of ligands play a critical role in determining selectivities. Binding between the metal and heteroatom as well as coordinative interactions can work as the principal interaction for molecular recognition.[28] This selective formation of a carbonyl–acid complex has realized the chemoselective functionalization of carbonyl compounds.[29–32] Several accomplishments of the chemoselective transformation of carbonyls have become available, based on the size of reagents,[33–39] the difference in the Lewis basicity of carbonyls,[38,40,41] and the use of the supramolecular donor-acceptor interactions.[42] However, the discrimination between similarly sized aromatic and aliphatic aldehydes that have no functional anchors to strongly interact with the metal center still remains a challenging issue[41,43,44] due to the lack of suitable methodologies including the developments of acceptable catalytic systems.

For extrication from this problem, we have focused on clathrate structures, which can embed the Lewis acid center into the π-space cavity (Figure 1A). The π-space surrounding the metal center of the Lewis acid is referred to as a *π-pocket*. Aromatic components with a π-pocket can behave as a host unit and should mainly distinguish aromatic over aliphatic aldehydes as guest molecules through multipoint aromatic–aromatic non-covalent interactions involving π–π stacking, CH–π interactions and CH–CH interactions, which are typified by London dispersion.[44–51] The molecular recognition ahead of the usual carbonyl-acid interaction capturing certain aldehydes leads to the chemoselective transformation of aromatic aldehydes over aliphatic ones. On the basis of the design concept, a cage-shaped borate **1a**B

has been identified as a key framework (Figure 1A).[52],[53] Our previous study demonstrated that the *ortho*-phenyl substituted cage-shaped borate **1b**B catalyzed the chemoselective hetero Diels-Alder reaction of Danishefsky's diene **2** with a mixture of aldehydes **3a**/**3b** (Figure 1B).[54] The borate **1b**B·thf selectively activated benzaldehyde **3b** over butanal **3a** in a competitive reaction to give the corresponding adducts (**4a**/**4b**) in a ratio of 30:70. The chemoselectivity did not appear when loading the borate **1a**B·thf, which has no π-pocket. This selectivity was the first example where an aromatic aldehyde was recognized over an aliphatic one in a catalytic manner. Within **1b**B, the three phenyl groups built a π-pocket around the B atom of the Lewis acid center, which may function as the site for molecular recognition. The preferential recognition of aromatic aldehydes over aliphatic ones might be driven by aromatic–aromatic interactions among π-pocket components and aldehydes; however, further insights into the mechanistic details remain elusive. Scoping the generality of the chemoselectivity and evaluating its origin should allow for the discovery of novel catalytic design based on the concept of the π-pocket.

The high accessibility of the tripodal ligand has ensured that the chemical modifications of cage-shaped Lewis acids, which lead to fine control of the Lewis acidity,[55],[56] enables a variety of catalytic activities.[57–59] The feasibility of the chemical modifications of the complex **1b**B prompted us to investigate the electronic and/or geometric effect of a π-pocket on molecular recognition. For assessment of these factors, we designed the three types of cage-shaped borates by changing the *ortho*-substituents. The first derivatives (**1a**B, **1b**B, **1c**B, and **1d**B) have varying numbers of *ortho*-phenyl groups from zero to three, making a non-, partially, and fully constructed π-pocket (Figure 1C-I). The second derivatives (**1b**B and **1e**–**j**B) have the π-pocket built by various aryl groups with electron-donating/withdrawing or bulky substituents, creating an electronically and sterically perturbed π-pocket (Figure 1C-II). The third derivative (**1k**B) has no π-pocket but a space built by three alkyl groups (Figure 1C-III). The synthesis and characterization of these derivatives of cage-shaped borates, including competitive reactions, kinetic studies, and quantum chemical calculations, demonstrate that the geometric and electronic environments of a π-pocket have a significant impact on the step of substrates approaching the metal center, which leads to the preferred selectivity of aromatic aldehydes.

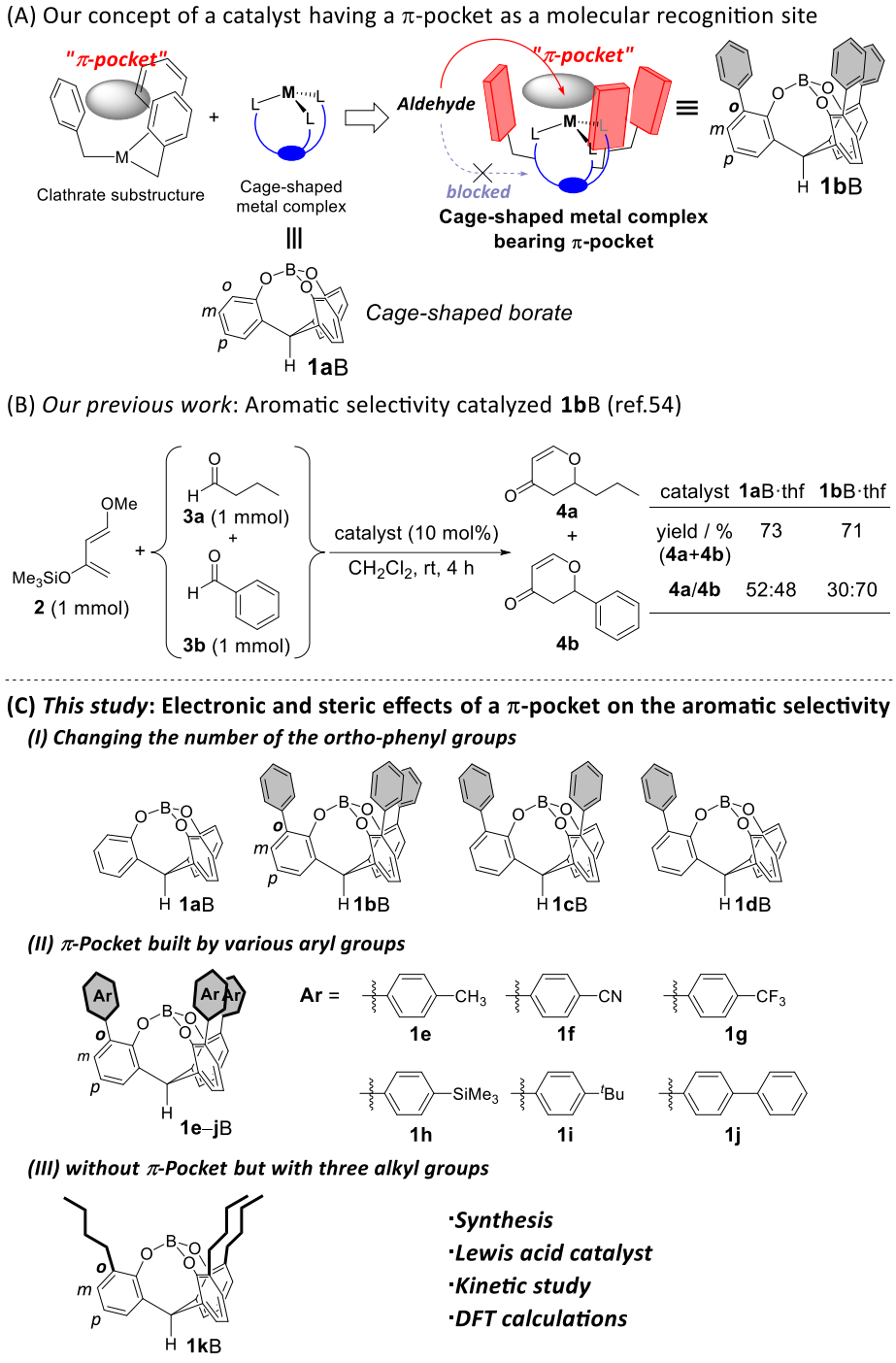

Figure 1. (A) Our concept of the design for the cage-shaped borate with a π-pocket. (B) Our previous result for the aromatic selective hetero Diels-Alder reaction of **2** with **3** catalyzed by **1a**B or **1b**B·thf. (C) Molecular structures of **1**B described in the manuscript to investigate the electronic and/or geometric effect of a π-pocket on molecular recognitions.

1-2. Results and Discussion

Synthesis

The cage-shaped borates having either no π-pocket (**1a**B·L; L = ligand: THF or pyridine) or a π-pocket (**1b**B·L) were synthesized according to our previous studies.[52],[55] In Scheme 1A, the synthetic route of the partially phenyl substituted cage-shaped borates **1c**B·L and **1d**B·L are represented. *Ortho*-lithiation of anisole derivatives followed by treatment with *N*,*N*-dimethylcarbamoyl chloride gave the benzophenone derivative **5**.[60] The introduction of the third aromatic group was conducted by treating **5** with anisyllithium salts to afford the triarylmethanol derivative **6**. The treatment of **6** with chlorodimethylsilane in the presence of a catalytic amount of $InCl_3$[61] gave the reduced compound **7**. The triphenol derivatives **1c**/**d**H_3 were obtained after treatment of **7** with BBr_3. The reaction of **1c**/**d**H_3 with BH_3·thf generated cage-shaped borates **1c**/**d**B·thf as a THF complex.

The feasible scrutiny of the modulated π-pocket on chemoselectivity required the late-stage diversification of the tripodal ligand for the cage-shaped borates bearing various aromatic group at the *ortho*-positions. The presence of three *ortho*-bromo groups in precursor **9** of the tripodal ligand is suitable for the introduction of various aromatic or aliphatic substituents through transition metal–catalyzed coupling reactions. The synthetic route for the cage-shaped borates **1e**–**j**H_3 with various *ortho*-aryl groups is shown in Scheme 1B. After methylation of the hydroxyl group of 2,6-dibromophenol, the monolithiation of 1,3-dibromo-2-methoxybenzene followed by treatment with ethyl chloroformate gave *ortho*-brominated triarylmethanol **8**. The use of less than a stoichiometric amount of *n*BuLi suppressed the undesirable dilithiation. The treatment of **8** with chlorodimethylsilane in the presence of a catalytic amount of $InCl_3$[61] gave the reduced compound **9**. The introduction of aromatic groups into **9** was carried out under Suzuki-Miyaura coupling conditions. The palladium-catalyzed coupling of **9** with various arylboronic acids having electron-donating/withdrawing and bulky substituents proceeded to give the *ortho*-arylated triarylmethane derivative **10**. Changing the arylboronic acids into tributylborane under the palladium-catalyzed coupling conditions[62] furnished tributylated triarylmethane **11**. The triphenol derivatives **1e**–**k**H_3 were obtained after treatment of **10**/**11** with BBr_3 or 1-dodecanethiol.[63] The reaction of **1e**–**k**H_3, with BH_3·thf, generated the cage-shaped borates **1e**–**k**B·thf (Scheme 1B). All cage-shaped borates were fully characterized by ^{1}H, ^{13}C, and ^{11}B NMR spectroscopies.

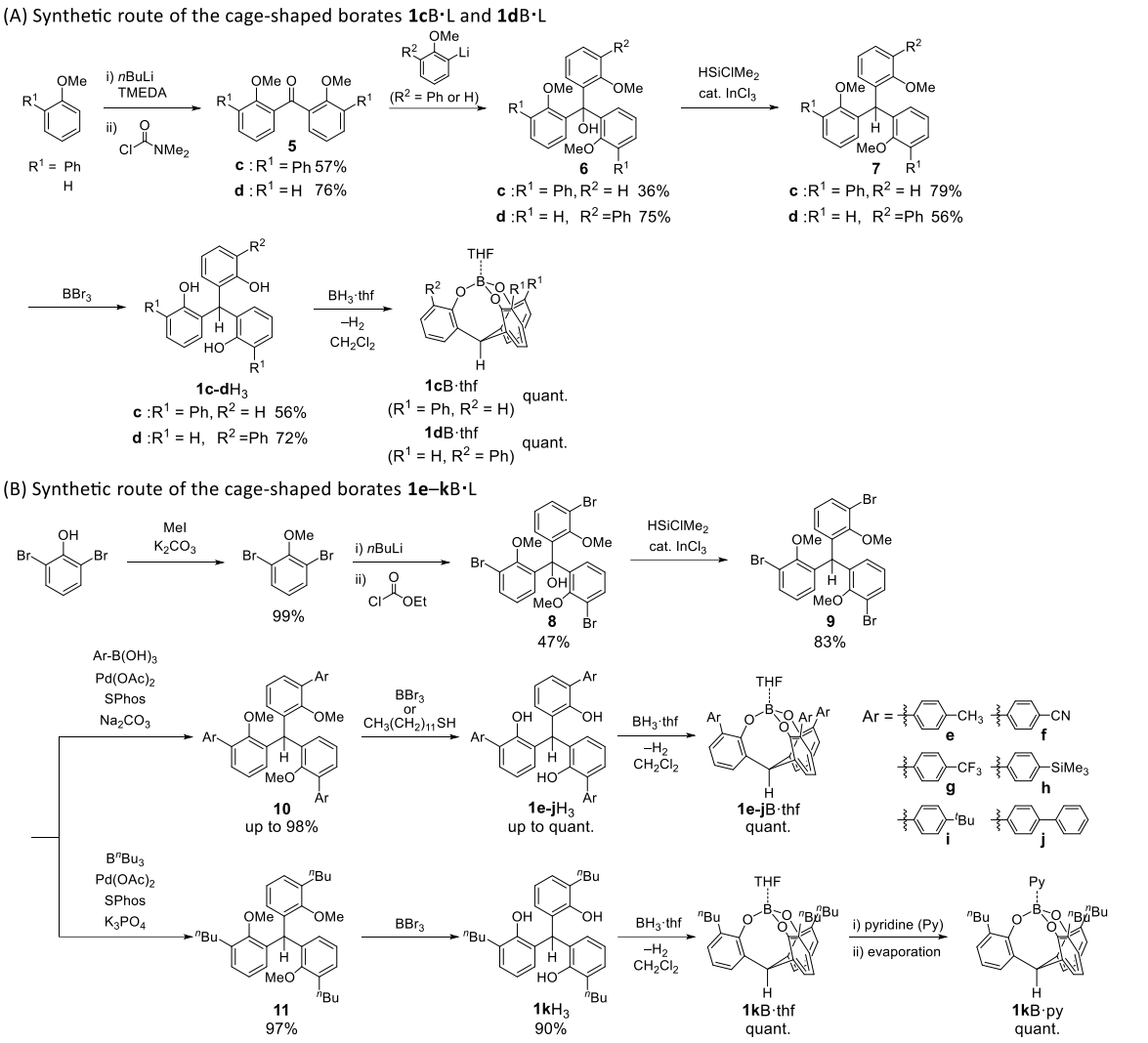

Scheme 1. Synthetic routes for cage-shaped borates of (A) **1c**B·L and **1d**B·L and (B) **1e**–**k**B·L.

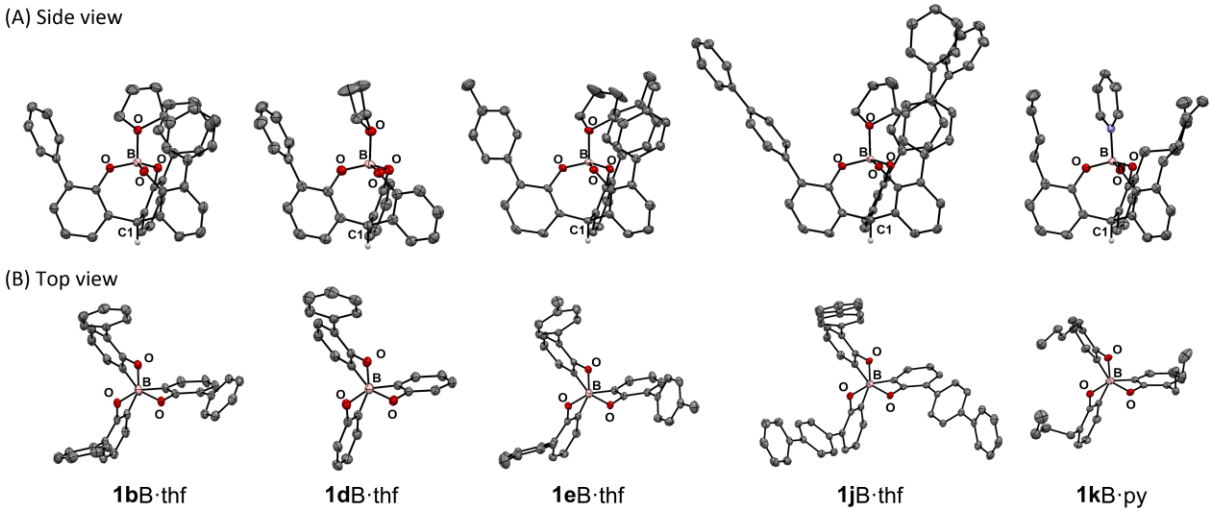

Figure 2. Ortep drawings of cage-shaped borates **1b**B·thf, **1d**B·thf, **1e**B·thf, **1j**B·thf, and **1k**B·py with 50% probability ellipsoids. Some hydrogen atoms are omitted for clarity. (A) Side view and (B) top view.

Molecular geometries and Lewis acidity of cage-shaped borates having a π-pocket

First, we examined the molecular geometries and the fundamental catalytic activity of cage-shaped borates with a π-pocket. Cage-shaped borates **1b**B·thf, **1d**B·thf, **1e**B·thf, **1j**B·thf, and **1k**B·py gave crystals of sufficient quality to be analyzed as single-crystal structures. The ORTEP drawings of the cage-shaped borates are shown in Figure 2 and the selected geometrical parameters and tetrahedral character (THC)[64] of the boron atom are summarized in Table 1.

Table 1. Summary of selected bond lengths, angles, and tetrahedral character (THC) of the boron atom for **1b**B·thf, **1e**B·thf, **1j**B·thf, and **1k**B·py.

	1bB·thf	**1d**B·thf	**1e**B·thf	**1j**B·thf	**1k**B·py
B–C1 / Å	2.946	2.968	2.950[a]	2.916	3.003[a]
B–O_{THF} (N_{Py}) / Å	1.594(2)	1.592(2)	1.592(2)[a]	1.597(2)	1.544(2)[a]
∠O–B–O / °[a]	114.9(1)	114.9(1)	114.8(2)	114.8(1)	114.3(1)
THC / %	48.2	48.5	49.6	50.0	54.1

[a] Mean values.

No significant structural differences were observed in the molecular geometries of **1b**B·thf, **1d**B·thf, **1e**B·thf, **1j**B·thf, and **1k**B·py, as shown in Table 1. This observation indicates that the steric and/or electronic effects of the *ortho*-substituents on molecular geometry is quite small. The ligand on the B atom slightly influenced the THC values; the pyridine complex of **1k**B·py exhibited a somewhat larger THC (54.1%) than those of the THF complexes (~49%).

In contrast to the structural similarity of these cage-shaped borates, the Lewis acidity of the cage-shaped borates **1b**B and **1e**–**k**B, which are the analogues bearing three aromatic substituents at the *ortho*-positions, gradually shifted depending on the introduced substituents. The Lewis acidity was evaluated via the infrared (IR) stretching frequency of 2,6-dimethyl-γ-pyrone **12** ligated to the complex, as shown in Table 2. The stretching frequency of the carbonyl (C=O) in **12** clearly shows the degree of Lewis acidity. The larger Δν(C=O) values mean higher Lewis acidities. The electron-donating groups (**1e**B: *p*-CH_3; **1h**B: *p*-$SiMe_3$; **1i**B: *p*-^{t}Bu) on the π-pocket exhibited a small shift of Δν values compared to that of **1b**B. In contrast, the introduction of electron-withdrawing groups (**1f**B: *p*-CN; **1g**B: *p*–CF_3) and the extension of π-conjugation (**1j**B: *p*-Ph) on the π-pocket effectively increased the Lewis acidity of borates. The highest Lewis acidity of **1f**B should be derived from both the electron-withdrawing and π-extension features of CN-groups. The effect of alkyl groups on the shift of the Δν(C=O) value was minimal; the

borate **1k**B with three butyl groups exhibited the same value as that of **1a**B. According to our previous studies, [52][55][57] we calculated the LUMO energy levels of the cage-shaped borates. The calculated LUMO levels at the B3PW91/6-31+G**//B3PW91/6-31G** level correlated with the experimental observations. An effective conjugation between the B atom and the aryl groups of the π-pocket was estimated in the LUMO. The electronic communications between the B atom and the surrounding aryl groups including the *para*-substituents contributed to the gradual shift of the energy level of the LUMOs, providing precise control of the Lewis acidity of the cage-shaped borates having a π-pocket (Figure S7).

Table 2. Estimation of Lewis acidity and LUMO level.

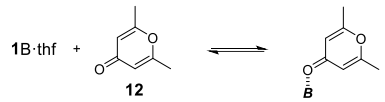

borate **1**	*ortho*-group within **1**B	Δν(C=O)[a]/ cm^{-1}	LUMO[b]/ eV
1aB·thf	non	13.7	–0.79
1bB·thf	C_6H_5	13.9	–1.16
1eB·thf	*p*-$CH_3C_6H_4$	14.5	–1.05
1fB·thf	*p*-CNC_6H_4	17.4	–2.20
1gB·thf	*p*-$CF_3C_6H_4$	15.7	–1.76
1hB·thf	*p*-$SiMe_3C_6H_4$	14.0	-[c]
1iB·thf	*p*-^{t}BuC_6H_4	14.0	-[c]
1jB·thf	*p*-PhC_6H_4	16.2	–1.40
1kB·thf	^{n}Bu	13.7	–0.63

[a] The stretching frequency of the carbonyl of free **12** appears at 1670.1 cm^{-1}. [b] The calculations were conducted at the B3PW91/6-31+G**//B3PW91/6-31G** level. The coordinated THF was omitted for the calculations. [c] The structural optimizations failed due to the high cost of the calculations.

To test the catalytic activity of the borates with π-pockets, we used the borates as catalysts in the hetero Diels-Alder reaction with 1,3-butadiene **13** and 4-methoxybenzaldehyde **3c** (Table 3 and S1). The conventional Lewis acids, such as $B(OPh)_3$ and $BF_3{\cdot}Et_2O$, did not catalyze the reaction (Table S2). The Lewis acidity of these conventional Lewis acids would be too weak to activate the substrates or too strong to dissociate from the products. Both situations are unfavorable to establishing the catalytic reaction system. The borate **1a**B·thf without a π-pocket also exhibited no catalytic activity (entry 1). In

contrast, the borates with a π-pocket demonstrated catalytic activities (entries 2–6). The yield of the adduct **14** approximately correlates with the order of the Lewis acidity, which is estimated by IR measurements of the applied borate catalyst (**1a**B < **1b**B < **1i**B < **1e**B < **1g**B < **1j**B). Notably, the borates with a π-pocket around the B atom furnished sufficient yields, which implies that the distinctive cage-shaped structure plays an important role in enhancing the catalytic activity. The borates of **1g**B·thf and **1j**B·thf demonstrated high catalytic activities despite the low reactivity of the electron-rich aldehyde **3c**. The modifications of the π-pocket at distant positions from the B atom center can impact the catalytic activity of cage-shaped borates.

Table 3. Catalytic activity of borates with various π-pockets in the hetero Diels-Alder reaction with **13** and **3c**

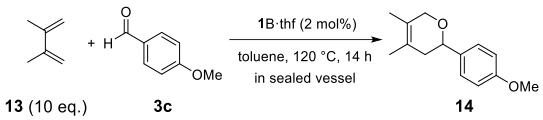

13 (10 eq.) **3c** **14**

entry	borate **1**	*ortho*-group within **1**B	yield of **14**[a]/ %	Δν(C=O)/ cm^{-1}
1	**1a**B·thf	non	5	13.7
2	**1b**B·thf	C_6H_5	43	13.9
3	**1e**B·thf	*p*-$CH_3C_6H_4$	49	14.5
4	**1g**B·thf	*p*-$CF_3C_6H_4$	96	15.7
5	**1i**B·thf	*p*-^{t}BuC_6H_4	38	14.0
6	**1j**B·thf	*p*-PhC_6H_4	73	16.2

[a] Yields were determined by ^{1}H NMR measurement using 1,1,2,2-tetrachloroethane as an internal standard.

Effect of the number of phenyl groups for the π-pocket on aromatic selectivity

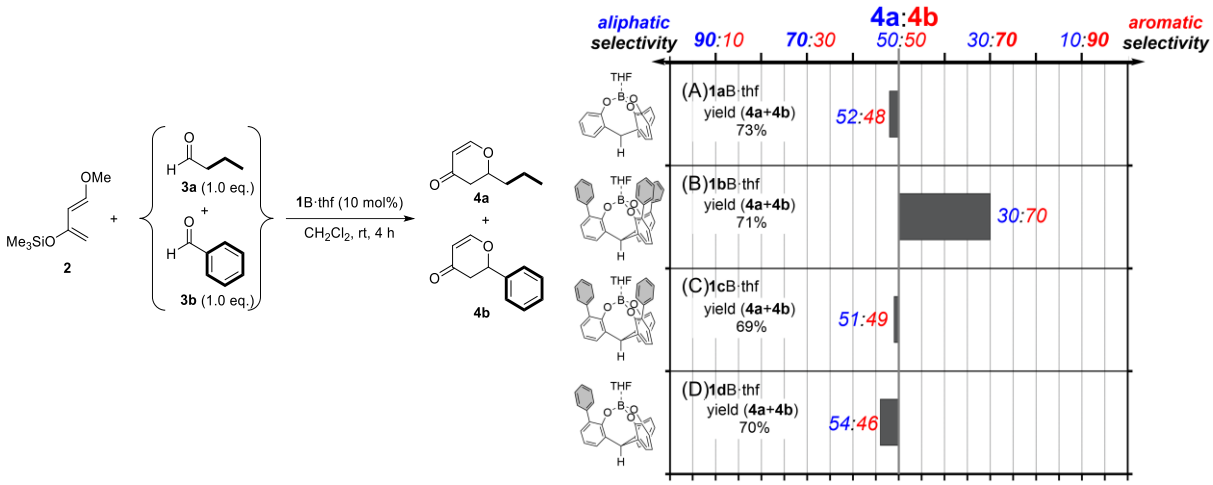

Figure 3. Competitive hetero Diels-Alder reaction between **3a** and **3b** catalyzed by cage-shaped borates **1a**B, **1b**B, **1c**B, and **1d**B. Yields were determined by ^{1}H NMR measurement using 1,1,2,2-tetrachloroethane as an internal standard.

Secondly, we investigated the importance of π-pocket structure around the B center by using a series of borate catalysts **1a**B, **1b**B, **1c**B, and **1d**B. To test chemoselectivity, we used these borates as catalysts in a competitive hetero Diels-Alder reaction of Danishefsky's diene **2** with a mixture of **3a** and **3b**. This competitive cycloaddition had already served as a model reaction previously (Figure 1B).[54] Because butanal **3a** and benzaldehyde **3b** have similar steric demands,[65] the competitive reaction between these aldehydes with Danishefsky's diene **2** would be a suitable combination of substrates to investigate chemoselectivity.

The yields with a ratio of **4a**/**4b** in the competitive hetero Diels-Alder reaction are summarized in Figure 3. As previously reported, the cage-shaped borate **1a**B·thf having no π-pocket gave the products in a 73% yield with the ratio of 52:48, indicating that two aldehydes **3a** and **3b** exhibited the same affinities with the B center (Figure 3A). Next, fully or partially *ortho*-phenyl substituted cage-shaped borates **1b**B·thf, **1c**B·thf, and **1d**B·thf were examined (Figures 3B–D). Although the catalytic activity was irreverent to the whether there were one or two or three (the total yields [**4a**+**4b**] were similar among all entries in Figure 3), the selective ratio of **4a**/**4b** was highly dependent on the structural integrity of the π-pocket. The significant selectivity of **3b** over **3a** appeared only in the catalytic system of the borate **1b**B having the fully constructed π-pocket (**4a**/**4b** = 30:70). The others, having the partially constructed π-pockets exhibited no selectivity, which is comparable to that of **1a**B (**4a**/**4b** = 52:48) having no π-pocket (51:49 (**1c**B); 54:46 (**1d**B)).

Effect of the electronically and sterically perturbed π-pocket on the selectivity for aromatic compounds

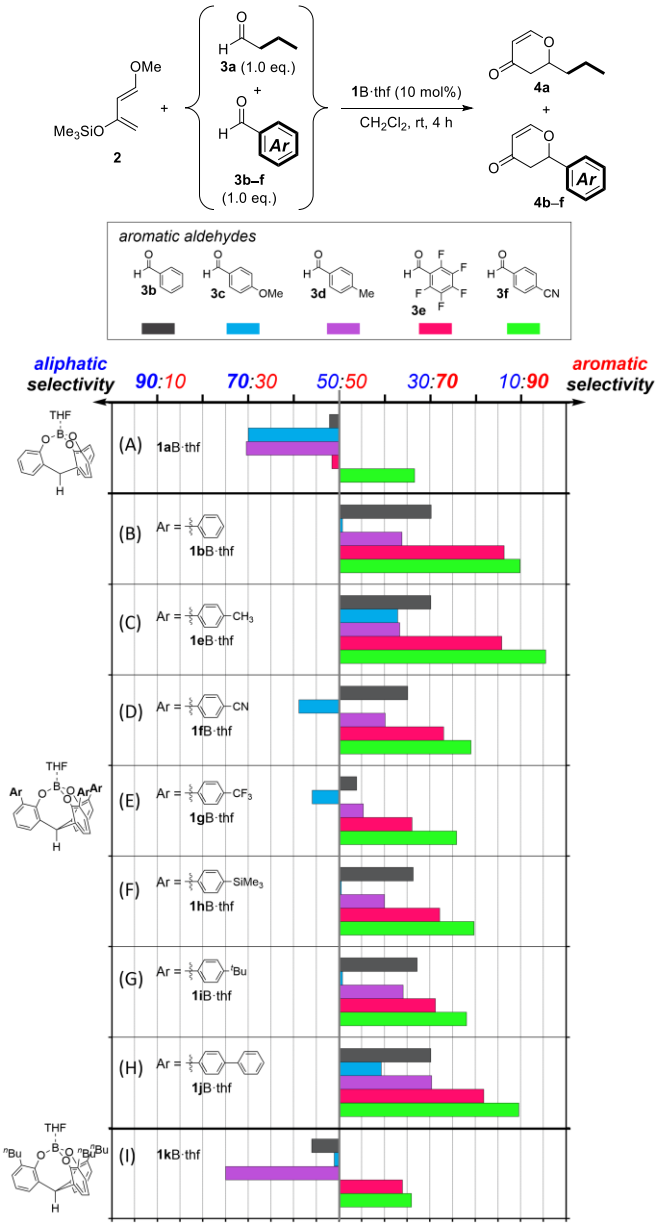

Figure 4. Observed chemoselectivity in competitive hetero Diels-Alder reaction between **3a** and various benzaldehyde derivatives **3b**–**f**.

Next, we examined the effect of the electronically or sterically perturbed π-pocket on the selectivity of aromatic aldehydes. The borates **1b**B and **1e**–**j**B were used as catalysts in the competitive hetero Diels-Alder reactions between **3a** and various benzaldehyde derivatives **3b**–**3f** with Danishefsky's diene **2**. These results should provide valuable information on the interaction between the aromatic groups for the applied π-pockets and aldehydes. A total of 45 reactions was investigated. The summary for the yields of the adducts (**4a**+**4b**–**f**) is shown in Table S3. All reactions were sufficiently catalyzed by the

borates to give the adducts in acceptable yields, thus, we herein concentrated on the chemoselectivity of **3b**–**3f** over **3a**.

The observed chemoselectivity between aliphatic (**3a**) and aromatic (**3b**–**f**) aldehydes is depicted in Figure 4. The borate **1a**B without a π-pocket exhibited no selectivity for aromatic aldehydes **3b**–**e**, which tends to be a low preference of aliphatic aldehyde **3a** (Figure 4A). For 4-cyanobenzaldehyde **3f**, moderate chemoselectivity for the aromatic aldehyde appeared, which might be caused by the high reactivity of **3f** induced by the low LUMO energy level. In contrast to the results of **1a**B·thf, the cage-shaped borates with various π-pockets **1b**B·thf and **1e**–**j**B·thf demonstrated the significant chemoselectivity of aromatic aldehydes **3b**–**f** over **3a** (Figures 4B–H). The following noteworthy aspects are represented.

(i) *The Lewis acidity of borates is indirectly correlated with the observed selectivity of the aromatic aldehydes.* While the borate **1f**B with the highest Lewis acidity gave moderate selectivity for all aldehydes (Figure 4D), the borate **1e**B with moderate Lewis acidity among them showed high selectivity for a wide range of aromatic aldehydes (Figure 4C). The highest selectivity for **3f** (**4a**/**4f** = 4:96) yielded by **1e**B was comparable to the one previously reported.[54] These results suggest that the observed selectivity is determined by the approaching steps of the substrates to the B center rather than the generation steps of carbonyl–acid complexes.

(ii) *Steric hindrance on a π-pocket has a small impact on selectivity.* The borates **1h**B and **1i**B, which have the large substituents on the π-pockets, showed comparable selectivity to that of **1b**B (Figures 4F and G). The uptake of substrates into the π-pocket is not inhibited by these large substituents.

(iii) *The electrostatic interaction between the π-pocket and substrates might be effective for selectivity but the selectivity depends on the combination of borates and aldehydes.* We previously reported that high selectivity was attained when applying the electron-poor aromatic aldehydes, such as **3e** and **3f**, to the reactions catalyzed by **1b**B (Figure 4B). The same trends were observed in the reactions catalyzed by the borates **1e**B and **1j**B with the methylated and phenylated π-pocket, respectively (Figures 4C and H). These observations imply that an electron-rich π-pocket assists with some electrostatic interactions,[7],[66] such as donor-acceptor or dipolar interaction, with aromatic aldehydes, realizing high chemoselectivity. However, the borate with a π-pocket with electron-donating/withdrawing groups does not always exhibit preferential activation of the aromatic aldehyde with electron-withdrawing/donating groups. For the borate **1e**B with the methylated π-pocket, a better selectivity for the electron-rich aldehyde, 4-methoxybenzaldehyde **3c**, was observed compared with those catalyzed by the other borates (Figure 4C). The catalytic systems of **1f**B with the cyanated π-pocket and **1g**B with the trifluoromethylated π-pocket showed low selectivity for the electron-rich aldehydes **3c** and **3d** (Figures

4D and E). These results suggest that other non-covalent interactions, such as CH–π and π–π stacking interactions, play a more important role in selectivity.

(iv) *The three aromatic panels are essential for determining the chemoselectivity of aromatic aldehydes over butanal **3a**.* The borate **1k**B that has three butyl groups instead of aromatic groups for the π-pocket showed no chemoselectivity towards aromatic aldehydes **3b**–**d** over **3a** (Figure 4i). Even when the aldehydes **3e** and **3f** with electron-withdrawing groups, which are apt to show the selectivity of aromatic aldehydes, were employed, the preferences of these aldehydes over **3a** were constrained compared with the reactions catalyzed by other borates with π-pocket moieties. These results strongly indicate that merely introducing some substituents into the *ortho*-positions of the borate is not necessary nor sufficient for the selectivity of aromatic aldehydes. The presence of the three aromatic panels around the B center is an essential factor to give the observed chemoselectivity of aromatic substrates.

Table 4. Kinetic studies for hetero Diels-Alder reaction.

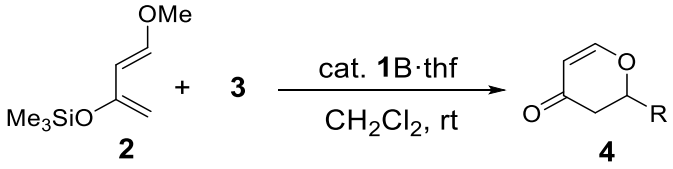

entry	borate **1**	aldehyde **3**	$\Delta H^{\ddagger}$/ kcal·mol^{-1}	$\Delta S^{\ddagger}$/ cal·(K·mol)$^{-1}$	$\Delta G^{\ddagger}$(298 K)/ kcal·mol^{-1}
1	**1a**B·thf	**3a**	3.15	–54.1	19.3
2		**3b**	3.95	–55.6	20.5
3	**1b**B·thf	**3a**	7.02	–41.2	19.3
4		**3b**	7.51	–40.6	19.6

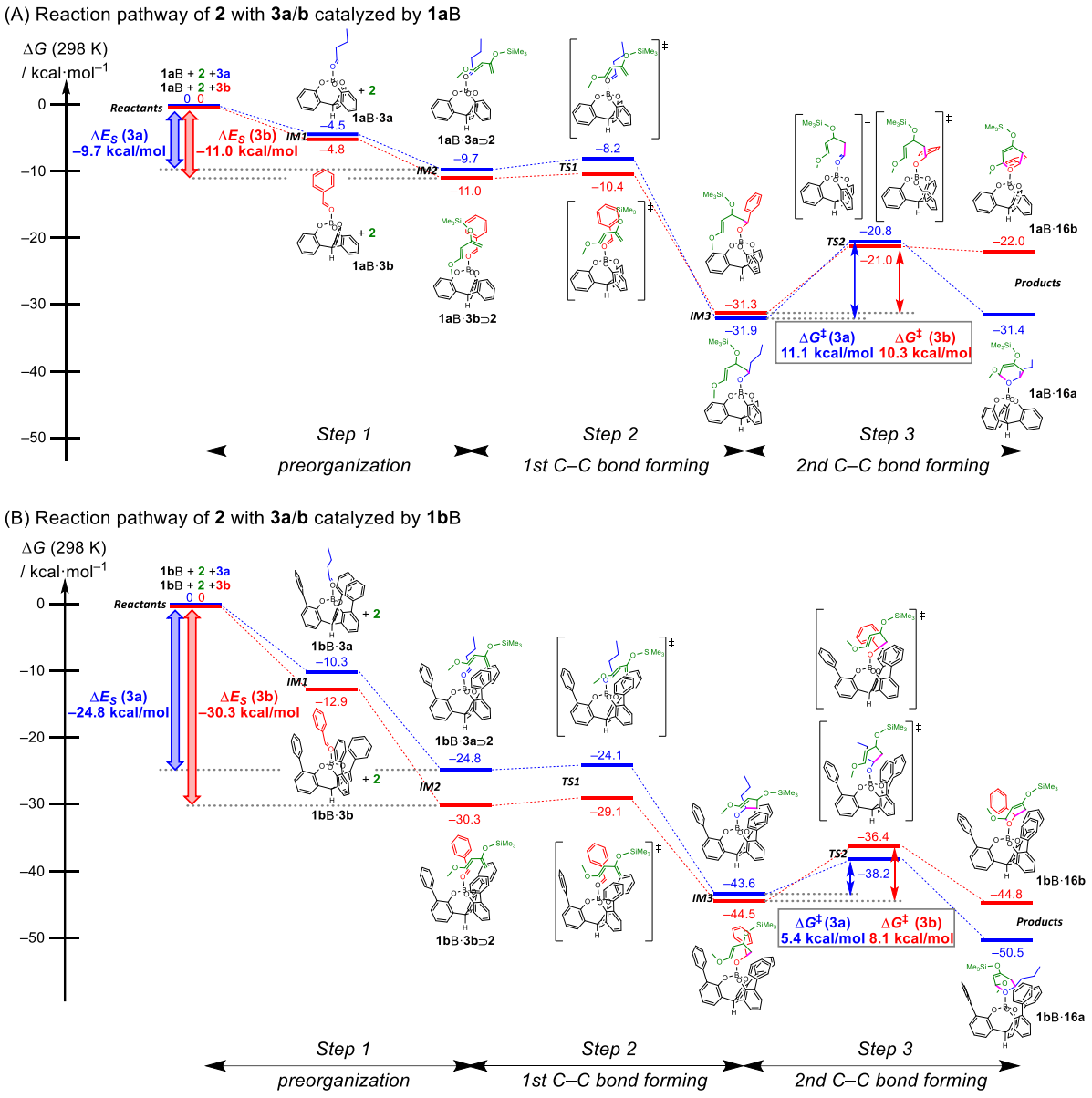

Figure 5. The energy profiles of the hetero Diels-Alder reaction of **2** with **3a** or **3b** catalyzed by (A) **1a**B or (B) **1b**B. DFT calculation was performed using ωB97XD/def2svp. Solvation effect was introduced using the IEFPCM model, and dichloromethane was used as a solvent.

To gain further insights into the chemoselectivity of **3b** over **3a**, kinetic studies of the hetero Diels-Alder reactions of **2** with **3a**/**b** catalyzed by borates **1a**/**b**B·thf were conducted using *in situ* React IR spectroscopy. Kinetic parameters were assumed by monitoring the decay of the ν(C=O) of aldehyde **3** around 1700 cm^{-1} in the reaction mixture in CH_2Cl_2 (Figure S6). The detailed reaction profiles are summarized in the Supporting Information. All reactions obey the first order for **2**, aldehyde **3**, and the borate **1**B·thf (rate = k_{obs}[**2**]^1[**3**]^1[**1**B·thf]^1); the reaction order was irrelevant of the types of aldehydes and borates. The estimated activation parameters are summarized in Table 4. No significant difference

in these parameters was observed between the reactions of **3a** and **3b** with each borate catalyst (entries 1 vs. 2 or 3 vs. 4). The negative values for the activation entropy ($\Delta S^{\ddagger}$) suggested that the rate-determining steps of the reactions include the associative step for the C–C bond formations between **2** and **3**. When comparing the catalysts **1a**B and **1b**B, the activation enthalpies ($\Delta H^{\ddagger}$) of **1b**B were twice as large as those of **1a**B. These results imply that the initial state driven by **1b**B should be energetically more stable than that driven by **1a**B. Considering the small differences in the activation free energy ($\Delta G^{\ddagger}$), the initial reaction step, which includes the approach of the substrates to the B center, rather than the rate-determining stage, would be essential for the observed chemoselectivity of **3b** catalyzed by **1b**B over **3a** catalyzed by **1b**B.

Theoretical studies on chemoselectivity

The small difference of the activation free energy ($\Delta G^{\ddagger}$) between **3a** and **3b** raises the question regarding the factor that determines chemoselectivity. To reveal the reaction mechanisms for the hetero Diels-Alder reactions of **2** with **3a**/**b** catalyzed by the borate **1a**/**b**B·thf, quantum chemical calculations at the ωB97XD/def2svp level (including solvent effect by the IEFPCM model for CH_2Cl_2) were performed. Figure 5 shows the computational results for the reaction mechanism.

In all reactions, the estimated mechanism consists of three steps. Initially, the borate **1**B activates the aldehyde **3** to give the carbonyl–acid complex **1**B·**3** at the **IM1** state; subsequently, the diene **2** approaches the complex **1**B·**3** to form an inclusion complex **1**B·**3**⊃**2** at the preorganized state **IM2** (Step 1). The addition of diene **2** to the carbonyl of **3** occurs from **1**B·**3**⊃**2**. Although a concerted addition is predicted in the non-catalyzed reaction (Figure S8), the catalyst **1**B shifts the mechanism to a step-wise formation of the two C–C bonds. The first C–C bond formation passes through a transition state with a small energy barrier (**TS1**) to exergonically give the **IM3** state (Step 2). The second C–C bond formation proceeds through a transition state (**TS2**), giving rise to the adduct **16** as an adduct–borate complex **1**B·**16** (Step 3). The highest activation energy observed at **TS2** indicates that Step 3 is the rate-determining step. For reactions catalyzed by **1a**B without a π-pocket, the activation energy for butanal **3a** (11.1 kcal/mol at 298 K) is comparable to that of benzaldehyde **3b** (10.3 kcal/mol). In the case of **1b**B with a π-pocket, the more both activation energies are lowered, the slightly larger value of **3b** (8.1 kcal/mol) is estimated compared to that of **3a** (5.4 kcal/mol). These low and similar activation energies between **3a** and **3b** in the reactions catalyzed by **1b**B illustrate that Step 3 hardly participates in the chemoselectivity given by the π-pocket catalyst **1b**B, which agrees with the results of the kinetic studies (Table 4).

Alternatively, the preorganization from the initial reactants to the inclusion complex **1**B·**3**⊃**2** (Step 1) gives an evocative difference in the stabilization energy (ΔE_S). For the reactions catalyzed by **1a**B

without a π-pocket, the stabilization energy for **1a**B·**3a**⊃**2** (–9.7 kcal/mol) is comparable to that of **1a**B·**3b**⊃**2** (–11.0 kcal/mol). In contrast, the borate **1b**B with a π-pocket shows the widening gap of ΔE_S between **1b**B·**3a**⊃**2** and **1b**B·**3b**⊃**2**. For the **1b**B·**3b**⊃**2**, the **IM2** state is 5.5 kcal/mol more stabilized relative to that of **1b**B·**3a**⊃**2**, which should lead to the observed chemoselectivity of **3b** over **3a** (**4a**/**4b** = 30:70).

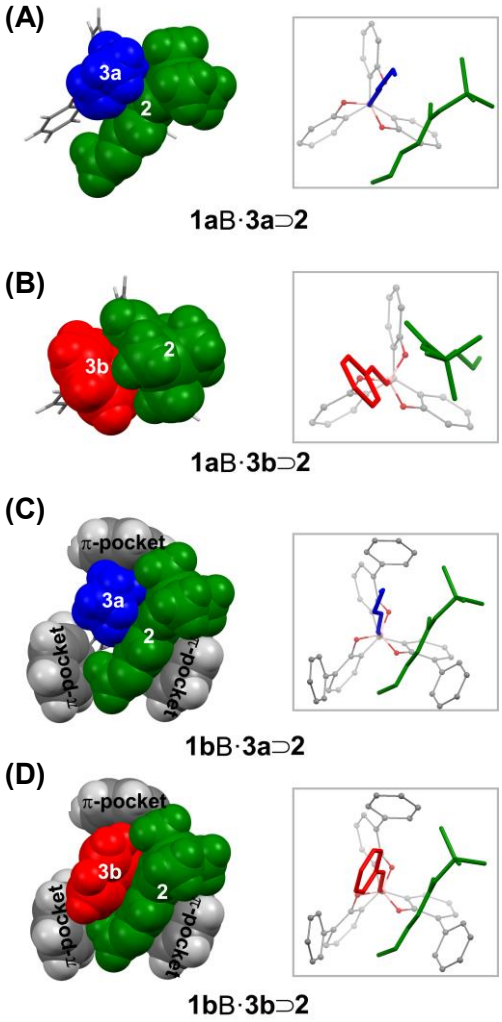

Figure 6. The top views of the inclusion complexes of **1a**B·**3**⊃**2** and **1b**B·**3**⊃**2** at the **IM2** states. The geometries are optimized by ωB97XD/def2svp with a IEFPCM model of CH_2Cl_2. The selected atoms are drawn by a space-filling model and the others are drawn by a capped sticks model. In the gray boxes, the inclusion complexes are drawn by a wireframe and a ball and stick model.

The molecular geometries of **1a**B·**3**⊃**2** and **1b**B·**3**⊃**2** drawn by a space-filling model are shown in Figure 6. Three aromatic panels of the π-pocket within **1b**B nicely encapsulate the aldehyde **3** and diene **2** (Figures 6C and D). The figure also suggests that the inclusion complex **1b**B·**3b**⊃**2** exhibits a tighter capsulated structure than that of **1b**B·**3a**⊃**2**. To obtain further insights, the non-covalent interactions

(NCI) among the π-pocket and the substrates were evaluated by NCIPLOT analysis[67],[68] of the inclusion complexes **1b**B·**3**⊃**2** (Figures 7 and S9–11). For both inclusion complexes **1b**B·**3**⊃**2**, two of the three aromatic panels of the π-pocket nicely interact with the diene **2** via π–π/CH–π contacts and with aldehyde **3** via CH–π contacts, which creates a moderately *attractive* isosurface (green to blue) area within the π-pocket. The interactions between the diene **2** and aldehyde **3**, which resemble π–π stacking interactions, is also shown as a moderately attractive isosurface in both inclusion complexes. The significant difference in the attractive isosurface within the π-pocket between **1b**B·**3a**⊃**2** and **1b**B·**3b**⊃**2** was observed in the interaction between the remaining one aromatic panel and the aldehyde **3** (magnifications in Figure 7). In **1b**B·**3b**⊃**2**, a moderate CH–π interaction between the remaining one aromatic panel and **3b** widely extended the attractive isosurface area. Conversely, in **1b**B·**3a**⊃**2**, the attractive contact between the remaining one aromatic panel and **3a** was insignificant, which led to the looser capsulated structure than that of **1b**B·**3b**⊃**2**.

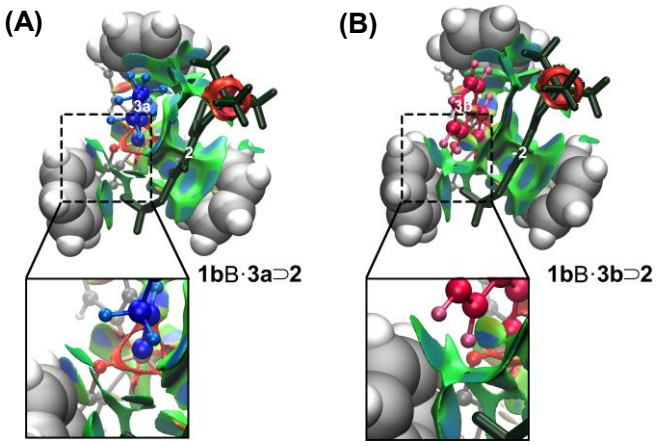

Figure 7. Non-covalent interaction (NCI) plots for (A) **1b**B·**3a**⊃**2** and (B) **1b**B·**3b**⊃**2**. (reduced density gradient [RDG] surfaces = 0.65 a.u. and the color range blue (attractive)–green–red (repulsive) for $-0.018 < \rho < +0.030$ a.u.).

The similar non-covalent interactions were also estimated in the carbonyl–acid complexes **1b**B·**3** at the **IM1** states. Although no significant attractive contact was observed within the π-pocket of the complex **1b**B·**3a**, the complex **1b**B·**3b** formed a more attractive isosurface area among the aromatic panels of the π-pocket and **3b** (Figures S12–14). During preorganization (Step 1), the NCI with the π-pocket helped the catalyst **1b**B selectively recognize **3b** over **3a** and import the diene **2** into the π-pocket space. More precise fitting of **3b** compared to **3a** into the π-pocket of **1b**B should lead to a more stabilized inclusion complex **1b**B·**3b**⊃**2** compared to **1b**B·**3a**⊃**2**.

Table 5. Summary for the stabilization energy (ΔE_S) in the reactions catalyzed **1b**B.

entry	inclusion complex	ΔE_S/ kcal·mol^{-1}	dispersion energy[a]/ kcal·mol^{-1}
1	**1a**B·**3a**⊃2	–9.7	–116.6
2	**1a**B·**3b**⊃2	–11.0	–127.6
3	**1b**B·**3a**⊃2	–24.8	–188.9
4	**1b**B·**3b**⊃2	–30.3	–198.4

[a] Grimme's D3 dispersion correction with Becke–Johnson (BJ) damping calculated by the B3LYP/6-31G**//ωB97XD/def2svp level.

The dispersion energy estimated by the DFT-D3(BJ) method of Grimme[69] supported these interactions; **1b**B·**3**⊃**2** showed a larger dispersion energy than that of **1a**B·**3**⊃**2** (Table 5), which should be driven by the close contacts among the π-pocket and substrates. In the capsulated structure, a larger dispersion energy should be effectively gained by multipoint CH–π, π–π, and CH–CH contacts,[51,70–75] which stabilize the preorganized structure and realizes the unique chemoselectivity of aromatic aldehydes over aliphatic ones. The generation of the inclusion complex might seemingly be an unfavorable process; within the complex, the degree of molecular freedom is severely restricted and the sizable Pauli repulsions among the components destabilize the structure. Considering the importance of the integrity of the π-pocket in the selectivity of aromatic aldehyde (Figure 3), the rigid π-cavity built by three aromatic panels is absolutely essential for selectivity. The large dispersion energies driven by the densely arranged structure at the **IM2** state would compensate for these unfavorable factors, which assist in molecular recognition and facilitate the chemoselective reaction.

The appearance of selectivity should require some rapid exchanges between **3a** and **3b** on the B atom during the preorganized period. However, our DFT calculations do not support the exchange process because the small energy barriers at the **TS1** and **TS2** states proved unable to give the π-pocket catalyst enough time to select one aldehyde. The approaching step of each substrate to the B atom might accompany some energy barriers for the molecular recognition.

Intramolecular recognition of aromatic moiety

These experimental and theoretical insights into the chemoselectivity driven by a π-pocket raise the hope of intramolecular recognition of aromatic moieties. To test the intramolecular selectivity, the hetero Diels-Alder reactions of **2** with a dialdehyde **17**[42] that has both aromatic and aliphatic carbonyls

were investigated. We selected the borates **1b**B, **1e**B, and **1j**B as catalysts because these borates with π-pockets exhibited high selectivity toward various aromatic aldehydes (Figure 4). The obtained results are summarized in Table 6. For all entries, the generation of **18c**, the product of the two-fold cycloadditions of **2** with both carbonyl moieties, was not perfectly suppressed presumably due to the high reactivity of **17** with **2**. The borate **1a**B with no π-pocket afforded a mixture of **18a**, **18b**, and **18c** in a total yield of 61% (entry 1). Importantly, the ratio of the product **18a**/**18b** was 51:15, illustrating the preference of the aliphatic carbonyl over the aromatic one. In sharp contrast to the result, borates with a π-pocket moiety showed significant selectivity toward the aromatic carbonyl (entries 2–4). It should be noted that the yields of **18b** dramatically increased for these catalytic systems. **1b**B showed the double production ratio of **18b** to **18a** (entry 2). For the catalyst **1e**B and **1j**B (entries 3 and 4), which have a methylated or phenylated π-pocket, respectively, an improved selectivity of the aromatic carbonyl over the aliphatic one (**18a**/**18b**) was observed (**1e**B: 15:66; **1j**B: 2:57). The highest selectivity was attained when using a flow system (entry 5; the details are described in the Supporting information.). Whilst the total yield was moderate, the generation of **18c** was suppressed and the ratio of **18a**/**18b** dramatically increased (7:78). The high mixing efficiency in the flow system even at short reaction time might effectively inhibit undesired overreactions, giving the high selectivity of **18b** over **18a**.

Table 6. Intramolecular recognition of aromatic carbonyl of **17**.

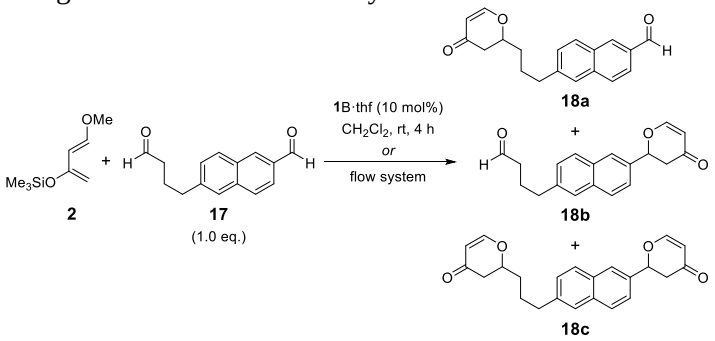

entry	borate **1**B·thf	yield / % (**18a**+**18b**+**18c**)	Ratio **18a**/**18b**/**18c**
1	**1a**B	61	51:15:34
2	**1b**B	68	26:52:22
3	**1e**B	52	15:66:19
4	**1j**B	42	2:57:41
5[a]	**1b**B	41	7:78:15

[a] Using flow system.

1-3. Conclusion

We synthesized and characterized the cage-shaped borate **1**B with various π-pocket cavities that are sterically and electronically modulated. The borate **1**B exhibits the controlled Lewis acidity and enough catalytic activities for hetero Diels-Alder reactions. The B atom center surrounded by three aromatic panels selectively activates aromatic aldehydes over aliphatic ones in the competitive inter- and intramolecular hetero Diels-Alder reactions of **2** with **3**/**17**. The mechanistic and theoretical studies demonstrated that the selective activation of aromatic substrates would be driven by the preorganized step rather than the rate-determining step of the C–C bond formations. In the preorganized step, an inclusion complex **1**B·**3**⊃**2** is generated ahead of C–C bond formations. The inclusion complex of the π-pocket borates with aromatic aldehydes (e.g. **1b**B·**3b**⊃**2**) was estimated to have a larger dispersion interaction than that of aliphatic aldehydes (e.g. **1b**B·**3a**⊃**2**), and this likely contributes to the preferred activation of aromatic substrates over aliphatic ones.

The present study not only introduces new borate-based Lewis acid catalysts with π-pocket cavities but also emphasizes the importance of the interactions within aromatic–aromatic groups in chemoselective reactions. Our borates are acceptable metallic catalysts that have the ability to selectively distinguish similarly sized carbon frameworks that have no functional anchors, to strongly interact with the metal center. Thus, it broadens strategies supporting the design of other cage-shaped catalysts with different metal centers.

1-4. Experimantal Section

General

NMR spectra were recorded on a JEOL-AL400 and a JEOL-ECS400 spectrometers (400 MHz for ^{1}H, and 100 MHz for ^{13}C) and a Bruker AVANCE III spectrometer (600 MHz for ^{1}H, and 150 MHz for ^{13}C) with TMS as an internal standard. ^{1}H and ^{13}C NMR signals of compounds were assigned using HMQC, HSQC, HMBC, COSY, NOESY, and ^{13}C off-resonance techniques. Positive and negative FAB and EI mass spectra were recorded on a JEOL JMS-700 and Shimadzu GCMS-QP2010 Ultra, respectively. High-resolution mass spectra were obtained by magnetic sector type mass spectrometer. IR spectra were recorded as thin films or as solids in KBr pellets on a HORIBA FT-720 and a JASCO FT/IR 6200 spectrophotometer.

Purification by recycled HPLC was performed using a SHIMADZU recycling HPLC system (SPD-20A, RID-10A, DGU-20A, LC-6AD, and FCV-20H2).

For the kinetic studies of the hetero Diels-Alder reaction of **2** with **3** catalyzed by **1**B, the reaction was monitored on a Mettler Toledo React IR TM 15 spectrometer with a diamond prob. The recorded spectra were analyzed by a iC IRTM software package.

Data collection for X-ray crystal analysis was performed on a Rigaku/ R-AXIS RAPID (MoK_{α} λ =

0.71075 Å, and CuK$_\alpha$ λ = 1.54187 Å), Rigaku/XtaLAB Synergy-S/Mo (MoK$_\alpha$ λ = 0.71075 Å), and Rigaku/XtaLAB Synergy-S/Cu (CuK$_\alpha$ λ = 1.54187 Å) diffractometers. All non-hydrogen atoms were refined with anisotropic displacement parameters and hydrogen atoms were placed at calculated positions and refined "riding" on their corresponding carbon atoms by the program CrystalStructure crystallographic software packages[76] and Olex2[77] program.

All apparatuses for flow synthesis were purchased from YMC. CO., LTD. Stainless steel (SUS316) T-shaped microreactor (YMC-P-0019) with inner diameters of 0.5 mm was used. The microreactor and gastight syringes were connected with PTFE tube (YMC-P-0025, inner diameter of 0.5 mm, OUW 1/16) equipped with PEEK fittings (YMC-P-0064, 1/16 OUW). Solutions were continuously introduced to the flow microreactor system via using syringe pumps (YSP-101), equipped with gastight syringes (YMC-P-1007, 5 mL).

Materials

Anhydrous dichloromethane, THF, acetonitrile, diethylether, toluene and hexane were purchased and used as obtained. All reagents were obtained from commercial suppliers and used as received. All reactions were carried out under nitrogen. The products of model reactions **4a**,[54] **4b**,[54] **4c**,[78] **4d**,[79] **4e**,[54] **4f**,[79] **5d**,[60] **14**,[80] **S1**,[80] **S2a**,[81] and **S2b**[81] were known in literatures. The dialdehyde **17**[42] was prepared by the same procedure found in the literature.

Computational method

For the cage-shaped borates **1a**B, **1b**B, **1e**B, **1f**B, **1g**B, **1j**B, and **1k**B, the structural optimizations and the estimations of the LUMO level were conducted using the Gaussian 09 Rev. D. 01 program.[82] The geometries of these borates were optimized with the B3PW91 functional and 6-31G** basis set, to afford the optimized structures as a local minimum structures giving all positive vibrational frequencies. The LUMO energy levels of these borates were calculated at the B3PW91/6-31+G** level using the optimized geometries.

The reaction profiles for the reaction of **2** with **3a** or **3b** catalyzed by the borate **1a**B or **1b**B were calclulated using the Gaussian 16 Rev. A. 03 program.[83] The ωB97X-D density functional and Def2-SVP were used. All molecular geometries were fully optimized and Gibbs free energies including contribution of vibrational entropy at an appropriate temperature were described in energy profiles. Solvation effect was introduced using the IEFPCM model and dichloromethane was used as a solvent.

Using the optimized structures of **1**B·**3**⊃**2** at the ωB97X-D/Def2-SVP level, non-covalent interactions (NCI) of inclusion complexes **1**B·**3**⊃**2** were computed using the non-covalent interaction index from the optimized electron density at the ωB97X-D/cc-pVTZ level of theory. The optimizations of the

electron density were calculated using the Gaussian 16 Rev. C. 01 program.[83] The generation of the NCI plot surfaces were obtained by NCIPLOT program.[67],[68] The surfaces were colored on a blue-green-red (BGR) scale using VMD program[84] with a reduced density gradient (RDG) surfaces = 0.65 a.u. and the color range blue(attractive)-green-red(repulsive) for $-0.018 < \rho < +0.030$ a.u.. The blue region indicates strong attractive interactions and the red region indicates strong repulsive interactions.

Synthetic procedures

2,2'-dimethoxy-3,3'-diphenylbenzophenone 5c

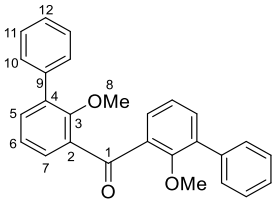

A solution of ^{n}BuLi in hexane (106 mmol, 66 mL, 1.6 M) was introduced in the flask and the volatiles were removed under reduced pressure (20 torr, 30 °C). A dehydrated Et_2O (100 mL) and *N*,*N*,*N*',*N*'-tetramethylethylenediamine (0.381 g, 3.3 mmol) were added to the flask and the mixture was gently refluxed. The dropping funnel was charged with 2-methoxy-1,1'-biphenyl (19 g, 106 mmol) and Et_2O (5 mL). The biphenyl solution was dropped to the flask at the refluxed temperature. After refluxed for 2 h and extra stirred at room temperature for 7 h, the flask was cooled to 0 °C. The dropping funnel was charged with *N*,*N*-dimethycarbamoyl chloride (5.7 g = 53 mmol) and Et_2O (5 mL). The solution was dropped to the flask at 0 °C. The reaction mixture was stirred at 0 °C for 2 h. 1N HCl aq. was added to quench the reaction and the mixture was extracted with Et_2O (3 x 50 mL). The obtained organic layer was dried ($MgSO_4$) and evaporated. The obtained residue was recrystallized from a hexane solution to give **5c** as a colorless solid (12 g, 57%).

mp 106.1–106.3 °C; IR (KBr) ν = 3027 (w), 2934 (w), 1651 (s), 1586 (m), 1462 (s), 1314 (s), 1227 (s), 1176 (m), 1005 (s), 807 (m), 762 (s), 702 (s) cm^{-1}; ^{1}H NMR (400 MHz, $CDCl_3$) 7.57–7.52 (m, 6H, 10-H, 7-H), 7.48 (dd, *J* = 7.4, 2.0 Hz, 2H, 5-H), 7.41 (t, *J* = 7.6 Hz, 4H, 11-H), 7.35 (t, *J* = 7.6 Hz, 2H, 12-H), 7.24 (t, *J* = 7.6 Hz, 2H, 6-H), 3.23 (s, 6H, 8-H); ^{13}C NMR (100 MHz, $CDCl_3$) 196.94 (s, C-1), 156.21 (s, C-3), 137.81 (s, C-9), 135.29 (s), 135.28 (s), 134.30 (d, C-5), 129.02 (d), 128.98 (d), 128.36 (d, C-11), 127.42 (d, C-12), 123.76 (d, C-6), 61.36 (q, C-8); MS (EI^+, 70 eV) *m*/z 394 (M^+, 100), 363 (52), 333 (35), 211 (56), 197 (82); HRMS (EI^+, 70 eV) Calculated ($C_{27}H_{22}O_3$): 394.1569 (M^+), Found: 394.1573 (M^+).

General procedure for the synthesis of triphenylmethanol derivative 6

A solution of ^{n}BuLi in hexane (30 mmol, 19 mL, 1.6 M) was introduced in the flask and the volatiles were removed under reduced pressure (20 torr, 30 °C). A dehydrated Et_2O (100 mL) and *N*,*N*,*N*',*N*'-tetramethylethylenediamine (0.11 g, 0.93 mmol) were added to the flask and the mixture was gently refluxed. The dropping funnel was charged with anisole (3.2 g, 30 mmol) and Et_2O (5 mL). The solution was dropped to the flask at the refluxed temperature. After refluxed for 2 h and extra stirred at room temperature overnight, the flask was cooled to 0 °C. The dropping funnel was charged with benzophenone derivative **5** (30 mmol) and THF (20 mL). The solution was dropped to the flask at 0 °C. The reaction mixture was stirred at 0 °C for 2 h. 1N HCl aq. was added to quench the reaction and the mixture was extracted with Et_2O (3 x 50 mL). The obtained organic layer was dried ($MgSO_4$) and evaporated. The obtained residue was purified by column chromatography (hexane/ether acetate = 85:15, column length 17 cm, diameter 48 mm silicagel) to give **6** as a colorless solid.

Bis(2-methoxy-[1,1'-biphenyl]-3-yl)(2-methoxyphenyl)methanol 6c

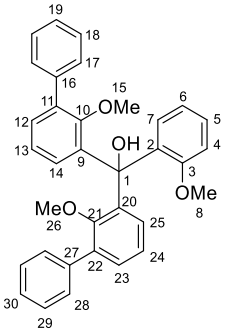

yield: 36%; mp 196.2–196.4 °C; IR (KBr) ν = 3471 (m), 3056 (w), 2935 (m), 1940 (w), 1810 (w), 1739 (w), 1599 (m), 1459 (s), 1355 (s), 1241 (s), 1174 (m), 1025 (s), 935 (w), 804 (s), 763 (s), 627 (m) cm^{-1}; ^{1}H NMR (400 MHz, $CDCl_3$) 7.65–7.63 (m, 1H), 7.56–7.52 (m, 4H), 7.39–7.18 (m, 11H), 7.04–6.97 (m, 4H), 5.76 (s, 1H, OH), 3.65 (s, 3H), 2.76 (s, 3H), 2.46 (s, 3H); ^{13}C NMR (100 MHz, $CDCl_3$) 157.56 (s), 156.41 (s), 155.29 (s), 139.24 (s), 138.96 (s), 135.13 (s), 134.63 (s), 133.24 (s), 130.78 (d), 129.62 (d), 129.50 (d), 128.89 (d), 128.31 (d), 126.91 (d), 123.08 (d), 122.60 (d), 120.88 (d), 112.20 (d), 80.76 (s, C-1), 59.96 (q), 59.26 (q), 55.49 (q) (The 8 signals were not detected due to the severe overlapping.); MS (EI^+, 70 eV) *m*/z 502 (M^+, 55), 395 (18), 319 (70), 211 (100), 135 (48); HRMS (EI^+, 70 eV) Calculated ($C_{34}H_{30}O_4$): 502.2144 (M^+), Found: 502.2145 (M^+).

(2-Methoxy-[1,1'-biphenyl]-3-yl)bis(2-methoxyphenyl)methanol 6d

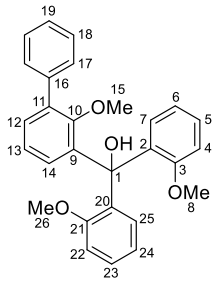

yield: 75%; mp 169.2–170.0 °C; IR (KBr) ν = 3490 (m), 3064 (w), 2937 (m), 1598 (m), 1487 (s), 1362 (m), 1243 (s), 1162 (m), 1024 (s), 927 (w), 760 (s), 706 (m), 577 (m) cm^{-1}; ^{1}H NMR (400 MHz, $CDCl_3$) 7.56 (dd, J = 7.8, 1.2 Hz, 2H), 7.36 (t, J = 7.4 Hz, 2H), 7.30–7.25 (m, 5H), 7.24–7.20 (m, 2H), 7.10–6.85 (m, 5H), 5.63 (s, 1H, OH), 3.63 (s, 3H), 3.47 (s, 3H), 2.48 (s, 3H); ^{13}C NMR (100 MHz, $CDCl_3$) 155.73, 139.34, 138.87, 134.56, 134.18, 132.93, 130.37, 129.94, 129.54, 129.15, 128.92, 128.52 (two signals were overlapped.), 128.24, 126.80, 122.19, 120.81, 120.36, 112.37, 80.45 (s, C-1), 59.50 (q), 55.52 (q, two signals were overlapped.); MS (FAB$^+$, 70 eV) m/z 449 ([M+Na]$^+$, 100), 426 (M$^+$, 9), 409 (31), 329 (35), 176 (97), 154 (70); HRMS (FAB$^+$, 70 eV) Calculated ($C_{28}H_{26}NaO_4$): 449.1729 [M+Na]$^+$, Found: 449.1727 [M+Na]$^+$.

Tris(3-bromo-2-methoxyphenyl)methanol 8

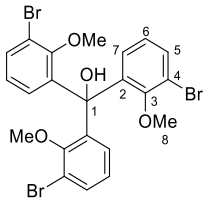

To a solution of 1,3-dibromo-2-methoxybenzene (2.68 g, 10.0 mmol) in dehydrated diethyl ether (35 mL) was slowly added ^{n}BuLi (5.5 mL, 9.00 mmol, 1.6 M in hexane) at 0 °C via a dropping funnel. After the reaction mixture was stirred for 10 minutes, ethyl chloroformate (0.3 mL, 3.00 mmol) in diethyl ether (5 mL) was dropwisely added into the reaction mixture. After stirring for 15 h, the reaction was quenched by NH_4Cl aq. The reaction mixture was extracted with AcOEt (3 x 15 mL). The organic layer was dried over anhydrous $MgSO_4$, and the solvent was evaporated. The residue was purified by a silica gel column chromatography (hexane/ ethyl acetate = 90:10) to give the product as colorless viscous oil (0.93 g, 47%).

mp 57.2–57.5 °C; IR (KBr) ν = 3471 (w), 3062 (w), 2942 (w), 1459 (s), 1356 (m), 1244 (s), 1126 (m), 995 (s), 782 (m), 670 (m) cm^{-1}; ^{1}H NMR (400 MHz, $CDCl_3$) 7.54 (dd, J = 8.0, 1.6 Hz, 3H, 5-H), 7.11 (dd, J = 8.0, 1.6 Hz, 3H, 7-H), 6.95 (t, J = 8.0 Hz, 3H, 6-H), 5.70 (s, 1H, OH), 3.39 (s, 9H, 8-H); ^{13}C NMR (100 MHz, $CDCl_3$) 155.37 (s, C-3), 140.70 (s, C-2), 133.80 (d, C-5), 129.21 (d, C-7), 124.56 (d,

C-6), 117.90 (s, C-4), 81.18 (s, C-1), 60.96 (q, C-8); MS (EI^+, 70 eV) *m*/z 590 ($[M+6]^+$, 4), 588 ($[M+4]^+$, 11), 586 ($[M+2]^+$, 11), 584 (M^+, 4), 401 (51), 213 (100); HRMS (EI^+, 70 eV) Calculated ($C_{22}H_{19}Br_3O_4$): 583.8833 (M^+) Found: 583.8832 (M^+).

General procedure for the synthesis of triphenylmethane derivative 7

To a mixture of **6** (6.5 mmol) and $InCl_3$ (72 mg, 0.33 mmol, 5 mol%) in dichloromethane (45 mL) was added chlorodimethylsilane (1.2 g, 13 mmol, 2 eq.). The reaction mixture was stirred at rt for 15 min. Saturated $NaHCO_3$ aq (30 mL) was added to the mixture, which was extracted with ethyl acetate (3 × 30 mL). The collected organic layers were washed with saturated NaCl aq (2 × 30 mL) and then dried over $MgSO_4$ and evaporated to obtain a yellow solid. The solid was recrystallized from hexane to give **7** as a colorless solid.

3,3''-((2-Methoxyphenyl)methylene)bis(2-methoxy-1,1'-biphenyl) 7c

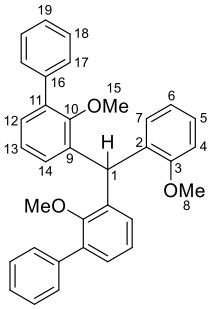

yield: 79%; mp 138.7–139.2 ℃; IR (KBr) ν = 3028 (w), 2935 (m), 1598 (w), 1461 (s), 1415 (s), 1222 (m), 1108 (m), 1005 (s), 762 (s), 701 (m) cm^{-1}; ^1H NMR (400 MHz, $CDCl_3$) 7.60 (dd, *J* = 8.6, 1.2 Hz, 4H, 17-H), 7.38 (t, *J* = 7.4 Hz, 4H, 18-H), 7.30 (t, *J* = 7.4 Hz, 2H, 19-H), 7.24–7.21 (m, 3H, 12-H, 5-H), 7.06 (t, *J* = 7.8 Hz, 2H, 13-H), 6.96 (dd, *J* = 7.8, 1.6 Hz, 1H, 7-H), 6.92–6.87 (m, 4H, 4-H, 6-H, 14-H), 6.71 (s, 1H, 1-H), 3.74 (s, 3H, 8-H), 3.12 (s, 6H, 15-H); ^{13}C NMR (100 MHz, $CDCl_3$) 156.96 (s, C-3), 155.63 (s, C-10), 138.96 (s, C-16), 137.76 (s, C-9), 134.63 (s, C-11), 132.49 (s, C-2), 130.19 (d, C-7), 129.45 (d, C-12), 129.34 (d, C-14), 129.04 (d, C-17), 128.18 (d, C-18), 127.40 (d, C-5), 126.90 (d, C-19), 123.43 (d, C-13), 120.06 (d), 110.69 (d), 59.92 (q, C-15), 55.61 (q, C-8), 37.55 (d, C-1); MS (FAB^+, 70 eV) *m*/z 486 (29), 455 (6), 379 (9), 307 (34), 289 (17), 197 (10), 154 (100), 136 (69); HRMS (FAB^+, 70 eV) Calculated ($C_{34}H_{30}O_3$): 486.2195 (M^+), Found: 486.2197.

3-(Bis(2-methoxyphenyl)methyl)-2-methoxy-1,1'-biphenyl 7d

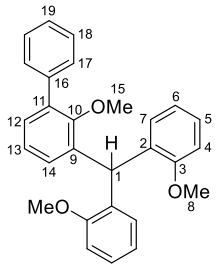

yield: 56%; mp 155.1–155.5 °C; IR (KBr) ν = 3059 (w), 2931 (w), 1598 (w), 1488 (s), 1417 (m), 1242 (s), 1106 (m), 1030 (m), 754 (s), 700 (m) cm^{-1}; ^1H NMR (400 MHz, $CDCl_3$) 7.60 (d, J = 7.6 Hz, 2H, 17-H), 7.38 (t, J = 7.6 Hz, 2H, 18-H), 7.30 (t, J = 7.6 Hz, 1H, 19-H), 7.23–7.18 (m, 3H), 7.02 (t, J = 7.6 Hz, 1H, 13-H), 6.89–6.85 (m, 6H), 6.81 (dd, J = 7.6, 2.0 Hz, 1H), 6.59 (s, 1H, 1-H), 3.72 (s, 6H, 8-H), 3.06 (s, 3H, 15-H); ^{13}C NMR (100 MHz, $CDCl_3$) 157.15 (s, C-3), 155.63 (s, C-10), 139.04 (s, C-16), 137.93 (s, C-9), 134.45 (s, C-11), 132.37 (s, C-2), 129.95 (d, C-14), 129.14 (d), 129.09 (d), 129.06 (d), 128.13 (d, C-18), 127.23 (d), 126.83 (d, C-19), 123.32 (d, C-13), 119.97 (d), 110.69 (d), 59.93 (q, C-15), 55.69 (q, C-8), 37.09 (d, C-1); MS (FAB$^+$, 70 eV) *m*/z 410 (37), 379 (7), 307 (34), 227 (14), 154 (100), 107 (16); HRMS (FAB$^+$, 70 eV) Calculated ($C_{28}H_{26}O_3$): 410.1882 (M^+), Found: 410.1875 (M^+).

Tris(3-bromo-2-methoxyphenyl)methane 9

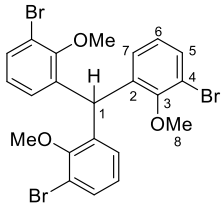

yield: 92%; mp 200.1–200.5 °C; IR (KBr) ν = 3067 (w), 2937 (w), 2823 (w), 1983 (w), 1460 (s), 1419 (s), 1249 (m), 1230 (m), 1085 (m), 998 (s), 784 (s), 759 (s), 651 (m) cm^{-1}; ^1H NMR (400 MHz, $CDCl_3$) 7.46 (dd, J = 8.0, 1.6 Hz, 3H, 5-H), 6.90 (t, J = 8.0 Hz, 3H, 6-H), 6.76 (dd, J = 7.8, 1.6 Hz, 3H, 7-H), 6.58 (s, 1H, 1-H), 3.73 (s, 9H, 8-H); ^{13}C NMR (100 MHz, $CDCl_3$) 154.9 (s, C-3), 138.2 (s, C-2), 132.4 (d, C-5), 129.4 (d, C-7), 125.0 (d, C-6), 117.7 (s, C-4), 60.6 (q, C-8), 39.3 (d, C-1); MS: (EI$^+$, 70 eV) *m*/z 574 ([M+6]$^+$, 21), 572 ([M+4]$^+$, 62), 570 ([M+2]$^+$, 62), 568 (M^+, 21), 541 (25), 199 (100); HRMS (EI$^+$, 70 eV) Calculated ($C_{22}H_{19}Br_3O_3$): 567.8884 (M^+), Found: 567.8875 (M^+); Analysis $C_{22}H_{19}Br_3O_3$ (571.1030) Calculated: C, 46.27; H, 3.35; Br, 41.97; O, 8.40, Found: C, 46.12; H, 3.46.

General procedure for the introduction of aryl groups into 9 under the Suzuki-Miyaura conditions

The mixture of tris(3-bromo-2-methoxyphenyl)methane **9** (1.00 g, 1.75 mmol), arylboronic acid (3.3 eq. 5.78 mmol), palladium(II) acetate (0.06 g, 0.26 mmol), 2-dicyclohexylphosphino-2',6'-

dimethoxybiphenyl (0.22 g, 0.52 mmol), and sodium carbonate (1.85 g, 17.50 mmol) in toluene (6 mL), ethanol (6 mL) and distilled water (2 mL) was heated at 100 ℃ for 22 h. The reaction was quenched by HCl aq. at 0 ℃. The product was extracted with dichloromethane (3 x 15 mL). The organic layer was dried over anhydrous $MgSO_4$, and the filtrate was evaporated. The residue was purified by a silica gel column chromatography (hexane/ ethyl acetate = 90:10) to give the product as a colorless solid.

Tris{3-(4-methylpheynyl)-2-methoxyphenyl}methane 10e

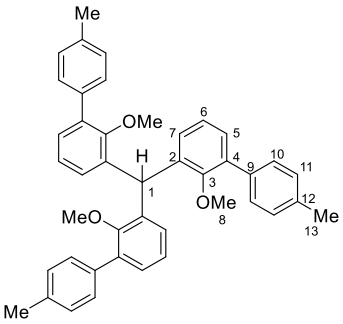

yield: quant.; mp 99.8–100.2 ℃; IR (KBr) ν = 3023 (w), 2936 (m), 1515 (m), 1458 (s), 1399 (m), 1221 (s), 1009 (s), 800 (s), 763 (s), 613 (m) cm^{-1}; ^1H NMR (400 MHz, $CDCl_3$) 7.50 (dd, J = 8.4, 2.0 Hz, 6H, 10-H), 7.24–7.19 (m, 9H, 5-H, 11-H), 7.08 (td, J = 8.0, 2.0 Hz, 3H, 6-H), 6.94 (d, J = 8.0 Hz, 3H, 7-H), 6.78 (s, 1H, 1-H), 3.16 (s, 9H, 8-H), 2.38 (s, 9H, 13-H); ^{13}C NMR (100 MHz, $CDCl_3$) 155.55 (s, C-3), 137.88 (s, C-2), 136.61 (s, C-12), 135.98 (s, C-9), 134.60 (s, C-4), 129.46 (d, C-7), 129.43 (d, C-5), 128.92 (d, C-11), 128.85 (d, C-10), 123.46 (d, C-6), 59.82 (q, C-8), 38.30 (d, C-1), 21.21 (q, C-13); MS (EI^+, 70 eV) m/z 604 (M^+, 100), 573 (63), 211 (49), 197 (30); HRMS (EI^+, 70 eV) Calculated ($C_{43}H_{40}O_3$): 604.2977 (M^+), Found: 604.2982 (M^+).

Tris{3-(4-cyanophenyl)-2methoxyphenyl}methane 10f

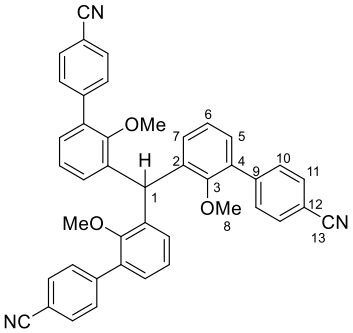

yield: 89%; mp: 242.8–243.3 ℃; IR (KBr) ν = 2942 (m), 2225 (s), 1607 (s), 1460(s), 1245 (s), 1088 (m), 1002 (s), 849 (s), 761 (s), 677 (w), 608 (m) cm^{-1}; ^1H NMR (400 MHz, $CDCl_3$) 7.75 (d, J = 8.0 Hz, 6H, 10-H), 7.71 (d, J = 8.0 Hz, 6H, 11-H), 7.28 (td, J = 7.8, 1.6 Hz, 3H, 5-H), 7.18 (t, J = 7.8 Hz, 3H,

6-H), 7.03 (dd, J = 7.8, 1.6 Hz, 3H, 7-H), 6.78 (s, 1H, 1-H), 3.20 (s, 9H, 8-H); ^{13}C NMR (100 MHz, $CDCl_3$) 155.33 (s, C-3), 143.29 (s, C-9), 137.56 (s, C-2), 132.90 (s, C-4), 132.01 (d, C-11), 130.60 (d, C-7), 129.54 (d, C-5), 129.44 (d, C-10), 124.04 (d, C-6), 118.80 (s, C-13), 110.68 (s, C-12), 60.24 (q, C-8), 37.89 (d, C-1); MS (EI$^+$, 70 eV) m/z 637 (M^+, 92), 606 (63), 397 (15), 222 (100), 192 (48); HRMS (EI$^+$, 70 eV) Calculated ($C_{43}H_{31}N_3O_3$): 637.2365 (M^+), Found: 637.2361 (M^+).

Tris{3-(4-trifluoromethylphenyl)-2-methoxyphenyl}methane 10g

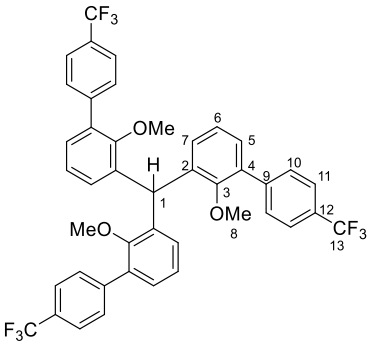

yield: 94%; mp 165.2–165.8 ℃; IR (KBr) ν = 3082 (w), 3028 (s), 2914 (s), 1953 (w), 1885 (w), 1810 (w), 1696 (s), 1601 (m), 1453 (m), 1351 (s), 1140 (m), 969 (s), 767 (s), 701 (s) cm^{-1}; ^{1}H NMR (400 MHz, $CDCl_3$) 7.73 (d, J = 8.0 Hz, 6H, 10-H), 7.66 (d, J = 8.0 Hz, 6H, 11-H), 7.27 (d, J = 7.6 Hz, 3H, 5-H), 7.15 (t, J = 7.6 Hz, 3H, 6-H), 7.01 (d, J = 7.6 Hz, 3H, 7-H), 6.79 (s, 1H, 1-H), 3.18 (s, 9H, 8-H); ^{13}C NMR (100 MHz, $CDCl_3$) 155.58 (s, C-3), 142.42 (qd, $^4J_{C\text{-}F}$ = 1.6 Hz, C-9), 137.80 (s, C-2), 133.52 (s, C-4), 130.40 (d, C-7), 129.64 (d, C-5), 129.30 (d, C-10), 129.21 (q, $^2J_{C\text{-}F}$ = 32.1 Hz, C-12), 125.23 (qd, $^3J_{C\text{-}F}$ = 3.7 Hz, C-11), 124.26 (q, $^1J_{C\text{-}F}$ = 273.2 Hz, C-13), 123.95 (d, C-6), 60.24 (q, C-8), 38.16 (d, C-1); ^{19}F NMR (128 MHz, $CDCl_3$, CF_3COOH in $CDCl_3$ as external standard) –63.39; MS (EI$^+$, 70 eV) m/z 766 (M^+, 96), 747 (14), 735 (62), 514 (5), 265 (100), 251 (43); HRMS (EI$^+$, 70 eV) Calculated ($C_{43}H_{31}F_9O_3$): 766.2129 (M^+), Found: 766.2118 (M^+); Analysis $C_{43}H_{31}F_9O_3$ (766.7036) Calculated: C, 67.36; H, 4.08; F, 22.30; O, 6.26, Found: C, 67.21; H, 4.20.

Tris{3-(4-trimethylsilylpheynyl)-2-methoxyphenyl}methane 10h

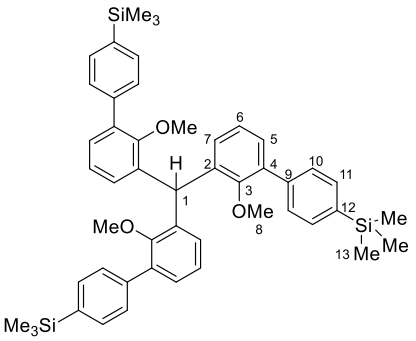

yield: 62%; mp 112.7–113.1 °C; IR (KBr) ν = 3016 (w), 2953 (s), 1600 (m), 1458 (s), 1248 (s), 1118 (s), 1009 (s), 851 (s), 763 (s), 659 (m) cm^{-1}; ^{1}H NMR (400 MHz, $CDCl_3$) 7.59 (d, *J* = 7.6 Hz, 6H), 7.54 (d, *J* = 7.6 Hz, 6H), 7.25 (dd, *J* = 7.8, 1.2 Hz, 3H, 5-H), 7.10 (t, *J* = 7.8 Hz, 3H, 6-H), 6.98 (dd, *J* = 7.8, 1.2 Hz, 3H, 7-H), 6.81 (s, 1H, 1-H), 3.16 (s, 9H, 8-H), 0.29 (s, 27H, 13-H); ^{13}C NMR (100 MHz, $CDCl_3$) 155.66 (s, C-3), 139.29 (s, C-12), 138.88 (s), 137.86 (s), 134.66 (s), 133.23 (d), 129.68 (d, C-7), 129.57 (d, C-5), 128.22 (d), 123.51 (d, C-6), 60.06 (q, C-8), 38.25 (d, C-1), –1.06 (q, C-13); ^{29}Si NMR (78.7 MHz, $CDCl_3$, Me_4Si in $CDCl_3$ as an external standard) –4.16; MS (EI^+, 70 eV) *m*/z 778 (M^+, 100), 763 (24), 747 (53), 374 (49), 239 (27); HRMS (EI^+, 70 eV) Calculated ($C_{43}H_{40}O_3$): 778.3694 (M^+), Found: 778.3698 (M^+).

Tris{3-(4-*tert*-butylpheynyl)-2-methoxyphenyl}methane 10i

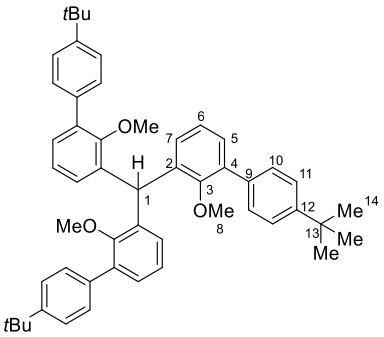

yield: 76%; mp 127.2–127.5 °C; IR (KBr) ν = 2962 (s), 1458 (s), 1244 (m), 1087 (m), 1010 (s), 841 (m), 766 (s) cm^{-1}; ^{1}H NMR (400 MHz, $CDCl_3$) 7.56 (d, *J* = 8.8 Hz, 6H, 10-H), 7.41 (d, *J* = 8.8 Hz, 6H, 11-H), 7.26 (dd, 3H, *J* = 8.0, 2.0 Hz, 5-H), 7.09 (t, *J* = 8.0 Hz, 3H, 6-H), 6.97 (dd, *J* = 8.0, 2.0 Hz, 3H, 7-H), 6.82 (s, 1H, 1-H), 3.17 (s, 9H, 8-H), 1.36 (s, 27H, 14-H); ^{13}C NMR (100 MHz, $CDCl_3$) 155.66 (s, C-3), 149.82 (s, C-12), 137.90 (s, C-2), 135.90 (s, C-9), 134.55 (s, C-4), 129.48 (d), 129.43 (d), 128.55 (d, C-10), 125.08 (d, C-11), 123.42 (d, C-6), 59.91 (q, C-8), 38.29 (d, C-1), 34.49 (s, C-13), 31.38 (q, C-14); MS (EI^+, 70 eV) *m*/z 730 (M^+, 100), 699 (57), 403 (14), 350 (54), 253 (22), 195 (19), 57 (34); HRMS (EI^+, 70 eV) Calculated ($C_{52}H_{58}O_3$): 730.4386 (M^+), Found: 730.4388 (M^+).

Tris(3-*p*-bipheynyl-2-methoxyphenyl)methane 10j

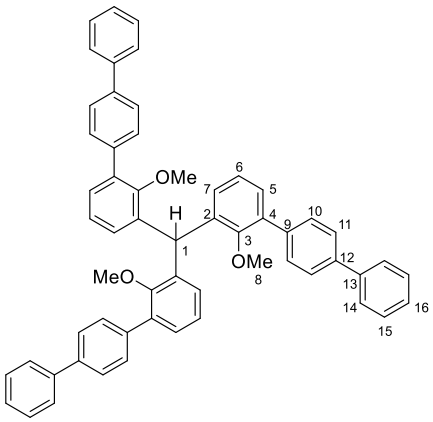

yield: 90%; mp 164.2–164.4 ℃; IR (KBr) ν = 3028 (w), 2936 (w), 1803 (w), 1459 (s), 1244 (m), 1223 (m), 1114 (m), 1090 (m), 1008 (s), 767 (s) cm^{-1}; ^1H NMR (400 MHz, $CDCl_3$) 7.80 (d, J = 8.4 Hz, 6H, 10-H), 7.74–7.72 (m, J = 6.8 Hz, 12H, 11-H, 14-H), 7.52 (t, J = 7.6 Hz, 6H, 15-H), 7.44–7.36 (m, 6H, 5-H, 16-H), 7.21 (t, J = 7.8 Hz, 3H, 6-H), 7.11 (dd, J = 7.8, 1.6 Hz, 3H, 7-H), 6.96 (s, 1H, 1-H), 3.34 (s, 9H, 8-H); ^{13}C NMR (100 MHz, $CDCl_3$) 155.65 (s, C-3), 140.66 (s), 139.65 (s), 137.91 (s, C-2), 137.87 (s, C-9), 134.27 (s, C-4), 129.73 (d, C-10), 129.51 (d), 129.38 (d, C-5), 128.74 (d, C-15), 127.25 (d), 126.95 (d), 126.89 (d), 123.65 (d, C-6), 60.04 (q, C-8), 38.33 (d, C-1); MS (EI^+, 70 eV) m/z 790 (M^+, 100), 759 (52), 530 (8), 273 (88), 259 (45); HRMS (EI^+, 70 eV) Calculated ($C_{58}H_{46}O_3$): 790.3447 (M^+), Found: 790.3454 (M^+).

Tris(3-butyl-2-methoxyphenyl)methane 11

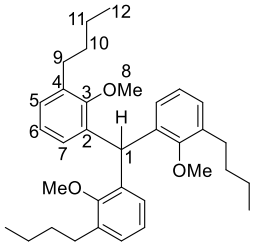

The mixture of tris(3-bromo-2-methoxyphenyl)methane **9** (0.789 g, 1.38 mmol), tributylborane (1.0 M in Et_2O, 4.97 ml, 4.97 mmol), palladium(II) acetate (7.9 mg, 0.035 mmol), 2-dicyclohexylphosphino-2',6'-dimethoxybiphenyl (28.7 mg, 0.070 mmol), and K_3PO_4 (1.75 g, 8.28 mmol) in toluene (10 mL), and degassed water (1 mL) was heated at 100 ℃ for 16 h. After cooled to room temperature, the reaction was quenched by water. The product was extracted with dichloromethane (3 x 15 mL). The organic layer was dried over anhydrous $MgSO_4$, and the filtrate was evaporated. The residue was purified by a silica gel column chromatography (hexane/ ethyl acetate = 97:3) to give the product **11** as colorless oil (0.672 g, 97%).

IR ν = 3063 (m), 2956 (s), 2860 (m), 2828 (m), 2248 (w), 2013 (w), 1587 (m), 1462 (s), 1424 (m), 1378

(m), 1243 (s), 1011 (s), 801 (m), 768 (m), 603 (w) cm^{-1}; ^1H NMR (400 MHz, $CDCl_3$) 7.07 (dd, J = 7.2, 1.6 Hz, 3H, 5-H), 6.92 (t, J = 7.6 Hz, 3H, 6-H), 6.75 (dd, J = 7.8, 1.6 Hz, 3H, 7-H), 6.61 (s, 1H, 1-H), 3.50 (s, 9H, 8-H), 2.62 (t, J = 8.0 Hz, 6H, 9-H), 1.63–1.55 (m, 6H, 10-H), 1.37 (sext, J = 7.5, 6H, 11-H), 0.92 (t, J = 7.4 Hz, 9H, 12-H); ^{13}C NMR (100 MHz, $CDCl_3$) 156.18 (s, C-3), 137.52 (s, C-2), 135.79 (s, C-4), 128.22 (d, C-5), 128.08 (d, C-7), 123.37 (d, C-6), 60.66 (q, C-8), 37.83 (d, C-1), 32.88 (t, C-10), 29.42 (t, C-9), 22.81 (t, C-11), 13.97 (q, C-12); MS (EI, 70 eV) *m/z* 502 (M^+, 100), 471 (74), 445 (28), 177 (42), 135 (43); HRMS (EI, 70 eV) Calculated ($C_{34}H_{46}O_3$): 502.3447 (M^+), Found: 502.3438.

General procedure for the synthesis of 1H_3 using BBr_3

To the solution of **7** or **10** or **11** (5.2 mmol) in dichloromethane (50 mL) was added BBr_3 (1M in dichloromethane, 17 mL, 17 mmol) at –78 °C. After stirring with warming to rt for 24 h, 30 mL of water was added to the mixture at 0 °C. The mixture was extracted with Et_2O (3 x 30 mL). The obtained organic layer was dried ($MgSO_4$) and evaporated to give a solid. It was purified by column chromatography (hexane/ethyl acetate = 70:30, column length 10 cm, diameter 26 mm silicagel) to give the product as a colorless solid.

Bis(3-phenyl-2-hydroxyphenyl)(2-hydroxyphenyl)methane 1cH_3

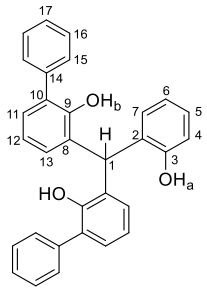

yield: 56%; mp 161.1–161.4 °C; IR (KBr) ν = 3555 (s), 3513 (s), 3034 (w), 2928 (w), 1594 (m), 1451 (s), 1315 (s), 1189 (s), 1075 (s), 924 (w), 828 (s), 757 (s), 704 (s) cm^{-1}; ^1H NMR: (400 MHz, $CDCl_3$) 7.46–7.44 (m, 8H), 7.41–7.35 (m, 2H), 7.21–7.16 (m, 3H), 7.00–6.88 (m, 6H), 6.86 (dd, J = 8.0, 1.2 Hz, 1H), 6.32 (s, 1H, 1-H), 5.46 (s, 2H, OH_b), 5.00 (s, 1H, OH_a); ^{13}C NMR (100 MHz, $CDCl_3$) 153.50 (s), 150.07 (s), 137.02 (s), 129.70 (d), 129.34 (d), 129.18 (d), 129.12 (d), 128.86 (d), 128.69 (s), 128.52 (s), 128.36 (s), 127.96 (d), 127.79 (d), 120.73 (d), 120.41 (d), 116.12 (d), 38.11 (d, C-1); MS (EI^+, 70 eV) *m*/z 444 (M^+, 50), 349 (17), 333 (56), 275 (38), 257 (100); HRMS (EI^+, 70 eV) Calculated ($C_{31}H_{24}O_3$): 444.1725 (M^+), Found: 444.1729 (M^+).

Bis(2-hydroxyphenyl)(3-phenyl-2-hydroxyphenyl)methane 1dH_3

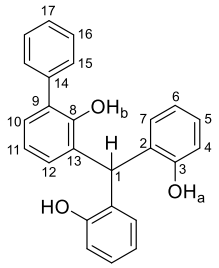

yield: 72%; mp 200.1–200.4 °C; IR (KBr) ν = 3542 (s), 3516 (s), 3060 (w), 1587 (m), 1453 (s), 1323 (s), 1256 (s), 1195 (s), 1087 (s), 828 (s), 756 (s), 613 (m) cm^{-1}; ^1H NMR (400 MHz, $CDCl_3$) 7.49–7.36 (m, 5H), 7.21–7.16 (m, 3H), 6.98–6.87 (m, 6H), 6.85 (dd, J = 8.0, 0.8 Hz, 2H), 6.20 (s, 1H, 1-H), 5.49 (s, 1H, OH_b), 5.01 (s, 2H, OH_a); ^{13}C NMR: (100 MHz, $CDCl_3$) 153.48 (s), 149.97 (s), 136.83 (s), 129.70 (s), 129.42 (s), 129.29, 129.16, 129.10, 128.44, 128.27, 127.99, 127.85, 127.60, 120.98 (d), 120.65 (d), 116.21 (d), 38.19 (d, C-1); MS (EI^+, 70 eV) m/z 368 (M^+, 47), 273 (29), 257 (100), 199 (26), 181 (33); HRMS (EI^+, 70 eV) Calculated ($C_{25}H_{20}O_3$): 368.1412 (M^+), Found: 368.1409 (M^+).

Tris{3-(4-methylphenyl)-2-hydroxyphenyl}methane 1eH_3

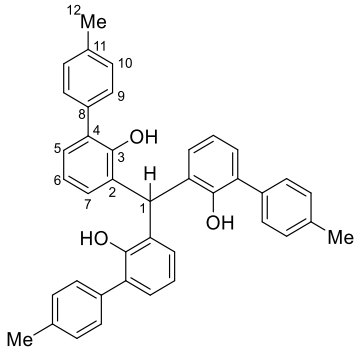

yield: 77%; mp 205.9–206.1 °C; IR (KBr) ν = 3539 (s), 3024 (w), 2954 (w), 2920 (w), 2860 (w), 1514(m), 1446 (s), 1325 (m), 1227 (m), 1189 (m), 1076 (m), 821 (m), 752 (m) cm^{-1}; ^1H NMR (400 MHz, $CDCl_3$) 7.36 (d, J = 8.2 Hz, 6H, 9-H), 7.25 (d, J = 8.2 Hz, 6H, 10-H), 7.17 (dd, J = 7.6, 2.0 Hz, 3H, 5-H), 6.97 (dd, J = 7.6, 2.0 Hz, 3H, 7-H), 6.93 (t, J = 7.6 Hz, 3H, 6-H), 6.45 (s, 1H, 1-H), 5.46 (s, 3H, OH), 2.38 (s, 9H, 12-H); ^{13}C NMR (100 MHz, $CDCl_3$) 150.27 (s, C-3), 137.52 (s, C-11), 134.26 (s, C-8), 129.79 (d, C-10), 129.20 (d, C-7), 129.10 (d, C-9), 128.93 (s, C-4), 128.69 (d, C-5), 128.27 (s, C-2), 120.22 (d, C-6), 38.33 (d, C-1), 21.18 (q, C-12); MS (EI^+, 70 eV) m/z 562 (M^+, 20), 379 (24), 361 (100), 184 (12); HRMS (EI^+, 70 eV) Calculated ($C_{40}H_{34}O_3$): 562.2508 (M^+), Found: 562.2498 (M^+).

Tris{3-(4-*tert*-butylphenyl)-2-hydroxyphenyl}methane 1iH_3

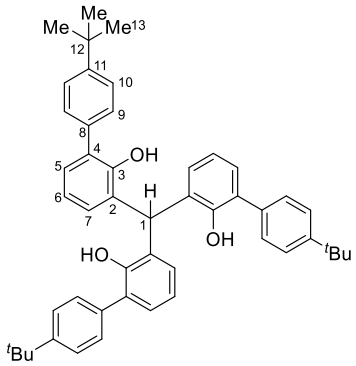

yield: 51%; mp 246.1–246.5 °C; IR (KBr) ν = 3538 (s), 3031 (w), 2962 (s), 2903 (w), 1446 (s), 1191 (m), 828 (m), 755 (m) cm^{-1}; ^1H NMR (400 MHz, $CDCl_3$) 7.45 (d, J = 8.4 Hz, 6H, 10-H), 7.40 (d, J = 8.4 Hz, 6H, 9-H), 7.19 (dd, J = 7.6, 2.0 Hz, 3H, 5-H), 6.98 (dd, J = 7.6, 2.0 Hz, 3H, 7-H), 6.93 (t, J = 7.6 Hz, 3H, 6-H), 6.44 (s, 1H, 1-H), 5.49 (s, 3H, OH), 1.33 (s, 27H, 13-H); ^{13}C NMR (100 MHz, $CDCl_3$) 150.63 (s, C-11), 150.34 (s, C-3), 134.25 (s, C-8), 129.15 (d, C-7), 128.87 (d, C-9), 128.80 (s, C-4), 128.66 (d, C-5), 128.21 (s, C-2), 125.99 (d, C-10), 120.22 (d, C-6), 38.47 (d, C-1), 34.57 (s, C-12), 31.28 (q, C-13); MS (EI^+, 70 eV) m/z 688 (M^+, 25), 463 (39), 445 (100), 329 (25), 57 (21); HRMS (EI^+, 70 eV) Calculated ($C_{49}H_{52}O_3$): 688.3916 (M^+), Found: 688.3914 (M^+).

Tris(3-*p*-bipheynyl-2-hydroxyphenyl)methane 1jH_3

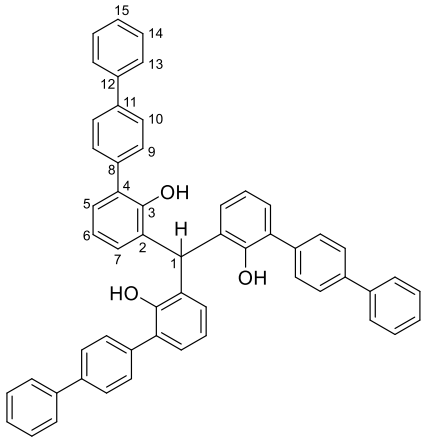

yield: 82%; mp 181.1–181.5 °C; IR (KBr) ν = 3533 (s), 3028 (w), 1600 (w), 1585 (w), 1453 (s), 1325 (w), 1226 (w), 1182 (w), 763 (s), 696 (m) cm^{-1}; ^1H NMR (400 MHz, $CDCl_3$) 7.66 (d, J = 8.4 Hz, 6H, 9-H), 7.61 (d, J = 7.4 Hz, 6H, 13-H), 7.55 (d, J = 8.4 Hz, 6H, 10-H), 7.44 (t, J = 7.4 Hz, 6H, 14-H), 7.35 (t, J = 7.4 Hz, 3H, 15-H), 7.25 (dd, J = 7.6, 1.6 Hz, 3H, 5-H), 7.05 (dd, J = 7.6, 1.6 Hz, 3H, 7-H), 6.99 (t, J = 7.6 Hz, 3H, 6-H), 6.50 (s, 1H, 1-H), 5.51 (s, 3H, OH); ^{13}C NMR (100 MHz, $CDCl_3$) 150.31 (s, C-3), 140.54 (s, C-12), 140.45 (s, C-11), 136.19 (s), 129.65 (d, C-10), 129.45 (d, C-7), 128.88 (d, C-5), 128.83 (s, C-8), 128.82 (d, C-14), 128.04 (s), 127.75 (d, C-15), 127.46 (d, C-9), 127.06 (d, C-13), 120.49

(d, C-6), 38.42 (d, C-1); MS (EI^+, 70 eV) *m*/z 748 (M^+, 2), 500 (10), 486 (100), 246 (63); HRMS (EI^+, 70 eV) Calculated ($C_{55}H_{40}O_3$): 748.2977 (M^+), Found: 748.2990 (M^+).

Tris(3-butyl-2-hydroxyphenyl)methane 1kH_3

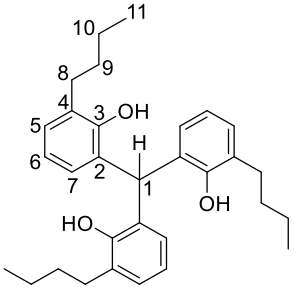

yield: 90%; mp 108.1–108.5 °C; IR (KBr) ν = 3460 (s), 3034 (w), 2954 (s), 2927 (s), 2870 (m), 1590 (w), 1454 (s), 1318 (m), 1173 (s), 1069 (w), 828 (m), 755 (s) cm^{-1}; ^1H NMR (400 MHz, $CDCl_3$) 7.09 (d, *J* = 7.6, 3H, 5-H), 6.83 (t, *J* = 7.8 Hz, 3H, 6-H), 6.76 (d, *J* = 7.6 Hz, 3H, 7-H), 5.95 (s, 1H, 1-H), 4.89 (s, 3H, OH), 2.59 (t, *J* = 7.8 Hz, 6H, 8-H), 1.62–1.54 (m, 6H, 9-H), 1.38 (sext, *J* = 7.5 Hz, 6H, 10-H), 0.93 (t, *J* = 7.4 Hz, 9H, 11-H); ^{13}C NMR (100 MHz, $CDCl_3$) 151.69 (s, C-3), 129.61 (s, C-4), 129.15 (d, C-5), 127.15 (d, C-7), 126.65 (s, C-2), 120.83 (d, C-6), 39.79 (d, C-1), 31.90 (t, C-9), 29.81 (t, C-8), 22.66 (t, C-10), 13.97 (q, C-11); MS (EI, 70 eV) *m*/*z* 460 (M^+, 16), 311 (34), 293 (31), 253 (100); HRMS (EI, 70 eV) Calculated ($C_{31}H_{40}O_3$): 460.2977 (M^+), Found: 460.2969 (M^+).

General procedure for the synthesis of 1H_3 using 1-dodecanethiol

Sodium methoxide (12 mmol) and 1-dodecanethiol (12 mmol) were added to a solution of **10** (1 mmol) in DMF (15 mL). After stirring at 100 °C for 4 h, NaOH aq. (5M, 10 mL) and diethyl ether (15 mL) were added to the reaction mixture at rt. The aqueous layer was washed with diethyl ether to remove thiol byproducts. The aqueous layer was neutralized to pH 6 by the addition of conc HCl, and the reaction mixture was extracted with diethyl ether (3 x 15 mL). The organic layer was dried over anhydrous $MgSO_4$, and the solvent was evaporated. The residue was purified by a silica gel column chromatography (hexane/ ethyl acetate = 80:20) to give the product as a colorless solid.

Tris{3-(4-cyanophenyl)-2-hydroxyphenyl}methane 1fH_3

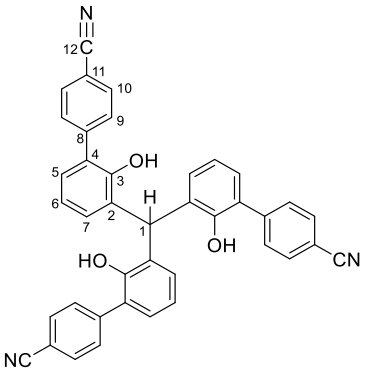

yield: 92%; mp 196.1–196.2 °C; IR (KBr) ν = 3566 (w), 3505 (m), 3064 (w), 2920 (w), 2226 (s), 1606 (s), 1454 (s), 1227 (m), 1189 (m), 831 (s), 752 (s), cm^{-1}; ^1H NMR (400 MHz, $CDCl_3$) 7.74 (d, J = 8.4 Hz, 6H), 7.62 (d, J = 8.4 Hz, 6H), 7.23 (dd, J = 6.2, 3.0 Hz, 3H), 7.06–7.01 (m, 6H), 6.33 (s, 1H, 1-H), 5.29 (s, 3H, OH); ^{13}C NMR (100 MHz, $CDCl_3$) 150.06 (s, C-3), 142.13 (s), 132.67 (d), 130.24 (d), 130.04 (d), 129.34 (d), 128.37 (d), 127.23 (s), 121.33 (s), 118.56 (s), 111.50 (s), 38.39 (d, C-1); MS (EI^+, 70 eV) m/z 595 (M^+, 5), 577 (2), 399 (14), 383 (100), 195 (76); HRMS (EI^+, 70 eV) Calculated ($C_{40}H_{25}N_3O_3$): 595.1896 (M^+), Found: 595.1888 (M^+).

Tris{3-(4-trifluoromethylphenyl)-2-hydroxyphenyl}methane 1gH_3

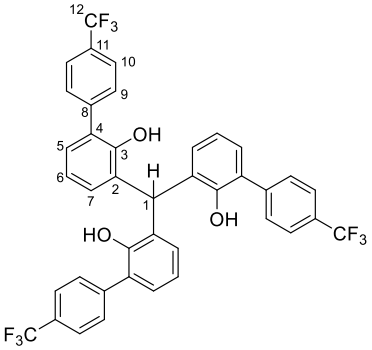

yield: 69%; mp 186.5–187.0 °C; IR (KBr) ν = 3546 (m), 3068 (w), 2933 (w), 1618 (m), 1450 (m), 1405 (m), 1170 (s), 1125 (s), 851 (m), 830 (m), 753 (m) cm^{-1}; ^1H NMR (400 MHz, $CDCl_3$) 7.71 (d, J = 8.4 Hz, 6H, 10-H), 7.61 (d, J = 8.2 Hz, 6H, 9-H), 7.23 (dd, J = 7.6, 2.0 Hz, 3H, 5-H), 7.06 (dd, J = 7.6, 2.0 Hz, 3H, 7-H), 7.02 (t, J = 7.6 Hz, 3H, 6-H), 6.41 (s, 1H, 1-H), 5.35 (s, 3H, OH); ^{13}C NMR (100 MHz, $CDCl_3$) 150.16 (s, C-3), 141.03 (s, C-8), 129. 98 (d, C-9), 129.87 (q, $^2J_{C\text{-}F}$ = 32.9 Hz, C-11), 129.67 (d, C-7), 129.20 (d, C-5), 128.61 (s, C-2), 127.48 (s, C-4), 125.90 (qd, $^3J_{C\text{-}F}$ = 3.3 Hz, C-10), 124.02 (q, $^1J_{C\text{-}F}$ = 273.3 Hz, C-12), 121.01 (d, C-6), 38.38 (d, C-1); ^{19}F NMR (128 MHz, $CDCl_3$, CF_3COOH in $CDCl_3$ as external standard) 11.35; MS (EI^+, 70 eV) m/z 724 (M^+, 14), 487 (24), 469 (100), 341 (9), 238 (9); HRMS (EI^+, 70 eV) Calculated ($C_{40}H_{25}F_9O_3$): 724.1660 (M^+), Found: 724.1648 (M^+).

Tris{3-(4-trimethylsilylphenyl)-2-hydroxyphenyl}methane 1hH_3

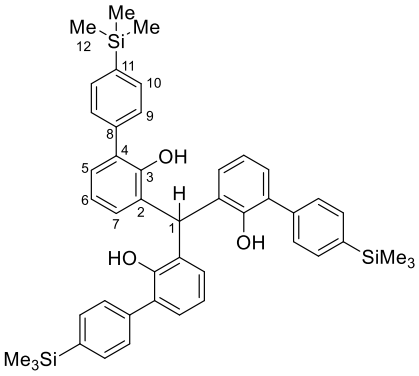

yield: 57%; mp 210.1–210.2 ℃; IR (KBr) ν = 3545 (m), 3016 (w), 2953 (m), 1598 (w), 1445 (s), 1325 (w), 1249 (s), 1119 (m), 842 (s), 754 (s), 659 (m) cm^{-1}; ^1H NMR (400 MHz, $CDCl_3$) 7.60 (d, J = 8.4 Hz, 6H), 7.47 (d, J = 8.4 Hz, 6H), 7.20 (dd, J = 7.6, 2.0 Hz, 3H), 7.01 (dd, J = 7.6, 2.0 Hz, 3H), 6.96 (t, J = 7.6 Hz, 3H), 6.44 (s, 1H, 1-H), 5.47 (s, 3H, OH), 0.29 (s, 27H, 12-H); ^{13}C NMR (100 MHz, $CDCl_3$) 150.26 (s), 139.95 (s, C-11), 137.64 (s), 134.04 (d), 129.37 (d), 128.77, 128.74, 128.48 (d), 128.36 (s), 120.37 (d), 38.44 (d, C-1), –1.16 (q, C-12); $^{29}Si\{^1H\}$ NMR (79 MHz, $CDCl_3$, TMS in $CDCl_3$ as external standard) –3.78; MS (EI^+, 70 eV) m/z 736 (M^+, 26), 495 (44), 477 (100); HRMS (EI^+, 70 eV) Calculated ($C_{46}H_{52}O_3Si_3$): 736.3224 (M^+), Found: 736.3232 (M^+).

General procedure for the synthesis of cage-shaped borates 1B·L

In a nitrogen-filled glove box, to a suspension of **1**H_3 (0.1 mmol) in dichloromethane (3 mL) was added BH_3·THF in THF (0.11 mmol, 0.9 M) at room temperature with stirring for 2 h under release of H_2 gas, to afford **1**B·THF as a colorless solid quantitatively. The corresponding ligands (pyridine, 0.15 mmol) were added to the CH_2Cl_2 (2 mL) solution of **1**B·THF and stirred for 0.5 h. Evaporation of volatiles gave a viscous liquid, which was washed by hexane to give the product **1**B·py as a colorless solid quantitatively.

Cage-shaped borate 1cB·thf

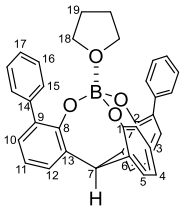

^1H NMR (400 MHz, $CDCl_3$) 7.44 (dd, J = 7.8, 1.2 Hz, 4H, 15-H), 7.33–7.18 (m, 9H), 7.13 (dd, J = 7.6, 1.6 Hz, 2H), 7.09 (dd, J = 7.6, 1.6 Hz, 1H), 6.95–6.89 (m, 3H), 6.83 (d, J = 8.0 Hz, 1H), 5.28 (s, 1H, 7-H), 3.74–3.62 (m, 4H, 18-H), 1.62–1.46 (m, 4H, 19-H); ^{13}C NMR (100 MHz, $CDCl_3$) 155.97 (s, C-1),

153.01 (s, C-8), 140.23 (s), 132.82 (s), 131.48 (s), 131.19 (d), 130.83 (s), 130.64 (d), 130.06 (d), 129.04 (d), 127.77 (d), 127.40 (d), 126.22 (d), 121.16 (d), 121.07 (d), 120.04 (d), 71.79 (t, C-18), 58.01 (d, C-7), 24.19 (t, C-19); $^{11}B\{^{1}H\}$ NMR: (127 MHz, $CDCl_3$, $BF_3{\cdot}OEt_2$ in $CDCl_3$ as external standard) 5.21.

Cage-shaped borate 1dB·thf

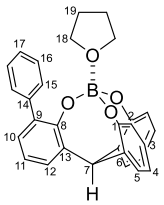

^{1}H NMR (400 MHz, $CDCl_3$) 7.47 (d, J = 7.2 Hz, 2H), 7.33–7.23 (m, 6H), 7.14 (d, J = 7.6 Hz, 1H), 7.09 (t, J = 7.4 Hz, 2H), 6.95–6.82 (m, 5H), 5.21 (s, 1H, 7-H), 4.14–4.06 (m, 4H, 18-H), 1.85–1.79 (m, 4H, 19-H); ^{13}C NMR (100 MHz, $CDCl_3$) 155.72 (s, C-1), 152.87 (s, C-8), 140.16 (s), 132.81 (s), 131.37 (s), 131.08 (d), 130.76 (s), 130.64 (d), 130.10 (d), 129.09 (d), 127.86 (d), 127.48 (d), 126.30 (d), 121.26 (d), 121.17 (d), 120.11 (d), 72.13 (t, C-18), 57.63 (d, C-7), 24.56 (t, C-19); $^{11}B\{^{1}H\}$ NMR (127 MHz, $CDCl_3$, $BF_3{\cdot}OEt_2$ in $CDCl_3$ as external standard) 5.35.

Cage-shaped borate 1eB·thf

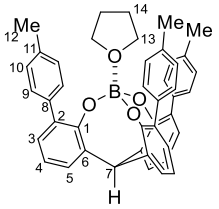

^{1}H NMR (400 MHz, $CDCl_3$) 7.35 (d, J = 8.0 Hz, 6H, 9-H), 7.30 (dd, J = 7.6, 1.6 Hz, 3H, 5-H), 7.14 (dd, J = 7.6, 1.6 Hz, 3H, 3-H), 7.09 (d, J = 8.0 Hz, 6H, 10-H), 6.94 (t, J = 7.6 Hz, 3H, 4-H), 5.35 (s, 1H, 7-H), 3.30–3.17 (m, 4H, 13-H), 2.31 (s, 9H, 12-H), 1.37–1.19 (m, 4H, 14-H); ^{13}C NMR (100 MHz, $CDCl_3$) 153.14 (s, C-1), 137.24 (s, C-8), 135.65 (s, C-11), 132.62 (s, C-2), 131.45 (s, C-6), 130.46 (d, C-5), 129.88 (d, C-9), 128.92 (d, C-3), 128.04 (d, C-10), 120.94 (d, C-4), 71.54 (t, C-13), 58.24 (d, C-7), 23.82 (t, C-14), 21.09 (q, C-12); $^{11}B\{^{1}H\}$ NMR (127 MHz, $CDCl_3$, $BF_3{\cdot}OEt_2$ in $CDCl_3$ as external standard) 5.04.

Cage-shaped borate 1fB·thf

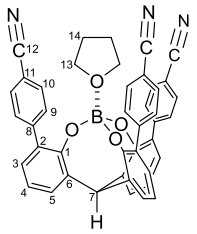

^{1}H NMR (400 MHz, $CDCl_3$) 7.61 (d, *J* = 8.0 Hz, 6H, 10-H), 7.56 (d, *J* = 8.0 Hz, 6H, 9-H), 7.38 (d, *J* = 7.6 Hz, 3H, 5-H), 7.15 (d, *J* = 7.6 Hz, 3H, 3-H), 7.03 (t, *J* = 7.6 Hz, 3H, 4-H), 5.39 (s, 1H, 7-H), 3.26–3.19 (m, 4H, 13-H), 1.39–1.31 (m, 4H, 14-H); ^{13}C NMR (100 MHz, $CDCl_3$) 152.64 (s, C-1), 144.86 (s, C-8), 131.94 (d, C-5), 131.41 (d, C-10), 131.36 (s, C-6), 130.87 (s, C-2), 130.55 (d, C-9), 129.20 (d, C-3), 121.72 (d, C-4), 118.89 (s, C-12), 110.12 (s, C-11), 72.14 (t, C-13), 57.64 (d, C-7), 24.11 (t, C-14); ^{11}B{^{1}H} NMR: (127 MHz, $CDCl_3$, $BF_3{\cdot}OEt_2$ in $CDCl_3$ as external standard) 2.97.

Cage-shaped borate 1gB·thf

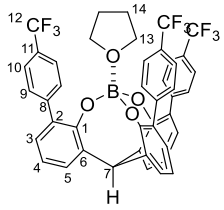

^{1}H NMR (400 MHz, $CDCl_3$) 7.59–7.52 (m, 12H, 9-H, 10-H), 7.38 (dd, *J* = 7.6, 1.6 Hz, 3H), 7.17 (dd, *J* = 7.6, 1.6 Hz, 3H), 7.02 (t, *J* = 7.6 Hz, 3H, 4-H), 5.40 (s, 1H, 7-H), 3.14–3.04 (m, 4H, 13-H), 1.32–1.20 (m, 4H, 14-H); ^{13}C NMR (100 MHz, $CDCl_3$) 150.16 (C-1), 141.03, 130.01, 129.97, 129.68, 129.20, 128.64, 127.47, 125.90, 124.01 (q, $^{1}J_{C\text{-}F}$ = 273.3 Hz, C-12), 121.01, 67.91 (C-13), 38.36 (C-7), 25.55 (C-14); ^{11}B{^{1}H} NMR (127 MHz, $CDCl_3$, $BF_3{\cdot}OEt_2$ in $CDCl_3$ as external standard) 4.83; ^{19}F NMR (128 MHz, $CDCl_3$, CF_3COOH in $CDCl_3$ as external standard) 11.53.

Cage-shaped borate 1hB·thf

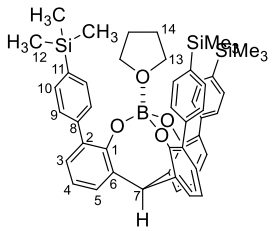

^{1}H NMR (400 MHz, $CDCl_3$) 7.46–7.44 (12H, m, 9, 10-H), 7.34 (3H, dd, *J* = 7.6, 1.6 Hz, 5-H), 7.17 (3H, dd, *J* = 7.6, 1.6 Hz, 3-H), 6.97 (3H, t, *J* = 7.6 Hz, 4-H), 5.38 (1H, s, 7-H), 3.15–3.07 (4H, m, 13-H), 1.22–1.13 (4H, m, 14-H), 0.25 (27H, s, 12-H); ^{13}C NMR (100 MHz, $CDCl_3$) 153.10 (s, C-1), 140.64 (s),

137.85 (s), 132.68 (s), 132.36 (d), 131.34 (s), 130.75 (d), 129.43 (d), 128.89 (d, C-3), 121.05 (d, C-4), 71.35 (t, C-13), 58.21 (d, C-7), 23.64 (t, C-14), –1.06 (q, C-12); $^{11}B\{^{1}H\}$ NMR: (127 MHz, $CDCl_3$, $BF_3{\cdot}OEt_2$ in $CDCl_3$ as external standard) 5.08; $^{29}Si\{^{1}H\}$ NMR: (79 MHz, $CDCl_3$, TMS in $CDCl_3$ as external standard) – 4.26.

Cage-shaped borate 1iB·thf

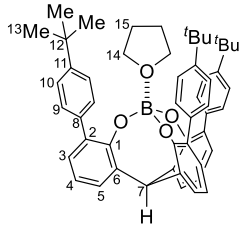

^{1}H NMR (400 MHz, $CDCl_3$) 7.38 (d, J = 8.8 Hz, 6H, 9-H), 7.32–7.30 (m, 9H, 5-H, 10-H), 7.16 (dd, J = 7.6, 1.6 Hz, 3H, 3-H), 6.95 (t, J = 7.6 Hz, 3H, 4-H), 5.35 (s, 1H, 7-H), 3.17–3.09 (m, 4H, 14-H), 1.30 (s, 27H, 13-H), 1.24–1.17 (m, 4H, 15-H); ^{13}C NMR (100 MHz, $CDCl_3$) 153.18 (s, C-1), 148.99 (s, C-11), 137.24 (s, C-8), 132.59 (s, C-2), 131.36 (s, C-6), 130.50 (d, C-5), 129.72 (d, C-9), 128.84 (d, C-3), 124.20 (d, C-10), 120.94 (d, C-4), 71.26 (t, C-14), 58.24 (d, C-7), 34.43 (t, C-15), 31.41 (q, C-13), 0.00 (s, C-12); $^{11}B\{^{1}H\}$ NMR: (127 MHz, $CDCl_3$, $BF_3{\cdot}OEt_2$ in $CDCl_3$ as external standard) 4.84.

Cage-shaped borate 1jB·thf

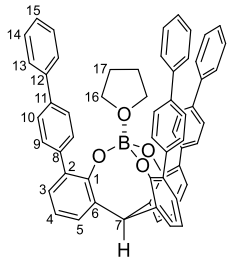

^{1}H NMR (400 MHz, $CDCl_3$) 7.57–7.50 (m, 18H), 7.45–7.30 (m, 12H), 7.22 (dd, J = 7.2, 1.2 Hz, 3H), 7.00 (t, J = 7.2 Hz, 3H), 5.42 (s, 1H, 7-H), 3.37–3.23 (m, 4H, 16-H), 1.34–1.14 (m, 4H, 17-H); ^{13}C NMR (100 MHz, $CDCl_3$) 153.15 (s, C-1), 140.90 (s), 139.20 (s), 139.01 (s), 132.31 (s), 131.47 (s), 130.83 (d), 130.43 (d), 128.95 (d), 128.78 (d), 127.17 (d), 126.87 (d), 126.10 (d), 121.16 (d), 71.76 (t, C-16), 58.15 (d, C-7), 23.88 (t, C-17); $^{11}B\{^{1}H\}$ NMR: (127 MHz, $CDCl_3$, $BF_3{\cdot}OEt_2$ in $CDCl_3$ as external standard) 5.25.

Cage-shaped borate 1kB·thf

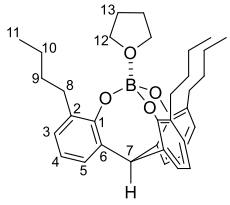

^{1}H NMR (400 MHz, $CDCl_3$) 7.00 (d, *J* = 6.8 Hz, 3H, 5-H), 6.89 (d, *J* = 7.2 Hz, 3H, 3-H), 6.70 (t, *J* = 7.6 Hz, 3H, 4-H), 5.06 (s, 1H, 7-H), 4.50 (t, *J* = 6.8 Hz, 4H, 12-H), 2.52 (t, *J* = 8.2 Hz, 6H, 8-H), 2.17 (t, *J* = 6.8 Hz, 4H, 13-H), 1.51–1.43 (m, 6H, 9-H), 1.27 (sext, *J* = 7.4 Hz, 6H, 10-H), 0.83 (t, *J* = 7.4 Hz, 9H, 11-H); ^{13}C NMR (100 MHz, $CDCl_3$) 153.57 (s, C-1), 132.21 (s, C-2), 130.63 (s, C-6), 129.00 (d, C-5), 127.67 (d, C-3), 120.55 (d, C-4), 72.14 (t, C-12), 58.39 (d, C-7), 32.01 (t, C-9), 30.25 (t, C-8), 25.24 (t, C-13), 23.01 (t, C-10), 14.13 (q, C-11); ^{11}B{^{1}H} NMR (127 MHz, $CDCl_3$, $BF_3{\cdot}Et_2O$ in $CDCl_3$ as an external standard) 6.49.

Cage-shaped borate 1kB·py

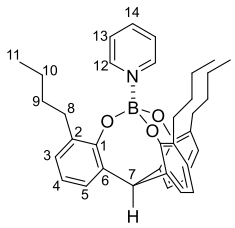

^{1}H NMR (400 MHz, $CDCl_3$) 9.34 (d, *J* = 4.8, 2H, 12-H), 8.13 (t, *J* = 7.6 Hz, 1H, 14-H), 7.73 (t, *J* = 7.2 Hz, 2H, 13-H), 7.17 (dd, *J* = 7.6, 1.6 Hz, 3H, 5-H), 7.00 (dd, *J* = 7.4, 1.6 Hz, 3H, 3-H), 6.82 (t, *J* = 7.6 Hz, 3H, 4-H), 5.25 (s, 1H, 7-H), 2.53 (t, *J* = 8.0, 6H, 8-H), 1.45–1.38 (m, 6H, 9-H), 1.21 (sext, *J* = 7.4, 6H, 10-H), 0.79 (t, *J* = 7.2 Hz, 9H, 11-H); ^{13}C NMR (100 MHz, $CDCl_3$) 154.22 (s, C-1), 143.97 (d, C-12), 141.85 (d, C-14), 132.64 (s, C-2), 131.11 (s, C-6), 129.06 (d, C-5), 127.80 (d, C-3), 125.06 (d, C-13), 120.35 (d, C-4), 58.83 (d, C-7), 32.41 (t, C-9), 30.71 (t, C-8), 22.86 (t, C-10), 13.95 (q, C-11); ^{11}B{^{1}H} NMR: (127 MHz, $CDCl_3$, $BF_3{\cdot}Et_2O$ in $CDCl_3$ as an external standard) 4.87.

Procedure for the intramolecular competitive hetero Diels-Alder Reaction

·In batch system

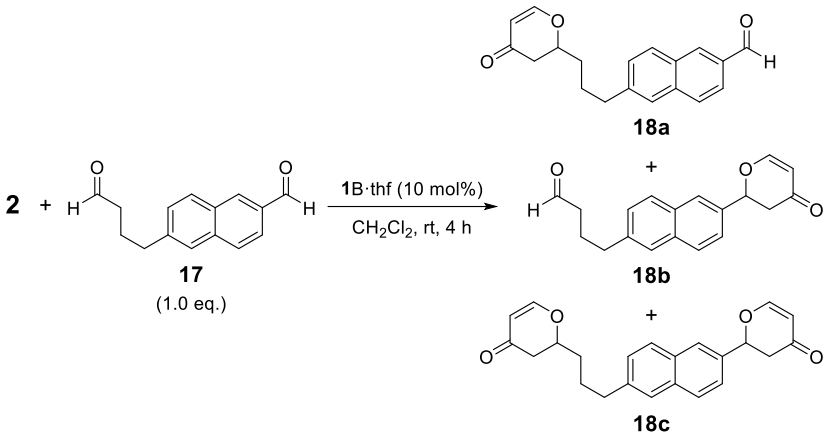

In a nitrogen-filled glove box, the dropwise solution of Danishefsky's diene **2** (17.2 mg, 0.10 mmol) in CH_2Cl_2 (2.0 mL) was gradually added to the solution of the dialdehyde **17**[42] (22.6 mg, 0.10 mmol) and borate catalyst (0.010 mmol) in CH_2Cl_2 (2.0 mL) at room temperature via a syringe. After stirring for 4 h at room temperature, methanol (10 mL) was added to the mixture. The solvents were removed under vacuum. The obtained crude mixture was analyzed by NMR using 1,1,2,2-tetracholoroethane as an internal standard.

For the isolation of the products **18**, the crude mixture was purified by silica gel column chromatography (hexane/ethyl acetate = 80:20, column length 11 cm and diameter 2.7 cm) followed by a recycled HPLC system, to give the three products **18a**–**c**.

·In flow system

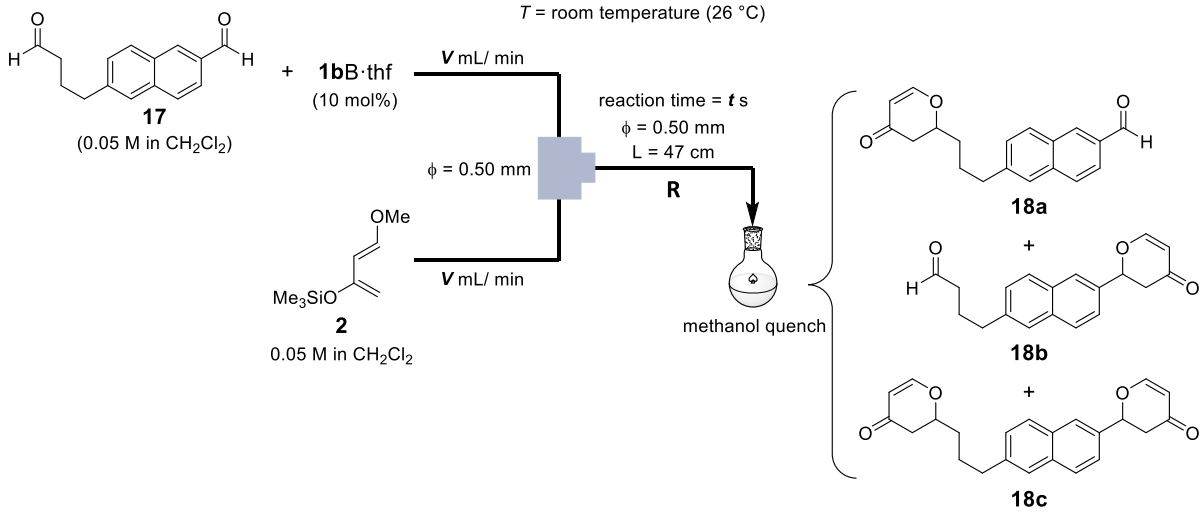

A solution of **17** and **1b**B·thf (10 mol%) in CH_2Cl_2 (0.05 M) (flow rate: *V* mL/min) and a solution of **2** in CH_2Cl_2 (0.05 M) (flow rate: *V* mL/min) were introduced to a T-shaped microreactor (ϕ = 0.50 mm) by syringe pumps. The resulting solution was passed through R (ϕ = 0.5 mm, L = 47 cm). After a steady state (reaction time: *t* s) was reached, the outcoming solution was collected in a vessel containing methanol. The solvents were removed under vacuum. The obtained crude mixture was analyzed by NMR using 1,1,2,2-tetracholoroethane as an internal standard. The yields of the products and the selectivity with the increase in the flow rate were summarized in the following table.

entry	flow rate ***V*** /mL·min^{-1}	reaction time ***t*** /s	yield / % (**18a**+**18b**+**18c**)	ratio **18a**/**18b**/**18c**
1	0.025	120	39	5 : 57 : 38
2	0.050	60	38	10 : 54 : 36
3	0.100	30	46	16 : 63 : 21
4	0.500	6	43	6 : 71 : 23
5	1.00	3	41	7 : 78 : 15

6-(3-(4-oxo-3,4-dihydro-2*H*-pyran-2-yl)propyl)-2-naphthaldehyde 18a

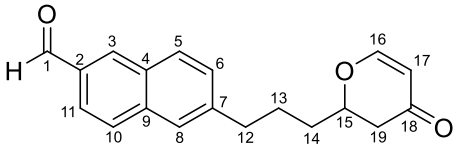

colorless solid; mp 84.2–84.8 °C; IR (KBr) *v* = 3045 (w), 2947 (w), 2924 (w), 2842 (w), 1692 (s), 1650 (s), 1586 (s), 1402 (w), 1285 (m), 1221 (m), 1171 (w), 1047 (w), 893 (m) cm^{-1}; ^{1}H NMR (400 MHz, $CDCl_3$) 10.15 (s, 1H, 1-H), 8.32 (s, 1H, 3-H), 7.95 (d, *J* = 9.6 Hz, 1H, 5-H), 7.95 (d, *J* = 8.4 Hz, 1H, 11-H), 7.88 (d, *J* = 8.8 Hz, 1H, 10-H), 7.69 (s, 1H, 8-H), 7.45 (dd, *J* = 8.6, 1.6 Hz, 1H, 6-H), 7.36 (d, *J* = 5.6 Hz, 1H, 16-H), 5.41 (dd, *J* = 5.8, 1.2 Hz, 1H, 17-H), 4.48–4.41 (m, 1H, 15-H), 2.88 (t, *J* = 7.0 Hz, 2H, 12-H), 2.53 (dd, *J* = 17.2, 13.6 Hz, 1H, 19-H), 2.43 (ddd, *J* = 17.1, 4.0, 0.8 Hz, 1H, 19-H), 2.02–1.83 (m, 2H, 13-H), 1.80–1.71 (m, 2H, 14-H); ^{13}C NMR (100 MHz, $CDCl_3$) 192.52 (s, C-18), 192.22 (d, C-1), 163.17 (d, C-16), 143.01 (s, C-7), 136.69 (s, C-9), 134.31 (d, C-3), 133.67 (s, C-2), 131.22 (s, C-4), 129.68 (d, C-5), 128.58 (d, C-10), 128.36 (d, C-6), 126.73 (d, C-8), 123.05 (d, C-11), 107.04 (d, C-17), 79.24 (d, C-15), 41.82 (t, C-19), 35.75 (t, C-12), 33.87 (t, C-14), 26.23 (t, C-13); MS (EI$^+$, 70 eV) *m*/z 294 (M$^+$,100), 182 (93), 169 (61), 141 (35), 97 (89); HRMS (EI$^+$, 70 eV) Calculated ($C_{19}H_{18}O_3$): 294.1256 (M$^+$); Found: 294.1252.

4-(6-(4-oxo-3,4-dihydro-2*H*-pyran-2-yl)naphthalen-2-yl)butanal 18b

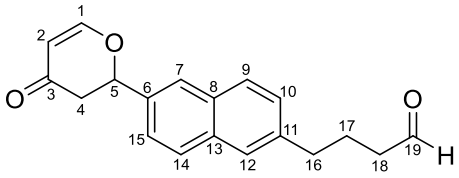

colorless solid; mp 35.5–36.0 °C; IR (KBr) ν = 3054 (w), 2924 (s), 2853 (m), 1722 (m), 1670 (s), 1591 (s), 1458 (w), 1403 (m), 1264 (s), 1226 (s), 1097 (s), 1039 (s), 818 (m) cm^{-1}; ^1H NMR (600 MHz, $CDCl_3$) 9.78 (t, J = 1.5 Hz, 1H, 19-H), 7.84 (d, J = 9.0 Hz, 1H, 14-H), 7.83 (s, 1H, 7-H), 7.81 (d, J = 8.4 Hz, 1H, 9-H), 7.64 (s, 1H, 12-H), 7.53 (d, J = 6.0 Hz, 1H, 1-H), 7.49 (dd, J = 8.7, 1.8 Hz, 1H, 15-H), 7.38 (dd, J = 8.4, 1.8 Hz, 1H, 10-H), 5.59 (dd, J = 14.4, 3.0 Hz, 1H, 5-H), 5.56 (dd, J = 6.0, 1.2 Hz, 1H, 2-H), 3.01 (dd, J = 17.1, 14.4 Hz, 1H, 4-H), 2.84 (t, J = 7.5 Hz, 2H, 16-H), 2.75 (ddd, J = 17.0, 3.3, 1.2 Hz, 1H, 4-H), 2.50 (td, J = 7.4, 1.8 Hz, 2H, 18-H), 2.06 (quin, J = 7.5 Hz, 2H, 17-H); ^{13}C NMR (150 MHz, $CDCl_3$) 202.12 (d, C-19), 192.13 (s, C-3), 163.22 (d, C-1), 139.77 (s, C-11), 134.64 (s, C-6), 133.59 (s, C-13), 131.75 (s, C-8), 128.38 (d, C-14), 128.36 (d, C-9), 127.97 (d, C-10), 126.53 (d, C-12), 125.25 (d, C-7), 123.76 (d, C-15), 107.47 (d, C-2), 81.27 (d, C-5), 43.42 (t, C-4), 43.11 (t, C-18), 35.13 (t, C-16), 23.42 (t, C-17); MS (EI^+, 70 eV) m/z 294 (M^+, 48), 224 (33), 180 (100), 167 (40); HRMS (EI^+, 70 eV) Calculated ($C_{19}H_{18}O_3$): 294.1256 (M^+); Found: 294.1253.

2-(3-(6-(4-oxo-3,4-dihydro-2*H*-pyran-2-yl)naphthalen-2-yl)propyl)-2,3-dihydro-4*H*-pyran-4-one 18c

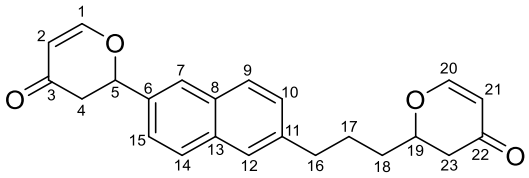

The product was isolated as a single diastereomer of colorless solids. mp 40.1–40.5 °C; IR (KBr) ν = 3056 (w), 2925 (w), 2858 (w), 1687 (s), 1627 (m), 1591 (m), 1456 (m), 1273 (m), 1157 (m), 1027 (w), 892 (w), 822 (w), 760 (m), 701 (w) cm^{-1}; ^1H NMR (600 MHz, $CDCl_3$) 7.84 (d, J = 9.0 Hz, 1H, 14-H), 7.83 (s, 1H, 7-H), 7.81 (d, J = 8.4 Hz, 1H, 9-H), 7.64 (s, 1H, 12-H), 7.53 (dd, J = 6.0, 0.6 Hz, 1H, 1-H), 7.49 (dd, J = 8.7, 1.8 Hz, 1H, 15-H), 7.38 (dd, J = 8.4, 1.8 Hz, 1H, 10-H), 7.35 (d, J = 6.0 Hz, 1H, 20-H), 5.59 (dd, J = 14.4, 3.6 Hz, 1H, 5-H), 5.56 (dd, J = 6.0, 1.2 Hz, 1H, 2-H), 5.40 (dd, J = 6.0, 1.2 Hz, 1H, 21-H), 4.46–4.41 (m, 1H, 19-H), 3.01 (dd, J = 16.8, 14.4 Hz, 1H, 4-H), 2.85 (td, J = 7.2, 2.4 Hz, 2H, 16-H), 2.75 (ddd, J = 17.0, 3.6, 1.2 Hz, 1H, 4-H), 2.51 (dd, J = 16.8, 13.2 Hz, 1H, 23-H), 2.42 (ddd, J = 16.8, 3.6, 1.2 Hz, 1H, 23-H), 1.97–1.78 (m, 2H, 17-H), 1.75–1.68 (m, 2H, 18-H); ^{13}C NMR (150 MHz, $CDCl_3$) 192.58 (s, C-22), 192.14 (s, C-3), 163.23 (d, C-1), 163.21 (d, C-20), 140.13 (s, C-11),

134.59 (s, C-6), 133.60 (s, C-13), 131.71 (s, C-8), 128.36 (d, C-14), 128.32 (d, C-9), 127.95 (d, C-10), 126.39 (d, C-12), 125.26 (d, C-7), 123.75 (d, C-15), 107.46 (d, C-2), 107.04 (d, C-21), 81.26 (d, C-5), 79.34 (d, C-19), 43.41 (t, C-4), 41.85 (t, C-23), 35.58 (t, C-16), 33.87 (t, C-18), 26.33 (t, C-17); MS (EI^+, 70 eV) *m*/z 362 (41), 292 (23), 247 (47), 180 (79), 167 (100), 125 (6), 110 (20), 97 (75); HRMS (EI^+, 70 eV) Calculated ($C_{23}H_{22}O_4$): 362.1518 (M^+); Found: 362.1523.

X-ray crystallographic data

Cage-shaped borate **1b**B·thf (CCDC 2015164)

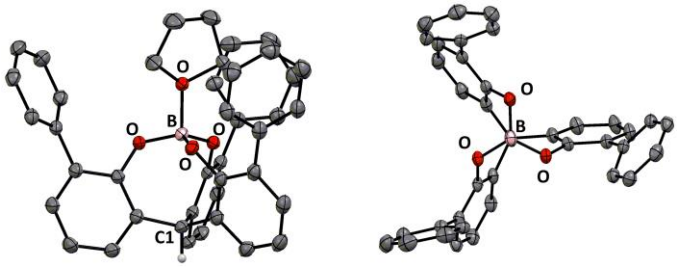

Figure S1. ORTEP drawings of **1b**B·thf at the 50% probability level.

Empirical Formula	$C_{41}H_{33}BO_4$	*Z* value	4
Formula Weight	600.48	D_{calc}	1.306 g/cm^3
Crystal Color, Habit	colorless, prism	F_{000}	1264.0
Crystal Dimensions	0.6 × 0.5 × 0.3 mm	μ(CuK$_\alpha$)	0.650 mm^{-1}
Crystal System	monoclinic	Temperature	123 K
Lattice Type	Primitive	Data/restraints/parameters	6203/0/415
Lattice Parameters	*a* = 15.03420(10) Å	Residuals: R_1 ($I > 2.00\sigma(I)$)	0.0496
	b = 12.87520(10) Å	Residuals: wR_2 (all data)	0.1372
	c = 15.8937(2) Å	Goodness of Fit Indicator	1.058
	β = 96.9600(10) °		
	V = 3053.85(5) Å^3		
Space Group	$P2_1/c$ (#14)		

Cage-shaped borate **1d**B·thf (CCDC 2015165)

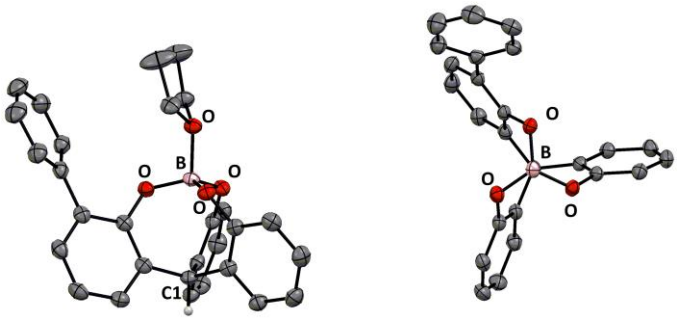

Figure S2. ORTEP drawings of **1d**B·thf at the 50% probability level.

Empirical Formula	$C_{29}H_{25}BO_4$	*Z* value	4
Formula Weight	448.30	D_{calc}	1.318 g/cm^3
Crystal Color, Habit	colorless, block	F_{000}	944.0
Crystal Dimensions	0.3 × 0.2 × 0.15 mm	μ(CuK$_\alpha$)	0.687 mm^{-1}
Crystal System	monoclinic	Temperature	123 K
Lattice Type	Primitive	Data/restraints/parameters	4603/0/307
Lattice Parameters	*a* = 12.9007(2) Å	Residuals: R_1 ($I > 2.00\sigma(I)$)	0.0704
	b = 15.7484(2) Å	Residuals: wR_2 (all data)	0.2049
	c = 11.5675(2) Å	Goodness of Fit Indicator	1.068
	β = 105.930(2) °		
	2259.87(6) Å^3		
Space Group	$P2_1$/c (#2)		

Cage-shaped borate 1eB·thf (CCDC 2015166)

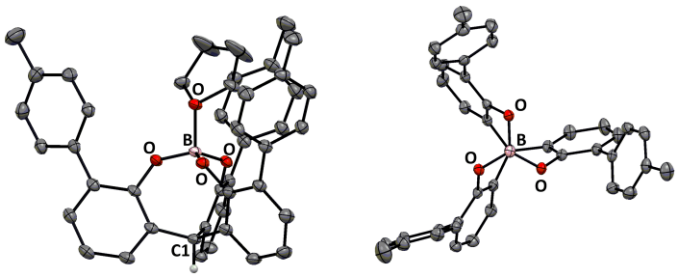

Figure S3. ORTEP drawings of **1e**B·thf at the 50% probability level.

Empirical Formula	$C_{45}H_{41}BCl_2O_4$	*Z* value	4
Formula Weight	727.49	D_{calc}	1.274 g/cm^3
Crystal Color, Habit	colorless, block	F_{000}	1528.00
Crystal Dimensions	0.323 × 0.317 × 0.184 mm	μ(CuK$_\alpha$)	1.878 mm^{-1}
Crystal System	triclinic	Temperature	123 K
Lattice Type	Primitive	Data/restraints/parameters	15352/0/962
Lattice Parameters	*a* = 13.7019(2) Å	Residuals: R_1 ($I > 2.00\sigma(I)$)	0.0573
	b = 14.19830(10) Å	Residuals: wR_2 (all data)	0.1644
	c = 20.2299(2) Å	Goodness of Fit Indicator	1.042
	α = 98.0900(10) °		
	β = 100.4380(10) °		
	γ = 96.3720(10) °		
	V = 3794.12(7) Å^3		
Space Group	*P*-1 (#2)		

Cage-shaped borate 1jB·thf (CCDC 2015167)

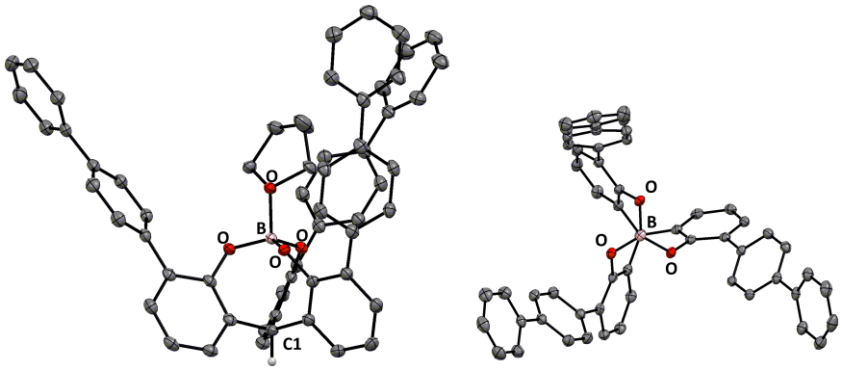

Figure S4. ORTEP drawings of **1j**B·thf at the 50% probability level.

Empirical Formula	$C_{59}H_{45}BO_4$	*Z* value	4
Formula Weight	828.76	D_{calc}	1.302 g/cm^3
Crystal Color, Habit	colorless, block	F_{000}	1744.00
Crystal Dimensions	0.255 × 0.189 × 0.102 mm	μ(MoK$_\alpha$)	0.080 mm^{-1}
Crystal System	monoclinic	Temperature	123 K
Lattice Type	Primitive	Data/restraints/parameters	10984/0/587
Lattice Parameters	*a* = 11.6298(5) Å	Residuals: R_1 ($I > 2.00\sigma(I)$)	0.0438
	b = 10.3690(3) Å	Residuals: wR_2 (all data)	0.1095
	c = 35.4258(10) Å	Goodness of Fit Indicator	1.048
	β = 98.208(3) °		
	V = 4228.2(3) Å^3		
Space Group	$P2_1/c$ (#14)		

Cage-shaped borate 1kB·py (CCDC 2015168)

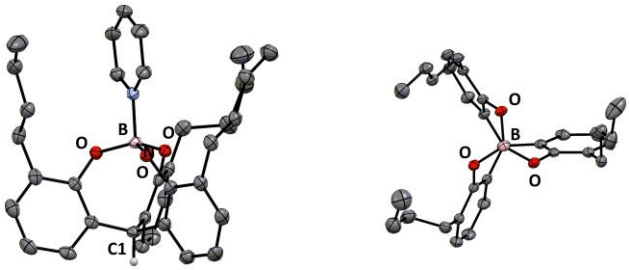

Figure S5. ORTEP drawings of **1k**B·py at the 50% probability level.

Empirical Formula	$C_{72}H_{84}B_2N_2O_6$	*Z* value	4
Formula Weight	1095.03	D_{calc}	1.177 g/cm^3
Crystal Color, Habit	colorless, block	F_{000}	2352.0
Crystal Dimensions	0.185 × 0.111 × 0.091 mm	μ(CuK$_\alpha$)	0.568 mm^{-1}
Crystal System	monoclinic	Temperature	123 K
Lattice Type	Primitive	Data/restraints/parameters	12509/0/745
Lattice Parameters	a = 18.6151(2) Å	Residuals: R_1 ($I > 2.00\sigma(I)$)	0.0603
	b = 16.3872(2) Å	Residuals: wR_2 (all data)	0.1874
	c = 20.2868(2) Å	Goodness of Fit Indicator	1.057
	β = 93.2950(10) °		
	V = 6178.24(12) Å^3		
Space Group	$P2_1/n$ (#14)		

IR measurements of the cage-shaped complex with 2,6-dimethyl-γ-pyrone

In a nitrogen-filled glove box, to a solution of cage-shaped complex (0.05 mmol) in CH_2Cl_2 (1 mL) was added 2,6-dimethyl-γ-pyrone (0.1 mmol). After stirring for 1 h, volatile was removed under reduced pressure and the residue was washed with hexane to afford the product. The ligation of 2,6-dimethyl-γ-pyrone was confirmed by NMR measurements. Infrared spectra of the obtained complex were recorded as CH_2Cl_2 solutions and the average values of five times measurements were employed.

Reaction of 2,3-dimethyl-1,3-butadiene with aldehyde catalyzed by cage-shaped borate

Experimental procedure

In a nitrogen-filled glove box, to a white solid of cage-shaped borate THF complex **1**B·thf (2 mol%, 0.01 mmol) was added 2,3-dimethyl-1,3-butadiene (0.41 g, 5.0 mmol) and benzaldehyde **3b** or **3c** (0.50 mmol) in toluene (2 mL) at rt in a sealed vessel. The mixture was stirred for 14 h at 120 °C and then H_2O was added to quench the reaction. The solution was extracted with CH_2Cl_2 (3 x 10 mL) and the organic layer was dried ($MgSO_4$) and evaporated to give a crude mixture, which was analyzed by NMR to obtain the yield using an internal standard.

Table S1. Summary for catalytic activity of borates with various π-pocket in the hetero Diels-Alder reaction of **13** with **3b**

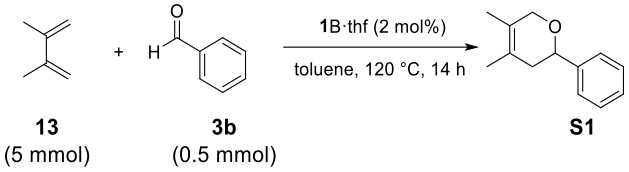

13 (5 mmol) **3b** (0.5 mmol) **S1**

entry	borate **1**	*ortho*-group	yield of **S1**[a]/ %
1	**1a**B·thf	non	53
2	**1b**B·thf	C_6H_5	100
3	**1e**B·thf	*p*-$CH_3C_6H_4$	100
4	**1g**B·thf	*p*-$CF_3C_6H_4$	100
5	**1i**B·thf	*p*-^{t}BuC_6H_4	88
6	**1j**B·thf	*p*-PhC_6H_4	96

[a]Yields were determined by ^{1}H NMR measurement using 1,1,2,2-tetrachloroethane as an internal standard.

Table S2. Summary for catalytic activity of borates with various π-pocket in the hetero Diels-Alder reaction of **13** with **3c**

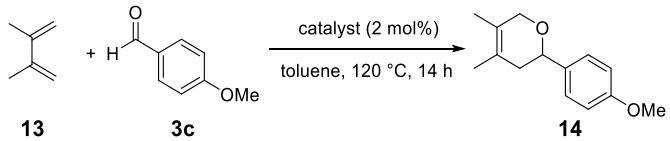

13 (5 mmol) **3c** (0.5 mmol) **14**

entry	catalyst	*ortho*-group	yield of **14**[a]/ %
1	**1a**B·thf	non	5
2	**1b**B·thf	C_6H_5	43
3	**1e**B·thf	*p*-$CH_3C_6H_4$	49
4	**1g**B·thf	*p*-$CF_3C_6H_4$	96
5	**1i**B·thf	*p*-^{t}BuC_6H_4	38
6	**1j**B·thf	*p*-PhC_6H_4	73
7	BF_3·Et_2O	–	0
8	$B(OPh)_3$	–	0

[a]Yields were determined by ^{1}H NMR measurement using 1,1,2,2-tetrachloroethane as an internal standard.

Competitive cycloaddition of the Danishefsky's diene 2 with the mixture of aldehydes 3a and 3b–f

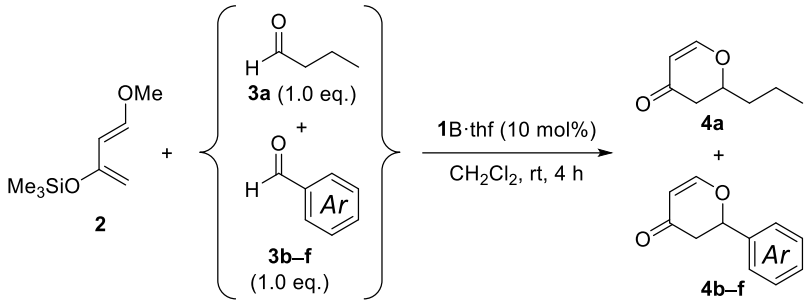

Ar = Ph (**b**), 4-$MeOC_6H_4$ (**c**), $4MeC_6H_4$ (**d**), C_6F_5 (**e**), 4-NCC_6H_4 (**f**)

In a nitrogen-filled glove box, to the solution of the borate catalyst (0.050 mmol) in CH_2Cl_2 (2 mL) was added Danishefsky's diene **2** (0.50 mmol), butanal **3a** (0.50 mmol), and benzaldehyde derivative **3b**–**f** (0.50 mmol) at room temperature. After stirring for 4 h at room temperature, HCl aq (10 mL) was added to the mixture. The products were extracted with dichloromethane (3 x 10 mL). The organic layer was dried with $MgSO_4$ and evaporated to give a crude mixture, which was analyzed by NMR using 1,1,2,2-tetracholoroethane as an internal standard.

Table S3. Summary for the competitive cycloaddition of the **2** with **3a** and various benzaldehydes **3b**–**f** catalyzed by **1**B·thf complexes.

catalyst **1**B·thf	benzaldehyde derivative **3**	total yield of **4**/ %		ratio of **4**	
1aB·thf 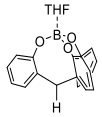	**3b**	**4a**+**4b**	73	**4a**/**4b**	52:48
	3c	**4a**+**4c**	78	**4a**/**4c**	70:30
	3d	**4a**+**4d**	100	**4a**/**4d**	71:29
	3e	**4a**+**4e**	66	**4a**/**4e**	52:48
	3f	**4a**+**4f**	72	**4a**/**4f**	33:67
1bB·thf 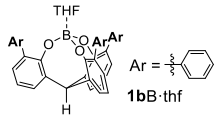	**3b**	**4a**+**4b**	71	**4a**/**4b**	30:70
	3c	**4a**+**4c**	79	**4a**/**4c**	49:51
	3d	**4a**+**4d**	93	**4a**/**4d**	36:64
	3e	**4a**+**4e**	66	**4a**/**4e**	14:86
	3f	**4a**+**4f**	79	**4a**/**4f**	10:90
1eB·thf 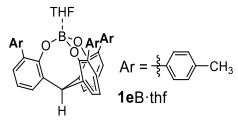	**3b**	**4a**+**4b**	82	**4a**/**4b**	30:70
	3c	**4a**+**4c**	78	**4a**/**4c**	37:63
	3d	**4a**+**4d**	82	**4a**/**4d**	36:64
	3e	**4a**+**4e**	60	**4a**/**4e**	15:85

	3f	**4a**+**4f**	69	**4a**/**4f**	4:96
1fB·thf	**3b**	**4a**+**4b**	98	**4a**/**4b**	35:65
	3c	**4a**+**4c**	76	**4a**/**4c**	59:41
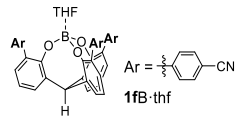	**3d**	**4a**+**4d**	75	**4a**/**4d**	40:60
	3e	**4a**+**4e**	45	**4a**/**4e**	27:73
	3f	**4a**+**4f**	91	**4a**/**4f**	21:79
1gB·thf	**3b**	**4a**+**4b**	100	**4a**/**4b**	46:54
	3c	**4a**+**4c**	86	**4a**/**4c**	56:44
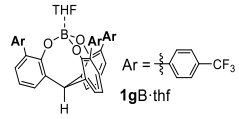	**3d**	**4a**+**4d**	87	**4a**/**4d**	45:55
	3e	**4a**+**4e**	71	**4a**/**4e**	64:36
	3f	**4a**+**4f**	88	**4a**/**4f**	24:76
1hB·thf	**3b**	**4a**+**4b**	71	**4a**/**4b**	34:66
	3c	**4a**+**4c**	74	**4a**/**4c**	49:51
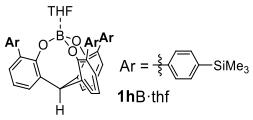	**3d**	**4a**+**4d**	78	**4a**/**4d**	40:60
	3e	**4a**+**4e**	68	**4a**/**4e**	28:72
	3f	**4a**+**4f**	70	**4a**/**4f**	20:80
1iB·thf	**3b**	**4a**+**4b**	92	**4a**/**4b**	33:67
	3c	**4a**+**4c**	81	**4a**/**4c**	49:51
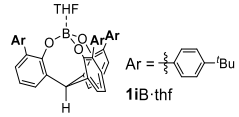	**3d**	**4a**+**4d**	78	**4a**/**4d**	36:64
	3e	**4a**+**4e**	60	**4a**/**4e**	29:71
	3f	**4a**+**4f**	73	**4a**/**4f**	22:78
1jB·thf	**3b**	**4a**+**4b**	81	**4a**/**4b**	30:70
	3c	**4a**+**4c**	85	**4a**/**4c**	41:59
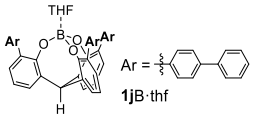	**3d**	**4a**+**4d**	76	**4a**/**4d**	30:70
	3e	**4a**+**4e**	66	**4a**/**4e**	18:82
	3f	**4a**+**4f**	78	**4a**/**4f**	10:90
1kB·thf	**3b**	**4a**+**4b**	71	**4a**/**4b**	56:44
	3c	**4a**+**4c**	52	**4a**/**4c**	51:49
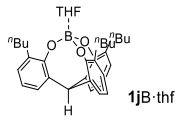	**3d**	**4a**+**4d**	52	**4a**/**4d**	75:25
	3e	**4a**+**4e**	53	**4a**/**4e**	36:64
	3f	**4a**+**4f**	82	**4a**/**4f**	34:66

Kinetic study of the cycloaddition of 2 with 3a or 3b catalyzed by 1aB·thf **or 1b**B·thf

Experimental procedure: Initial rate kinetics of the cycloaddition of **2** with **3a** or **3b**

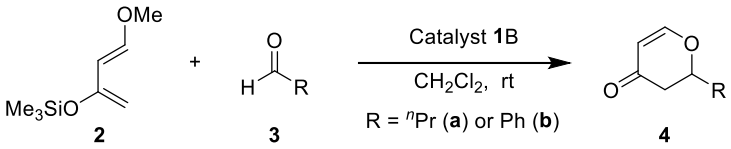

In a nitrogen-purged three-necked round-bottom flask equipped with a diamond probe of a React IR TM 15 spectrometer, the solution of Danishefsky's diene **2** (x mmol) and aldehyde **3** (y mmol) in CH_2Cl_2 was charged at the indicated temperature. After adding the solution of the isolated borate **1**B (z mmol) in CH_2Cl_2 via a syringe at the temperature, the monitoring of the decreased intensity of the C=O stretching frequency (**3a**: 1725 cm^{-1}; **3b**: 1703 cm^{-1}) was started using a React IR spectrometer. The obtained profiles of the reaction were summarized as below.

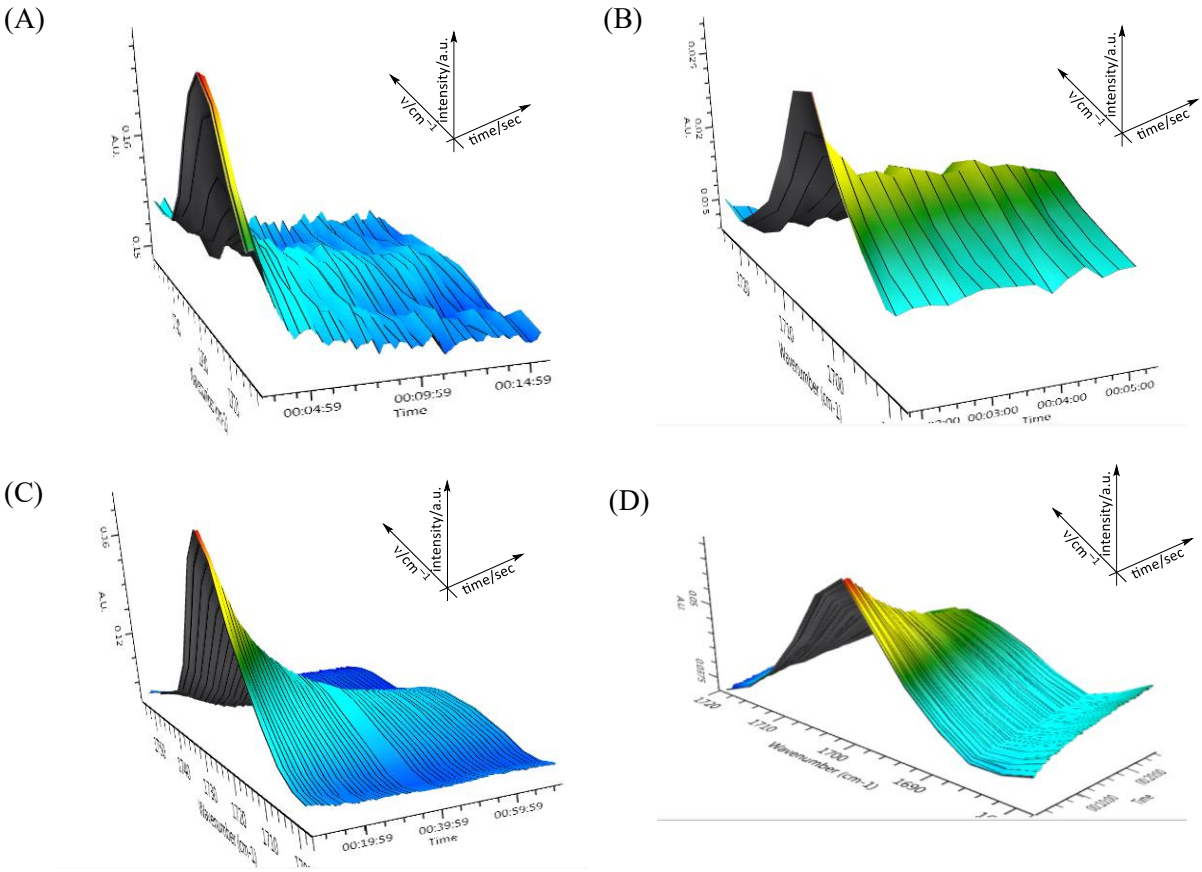

Figure S6. In situ monitoring the decay of the intensity of the C=O stretching for (A) **3a** and (B) **3b** in the reactions catalyzed by **1a**B·thf and for (C) **3a** and (D) **3b** in the reactions catalyzed by **1b**B·thf.

The reaction of 2 with 3a catalyzed by 1aB·thf

*Initial kinetic profile with varying amount of **2***

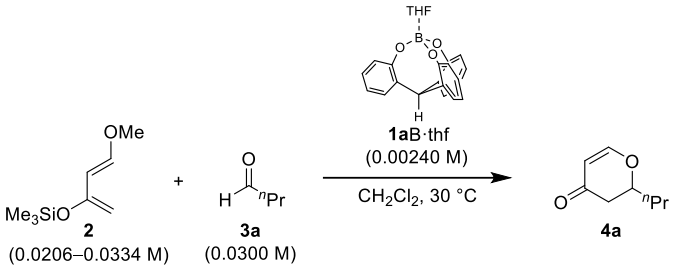

2 / M	initial rate v_0 / Ms^{-1}
0.0206	2.61×10^{-4}
0.0233	2.66×10^{-4}
0.0300	3.70×10^{-4}
0.0334	3.98×10^{-4}

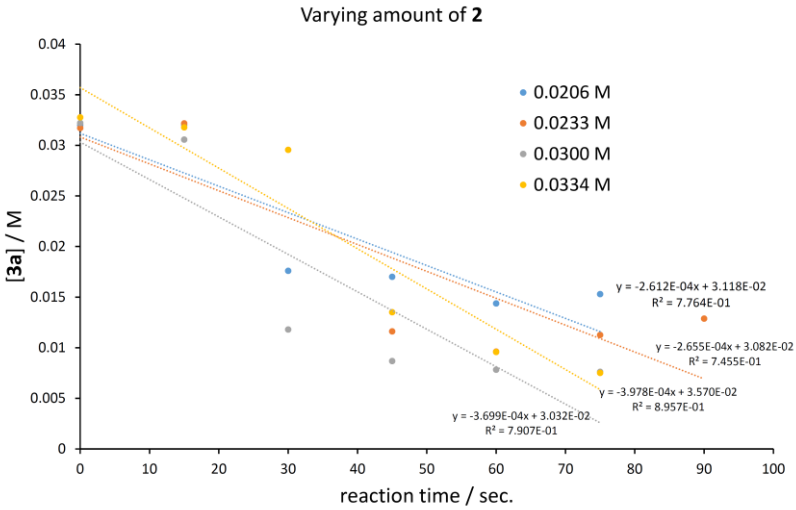

*Initial kinetic profile with varying amount of **3a***

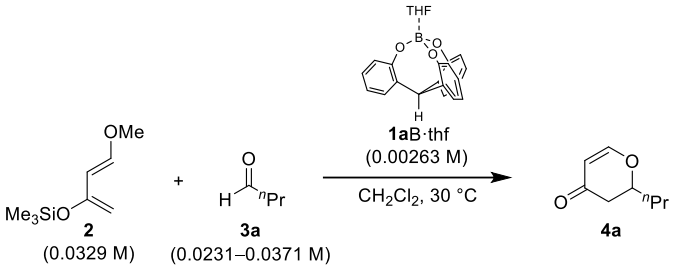

3a / M	initial rate v_0 / Ms^{-1}
0.0231	2.60×10^{-4}
0.0302	3.63×10^{-4}
0.0329	3.98×10^{-4}
0.0371	4.34×10^{-4}

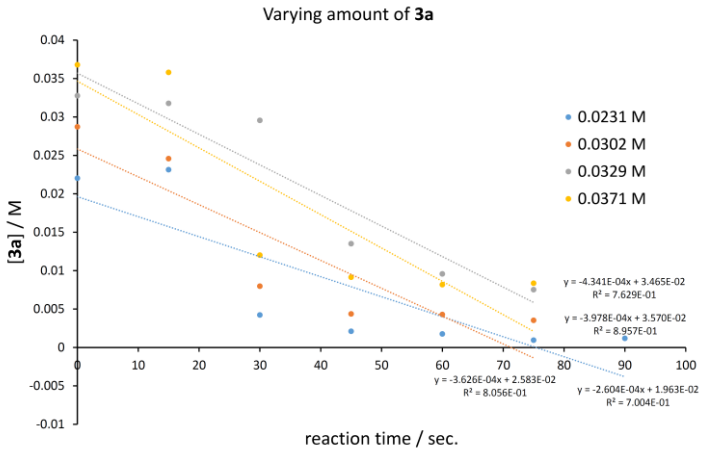

Initial kinetic profile with varying amount of **1a**B·thf

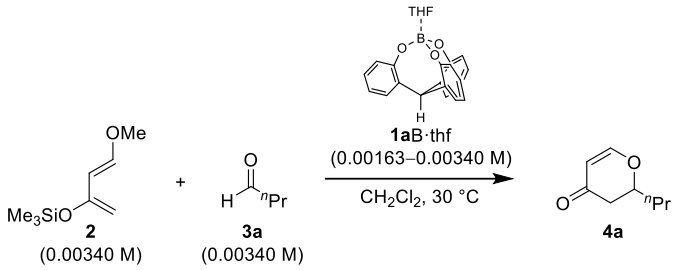

1aB·thf / M	initial rate v_0 / Ms^{-1}
0.00163	1.72×10^{-4}
0.00196	2.29×10^{-4}
0.00231	2.82×10^{-4}
0.00340	3.61×10^{-4}

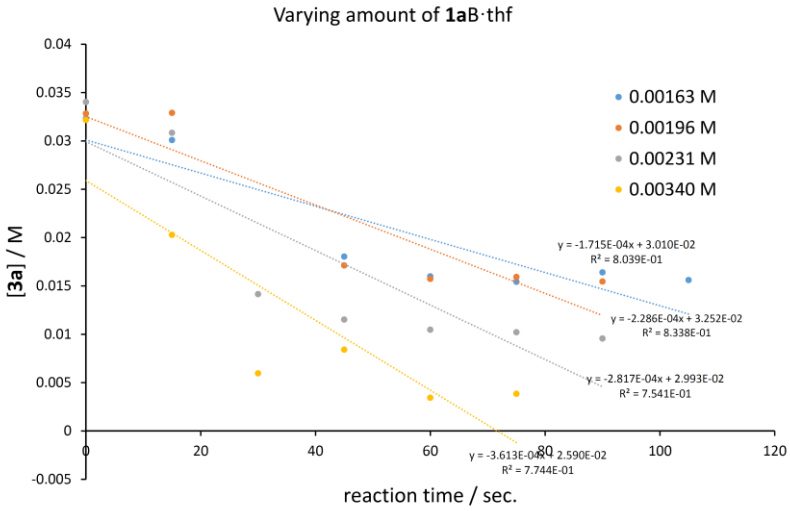

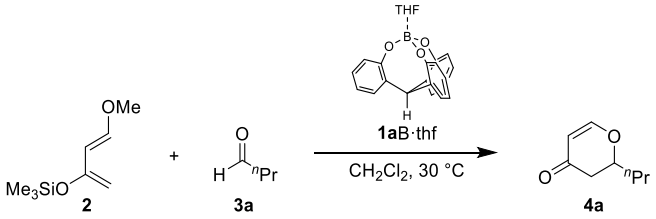

$$\text{rate} = k_{obs}[\mathbf{2}]^1[\mathbf{3a}]^1[\mathbf{1a}\text{B}\cdot\text{thf}]^1$$

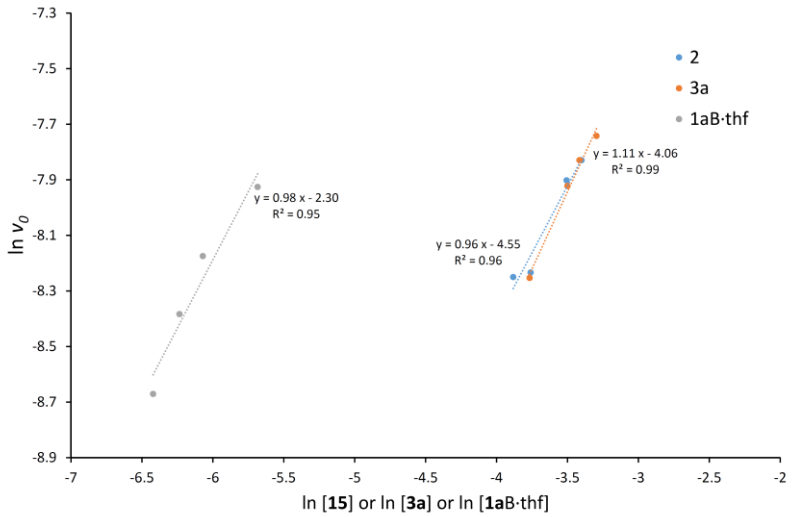

The reaction of 2 with 3b catalyzed by 1aB·thf

*Initial kinetic profile with varying amount of **2***

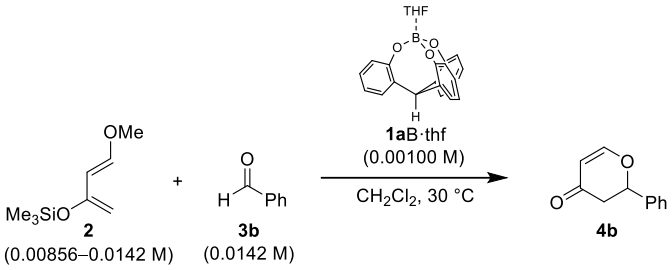

2 / M	initial rate v_0 / Ms^{-1}
0.00856	8.65×10^{-6}
0.00993	1.14×10^{-5}
0.0127	1.54×10^{-5}
0.0142	1.56×10^{-5}

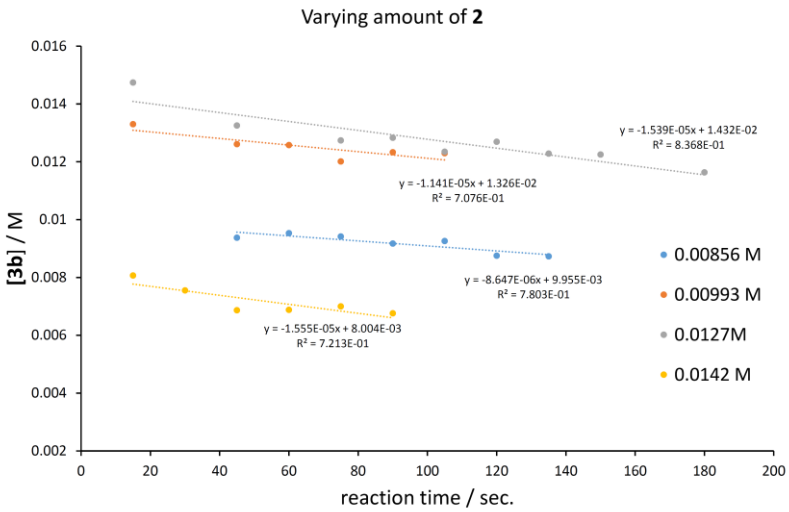

*Initial kinetic profile with varying amount of **3b***

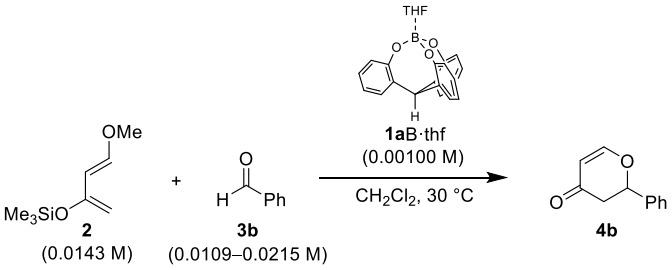

3b / M	initial rate v_0 / Ms^{-1}
0.0109	1.43×10^{-5}
0.0143	1.77×10^{-5}
0.0183	2.26×10^{-5}
0.0215	3.03×10^{-5}

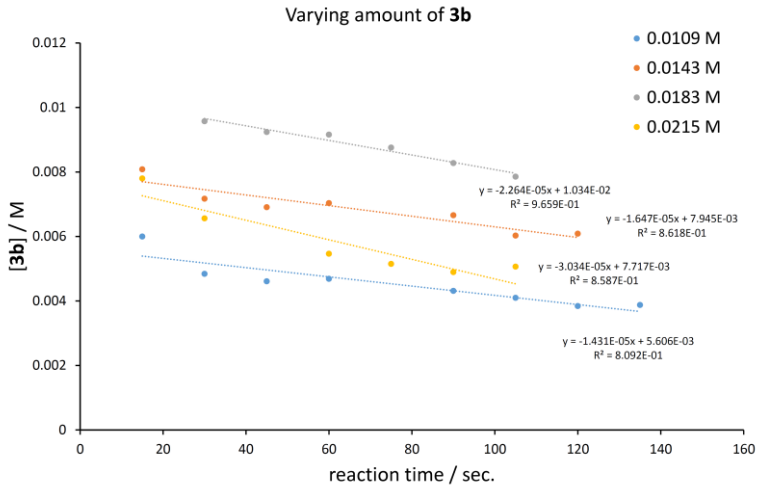

Initial kinetic profile with varying amount of **1a**B·thf

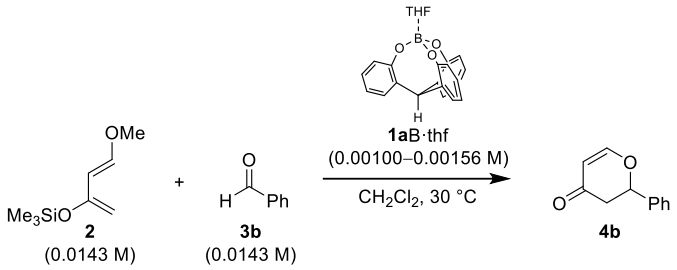

1aB·thf / M	initial rate v_0 / Ms^{-1}
0.00100	1.65×10^{-5}
0.00114	1.81×10^{-5}
0.00143	2.49×10^{-5}
0.00156	2.60×10^{-5}

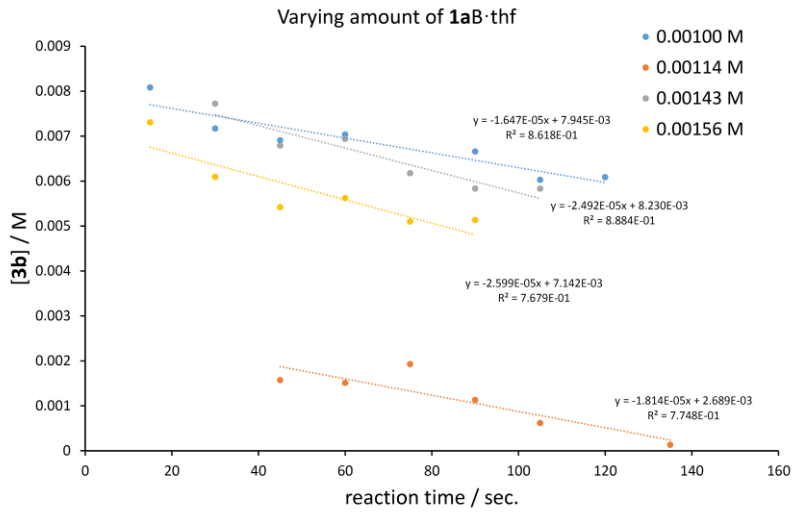

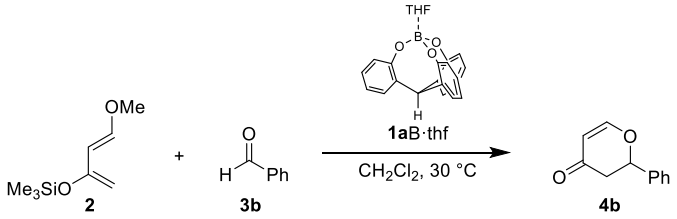

rate = k_{obs}[**2**]^1[**3b**]^1[**1a**B·thf]^1

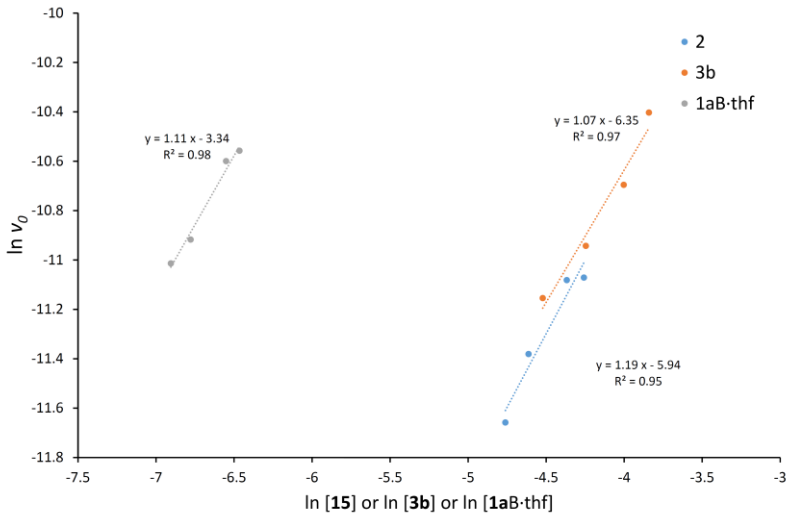

The reaction of 2 with 3a catalyzed by 1bB·thf

*Initial kinetic profile with varying amount of **2***

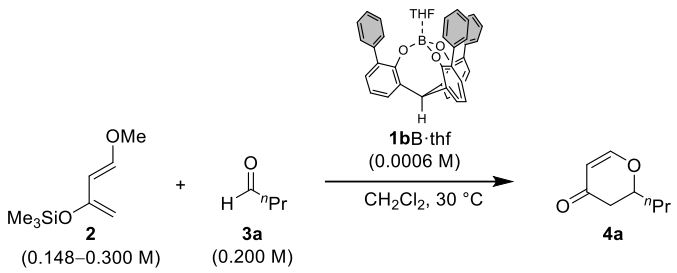

2 / M	initial rate v_0 / Ms^{-1}
0.148	7.90×10^{-4}
0.200	9.09×10^{-4}
0.279	1.30×10^{-3}
0.300	1.50×10^{-3}

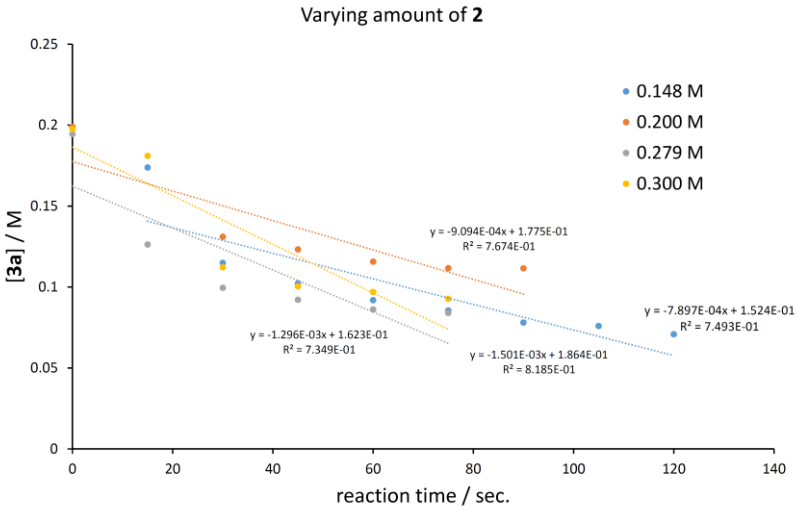

*Initial kinetic profile with varying amount of **3a***

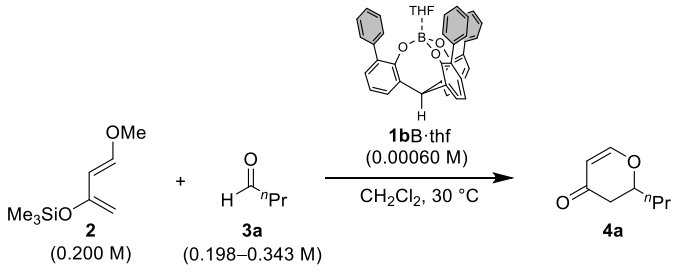

3a / M	initial rate v_0 / Ms^{-1}
0.198	1.22×10^{-4}
0.258	1.67×10^{-4}
0.323	2.18×10^{-4}
0.343	2.13×10^{-4}

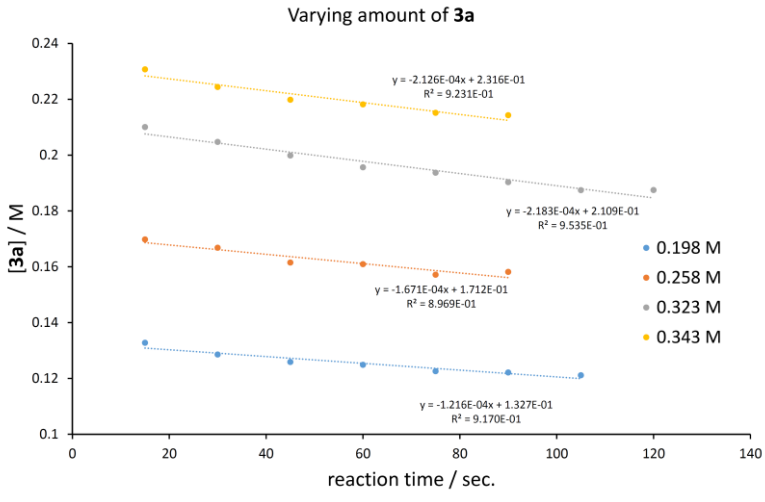

Initial kinetic profile with varying amount of **1b**B·thf

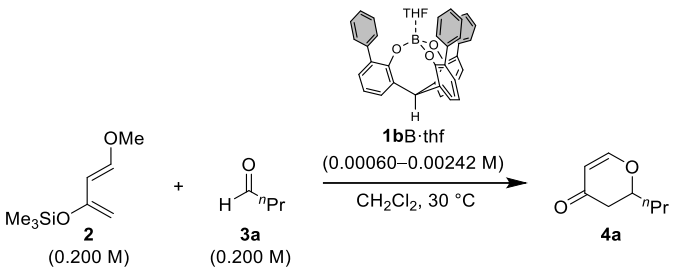

1bB·thf / M	initial rate v_0 / Ms^{-1}
0.00060	3.03×10^{-4}
0.00080	4.53×10^{-4}
0.0012	5.26×10^{-4}
0.00242	1.14×10^{-3}

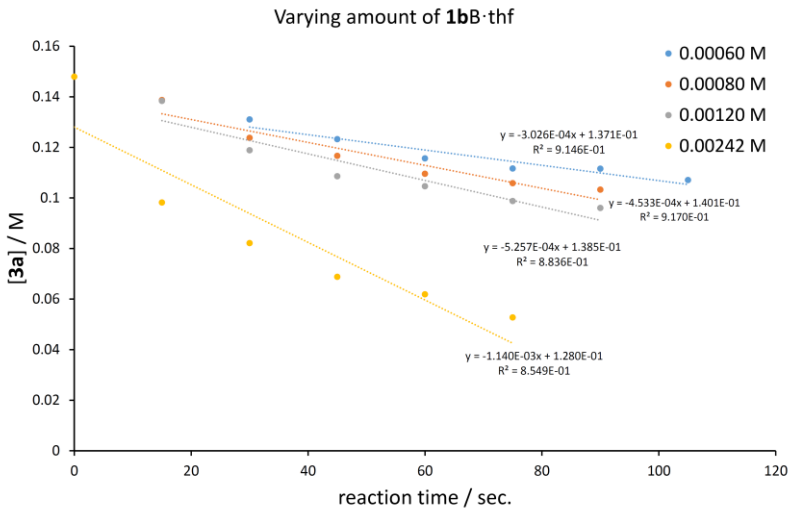

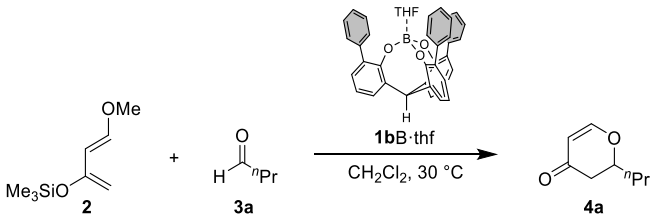

rate = k_{obs}[**2**]^1[**3a**]^1[**1b**B·thf]^1

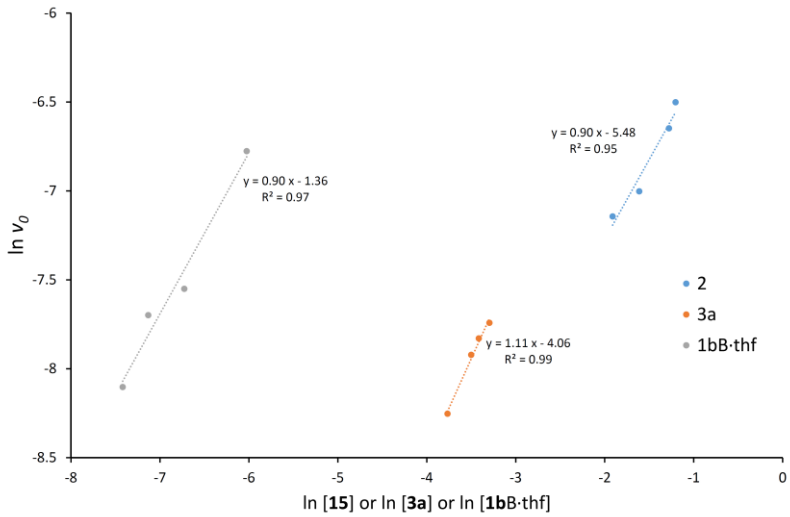

The reaction of 2 with 3b catalyzed by 1bB·thf

*Initial kinetic profile with varying amount of **2***

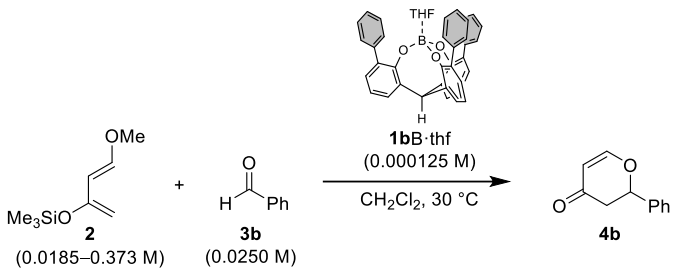

2 / M	initial rate v_0 / Ms^{-1}
0.0185	8.55×10^{-5}
0.0250	9.97×10^{-5}
0.0311	1.33×10^{-4}
0.0373	1.57×10^{-4}

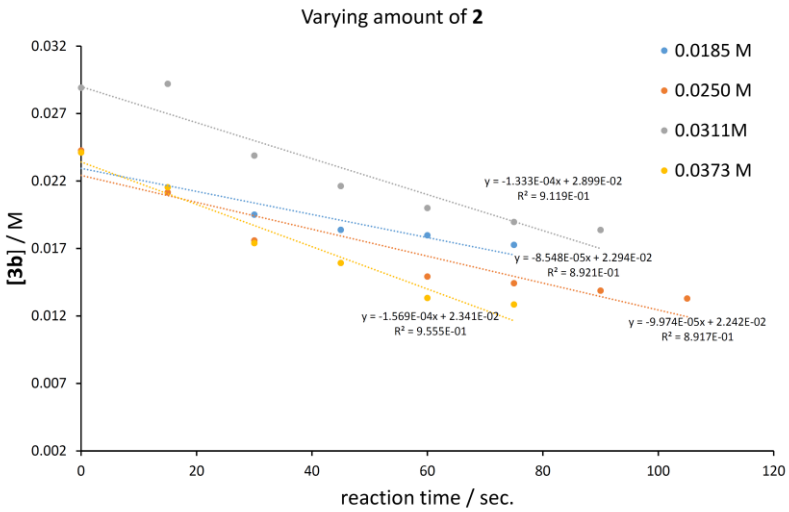

*Initial kinetic profile with varying amount of **3b***

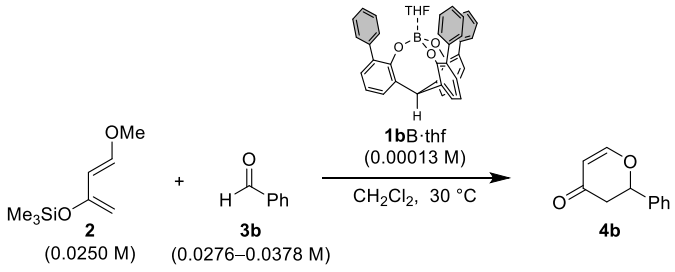

3b / M	initial rate v_0 / Ms^{-1}
0.0276	9.96×10^{-5}
0.0314	1.17×10^{-4}
0.0349	1.32×10^{-4}
0.0378	1.41×10^{-4}

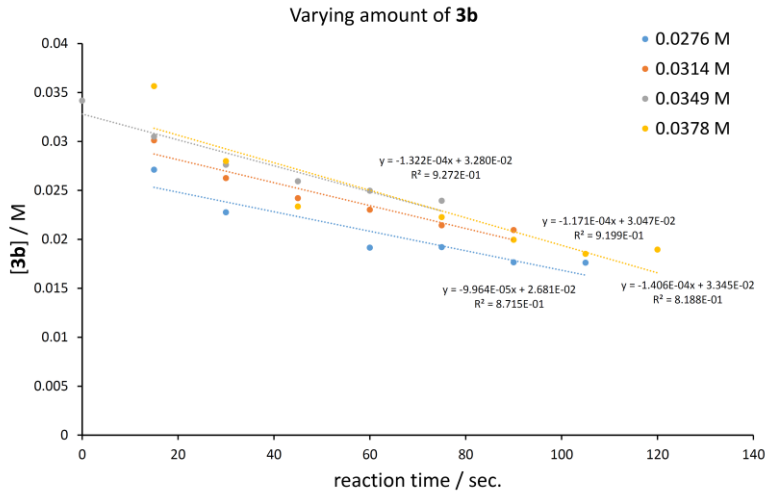

Initial kinetic profile with varying amount of **1b**B·thf

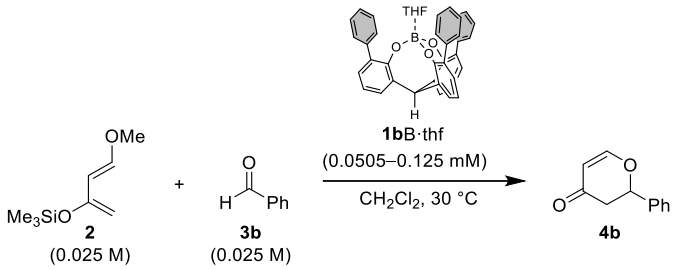

1bB·thf / mM	initial rate v_0 / Ms^{-1}
0.0505	4.82×10^{-5}
0.0758	6.93×10^{-5}
0.0988	9.61×10^{-5}
0.125	1.15×10^{-4}

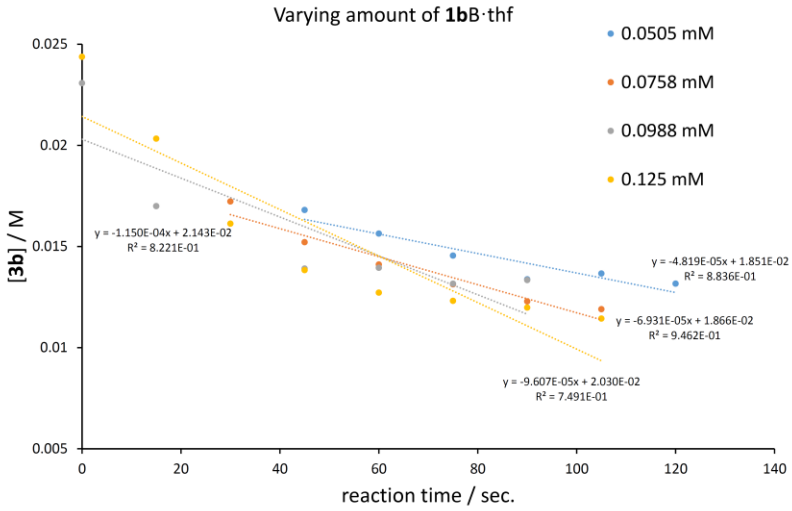

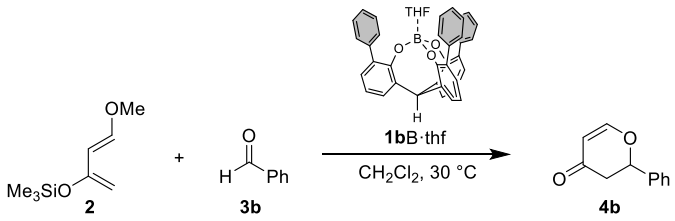

rate = k_{obs}[**2**]^1[**3b**]^1[**1b**B·thf]^1

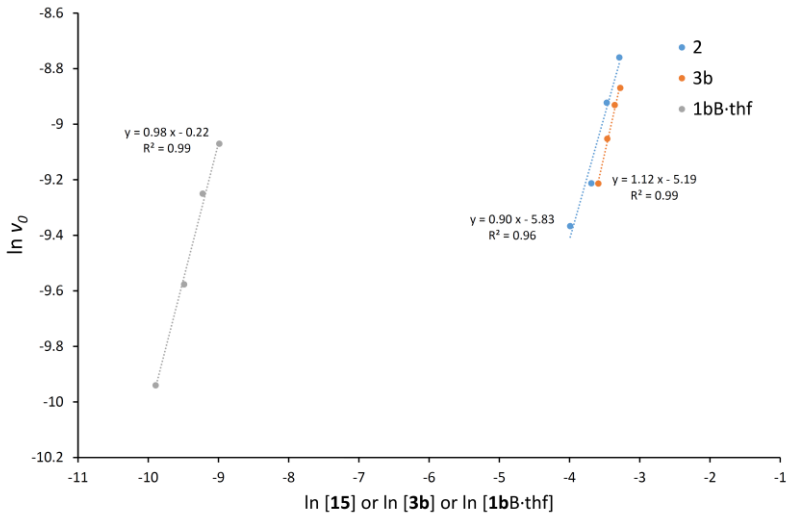

The determination of the activation parameters

*Cycloaddition of **2** with **3a** catalyzed by **1a**B·thf*

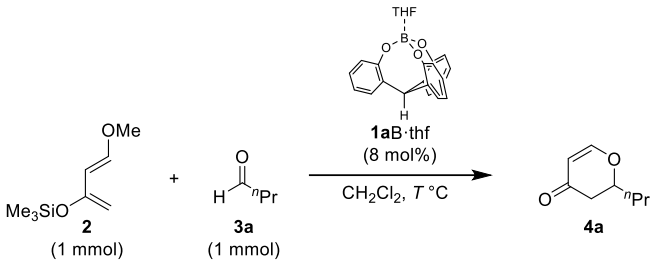

$$\text{rate} = k_{obs}[\mathbf{2}]^1[\mathbf{3a}]^1[\mathbf{1a}\text{B}\cdot\text{thf}]^1$$

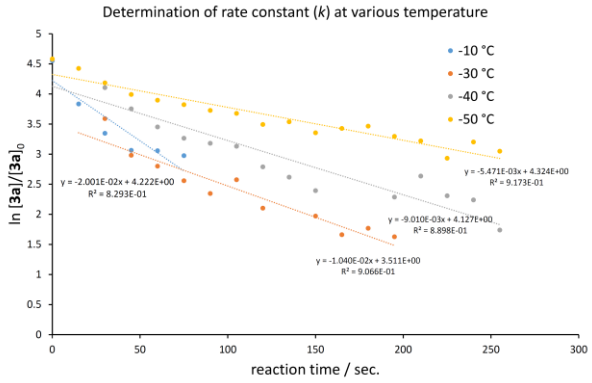

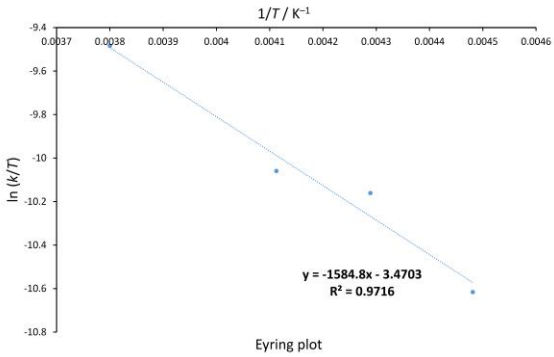

*Cycloaddition of **2** with **3b** catalyzed by **1a**B·thf*

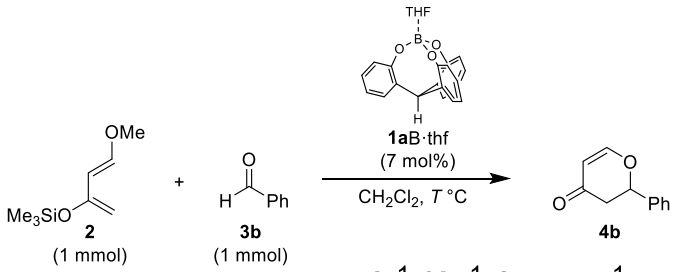

$$\text{rate} = k_{obs}[\mathbf{2}]^1[\mathbf{3b}]^1[\mathbf{1a}\text{B}\cdot\text{thf}]^1$$

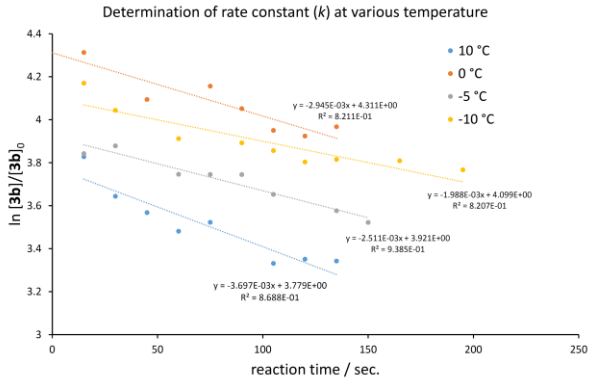

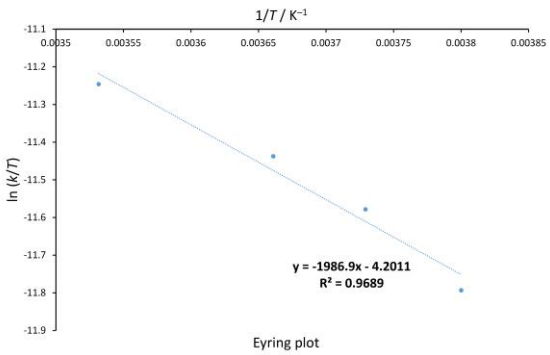

*Cycloaddition of **2** with **3a** catalyzed by **1b**B·thf*

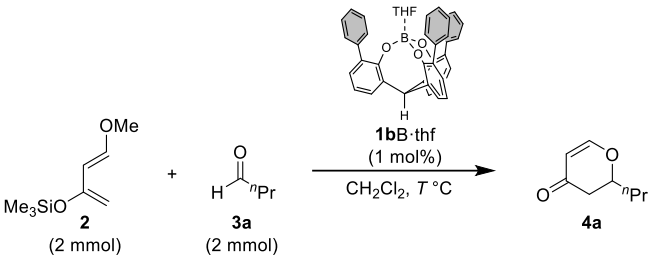

$$\text{rate} = k_{obs}[\mathbf{2}]^1[\mathbf{3a}]^1[\mathbf{1b}\text{B}\cdot\text{thf}]^1$$

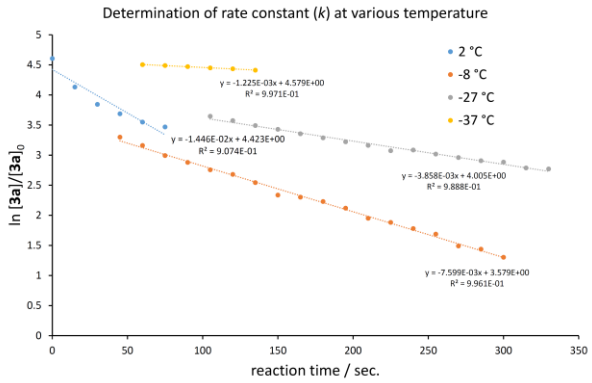

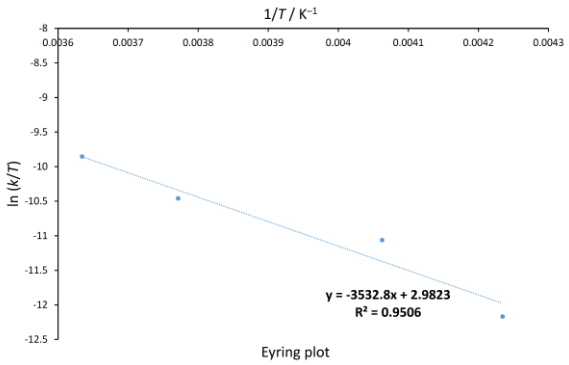

*Cycloaddition of **2** with **3b** catalyzed by **1b**B·thf*

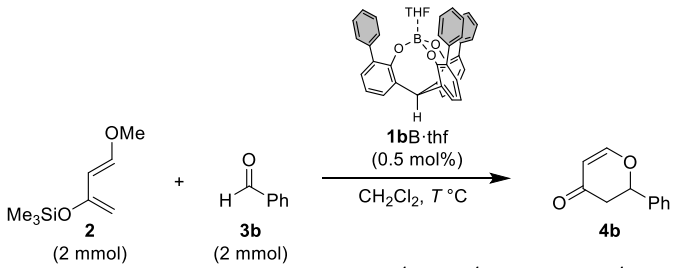

$$\text{rate} = k_{obs}[\mathbf{2}]^1[\mathbf{3b}]^1[\mathbf{1b}\text{B}\cdot\text{thf}]^1$$

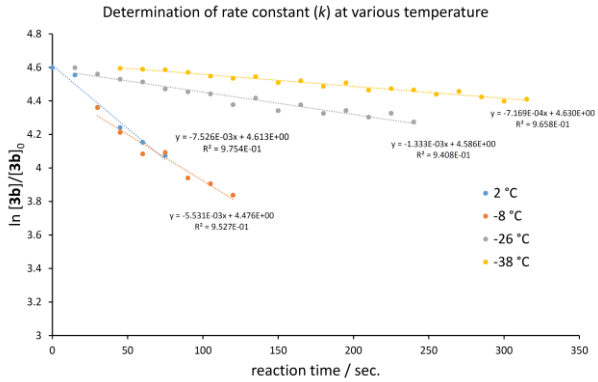

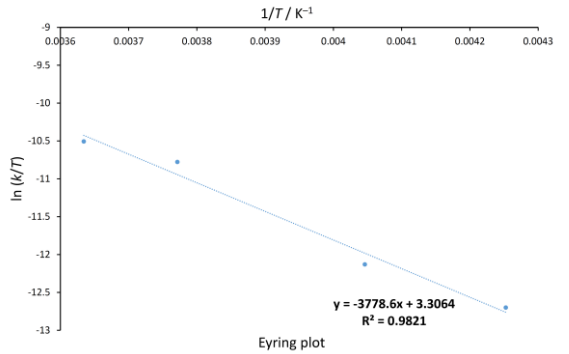

Summary for the activation parameters

Table S4. Summary for the activation parameters

entry	borate	aldehyde	$\Delta H^{\ddagger}$	$\Delta S^{\ddagger}$	$\Delta G^{\ddagger}$(298 K)
	1	**3**	/ kcal·mol^{-1}	/ cal·(K·mol)$^{-1}$	/ kcal·mol^{-1}
1	**1a**B·thf	**3a**	3.15	–54.1	19.3
2		**3b**	3.95	–55.6	20.5
3	**1b**B·thf	**3a**	7.02	–41.2	19.3
4		**3b**	7.51	–40.6	19.6

Unoccupied MOs concerning the Lewis acidity for the cage-shaped borates

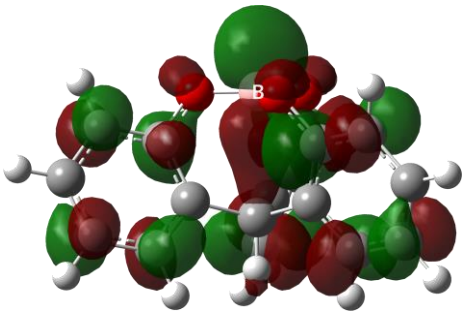

1aB

–0.789 eV (LUMO+1)

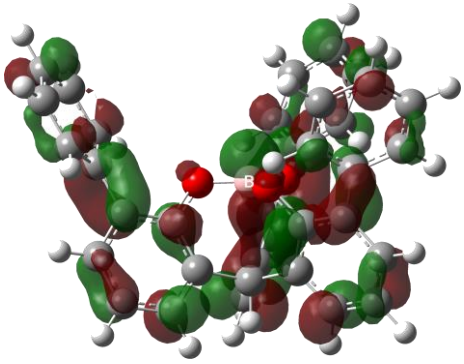

1bB

–1.16 eV (LUMO)

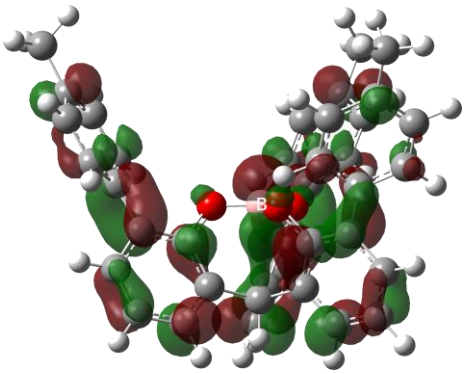

1eB

–1.05 eV (LUMO)

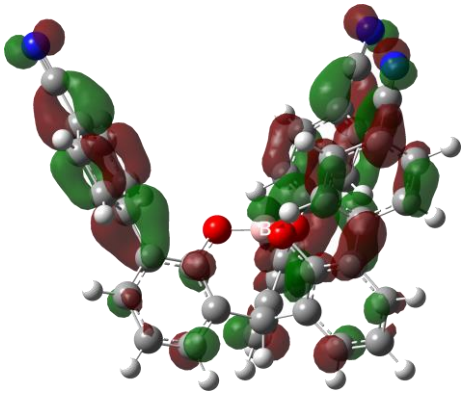

1fB

–2.20 eV (LUMO)

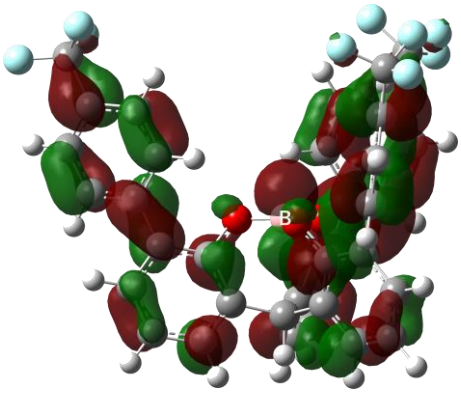

1gB

–1.76 eV (LUMO)

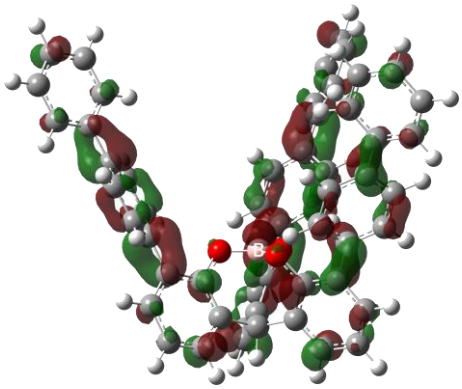

1jB

–1.40 eV (LUMO)

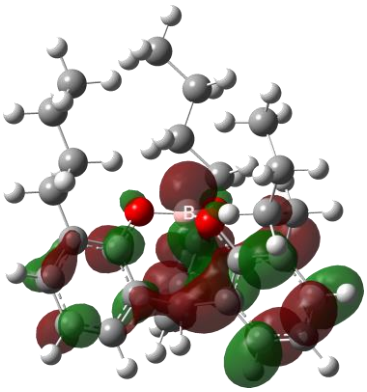

1kB

–0.633 eV (LUMO+1)

Figure S7. The molecular orbital of the unoccupied MO concerning the Lewis acidity calculated at the B3PW91/6-31+G**//B3PW91/6-31G** level (the contour level of 0.03 / $Å^3$)

Non-catalyzed reaction mechanisms for the hetero Diels-Alder reactions

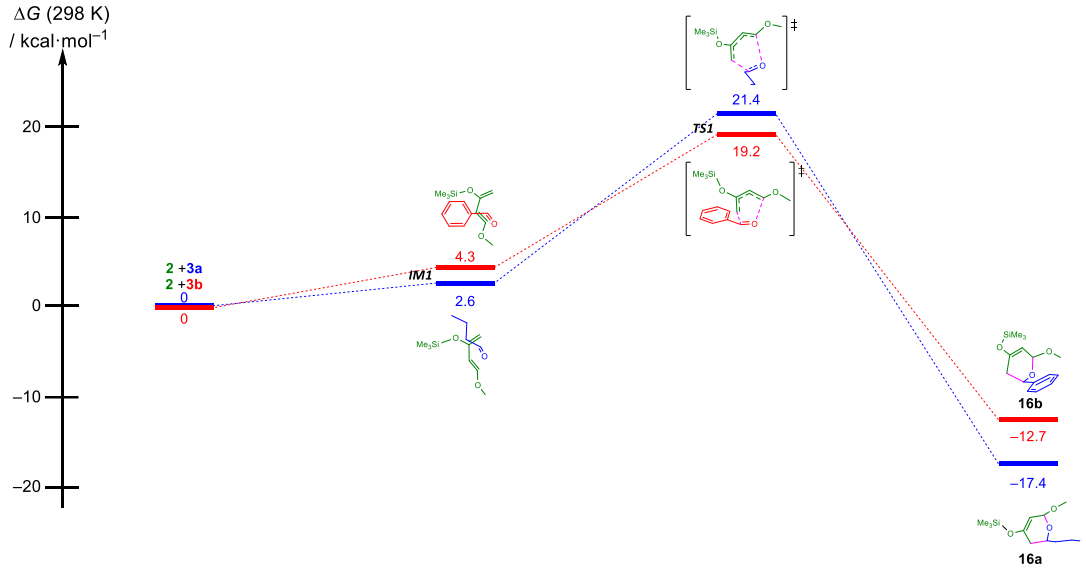

Figure S8. The energy profiles of the non-catalyzed hetero Diels-Alder reaction of **2** with **3a** or **3b**. DFT calculation was performed using ωB97XD/def2svp. Solvation effect was introduced using the IEFPCM model, and dichloromethane was used as a solvent.

Non-Covalent Interaction (NCI)-Plot

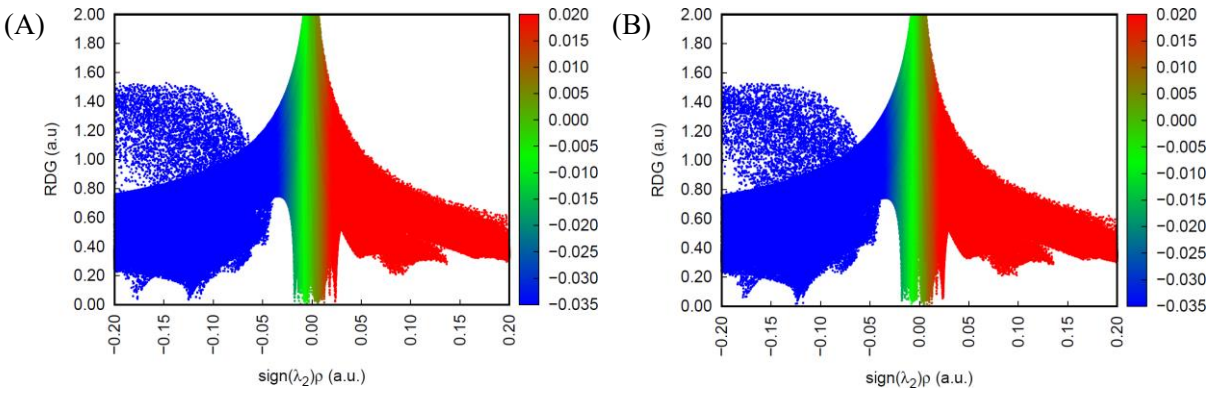

Figure S9. Scatter plots of the non-covalent interaction index within the inclusion complexes of (A) **1b**B·**3a**⊃**2** and (B) **1b**B·**3b**⊃**2** at the preorganized **IM2** states.

(A) (B)

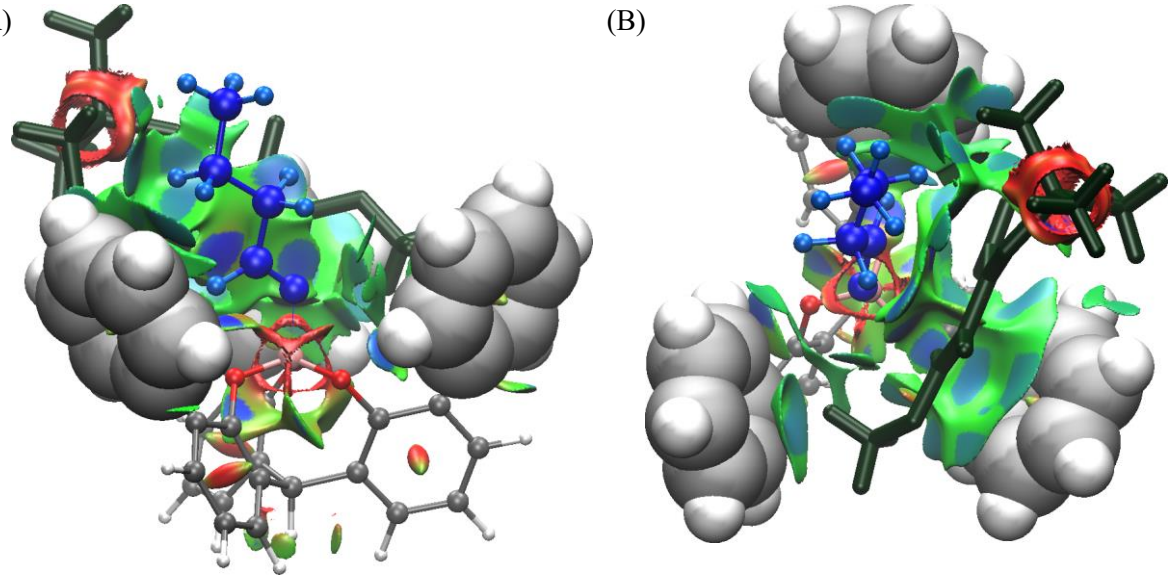

Figure S10. Non-covalent interaction (NCI) plots for **1b**B·**3a**⊃**2** (A) side view and (B) top view. (reduced density gradient (RDG) surfaces = 0.65 a.u. and the color range blue(attractive)-green-red(repulsive) for –0.018 < ρ < +0.030 a.u.)

(A) (B)

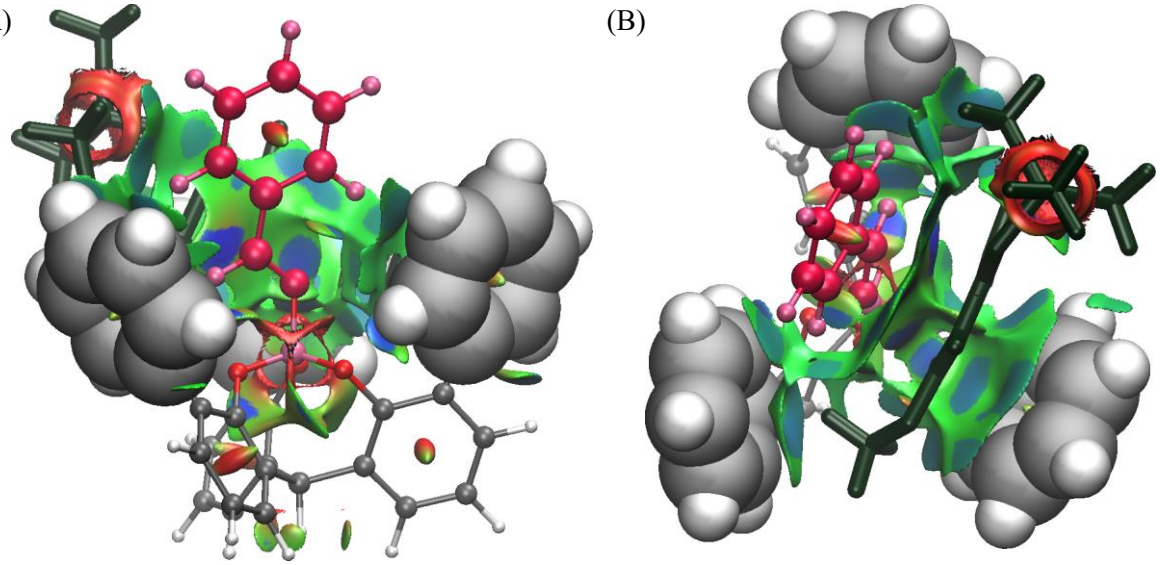

Figure S11. Non-covalent interaction (NCI) plots for **1b**B·**3b**⊃**2** (A) side view and (B) top view. (reduced density gradient (RDG) surfaces = 0.65 a.u. and the color range blue(attractive)-green-red(repulsive) for –0.018 < ρ < +0.030 a.u.)

(A) (B)

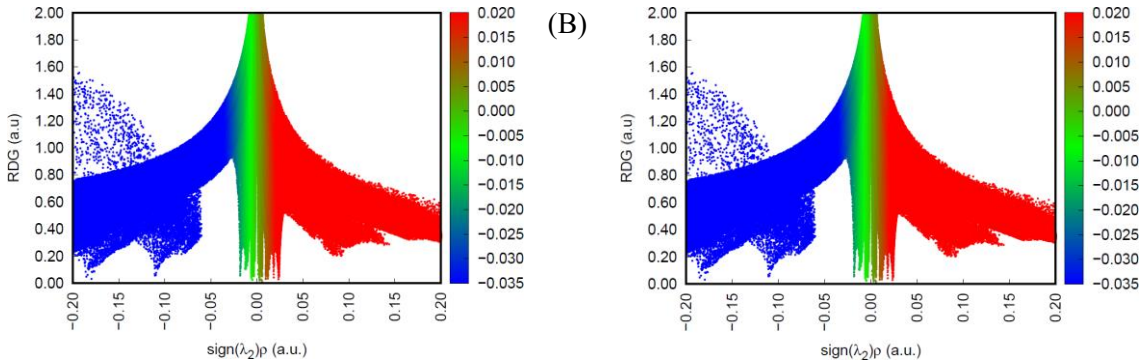

Figure S12. Scatter plots of the non-covalent interaction index within the complexes of (A) **1b**B·**3a** and (B) **1b**B·**3b** at the preorganized **IM1** states.

(A) (B)

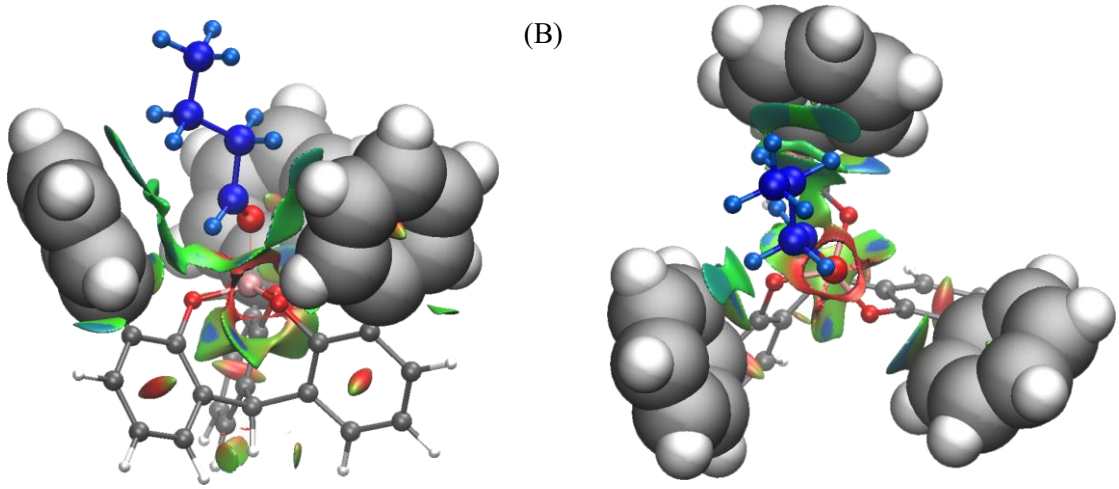

Figure S13. Non-covalent interaction (NCI) plots for **1b**B·**3a** (A) side view and (B) top view. (reduced density gradient (RDG) surfaces = 0.65 a.u. and the color range blue(attractive)-green-red(repulsive) for $-0.018 < \rho < +0.030$ a.u.)

(A) (B)

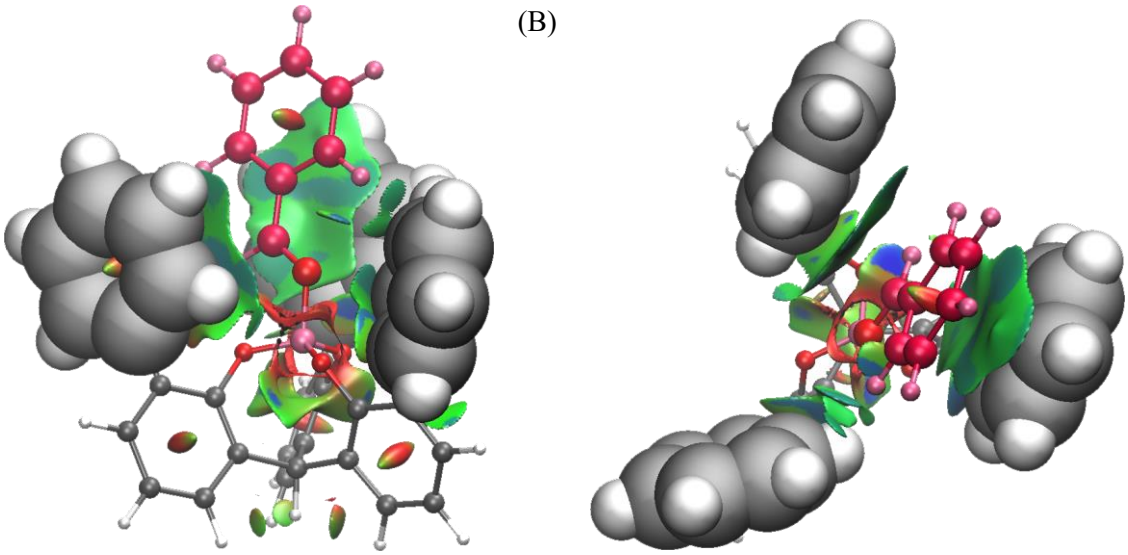

Figure S14. Non-covalent interaction (NCI) plots for **1b**B·**3b** (A) side view and (B) top view. (reduced density gradient (RDG) surfaces = 0.65 a.u. and the color range blue(attractive)-green-red(repulsive) for $-0.018 < \rho < +0.030$ a.u.)

1-5. References

[1] P. M. Pihko, Ed. , *Hydrogen Bonding in Organic Synthesis*, Wiley-VCH, **2009**.
[2] M. Nishio, Y. Umezawa, K. Honda, S. Tsuboyama, H. Suezawa, *CrystEngComm* **2009**, *11*, 1757–1788.
[3] M. Nishio, *Phys. Chem. Chem. Phys.* **2011**, *13*, 13873.
[4] L. C. Gilday, S. W. Robinson, T. A. Barendt, M. J. Langton, B. R. Mullaney, P. D. Beer, *Chem. Rev.* **2015**, *115*, 7118–7195.
[5] G. Cavallo, P. Metrangolo, R. Milani, T. Pilati, A. Priimagi, G. Resnati, G. Terraneo, *Chem. Rev.* **2016**, *116*, 2478–2601.
[6] H. Wang, W. Wang, W. J. Jin, *Chem. Rev.* **2016**, *116*, 5072–5104.
[7] C. Janiak, *J. Chem. Soc. Dalton Trans*. **2000**, 3885–3896.
[8] C. G. Claessens, J. F. Stoddart, *J. Phys. Org. Chem.* **1997**, *10*, 254–272.
[9] C. A. Hunter, *Chem. Soc. Rev.* **1994**, *23*, 101.
[10] C. R. Martinez, B. L. Iverson, *Chem. Sci.* **2012**, *3*, 2191.
[11] L. M. Salonen, M. Ellermann, F. Diederich, *Angew. Chem. Int. Ed.* **2011**, *50*, 4808–4842.
[12] S. Yamada, *Chem. Rev.* **2018**, *118*, 11353–11432.
[13] Y. Zhao, Y. Domoto, E. Orentas, C. Beuchat, D. Emery, J. Mareda, N. Sakai, S. Matile, *Angew. Chem. Int. Ed.* **2013**, *52*, 9940–9943.
[14] C. J. Pace, J. Gao, *Acc. Chem. Res.* **2013**, *46*, 907–915.
[15] J. M. Maier, P. Li, J. Hwang, M. D. Smith, K. D. Shimizu, *J. Am. Chem. Soc.* **2015**, *137*, 8014–8017.
[16] P. Li, E. C. Vik, J. M. Maier, I. Karki, S. M. S. Strickland, J. M. Umana, M. D. Smith, P. J. Pellechia, K. D. Shimizu, *J. Am. Chem. Soc.* **2019**, *141*, 12513–12517.
[17] T. Endo, A. Kuwahara, H. Tasai, T. Murata, M. Hashimoto, T. Ishigami, *Nature* **1977**, *268*, 74–76.
[18] S. Mataka, J. Ma, T. Thiemann, T. Mimura, T. Sawada, M. Tashiro, *Tetrahedron* **1997**, *53*, 6817–6824.
[19] G. Wulff, *Chem. Rev.* **2002**, *102*, 1–28.
[20] J. Meeuwissen, J. N. H. Reek, *Nat. Chem.* **2010**, *2*, 615–621.
[21] M. Raynal, P. Ballester, A. Vidal-Ferran, P. W. N. M. van Leeuwen, *Chem. Soc. Rev.* **2014**, *43*, 1660–1733.
[22] M. Raynal, P. Ballester, A. Vidal-Ferran, P. W. N. M. van Leeuwen, *Chem. Soc. Rev.* **2014**, *43*,

1734–1787.
[23] A. Berkessel, H. Groeger, *Asymmetric Organocatalysis: From Biomimetic Concepts to Applications in Asymmetric Synthesis*, Wiley-VCH, **2005**.
[24] B. List, Ed. , *Science of Synthesis: Asymmetric Organocatalysis 1*, Thieme, **2012**.
[25] K. Maruoka, Ed. , *Science of Synthesis: Asymmetric Organocatalysis 2*, Thieme, **2012**.
[26] H. Yamamoto, Ed. , *Lewis Acids in Organic Synthesis*, Wiley-VCH, Weinheim, **2000**.
[27] N. Asao, T. Asano, Y. Yamamoto, *Angew. Chem. Int. Ed.* **2001**, *40*, 3206–3208.
[28] M. Kruppa, B. König, *Chem. Rev.* **2006**, *106*, 3520–3560.
[29] S. Kobayashi, S. Nagayama, *J. Org. Chem.* **1997**, *62*, 232–233.
[30] S. Kobayashi, S. Nagayama, *J. Am. Chem. Soc.* **1997**, *119*, 10049–10053.
[31] S. Kobayashi, T. Busujima, S. Nagayama, *Chem. - A Eur. J.* **2000**, *6*, 3491–3494.
[32] E. Angelini, C. Balsamini, F. Bartoccini, S. Lucarini, G. Piersanti, *J. Org. Chem.* **2008**, *73*, 5654–5657.
[33] K. Maruoka, Y. Araki, H. Yamamoto, *J. Am. Chem. Soc.* **1988**, *110*, 2650–2652.
[34] K. Maruoka, S. Saito, A. B. Concepcion, H. Yamamoto, *J. Am. Chem. Soc.* **1993**, *115*, 1183–1184.
[35] H. Yamamoto, S. Saito, *Pure Appl. Chem.* **1999**, *71*, 239–245.
[36] S. Shirakawa, K. Maruoka, *Tetrahedron Lett.* **2002**, *43*, 1469–1472.
[37] J. Chen, J. Otera, *Synlett* **2004**, *1*, 29–30.
[38] K. Mikami, M. Terada, T. Nakai, *J. Org. Chem.* **1991**, *56*, 5456–5459.
[39] J. Chen, J. Otera, *Tetrahedron* **1997**, *53*, 14275–14286.
[40] D. Nakashima, H. Yamamoto, *Org. Lett.* **2005**, *7*, 1251–1253.
[41] T. Kawajiri, R. Ohta, H. Fujioka, H. Sajiki, Y. Sawama, *Chem. Commun.* **2018**, *54*, 374–377.
[42] T. Uchikura, K. Ono, K. Takahashi, N. Iwasawa, *Angew. Chem. Int. Ed.* **2018**, *57*, 2130–2133.
[43] J. Tian, N. Yamagiwa, S. Matsunaga, M. Shibasaki, *Angew. Chem. Int. Ed.* **2002**, *41*, 3636–3638.
[44] F. Li, Z. J. Zheng, J. Y. Shang, K. Z. Jiang, G. Q. Lai, J. X. Jiang, L. W. Xu, *Chem. - An Asian J.* **2012**, *7*, 2008–2013.
[45] J. P. Wagner, P. R. Schreiner, *Angew. Chem. Int. Ed.* **2015**, *54*, 12274–12296.
[46] Y. Murakami, J. Kikuchi, Y. Hisaeda, O. Hayashida, *Chem. Rev.* **1996**, *96*, 721–758.
[47] G. Yu, K. Jie, F. Huang, *Chem. Rev.* **2015**, *115*, 7240–7303.
[48] T. Kawase, H. Kurata, *Chem. Rev.* **2006**, *106*, 5250–5273.
[49] A. Mori, K. Hirayama, N. Kato, H. Takeshita, S. Ujiie, *Chem. Lett.* **1997**, *26*, 509–510.
[50] K. Miyamura, A. Mihara, T. Fujii, Y. Gohshi, Y. Ishii, *J. Am. Chem. Soc.* **1995**, *117*, 2377–2378.
[51] A. A. Fokin, D. Gerbig, P. R. Schreiner, *J. Am. Chem. Soc.* **2011**, *133*, 20036–20039.
[52] M. Yasuda, S. Yoshioka, S. Yamasaki, T. Somyo, K. Chiba, A. Baba, *Org. Lett.* **2006**, *8*, 761–764.
[53] M. Yasuda, S. Yoshioka, H. Nakajima, K. Chiba, A. Baba, *Org. Lett.* **2008**, *10*, 929–932.
[54] H. Nakajima, M. Yasuda, R. Takeda, A. Baba, *Angew. Chem. Int. Ed.* **2012**, *51*, 3867–3870.
[55] M. Yasuda, H. Nakajima, R. Takeda, S. Yoshioka, S. Yamasaki, K. Chiba, A. Baba, *Chem. - A Eur. J.* **2011**, *17*, 3856–3867.
[56] A. Konishi, K. Nakaoka, H. Nakajima, K. Chiba, A. Baba, M. Yasuda, *Chem. - A Eur. J.* **2017**, *23*, 5219–5223.
[57] A. Konishi, R. Yasunaga, K. Chiba, M. Yasuda, *Chem. Commun.* **2016**, *52*, 3348–3351.
[58] A. Konishi, K. Nakaoka, H. Maruyama, H. Nakajima, T. Eguchi, A. Baba, M. Yasuda, *Chem. - A Eur. J.* **2017**, *23*, 1273–1277.
[59] D. Tanaka, Y. Kadonaga, Y. Manabe, K. Fukase, S. Sasaya, H. Maruyama, S. Nishimura, M. Yanagihara, A. Konishi, M. Yasuda, *J. Am. Chem. Soc.* **2019**, *141*, 17466–17471.
[60] U. Verkerk, M. Fujita, T. L. Dzwiniel, R. McDonald, J. M. Stryker, *J. Am. Chem. Soc.* **2002**, *124*, 9988–9989.
[61] M. Yasuda, Y. Onishi, M. Ueba, T. Miyai, A. Baba, *J. Org. Chem.* **2001**, *66*, 7741–7744.
[62] H. Li, Y. Zhong, C. Chen, A. E. Ferraro, D. Wang, *Org. Lett.* **2015**, *17*, 3616–3619.
[63] L. Planas, M. Mogi, H. Takita, T. Kajimoto, M. Node, *J. Org. Chem.* **2006**, *71*, 2896–2898.
[64] S. Toyota, M. Oki, *Bull. Chem. Soc. Jpn.* **1992**, *65*, 1832–1840.
[65] J. A. Hirsch, in *Top. Stereochem.*, John Wiley & Sons, Ltd, **2007**, pp. 199–222.
[66] Q.-L. Ni, X.-F. Jiang, L.-C. Gui, X.-J. Wang, K.-G. Yang, X.-S. Bi, *New J. Chem.* **2011**, *35*, 2471.
[67] E. R. Johnson, S. Keinan, P. Mori-Sánchez, J. Contreras-García, A. J. Cohen, W. Yang, *J. Am. Chem. Soc.* **2010**, *132*, 6498–6506.

[68] J. Contreras-García, E. R. Johnson, S. Keinan, R. Chaudret, J.-P. Piquemal, D. N. Beratan, W. Yang, *J. Chem. Theory Comput.* **2011**, *7*, 625–632.
[69] S. Grimme, S. Ehrlich, L. Goerigk, *J. Comput. Chem.* **2011**, *32*, 1456–1465.
[70] I. K. Mati, S. L. Cockroft, *Chem. Soc. Rev.* **2010**, *39*, 4195.
[71] C. Zhao, P. Li, M. D. Smith, P. J. Pellechia, K. D. Shimizu, *Org. Lett.* **2014**, *16*, 3520–3523.
[72] J. Hwang, P. Li, M. D. Smith, K. D. Shimizu, *Angew. Chem. Int. Ed.* **2016**, *55*, 8086–8089.
[73] S. Ehrlich, H. F. Bettinger, S. Grimme, *Angew. Chem. Int. Ed.* **2013**, *52*, 10892–10895.
[74] S. Rösel, H. Quanz, C. Logemann, J. Becker, E. Mossou, L. Cañadillas-Delgado, E. Caldeweyher, S. Grimme, P. R. Schreiner, *J. Am. Chem. Soc.* **2017**, *139*, 7428–7431.
[75] J. Becker, W. D. Allen, P. R. Schreiner, *J. Am. Chem. Soc*. **2018**, *140*, 14421–14432.
[76] *CrystalStructure*, Rigaku Corporation, Tokyo, Japan, **2015**.
[77] O. V Dolomanov, L. J. Bourhis, R. J. Gildea, J. A. K. Howard, H. Puschmann, *J. Appl. Crystallogr.* **2009**, *42*, 339–341.
[78] Y. Huang, V. H. Rawal, *Org. Lett.* **2000**, *2*, 3321–3323.
[79] B. Wang, X. Feng, Y. Huang, H. Liu, X. Cui, Y. Jiang, *J. Org. Chem.* **2002**, *67*, 2175–2182.
[80] Y. Zhao, S. Qi, Z. Niu, Y. Peng, C. Shan, G. Verma, L. Wojtas, Z. Zhang, B. Zhang, Y. Feng, Y.-S. Chen, S. Ma, *J. Am. Chem. Soc.* **2019**, *141*, 14443–14450.
[81] N. Li, R. Qiu, X. Zhang, Y. Chen, S.-F. Yin, X. Xu, *Tetrahedron* **2015**, *71*, 4275–4281.
[82] M. J. Frisch, G. W. Trucks, H. B. Schlegel, G. E. Scuseria, M. A. Robb, J. R. Cheeseman, G. Scalmani, V. Barone, B. Mennucci, G. A. Petersson, H. Nakatsuji, M. Caricato, X. Li, H. P. Hratchian, A. F. Izmaylov, J. Bloino, G. Zheng, J. L. Sonnenberg, M. Hada, M. Ehara, K. Toyota, R. Fukuda, J. Hasegawa, M. Ishida, T. Nakajima, Y. Honda, O. Kitao, H. Nakai, T. Vreven, J. Montgomery, J. A., J. E. Peralta, F. Ogliaro, M. Bearpark, J. J. Heyd, E. Brothers, K. N. Kudin, V. N. Staroverov, R. Kobayashi, J. Normand, K. Raghavachari, A. Rendell, J. C. Burant, S. S. Iyengar, J. Tomasi, M. Cossi, N. Rega, J. M. Millam, M. Klene, J. E. Knox, J. B. Cross, V. Bakken, C. Adamo, J. Jaramillo, R. Gomperts, R. E. Stratmann, O. Yazyev, A. J. Austin, R. Cammi, C. Pomelli, J. W. Ochterski, R. L. Martin, K. Morokuma, V. G. Zakrzewski, G. A. Voth, P. Salvador, J. J. Dannenberg, S. Dapprich, A. D. Daniels, Ö. Farkas, J. B. Foresman, J. V. Ortiz, J. Cioslowski, D. J. Fox, *Gaussian 09*, Gaussian, Inc., Wallingford CT, **2009**.
[83] M. J. Frisch, G. W. Trucks, H. B. Schlegel, G. E. Scuseria, M. A. Robb, J. R. Cheeseman, G. Scalmani, V. Barone, G. A. Petersson, H. Nakatsuji, X. Li, M. Caricato, A. V. Marenich, J. Bloino, B. G. Janesko, R. Gomperts, B. Mennucci, H. P. Hratchian, J. V. Ortiz, A. F. Izmaylov, J. L. Sonnenberg, D. Williams-Young, F. Ding, F. Lipparini, F. Egidi, J. Goings, B. Peng, A. Petrone, T. Henderson, D. Ranasinghe, V. G. Zakrzewski, J. Gao, N. Rega, G. Zheng, W. Liang, M. Hada, M. Ehara, K. Toyota, R. Fukuda, J. Hasegawa, M. Ishida, T. Nakajima, Y. Honda, O. Kitao, H. Nakai, T. Vreven, K. Throssell, J. J. A. Montgomery, J. E. Peralta, F. Ogliaro, M. J. Bearpark, J. J. Heyd, E. N. Brothers, K. N. Kudin, V. N. Staroverov, T. A. Keith, R. Kobayashi, J. Normand, K. Raghavachari, A. P. Rendell, J. C. Burant, S. S. Iyengar, J. Tomasi, M. Cossi, J. M. Millam, M. Klene, C. Adamo, R. Cammi, J. W. Ochterski, R. L. Martin, K. Morokuma, O. Farkas, J. B. Foresman, D. J. Fox, *Gaussian 16*, Gaussian, Inc., Wallingford CT, **2016**.
[84] W. Humphrey, A. Dalke, K. Schulten, *J. Mol. Graph.* **1996**, *14*, 33–38.

Chapter 2
Synthesis of Cage-shaped Aluminum Aryloxides: Efficient Lewis Acid Catalyst for Stereoselective Glycosylation Driven by Flexible Shift of Four- to Five-Coordination

2-1. Introduction

Steric control of the coordination geometry of main group metal complexes is one of the important methods to expand their typical coordination numbers and/or to enhance their original reactivity.[1],[2],[3],[4],[5],[6],[7] Lewis acidic organoaluminum compounds designed by this concept have been engaged as operative intermediates in many reactions.[8],[9],[10],[11] Glycosylation is also an important playground for Lewis acid catalysts. The activation of a glycosyl donor leads to a series of reaction intermediates, such as α or β-configured covalent glycosyl intermediates and oxocarbenium species (contact or solvent-separated ion pairs).[12] Glycosylation with the covalent intermediates proceeds via an S_N2-like pathway, while glycosylation with the oxocarbenium species proceeds via an S_N1-like pathway. Since these reaction intermediates are on a dynamic continuum, the reaction of glycosyl acceptor with these intermediates often includes both S_N1 and S_N2 features. Although the structure of the intermediates and reaction mechanism can be somehow controlled by the reactivity of donors, acceptors,[13],[14] activators, solvents,[15] and reaction conditions, controlling of reaction pathway, especially S_N2 reaction under mild reaction conditions at room temperature, is of quite difficult. Actually, several S_N2 glycosylations, including leaving group investigation (Figure 1A-i),[16],[17],[18],[19],[20],[21] or the dual activation of donor and acceptor (Figure 1A-ii)[22],[23],[24] have been reported, however, the precise control of the reaction temperature is an indispensable factor. The electronic and steric modulations of Lewis acid catalysts would be more direct and effective alternatives. The moderate Lewis acidity with low affinity with the leaving group should sustain the stereochemistry of the donors. In addition, some bulkiness of the catalysts should effectively block the leaving group side and direct the backside attack of the nucleophiles. The Lewis acid with the two features allows the moderate activation of glycosyl donor to realize S_N2 glycosylation at ambient temperature (Figure 1D-i).

Aluminum aryloxide serves the objectives of the design of Lewis acid catalyts.[25] The bulky aryloxide ligands, 2,6-di-*tert*-butylphenol and its analogues,[26],[27] have been used to the isolate monomeric aluminum complexes allowing prominent chemoselective reactions.[28],[29] Another possible ligand design should be the use of polydentate ligands. Alumatranes derived from tripodal tetradentate ligands are representative examples.[30],[31],[32],[33] A transannular bond between the metal ion and an axial ligand atom facilitates the formation of high-coordinated aluminum center as active species.[34],[35] For the more precise tuning of the reactivity of the aluminum complex, however, some structural freedom around aluminum center is required. In this regard, triphenolic tripodal ligands without an axial coordination

site is an intriguing type of the ligand.[36],[37] We recently established the effectiveness of a cage-shaped triphenolic ligand in controlling the Lewis acidity of a boron atom (Figure 1B).[38] The Lewis acidity of the cage-shaped borate **1**B can be tailored by changing the tethered atom and its substituent (X–Y),[39],[40] the substituents (R)[41],[42] and/or the π-conjugated system (π).[43] On the basis of the same frameworks, the photo-activated[43] and asymmetric[44] Lewis acid catalysts were also developed. Despite its high potential, the synthesis of monomeric aluminum complexes based on triphenolic tripodal scaffolds remains a challenging issue.

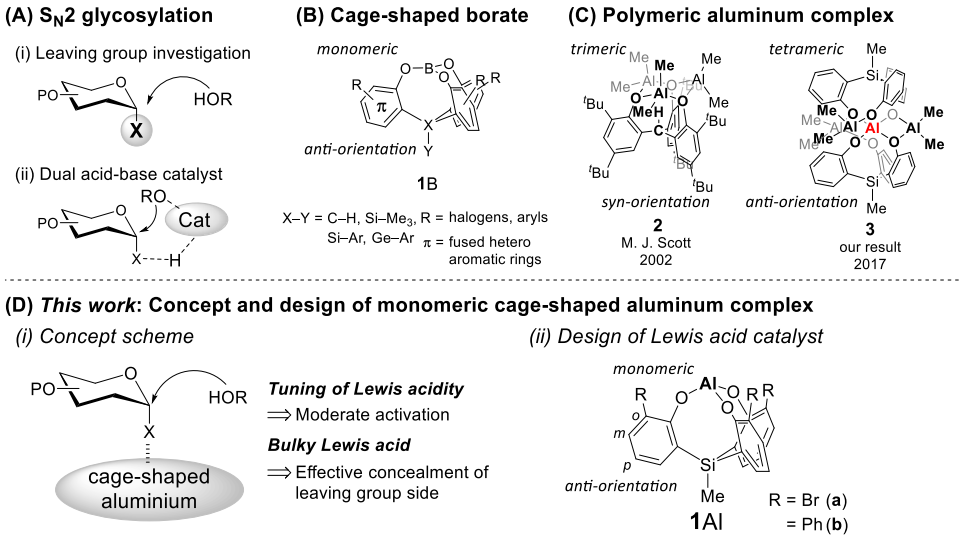

Figure 1. (A) Schemes of S_N2 glycosylation. Molecular structures of (B) cage-shaped borates and (C) polymeric aluminum complexes with triphenolic tripodal ligands. (D) Concept of stereoselective glycosylation and monomeric cage-shaped aluminum complexes.

The previous Scott's,[45] and our[46] works demonstrated that the trimeric **2**[47],[48] or tetrameric **3** aluminum complexes were dominantly formed (Figure 1C). Herein, we report the synthesis and characterization of monomeric aluminum complexes with cage-shaped triphenolic ligands (Figure 1D-ii). The obtained cage-shaped aluminum aryloxide **1**Al exhibited the high catalytic activity and *β*-selectivity in *O*-glycosylation, where the five-coordinated aluminum species plays a pivotal role for the glcosyl donor activation.

The reported polynuclear complexes **2**/**3** would arise from the higher Lewis acidity and the larger size of aluminum atom than those of boron atom. Thus, we modified our triphenolic ligands in the following two respects. One is the introduction of substituents into the *ortho*-positions of the phenolic site, allowing the steric protection around an aluminum center. The other is the control of the direction of the tethered group (X–Y) against the aluminum center by changing the tethered carbon atom to the silicon one, enabling an *anti*-orientation rather than a *syn*-orientation. The synthetic route for **1**Al is shown in

Scheme 1. Preparation of methoxymethyl (MOM)-protected ether **4**[49] from 2,6-dibromophenol and subsequent monolithiation followed by the treatment with trichloromethylsilane afforded the triarylmethylsilane **1a**$(MOM)_3$. A palladium-catalyzed Suzuki-Miyaura reaction[50] gave the triphenyl derivative **1b**$(MOM)_3$. With the triarylmethylsilanes **1**$(MOM)_3$ in hand, the deprotection of **1**$(MOM)_3$ was performed. Although other Brønsted acids (HCl aq. $HClO_4$ aq. and HPF_6 aq.) were unsuitable, the treatment of HBF_4 aq. effectively afforded **1**H_3 without cleavage of Si–aryl bonds. For the monomeric complexation of aluminum source with **1**H_3, some extra attentions were required. The direct treatment of **1**H_3 with $AlMe_3$ in CH_2Cl_2 was tried, but this approach gave a trimeric complex[46] by the indication of the NMR measurements. Alternatively, the gradual addition of a solution of **1**H_3 in CH_2Cl_2 into the pretreated solution of $AlMe_3$ with the stoichiometric pyridine in CH_2Cl_2 furnished the desired monomeric aluminum aryloxide **1**Al as a pyridine complex (**1**Al·py). The pretreatment of aluminum source with pyridine presumably inhibits the aggregation of aluminum(III) ion, which would be favorable for the formation of the monomeric aluminum complex. As references, the borates **1**B·py with the same ligands as **1**Al·py were prepared according to our previous literature.[41]

2-2. Results and Discussion

The monomeric structures for **1**Al·py were confirmed by X-ray crystallographic analyses (Figures 2 and S1–4). The ORTEP drawings for **1a**Al·py and **1a**B·py are shown in Figure 2. The selected geometric parameters are summarized in Table S1. The Si–Me bond at the tether position of **1**Al·py has an *anti*-orientation against the coordinated aluminum atoms, which reveals distinct differences with the trimeric aluminum complex **2** of a *syn*-orientation, as reported by Scott and coworkers.[45] The triphenyl derivative of **1b**Al·py has a similar structure to that of **1a**Al·py (Table S1). The significant difference in the geometry between **1**Al·py and **1**B·py was found in the tetrahedral character (THC).[51] The THCs of **1**Al·py (**1a**Al·py: 72.7%; **1b**Al·py: 70.5%) are much larger than that of **1**B·py (**1a**B·py: 59.0%; **1b**B·py: 49.5%), implying that the aluminum complex **1**Al·py has a higher Lewis acidity than the borate **1**B·py at the four-coordinated state.

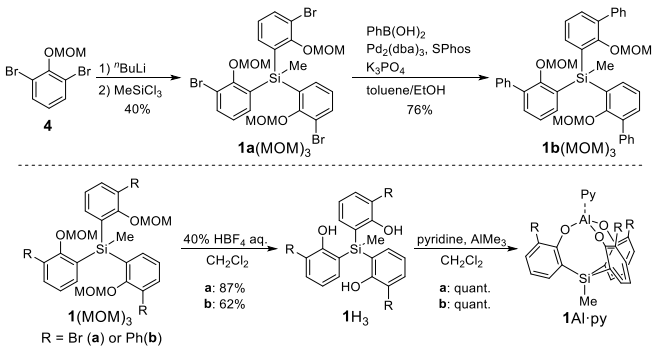

Scheme 1. Synthetic route for cage-shaped aluminum trioxides **1**Al·py.

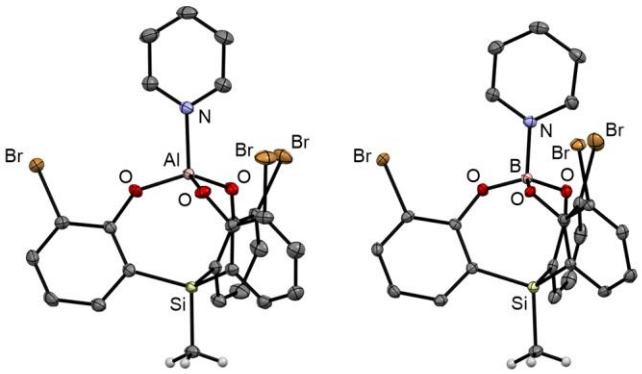

Figure 2. Molecular structures of cage-shaped complexes **1a**Al·py and **1a**B·py with 50% probability ellipsoids, respectively. Some hydrogen atoms are omitted for clarity.

The glycosylations using cage-shaped aluminum **1a**Al·py and **1b**Al·py were investigated (Table 1). Gratefully, the glycosylation of α-**5** and **6** catalyzed by **1a**Al·py in CH_2Cl_2 gave the corresponding disaccharide **7** in 81% yield with a high β-selectivity (α/β = 1/6.4) (Table 1, entry 1).[52] In sharply contrast, the cage-shaped borates, **1a**B·THF, gave an α-selectivity in a moderate yield (entry 2). The phenyl derivative **1b**Al·py did not work as a catalyst (entry 3). The high β-selectivity at an ambient temperature (entry 1) is quite unusual because the anomeric effect imposes the α-selectivity on the glycosylation.[53],[54] When β-excess imidate **5** was applied to the reaction, α-**7** was mainly obtained (entry 4), suggesting that the glycosylation catalyzed by **1a**Al·py proceeds via an S_N2-like pathway. Only a few *O*-glycosylation using aluminum as a catalyst was reported.[55],[56] When $AlCl_3$ as an inorganic aluminum salt was employed, no catalytic reaction occurred with a poor β-selectivity (entry 5). Furthermore, tris(2-bromophenoxy)aluminum pyridine complex, an open-shaped aluminum complex, gave an insufficient yield of **7** (entry 6). These results indicate that the cage-shaped scaffold of **1a**Al enhances the catalytic activity of aluminum and the β-selectivity of **7**. The solvent effect significantly enhanced the yield and β-selectivity. Although CH_3CN slightly decreased the yield (entry 7), THF and Et_2O accelerated the reaction (entries 8 and 9). Diethyl ether gave the highest β-selectivity (α/β = 1/19, entry 9). The reaction loaded with 0.1 eq of **1a**Al·py in Et_2O was accomplished without any decrease in the yield and β-selectivity (entry 10). It should be noted that no general solvent effect of ether, which the α-selectivity was enriched in the S_N1-type glycosylation,[57] was observed, supporting that the catalytic glycosylation by **1a**Al·py proceeds via an S_N2-type pathway. Typical other reactions catalyzed by Lewis acid catalysts were well performed by **1**Al·py (Tables S12–S14).

Table 1. Glycosylation of **5** with **6**.

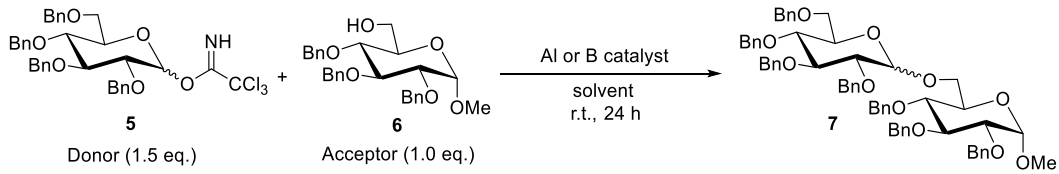

entry	Al catalyst (eq.)	donor	solvent	yield (%)[a]	ratio (α/β)
1	**1a**Al·py (0.3)	α-**5**	CH_2Cl_2	81	1/6.4
2	**1a**B·THF (0.3)	α-**5**	CH_2Cl_2	68	4.7/1
3	**1b**Al·py (0.3)	α-**5**	CH_2Cl_2	6	1/2.0
4	**1a**Al·py (0.3)	α-**5**/β-**5** (1/7.7)	CH_2Cl_2	44	2.1/1
5	$AlCl_3$ (0.3)	α-**5**	CH_2Cl_2	27	1/1.5
6	$(2\text{-}BrC_6H_4O)_3Al$ ·py (0.3)	α-**5**	CH_2Cl_2	Trace	-
7	**1a**Al·py (0.3)	α-**5**	CH_3CN	63	1/15
8	**1a**Al·py (0.3)	α-**5**	THF	95	1/8.5
9	**1a**Al·py (0.3)	α-**5**	Et_2O	95	1/19
10	**1a**Al·py (0.1)	α-**5**	Et_2O	96 (93[b])	1/19

[a]Estimated by ^{1}H-NMR spectra. [b]Isolated yield.

We next evaluated the Lewis acidity of the cage-shaped aluminum complex **1**Al·py for the clarification of the unique glycosylation. The Lewis acidity of **1**Al·py was estimated via infrared stretching frequency of 2,6-dimethyl-γ-pyrone **8** ligated to **1**Al·py,[43] as shown in Table 2. The stretching frequency of the carbonyl (C=O) in **8** clearly shows the degree of Lewis acidity. The cage-shaped aluminum complexes **1**Al are situated between $AlCl_3$ and open-shaped $(C_6H_5O)_3Al$. The larger Δν(C=O) values of **1**Al than that of **1**B indicate the enhanced Lewis acidity of **1**Al. Interestingly, the Lewis acidity of tris(2-bromophenoxy)aluminum pyridine complex, which is an unacceptable catalyst for the glycosylation, is comparable to those of **1**Al, supporting the importance of the cage-shaped structure of **1**Al in the catalytic cycle.

Table 2. Estimation of Lewis acidity.

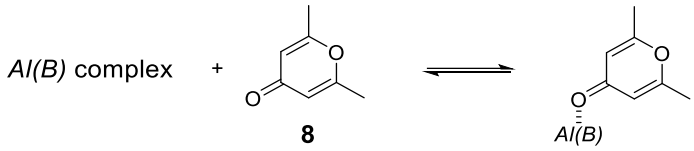

entry	Al(B) compound	$\Delta\nu$(C=O) (cm^{-1})
1	$AlCl_3$	18.7
2	$(2\text{-}BrC_6H_4O)_3Al\cdot py$	17.3
3	**1a**Al·py	16.9
4	**1b**Al·py	17.1
5	**1a**B·THF	14.5
6	**1b**B·THF	12.5
7	$(C_6H_5O)_3Al$	3.28

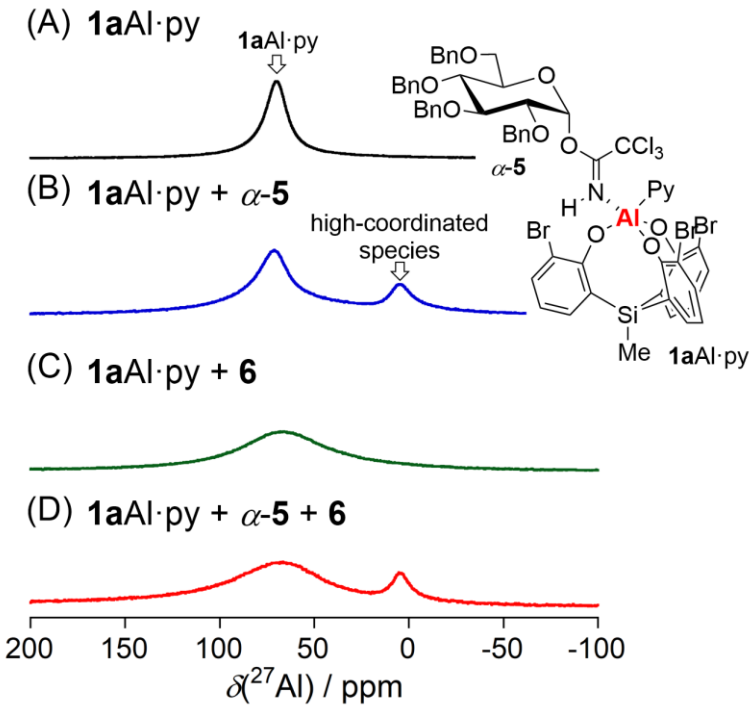

Figure 3. ^{27}Al NMR spectra (103 MHz, –60 °C, CD_2Cl_2) for (A) **1a**Al·py, (B) **1a**Al·py with donor *α*-**5**, (C) **1a**Al·py with acceptor **6**, and (D) **1a**Al·py with *α*-**5** and **6**. The inset structure represents the proposed 5-coordinated aluminum complex of **1a**Al·py with *α*-**5**.

The ^{27}Al NMR measurements demonstrated the selective and associative activation of *α*-**5** with **1a**Al·py. In the mixture of *α*-**5** with **1a**Al·py in CD_2Cl_2, an upfiled-shifted ^{27}Al signal was observed at lower temperature than –30 °C, strongly illustrating the generation of a high-coordinated aluminum

species by the coordination of α-**5** to **1a**Al·py (Figures 3A, 3B, and S6–10).[58] On the other hand, no coordination of acceptor **6** to **1a**Al·py was observed despite the high oxophilicity of aluminum (Figure 3C). The selective interaction of α-**5** with **1a**Al·py was demonstrated in the mixture consisting of both α-**5** and **6** (Figure 3D). The moderate Lewis acidity of **1a**Al·py facilitates assuming the high-coordinated state, realizing the improved catalytic activity via an S_N2 process. The appearance of an upfield-shifted ^{27}Al signal at low temperature is directly correlated to the catalytic activity of cage-shaped aluminum complexes. No upfiled-shifted signal of **1b**Al·py with α-**5** was observed, indicating that bulky phenyl groups of **1b**Al·py restricted the coordination of α-**5** to aluminum (Figure S8C).

The high-coordinated aluminum species was successfully isolates in the solid state. In the complexation step for the synthesis of **1a**Al, the employment of 2,2'-bipyridine as a bidentate ligand, instead of pyridine, quantitatively afforded a bipyridine complex **1a**Al·bpy. The molecular structure of **1a**Al·bpy was confirmed by X-ray crystallographic analysis (Figure 4). The ^{27}Al signal of **1a**Al·bpy appeared in the upper field than that of **1a**Al·py. In sharply contrast to the cage-shaped borates **1**B, our four-coordinated **1**Al·py would bear a sufficient Lewis acidity for the activation of substrates via an associative process involving the high-coordinated state.

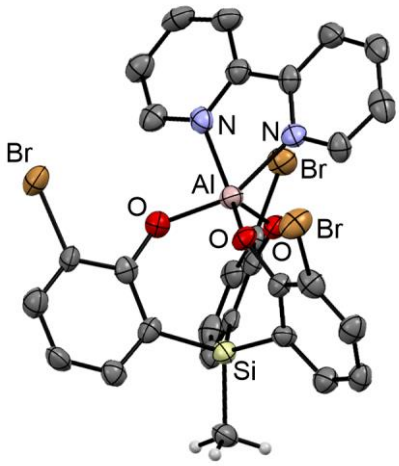

1aAl·bpy

Figure 4. Molecular structures of **1a**Al·bpy. Ortep drawing with 50% probability ellipsoids, some hydrogen atoms are omitted for clarity.

2-3. Conclusion

We have synthesized the monomeric cage-shaped aluminum complexes **1**Al. The flexible coordination change of an aluminum center in our complex, which was evidenced by the X-ray crystallographic analysis and spectroscopic studies, provided the enhanced Lewis acidity and catalytic activity. Additionally, the bulkiness of triphenolic ligand framework allowed the peculiar stereoselective reaction

in a *O*-glycosylation. Further studies on modification of the cage-shaped aluminum complex for other types of catalytic reactions are in progress.

2-4. Experimental Section

General

NMR spectra were recorded on JEOL-AL400 and JEOL-ECS400 spectrometers (400 MHz for ^{1}H, and 100 MHz for ^{13}C) and JEOL-ECA500 spectrometer (500 MHz for ^{1}H, and 125 MHz for ^{13}C) with TMS as an internal standard. ^{1}H and ^{13}C NMR signals of compounds were assigned using HMQC, HSQC, HMBC, COSY, NOESY, and ^{13}C off-resonance techniques. Positive and negative FAB and EI mass spectra were recorded on a JEOL JMS-700 and Shimadzu GCMS-QP2010 Ultra, respectively. High-resolution mass spectra were obtained by magnetic sector type mass spectrometer. IR spectra were recorded as thin films or as solids in KBr pellets on a HORIBA FT-720 and a JASCO FT/IR 6200 spectrophotometer.

Data collection for X-ray crystal analysis was performed on a Rigaku/ R-AXIS RAPID (MoK_α λ = 0.71075 Å, and CuK_α λ = 1.54187 Å), Rigaku/XtaLAB Synergy-S/Mo (MoK_α λ = 0.71075 Å), and Rigaku/XtaLAB Synergy-S/Cu (CuK_α λ = 1.54187 Å) diffractometers. All calculations were performed with the observed reflections [I>2σ(I)] by the program CrystalStructure crystallographic software packages.[59] All non-hydrogen atoms were refined with anisotropic displacement parameters and hydrogen atoms were placed at calculated positions and refined “riding” on their corresponding carbon atoms

Materials

Anhydrous dichloromethane, THF, acetonitrile, diethylether, toluene and hexane were purchased and used as obtained. All reagents were obtained from commercial suppliers and used as received. All reactions were carried out under nitrogen. 1,3-Dibromo-2-(methoxymethoxy)benzene **4**[49] was prepared by the reported procedures. The products of model reactions, **S15**,[42] **S17**,[44] and **S19**,[38] were known in literatures.

Synthetic procedures

Tris(2-bromo-3-methoxymethyl)(methyl)silane 1a$(MOM)_3$

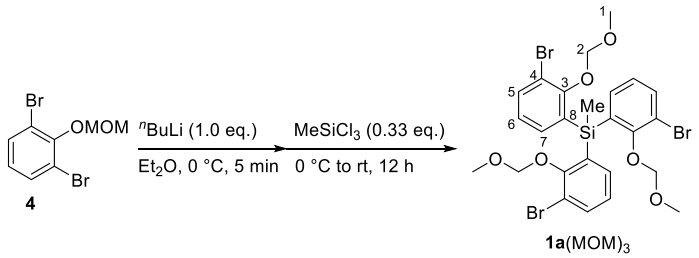

To a solution of 1,3-dibromo-2-(methoxymethyl)benzene **4**[49] (5.9 g, 20 mmol) in Et_2O (60 ml) was slowly added ^{n}BuLi (1.6 M, 11.3 mL, 18 mmol) at 0 ºC. After dropping *n*-BuLi, trichloro methyl silane (1.0 g, 6.7 mmol) in Et_2O (5 ml) were immediately added to the reaction mixture. The reaction mixture was stirred at rt for 12 h. H_2O (20 ml) was added to quench the reaction and the mixture was extracted with Et_2O (3×20 ml). The collected organic layer was washed with saturated NaCl aq (2×30ml) and then dried over $MgSO_4$ and concentrated in vacuo. The crude material was purified by column chromatography (hexane/ethyl acetate = 95:5, column length 10 cm, diameter 26 mm silicagel) on silicagel and recrystallized to give the pure product **1a**$(MOM)_3$ as a white solid (1.85 g, 40%).

mp 91.3–92.1 ºC; IR(KBr) ν = 3057 (w), 2987 (m), 2956 (m), 2912 (m), 2966 (m), 2826 (m), 1571 (m), 1485 (w), 1463 (m), 1439 (m), 1422 (s), 1387 (s), 1257 (m), 1232 (s), 1193 (s), 1158 (s), 1096 (s), 1067 (s), 934 (s), 847 (m), 835 (m), 810 (s), 791 (s), 781 (s), 762 (m), 751 (s), 744 (m), 732 (m), 635 (m), 599 (w), 580 (m), 555 (w), 530 (m), 411 (s) cm^{-1}; ^1H NMR (400 MHz, $CDCl_3$) 7.63 (dd, J = 8.0, 1.2 Hz, 3H, 5-H), 7.14 (dd, J = 7.2, 1.2 Hz, 3H, 7-H), 6.94 (t, J = 8.0 Hz, 3H, 6-H), 4.81 (s, 6H, 2-H), 3.32 (s, 9H, 1-H), 1.17 (s, 3H, SiMe); ^{13}C NMR (100 MHz, $CDCl_3$) 158.5 (s, C-3), 137.1 (d, C-7), 136.1 (d, C-5), 132.5 (s, C-8), 125.3 (d, C-6), 116.9 (s, C-4), 99.1 (t, C-2), 57.7 (q, C-1), –0.68 (q, SiMe); ^{29}Si NMR (78.7 MHz, $CDCl_3$, Me_4Si in $CDCl_3$ as an external standard) –8.61; MS (FAB$^+$, 70 eV) *m*/*z* 717 ([M+6]$^+$, 6), 715 ([M+4]$^+$, 17), 713 ([M+2]$^+$, 16), 711([M]$^+$, 5), 176 (81); HRMS (FAB$^+$, 70 eV) Calculated ($C_{25}H_{27}Br_3O_6SiNa$) 710.9025 (M$^+$): Found: 710.9024.

Tris(2-(methoxymethoxy)-[1,1'-biphenyl]-3-yl)(methyl)silane 1b$(MOM)_3$

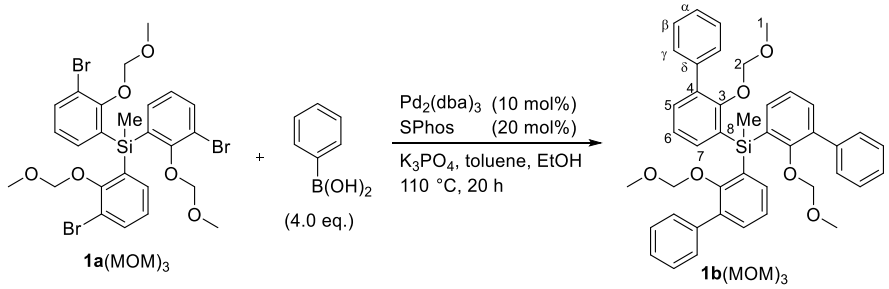

A mixture of tris(2-bromo-3-methoxymethyl)(methyl)silane **1a**$(MOM)_3$ (0.755 g, 1.09 mmol), phenyl boronic acid (0.552 g, 4.52 mmol), K_3PO_4 (0.927 g , 4.37 mmol), $Pd_2(dba)_3$ (98.1 mg, 0.107 mmol), SPhos (93.0 mg, 0.227 mmol) and ethanol (2.5 mL) in toluene (4.0 mL) was heated at 110 ºC for 20 h in the Schlenk tube. The crude material was purified by column chromatography (hexane/ethyl acetate = 95:5, column length 10 cm, diameter 26 mm silicagel) on silicagel and recrystallized to give the pure product **1b**$(MOM)_3$ as a white solid (0.570 g, 76%).

mp 53.7–54.1 °C; IR (KBr) ν = 3056 (w), 2954 (w), 1601 (w), 1579 (w), 1497 (w), 1386 (s), 1254 (w), 1209 (m), 1187 (m), 1160 (m), 1070 (m), 959 (s), 820 (m), 797 (m), 756 (m) cm^{-1}; ^1H NMR (400 MHz, $CDCl_3$) 7.54 (d, J = 7.6 Hz, 6H, γ-H), 7.41 (t, J = 7.6 Hz, 6H, β-H), 7.38 (dd, J = 7.6, 1.6 Hz, 3H), 7.33 －7.27 (m, 6H), 7.14 (t, J = 7.4 Hz, 3H, 6-H), 4.37 (s, 6H, 2-H), 2.82 (s, 9H, 1-H), 1.27 (s, 3H, SiMe); ^{13}C NMR (100 MHz, $CDCl_3$) 159.2 (s, C-3), 139.6 (s C-δ), 137.4 (d), 134.7 (s, C-4), 133.2 (d), 131.0 (s, C-8), 129.2 (d, C-γ), 128.3 (d, C-β), 127.0 (d, C-α), 123.8 (d, C-6), 98.7 (t, C-2), 56.8 (q, C-1), –0.14 (q, SiMe); ^{29}Si NMR (78.7 MHz, $CDCl_3$, Me_4Si in $CDCl_3$ as an external standard) –9.31; MS (FAB^+, 70 eV) *m*/z 705 ($[M+Na]^+$, 48), 211 (53), 195 (94), 45 (100); HRMS (FAB^+, 70 eV) Calculated: ($C_{43}H_{42}O_6SiNa$) 705.2648 ($[M+Na]^+$), Found: 705.2654.

Tris(2-bromo-3-hydroxy)(methyl)silane 1aH_3

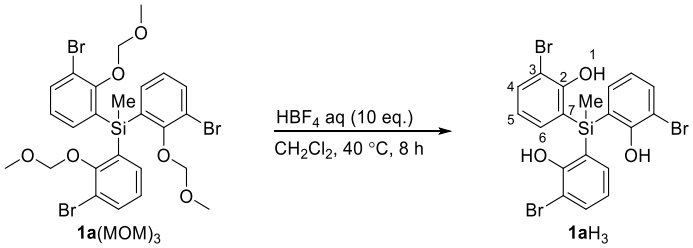

To a colorless solution of tris(2-bromo-3-methoxymethyl)(methyl)silane **1a**$(MOM)_3$ (1.63 mmol, 1.13 g) in CH_2Cl_2 (20 mL) was added HBF_4 (42% in water, 15 mmol, 3.1 g) at room temperature. The mixture was heated at 40 ºC and stirred for 8 h. Cooling down to room temperature, saturated $NaHCO_3$ aq (20 mL) was added to the mixture, which was extracted with CH_2Cl_2 (3 × 20 mL). The collected organic layers were washed with saturated NaCl aq (2 × 20 mL) and then dried over $MgSO_4$ and concentrated in vacuo. The crude material was purified by column chromatography (hexane/ether acetate = 90:10, column length 10 cm, diameter 26 mm silicagel) and recrystallized to give the pure product **1a**H_3 as a white solid (0.50 g, 87%).

mp 180.6–181.5 ºC; IR(KBr) ν = 3512 (m), 3485 (s), 1583 (m), 1424 (s), 1339 (m), 1316 (m), 1269 (w), 1234 (s), 1187 (m), 1171 (m), 1138 (w), 1083 (s), 1064 (m), 833 (m), 802 (m), 773 (m), 745 (m), 726 (m), 584 (m), 534 (w), 493 (w), 410 (s) cm^{-1};^1H NMR (400 MHz, $CDCl_3$) 7.54 (dd, J = 7.6, 1.4 Hz, 3H, 4-H), 7.15 (dd, J = 7.6, 1.4 Hz, 3H, 6-H), 6.80 (t, J = 7.6 Hz, 3H, 5-H), 5.79 (s, 3H, 1-H), 0.98 (s, 3H, SiMe); ^{13}C NMR (100 MHz, $CDCl_3$) 156.1 (s, C-2), 136.5 (d, C-6), 134.0 (d, C-4), 122.2 (s, C-7), 121.9 (d, C-5), 110.5 (s, C-3), –2.96 (q, SiMe); ^{29}Si NMR (78.7 MHz, $CDCl_3$, Me_4Si in $CDCl_3$ as an external standard) –10.1; MS (FAB^-,70 eV) *m*/*z* 561 ($[M+6]^-$, 3), 559 ($[M+4]^-$, 7), 557 ($[M+2]^-$, 7), 555($[M]^-$, 2), 183 (100); HRMS (FAB^-, 70 eV) Calculated ($C_{19}H_{14}Br_3O_3Si$) 554.8262 (M^-): Found: 554.8263.

Tris(2-hydroxy- [1,1'-biphenyl]-3-yl)(methyl)silane 1bH_3

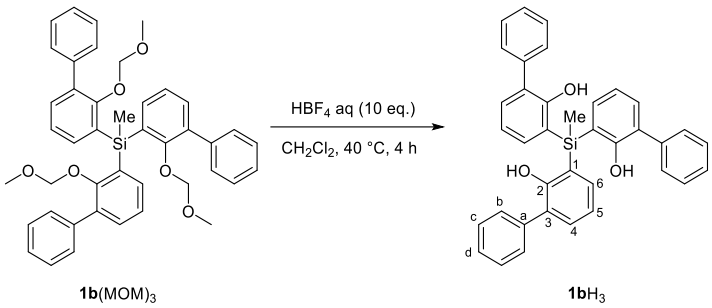

To a yellow solution of tris(2-(methoxymethoxy)-[1,1'-biphenyl]-3-yl)(methyl)silane **1b**$(MOM)_3$ (0.88 mmol, 0.60 g) in CH_2Cl_2 (20 mL) was added HBF_4 (42% in water, 8.8 mmol, 1.84 g) at room temperature. The mixture was heated at 40 ˚C and stirred for 4 h. Cooling down to room temperature, saturated $NaHCO_3$ aq (20 mL) was added to the mixture, which was extracted with CH_2Cl_2 (3 × 20 mL). The collected organic layers were washed with saturated NaCl aq (2 × 20 mL) and then dried over $MgSO_4$ and concentrated in vacuo. The crude material was purified by column chromatography (hexane/ether acetate = 90:10, column length 10 cm, diameter 26 mm silicagel) and recrystallized to give the pure product **1b**H_3 as a white solid (0.30 g, 62%).

mp 88.0–90.0 ˚C; IR (KBr) ν = 3552, 3510 (OH), 1412 cm^{-1}; ^1H NMR (400 MHz, $CDCl_3$) 7.50–7.42 (m, 12H, b-H and c-H), 7.39 (dd, *J* = 7.2, 2.0 Hz, 3H, 6-H), 7.38–7.32 (m, 6H, d-H and 4-H), 7.02 (t, *J* = 7.4 Hz, 3H, 5-H), 5.74 (s, 3H, OH, D_2O exchangeable), 1.04 (s, 3H, SiMe); ^{13}C NMR (100 MHz, $CDCl_3$) 157.3 (s, C-2), 137.4 (s, C-a), 136.4 (d, C-6), 132.4 (d, C-4), 129.2 (d, C-b), 129.1 (d, C-c), 127.7 (s, C-3), 127.6 (d, C-d), 121.4 (s, C-1), 120.9 (d, C-5), -2.4 (q, SiMe); ^{29}Si NMR (78.7 MHz, $CDCl_3$, Me_4Si in $CDCl_3$ as an external standard.) –13.8; MS (EI^+, 70 eV) *m/z* 550 (M^+, 100), 535 ([M–CH_3]$^+$, 7), 329 (30), 57 (35); HRMS (EI^+, 70eV) Calculated ($C_{37}H_{30}O_3Si$) 550.1964 (M^+): Found: 550.1961; Analysis $C_{37}H_{30}O_3Si$ (550.7290) Calculated: C, 80.69; H, 5.49, Found: C, 80.77; H, 5.57.

General procedure for the synthesis of cage-shaped aluminum complex 1 Al·L

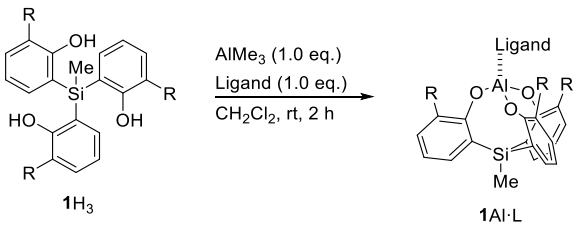

In a nitrogen-filled glove box, a solution of triphenol derivative **1**H_3 (0.3 mmol) in CH_2Cl_2 (3 mL) was gradually added to a solution of ligand (0.3 mmol) and $AlMe_3$ in hexane (1.0 M, 0.28 mL, 0.28 mmol) in CH_2Cl_2 (5 mL) at room temperature. After stirring for 2 h, volatiles were removed under reduced pressure. The obtained crude materials were washed with hexane and evaporated to give the product

1Al·L as a white solid quantitatively.

Cage-shaped aluminum complex 1a Al·py

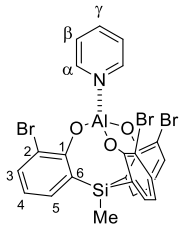

1aAl·py

^{1}H NMR (400 MHz, $CDCl_3$) 9.36 (d, *J* = 4.4 Hz, 2H, α-H), 8.34 (t, *J* = 7.8 Hz, 1H, γ-H), 7.91 (t, *J* = 6.6 Hz, 3H, β-H), 7.52 (dd, *J* = 7.6, 1.6 Hz, 3H, 3-H), 7.38 (dd, *J* = 7.2, 1.6 Hz, 3H, 5-H), 6.74 (t, *J* = 7.6 Hz, 3H, 4-H), 1.13(s, 3H, SiMe); ^{13}C NMR (100 MHz, $CDCl_3$) 159.8 (s, C-1), 148.4 (d, C-α), 143.9 (d, C-γ), 135.0 (d, C-5), 134.8 (d, C-3), 126.8 (s, C-6), 126.5 (d, C-β), 120.8 (d, C-4), 115.3 (s, C-2), –0.67 (q, SiMe); ^{27}Al NMR: (103 MHz, $CDCl_3$, $AlCl_3$ in D_2O as an external standard) 70.5 ($\omega_{1/2}$ = 3900 Hz); ^{29}Si NMR (78.7 MHz, $CDCl_3$, Me_4Si in $CDCl_3$ as an external standard) –21.0.

Cage-shaped aluminum complex 1b Al·py

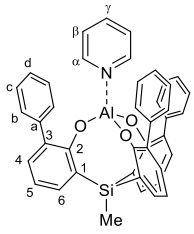

1bAl·py

^{1}H NMR (400 MHz, $CDCl_3$) 7.98 (t, *J* = 7.7 Hz, 1H, γ-H), 7.86 (d, *J* = 3.9 Hz, 2H, α-H), 7.53 (dd, *J* = 7.5, 1.7 Hz, 3H, 6-H), 7.38-7.36 (m, 6H, c-H), 7.28-7.23 (m, 5H, 4-H and β-H), 7.14-7.12 (m, 9H, b-H and d-H), 6.93 (t, *J* = 7.5 Hz, 3H, 5-H), 1.26 (s, 3H, SiMe); ^{13}C NMR (100 MHz, $CDCl_3$) 161.0 (s, C-2), 147.7 (d, C-α), 142.8 (d, C-γ), 140.8 (s, C-a), 135.6 (d, C-6), 132.0 (d, C-4), 131.1(s, C-3), 129.9 (d, C-c), 127.3 (d, C-b), 126.9 (s, C-1), 125.8 (d, C-d), 125.6 (d, C-β), 119.5 (d, C-5), 0.1 (q, SiMe); ^{27}Al NMR (103 MHz, $CDCl_3$, $AlCl_3$ in D_2O as an external standard.) 70.5 ($\omega_{1/2}$ = 3900 Hz); ^{29}Si NMR (78.7 MHz, $CDCl_3$, Me_4Si in $CDCl_3$ as an external standard) –22.2.

Cage-shaped aluminum complex 1a Al·bpy

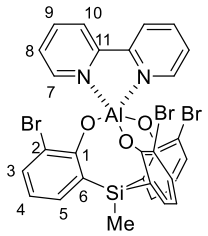

1aAl·bpy

^{1}H NMR (400 MHz, $CDCl_3$) 9.40 (d, *J* = 6.0 Hz, 2H), 8.15–8.09 (m, 4H), 7.62–7.58 (m, 2H, H-8), 7.41–7.37 (m, 6H, H-3, H-5), 6.63 (t, *J* = 7.8 Hz, 3H, H-4), 1.01 (s, 3H, SiMe); ^{13}C NMR (100 MHz, $CDCl_3$) 162.3 (s, C-1), 151.9 (d), 147.6 (s, C-11), 142.3 (d), 134.8 (d), 134.2 (d), 128.5 (s, C-6), 126.8 (d, C-8), 120.1 (d), 119.0 (d, C-4), 115.4 (s, C-2), –0.9 (q, $SiMe_3$); ^{27}Al NMR:(103 MHz, $CDCl_3$, $AlCl_3$, in D_2O as an external standard) 38.2; ^{27}Si NMR (78.7 MHz, $CDCl_3$, Me_4Si in $CDCl_3$ as an external standard) –19.8.

Cage-shaped borates 1B·THF or **1**B·py

In a nitrogen-filled glove box, to a suspension of **1**H_3 (0.1 mmol) in dichloromethane (3 mL) was added BH_3·THF in THF (0.11 mmol, 0.9 M) at room temperature with stirring for 2 h under release of H_2 gas, to afford **1**B·THF as a colorless solid quantitatively. The corresponding ligands (pyridine, 0.15 mmol) were added to the CH_2Cl_2 (2 mL) solution of **1**B·THF and stirred for 0.5 h. Evaporation of volatiles gave a viscous liquid, which was washed by hexane to give the product **1b**B·py as a colorless solid quantitatively.

Cage-shaped borate 1aB·THF

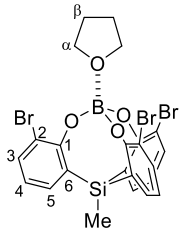

1aB·THF

^{1}H NMR (400 MHz, $CDCl_3$) 7.53 (dd, *J* = 7.6, 1.6 Hz, 3H, 3-H), 7.32 (dd, *J* = 7.6, 1.6 Hz, 3H, 5-H), 6.84 (t, *J* = 7.6 Hz, 3H, 4-H), 4.94 (t, *J* = 6.4 Hz, 4H, α-H), 2.32 (t, *J* = 6.8 Hz, 4H, β-H), 1.01 (s, 3H, SiMe); ^{13}C NMR (100 MHz, $CDCl_3$) 158.1 (s, C-1), 134.9 (d, C-3), 133.4 (d, C-5), 127.0 (s, C-6), 122.6 (d, C-4), 114.9 (s, C-2), 73.7 (t, C-α), 24.9 (t, C-β), –5.5 (q, SiMe); ^{11}B NNR (127 MHz, $CDCl_3$, in $CDCl_3$, $BF_3 \cdot Et_2O$ in $CDCl_3$ as an external standard) 4.73; ^{27}Si NMR (78.7 MHz, $CDCl_3$, Me_4Si in $CDCl_3$ as an external standard) –18.99.

Cage-shaped borate 1aB·py

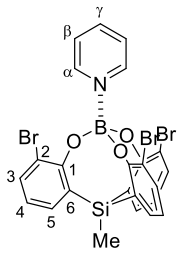

1aB·py

^{1}H NMR (400 MHz, $CDCl_3$) 9.76 (d, *J* = 5.2 Hz, 2H, H-α), 8.19 (t, *J* = 7.8 Hz, 1H H-γ), 7.77 (t, *J* = 7.2 Hz, 2H, H-β), 7.51 (dd, *J* = 7.8, 1.6 Hz, 3H, H-3), 7.37 (dd, *J* = 7.2, 1.6 Hz, 3H, H-5), 6.84 (t, *J* = 7.6 Hz, 3H, H-4), 1.06 (s, 3H, SiMe) ; ^{13}C NMR (100 MHz, $CDCl_3$) 158.7 (s, 1-C), 145.5 (d, α-C), 141.9 (d, γ-C), 134.6 (d, 3-C), 133.3 (d, 5-C), 127.6 (s, 6-C), 124.8 (d, β-C), 122.5 (d, 4-C), 115.5 (s, 2-C), –5.47 (q, SiMe); ^{11}B NNR (127 MHz, $CDCl_3$, in $CDCl_3$, $BF_3 \cdot Et_2O$ in $CDCl_3$ as an external standard) 4.10; ^{27}Si NMR (78.7 MHz, $CDCl_3$, Me_4Si in $CDCl_3$ as an external standard) –18.99.

Cage-shaped borate 1bB·THF

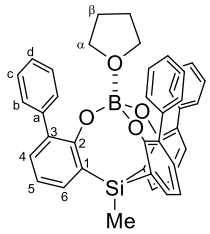

1bB·THF

^{1}H NMR (400 MHz, $CDCl_3$) 7.48 (dd, *J* = 7.6, 1.6 Hz, 3H), 7.44 (dd, *J* = 8.4 Hz, 1.6 Hz, 6H, b-H), 7.32–7.21 (m, 12H), 7.11 (t, *J* = 7.4 Hz, 3H, 5-H), 3.27–3.18 (m, 4H, α-H), 1.44–1.34 (m, 4H, β-H), 1.21 (s, 3H, SiMe); ^{13}C NMR (100 MHz, $CDCl_3$) 158.9 (s, C-2), 140.4 (s), 133.7 (d), 132.1 (s), 132.0 (d), 130.0 (d, C-b), 127.5 (d), 126.7 (d), 126.3 (s), 121.4 (d, C-5), 69.8 (t, C-α), 23.6 (t, C-β), –5.41 (q, SiMe); ^{11}B NMR (127 MHz, $CDCl_3$, $BF_3 \cdot OEt_2$ in $CDCl_3$ as external standard) 6.08; ^{29}Si NMR (78.7 MHz, $CDCl_3$, Me_4Si in $CDCl_3$ as an external standard) –20.72.

Cage-shaped borate 1bB·py

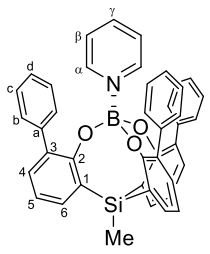

1bB·py

^{1}H NMR (400 MHz, $CDCl_3$) 7.54 (dd, *J* = 7.6, 1.6 Hz, 3H), 7.51–7.47 (m, 3H, α-H, γ-H), 7.28 (dd, *J* = 7.6, 1.6 Hz, 3H), 7.23 (dd, *J* = 8.4, 1.6 Hz, 6H), 7.06 (t, *J* = 7.4 Hz, 3H), 7.04–6.95 (m, 9H), 6.56 (t, *J* = 7.0 Hz, 2H, β-H), 1.21 (s, 3H, SiMe); ^{13}C NMR (100 MHz, $CDCl_3$) 159.8 (s), 143.0 (d, C-α), 140.5 (s), 139.5 (d, C-γ), 133.8 (d), 132.4 (s), 131.6 (d), 129.8 (d), 127.2 (d, s) (Two signals were overlapped.), 125.9 (d), 123.5 (d, C-β), 121.1 (d), –5.30 (q, SiMe); ^{11}B NMR (127 MHz, $CDCl_3$, $BF_3{\cdot}OEt_2$ in $CDCl_3$ as external standard) 3.83; ^{29}Si NMR (78.7 MHz, $CDCl_3$, Me_4Si in $CDCl_3$ as an external standard) –20.43.

Tris(2-bromophenoxy)aluminum-pyridine complex

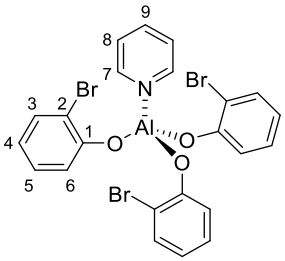

In a nitrogen-filled glove box, 2-bromophenol (0.467 g, 2.7 mmol) was gradually added to a solution of pyridine (0.079 g, 1.0 mmol) and $AlMe_3$ in toluene (1.8 M, 0.55 mL, 1.0 mmol) in CH_2Cl_2 (5 mL) at room temperature. After stirring for 2 h, volatiles were removed under reduced pressure. The obtained crude materials were washed with hexane and evaporated to give the product as a white solid quantitatively.

^{1}H NMR (400 MHz, $CDCl_3$) 9.14 (d, *J* = 5.2 Hz, 2H, 7-H), 8.22 (t, *J* = 6.8 Hz, 1H, 9-H), 7.76 (t, *J* = 6.8 Hz, 2H, 8-H), 7.44 (dd, *J* = 8.2, 1.6 Hz, 3H), 7.10 (td, *J* = 7.6, 1.6 Hz, 3H), 7.01 (dd, *J* = 8.2, 1.6 Hz, 3H), 6.68 (td, *J* = 7.6, 1.6 Hz, 3H); ^{13}C NMR (100 MHz, $CDCl_3$) 154.7 (s), 148.2 (d, C-7), 142.6 (d, C-9), 132.6 (d), 128.5 (d), 125.9 (d, C-8), 120.6 (d), 120.2 (d), 114.4 (s); ^{27}Al NMR (103 MHz, $CDCl_3$, $AlCl_3$ in D_2O as an external standard) 53.73.

X-ray crystallographic data

Cage-shaped aluminum complex **1a**Al·py (CCDC 1944128)

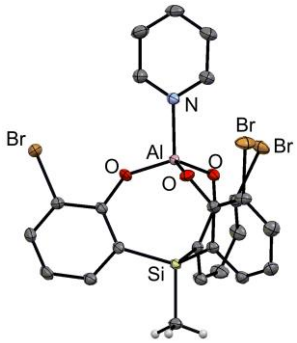

Figure S1. ORTEP drawings of **1a**Al·py at the 50% probability level.

Empirical Formula	$C_{24}H_{17}AlBr_3NO_3Si$	D_{calc}	1.826 g/cm^3
Formula Weight	662.18	F_{000}	1296.00
Crystal Color, Habit	colorless, prism	μ(CuK$_\alpha$)	72.873 cm^{-1}
Crystal Dimensions	0.100 X 0.100 X 0.100 mm	Temperature	-150.0 °C
Crystal System	monoclinic	Function Minimized	$\Sigma\, w\,(F_o^2 - F_c^2)^2$
Lattice Type	Primitive	Least Squares Weights	Chebychev polynomial with 3 parameters 3.2016, 1.2653, 2.3733
Lattice Parameters	a = 9.71975(18) Å		
	b = 31.8436(6) Å	No. Observations ($I > 2.00\sigma(I)$)	4149
	c = 9.22858(17) Å	No. Variables	315
	β = 122.5250(7) °	Reflection/Parameter Ratio	13.17
	V = 2408.35(8) Å^3	Residuals: R_1 ($I > 2.00\sigma(I)$)	0.0316
Space Group	$P2_1/c$ (#14)	Residuals: wR_2 ($I > 2.00\sigma(I)$)	0.0377
Z value	4	Goodness of Fit Indicator	1.079
		Max Shift/Error in Final Cycle	0.000
		Maximum peak in Final Diff. Map	1.21 e$^-$/Å^3
		Minimum peak in Final Diff. Map	-0.57 e$^-$/Å^3

Cage-shaped borate **1a**B·py (CCDC 1944129)

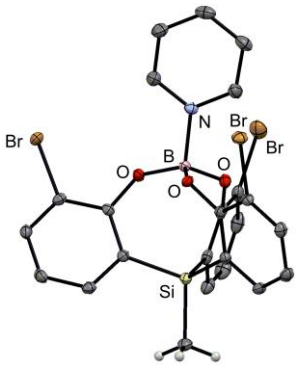

Figure S2. ORTEP drawings of **1a**B·py at the 50% probability level.

Empirical Formula	$C_{24}H_{17}BBr_3NO_3Si$	D_{calc}	1.848 g/cm^3
Formula Weight	646.01	F_{000}	1264.00
Crystal Color, Habit	translucent, intense, block	μ(MoK$_\alpha$)	53.090 cm^{-1}
Crystal Dimensions	0.224 X 0.171 X 0.121 mm	Temperature	-150.0 °C
Crystal System	monoclinic	Function Minimized	$\Sigma\, w\,(F_o^2 - F_c^2)^2$
Lattice Type	Primitive	Least Squares Weights	$w = 1/ [\sigma^2(F_o^2)+(0.0199\cdot P)^2 + 1.8756\cdot P]$ where $P = (\mathrm{Max}(F_o^2,0) + 2F_c^2)/3$
Lattice Parameters	a = 9.0037(3) Å		
	b = 17.1885(5) Å	No. Observations (all reflections)	5888
	c = 15.0515(5) Å	No. Variables	298
	β = 94.761(3) °	Reflection/Parameter Ratio	19.76
	V = 2321.33(13) Å^3	Residuals: R_1 ($I > 2.00\sigma(I)$)	0.0301
Space Group	$P2_1/n$ (#14)	Residuals: wR_2 (all reflections)	0.0591
Z value	4	Goodness of Fit Indicator	1.019
		Max Shift/Error in Final Cycle	0.001
		Maximum peak in Final Diff. Map	0.52 e$^-$/Å^3
		Minimum peak in Final Diff. Map	-0.38 e$^-$/Å^3

Cage-shaped aluminum complex 1b Al·py (CCDC 1944130)

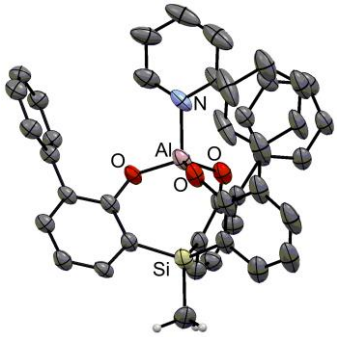

Figure S3. ORTEP drawings of **1b**Al·py at the 30% probability level.

Empirical Formula	$C_{42}H_{32}AlNO_3Si$	D_{calc}	1.298 g/cm^3
Formula Weight	653.79	F_{000}	2736.00
Crystal Color, Habit	colorless, prism	μ(CuK$_\alpha$)	12.051 cm^{-1}
Crystal Dimensions	0.300 X 0.200 X 0.200 mm	Temperature	-150.0 °C
Crystal System	monoclinic	Function Minimized	$\Sigma\, w\,(F_o^2 - F_c^2)^2$
Lattice Type	*C*-centered	No. Observations ($I > 2.00\sigma(I)$)	3675
Lattice Parameters	a = 32.240(2) Å	No. Variables	465
	b = 12.972(1) Å	Reflection/Parameter Ratio	7.90
	c = 16.191(1) Å	Residuals: R_1 ($I > 2.00\sigma(I)$)	0.0628
	β = 98.752(3) °	Residuals: wR_2 ($I > 1.00\sigma(I)$)	0.1376
	V = 6692.1(8) Å^3	Goodness of Fit Indicator	2.266
Space Group	*C*2/*c* (#15)	Max Shift/Error in Final Cycle	0.000
Z value	8	Maximum peak in Final Diff. Map	2.26 e$^-$/Å^3
		Minimum peak in Final Diff. Map	-1.59 e$^-$/Å^3

Cage-shaped borate 1bB·py (CCDC 1944131)

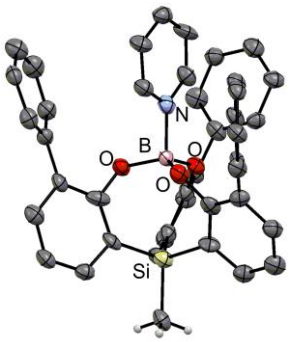

Figure S4. ORTEP drawings of **1b**B·py at the 30% probability level.

Empirical Formula	$C_{42}H_{32}BNO_3Si$	D_{calc}	1.327 g/cm^3
Formula Weight	637.62	F_{000}	2672.00
Crystal Color, Habit	colorless, prism	μ(CuK$_\alpha$)	9.903 cm^{-1}
Crystal Dimensions	0.400 X 0.100 X 0.100 mm	Temperature	-150.0 °C
Crystal System	monoclinic	Function Minimized	$\Sigma\, w\,(F_o^2 - F_c^2)^2$
Lattice Type	*C*-centered	Least Squares Weights	$1/\sigma^2(F_o^2) = 1/\sigma^2(F_o)/(4F_o^2)$
Lattice Parameters	a = 31.949(1) Å	No. Observations ($I > 1.00\sigma(I)$)	2823
	b = 12.4895(4) Å	No. Variables	465
	c = 16.1636(6) Å	Reflection/Parameter Ratio	6.07
	β = 98.324(2) °	Residuals: R_1 ($I > 2.00\sigma(I)$)	0.0797
	V = 6381.8(4) Å^3	Residuals: wR_2 ($I > 1.00\sigma(I)$)	0.1528
Space Group	*C*2/*c* (#15)	Goodness of Fit Indicator	1.194
Z value	8	Max Shift/Error in Final Cycle	0.003
		Maximum peak in Final Diff. Map	0.80 e$^-$/Å^3
		Minimum peak in Final Diff. Map	-0.78 e$^-$/Å^3

Cage-shaped aluminum complex 1a Al·bpy (CCDC 1944132)

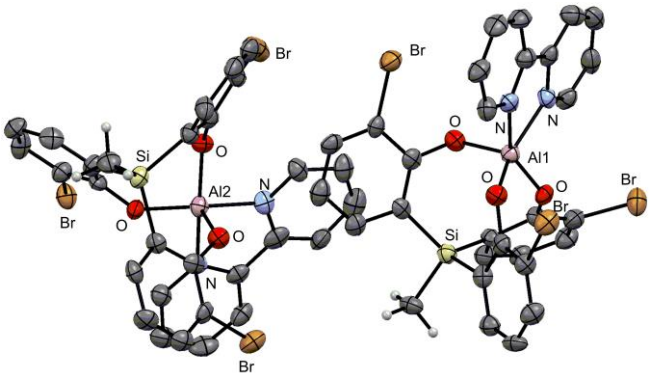

Figure S5. ORTEP drawings of **1a**Al·bpy at the 50% probability level.

Empirical Formula	$C_{58}H_{40}Al_2Br_6N_4O_6Si_2$	D_{calc}	1.813 g/cm^3
Formula Weight	1478.54	F_{000}	2912.00
Crystal Color, Habit	colorless, prism	μ(MoK$_\alpha$)	45.959 cm^{-1}
Crystal Dimensions	0.100 X 0.100 X 0.100 mm	Temperature	-150.0 °C
Crystal System	orthorhombic	Function Minimized	$\Sigma\, w\,(F_o^2 - F_c^2)^2$
Lattice Type	Primitive	Least Squares Weights	$w = 1/[\sigma^2(F_o^2) + (0.0669\cdot P)^2 + 0.0000\cdot P]$
Lattice Parameters	a = 24.586(3) Å		where $P = (\mathrm{Max}(F_o^2,0) + 2F_c^2)/3$
	b = 10.5567(10) Å	No. Observations (All reflections)	12302
	c = 20.865(2) Å	No. Variables	703
	V = 5415.4(10) Å^3	Reflection/Parameter Ratio	17.50
Space Group	$Pna2_1$ (#33)	Residuals: R_1 ($I > 2.00\sigma(I)$)	0.0699
Z value	4	Residuals: wR_2 (All reflections)	0.1594
		Goodness of Fit Indicator	0.999
		Max Shift/Error in Final Cycle	0.000
		Maximum peak in Final Diff. Map	0.89 e$^-$/Å^3
		Minimum peak in Final Diff. Map	-0.73 e$^-$/Å^3

Comparisons of the geometry for 1aAl·py, 1aB·py, 1bAl·py, and 1bB·py

Table S1. Selected geometric parameters for **1a**Al·py, **1a**B·py, **1b**Al·py, and **1b**B·py

	1aAl·py	**1a**B·py	**1b**Al·py	**1b**B·py
Al(B)–Si / Å	3.293	3.167	3.201	3.103
Al(B)–N / Å	1.924 (2)	1.639(3)	1.906(6)	1.641(12)
∠O–Al(B)–O / °	112.4(9)	113.8(2)	112.6(2)	114.8(7)
∠O–Al(B)–N / °	106.4(9)	104.7(2)	106.0(3)	103.4 (7)
THC / %	72.7	59.0	70.5	49.5

IR measurements of the cage-shaped complex with 2,6-dimethyl-γ-pyrone

In a nitrogen-filled glove box, to a solution of cage-shaped complex (0.05 mmol) in CH_2Cl_2 (1 mL) was added 2,6-dimethyl-γ-pyrone (0.1 mmol). After stirring for 1 h, volatile was removed under reduced pressure and the residue was washed with hexane to afford the product. The ligation of 2,6-dimethyl-γ-pyrone was confirmed by NMR measurements. Infrared spectra of the obtained complex were recorded as CH_2Cl_2 solutions and the average values of five times measurements were employed.

Table S2. Summary of Lewis acidity of aluminum compounds

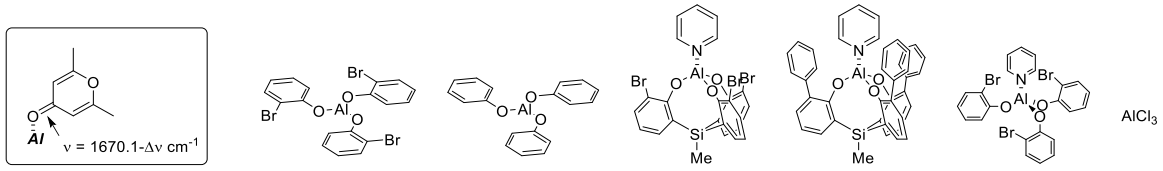

Δν/ cm^{-1} in CH_2Cl_2	1.69	3.28	16.9	17.1	17.3	18.7

Glycosylation using Al or B catalyst

Investigation of leaving groups of glycosyl donors

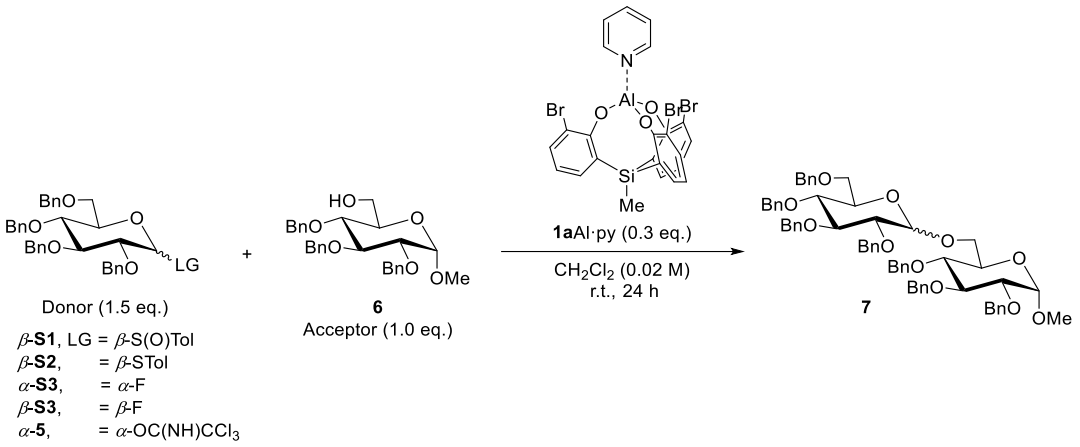

Procedure of entry 5

In a nitrogen-filled glove box, to a solution of donor α-**5** (57.0 mg, 0.083 mmol) and acceptor **6** (25.8 mg, 0.056 mmol) in CH_2Cl_2 (1.1 mL) was added a solution of **1a**Al·py (11.0 mg, 0.017 mmol) in CH_2Cl_2 (1.7 mL) at room temperature. After stirring for 24 h at room temperature, the mixture was quenched by bubbling of Air. The organic layer was evaporated to give a crude mixture, which was analyzed by ^{1}H NMR with $Cl_2CHCHCl_2$ as an internal standard reagent (81%, α:β = 1/6.2). Analytical data for **7** was referenced from literatures.[60–62]

(*In other entries, glycosylation was carried out by a similar procedure as entry 5 and the crude material was analyzed by ^{1}H NMR with $Cl_2CHCHCl_2$ as an internal standard reagent.)

Table S3. Investigation of leaving group of glycosyl donors

entry	donor	leaving group (LG)	yield of **7** / %[b]	ratio (α/β)[b]
1	β-**S1**	β-S(O)Tol	N.D.	-
2[a]	β-**S2**	β-STol	32%	1.1/1
3	α-**S3**	α-F	9	3.5/1
4	β-**S3**	β-F	13	1/3.0
5	α-**5**	α-OC(NH)CCl_3	81	1/6.2

[a]NBS (1.5 eq.) was added. [b]Estimated by ^{1}H NMR spectra.

Optimization of glycosylation

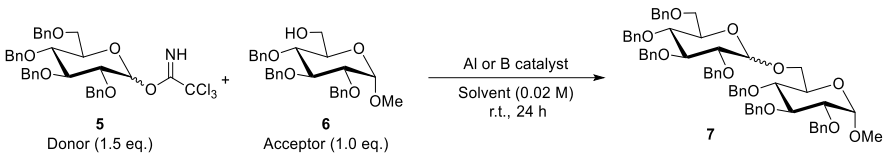

Procedure of Entry 13

In a nitrogen-filled glove box, to a solution of donor α-**5** (51.4 mg, 0.075 mmol) and acceptor **6** (23.2 mg, 0.05 mmol) in Et_2O (1.0 mL) was added a solution of **1a**Al·py (3.3 mg, 0.005 mmol) in Et_2O (1.5 mL) at room temperature. After stirring for 24 h at room temperature, the mixture was quenched by bubbling of Air. The organic layer was evaporated to give a crude mixture, which was analyzed by ^{1}H NMR with $Cl_2CHCHCl_2$ as an internal standard reagent (96%, α:β = 1:19). The crude material was purified by column chromatography (toluene/ethyl acetate = 94:6, column length 15 cm, diameter 10 mm silicagel) on silicagel to give the pure product **7** as a white solid (46.0 mg, 93%, α:β = 1:19). Analytical data for **7** was referenced from literatures.[60–62]

(*In other entries, glycosylation was carried out by a similar procedure as entry 13 and the crude material was analyzed by ^{1}H NMR with $Cl_2CHCHCl_2$ as an internal standard reagent.)

Table S4. Optimization of glycosylation by Al catalysts

entry	Al or B catalyst (eq.)	donor	solvent	yield of **7** / %[a]	ratio (α/β)[a]
1	**1a**Al·py (0.3)	α-**5**	CH_2Cl_2	81	1/6.2
2	**1a**B·THF (0.3)	α-**5**	CH_2Cl_2	68	4.6/1
3	**1a**B·py (0.3)	α-**5**	CH_2Cl_2	Trace	-
4	**1b**Al·py (0.3)	α-**5**	CH_2Cl_2	6	1/1.9
5	**1a**Al·py (0.3)	α-**5**/β-**5** (1/7.7)	CH_2Cl_2	44	2.2/1
6	**1a**Al·py (0.3)	α-**5**/β-**5** (1/9.1)	Et_2O	86	1.1/1
7	**1a**Al·py (0.3)	α-**5**/β-**5** (1/9.1)	Cyclopentyl methyl ether (CPME)	90	1.1/1
8	$AlCl_3$ (0.3)	α-**5**	CH_2Cl_2	27	1/1.5
9	$(2\text{-}BrC_6H_4O)_3Al$ ·py (0.3)	α-**5**	CH_2Cl_2	Trace	-
10	**1a**Al·py (0.3)	α-**5**	CH_3CN	63	1/13
11	**1a**Al·py (0.3)	α-**5**	THF	95	1/8.7
12	**1a**Al·py (0.3)	α-**5**	Et_2O	95	1/19
13	**1a**Al·py (0.1)	α-**5**	Et_2O	96 (93[b])	1/19

[a]Estimated by ^{1}H NMR spectra. [b]Isolated yield.

^{1}H NMR in entry 13 (500 MHz, $CDCl_3$)

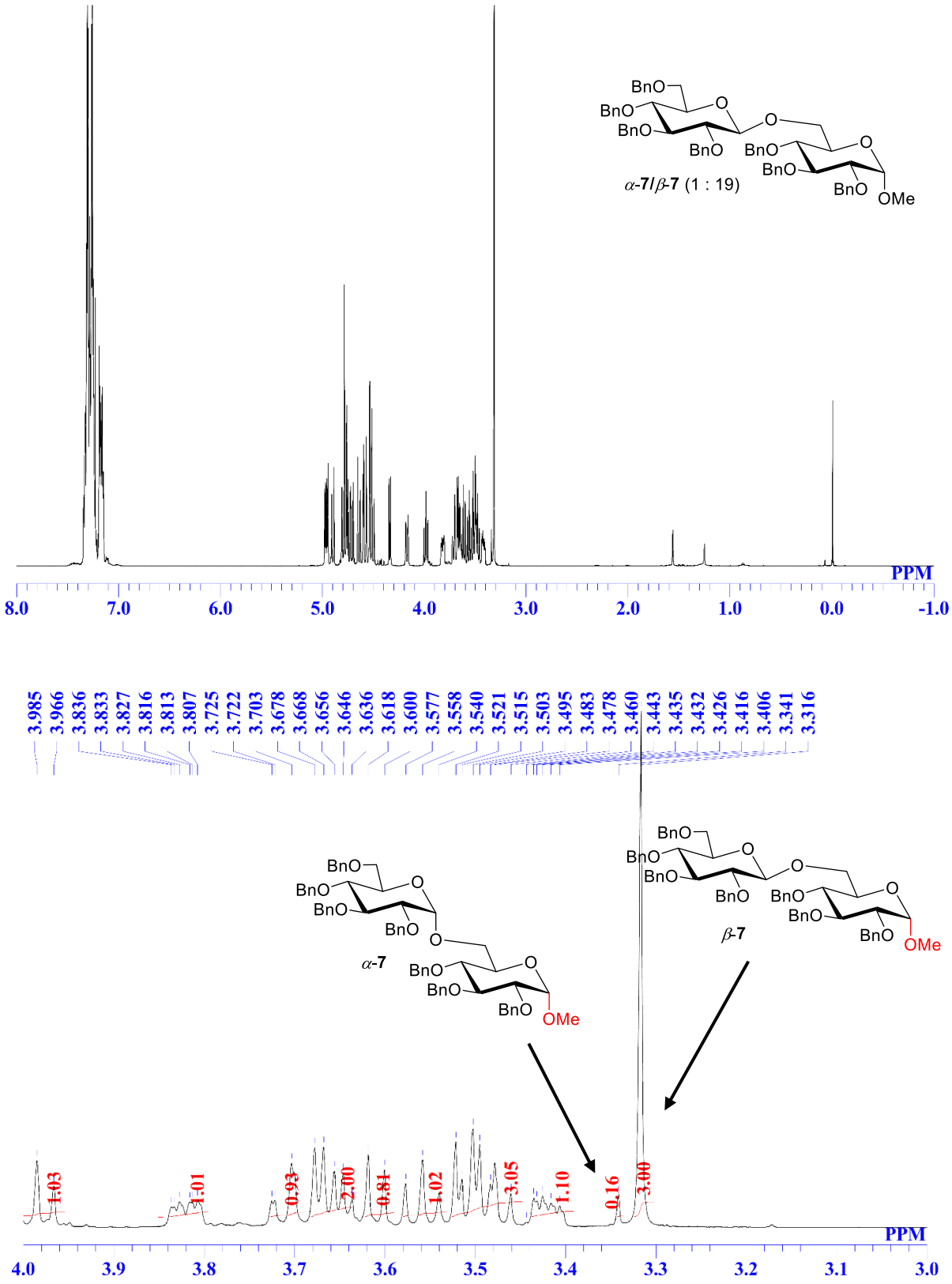

^{13}C NMR in entry 13 (125 MHz, $CDCl_3$)

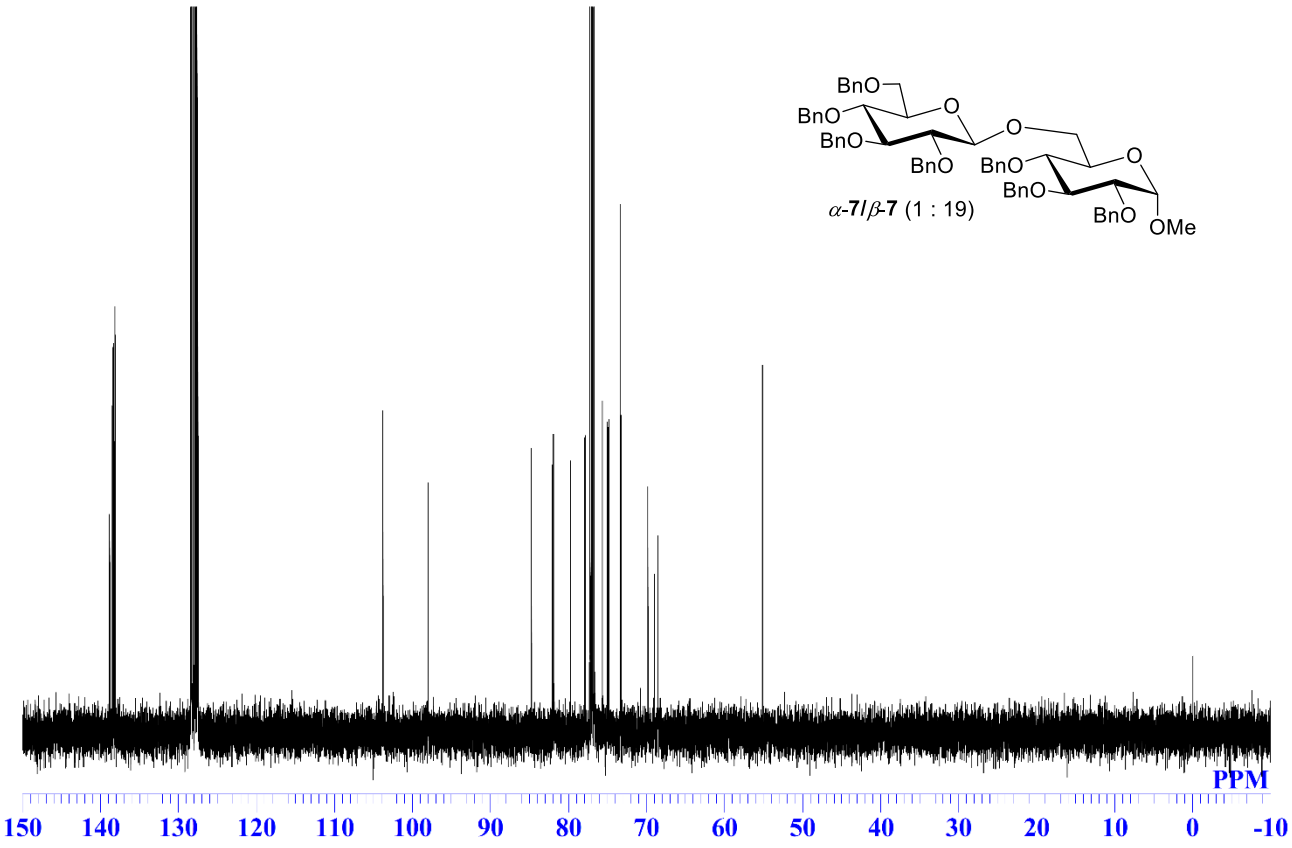

Concentration effect of the *α*/*β* stereoselectivity

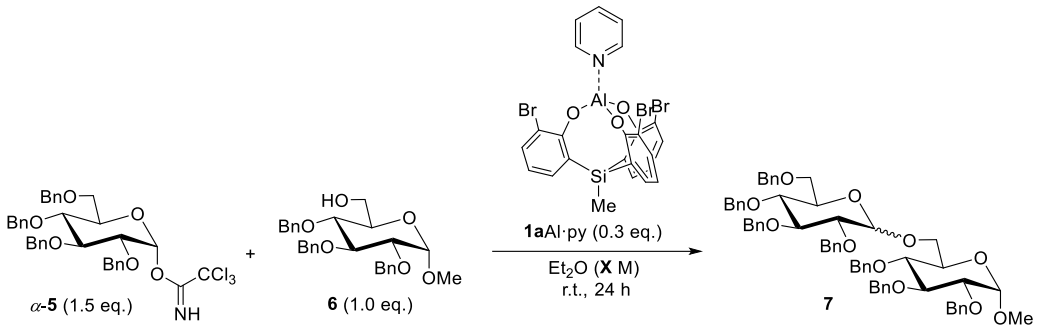

Procedure of Entry 2

In a nitrogen-filled glove box, to a solution of donor *α*-**5** (51.4 mg, 0.075 mmol) and acceptor **6** (23.2 mg, 0.05 mmol) in Et_2O (1.0 mL) was added a solution of **1a**Al·py (9.9 mg, 0.015 mmol) in Et_2O (1.5 mL) at room temperature. After stirring for 24 h at room temperature, the mixture was quenched by bubbling of Air. The organic layer was evaporated to give a crude mixture, which was analyzed by ^1H NMR with $Cl_2CHCHCl_2$ as an internal standard reagent (95%, α:β = 1:19). Analytical data for **7** was referenced from literatures.[60–62]

(*In other entries, glycosylation was carried out by a similar procedure as entry 2 and the crude material was analyzed by ^{1}H NMR with $Cl_2CHCHCl_2$ as an internal standard reagent.)

Table S5. Concentration effect of the α/β stereoselectivity

entry	X	yield of **7** / %[a]	ratio (α/β)[a]
1	0.1	96	1/19
2	0.02	95	1/19
3	0.004	94	1/21

[a]Estimated by ^{1}H NMR spectra.

Scope of substrates

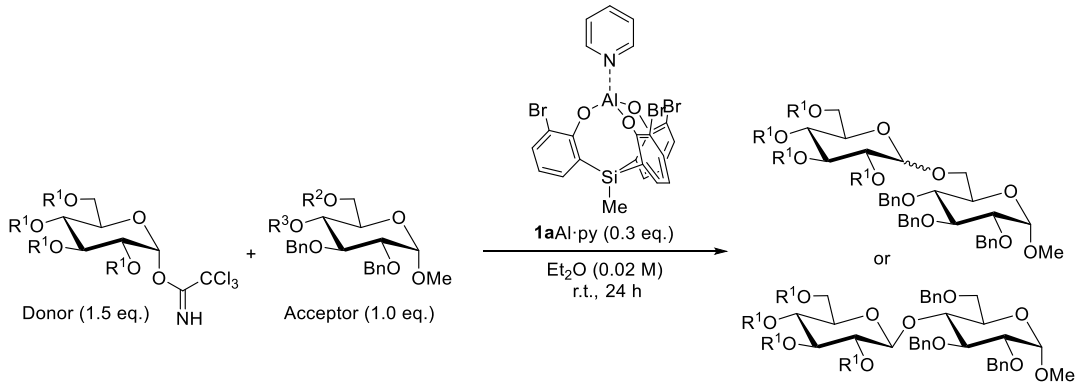

General procedure

In a nitrogen-filled glove box, to a solution of donor (0.075 mmol) and each acceptor (23.2 mg, 0.05 mmol) in Et_2O (1.0 mL) was added a solution of **1a**Al·py (9.9 mg, 0.015 mmol) in Et_2O (1.5 mL) at room temperature. After stirring for 24 h at room temperature, the mixture was quenched by bubbling of Air. The organic layer was evaporated to give a crude mixture, which was analyzed by ^{1}H NMR with $Cl_2CHCHCl_2$ as an internal standard reagent. Analytical data for **S6** was referenced from literatures. [60–62]

Table S6. Scope of Substrates by **1a**Al·py

entry	donor	Acceptor	yield of product / %[a]	ratio (α/β)[a]
1	α-**5** (R^1 = Bn)	**6** (R^2 = H, R^3 = Bn)	**7**: 95	1/19
2	α-**5** (R^1 = Bn)	**S5** (R^2 = Bn, R^3 = H)	**S6**: 70%	1/2.3
3	α-**S4** (R^1 = Bz)	**6** (R^2 = H, R^3 = Bn)	**S7**: <5%	-
4	α-**S4** (R^1 = Bz)	**S5** (R^2 = Bn, R^3 = H)	**S8**: <5%	-

[a]Estimated by ^{1}H NMR spectra.

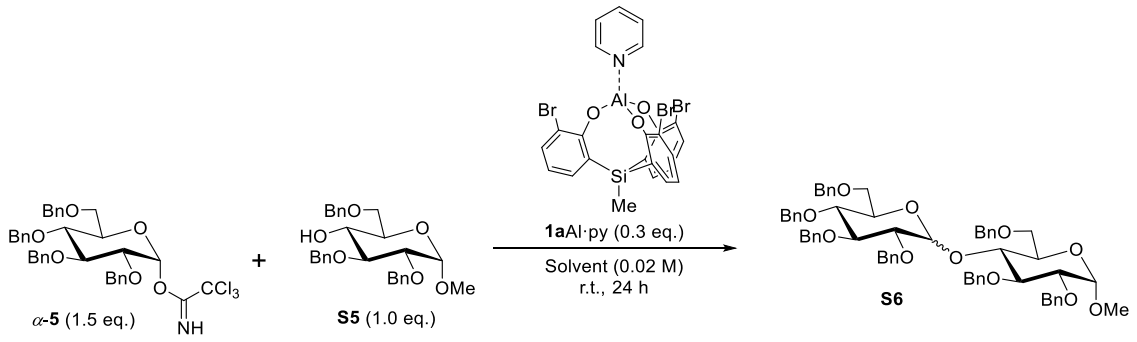

General procedure

In a nitrogen-filled glove box, to a solution of each donor α-**5** (51.4 mg, 0.075 mmol) and acceptor **S5** (23.2 mg, 0.05 mmol) in each solvent (1.0 mL) was added a solution of **1a**Al·py (9.9 mg, 0.015 mmol) in each solvent (1.5 mL) at room temperature. After stirring for 24 h at room temperature, the mixture was quenched by bubbling of Air. The organic layer was evaporated to give a crude mixture, which was analyzed by ^{1}H NMR with $Cl_2CHCHCl_2$ as an internal standard reagent. Analytical data for **S6** was referenced from literatures. [60–62]

Table S7. Optimization of 1,4-glucosylation

entry	Solvent	yield of **S6** / %[a]	ratio (α/β)[a]
1	CH_2Cl_2	49	1.5/1
2	Toluene	58	1/1.1
3	CH_3CN	39	1/1.8
4	THF	35	2.9/1
5	Et_2O	70	1/2.3
6	Cyclopentyl methyl ether (CPME)	56	1/1.8
7	^{t}BuOMe	50	1/2.3
8	dioxane	42	1/1.3

[a]Estimated by ^{1}H NMR spectra.

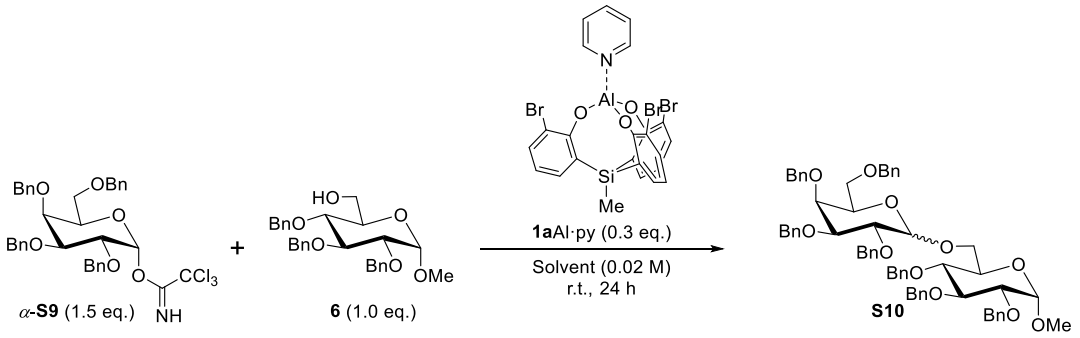

Procedure of entry 2

In a nitrogen-filled glove box, to a solution of each donor α-**S9** (51.4 mg, 0.075 mmol) and acceptor **6** (23.2 mg, 0.05 mmol) in CH_3CN (1.0 mL) was added a solution of **1a**Al·py (9.9 mg, 0.015 mmol) in CH_3CN (1.5 mL) at room temperature. After stirring for 24 h at room temperature, the mixture was quenched by bubbling of Air. The organic layer was evaporated to give a crude mixture, which was analyzed by ^{1}H NMR with $Cl_2CHCHCl_2$ as an internal standard reagent (65%, α:β = 1/2.7). Analytical data for **S10** was referenced from a literature. [62]

(*In other entries, glycosylation was carried out by a similar procedure as entry 2 and the crude material was analyzed by ^{1}H NMR with $Cl_2CHCHCl_2$ as an internal standard reagent.)

Table S8. Optimization of 1,6-galactosylation

entry	Solvent	yield of **S10** / %[a]	ratio (α/β)[a]
1	CH_2Cl_2	59	1/1.1
2	CH_3CN	65	1/2.7
3	Et_2O	67	1/1

[a]Estimated by ^{1}H NMR spectra.

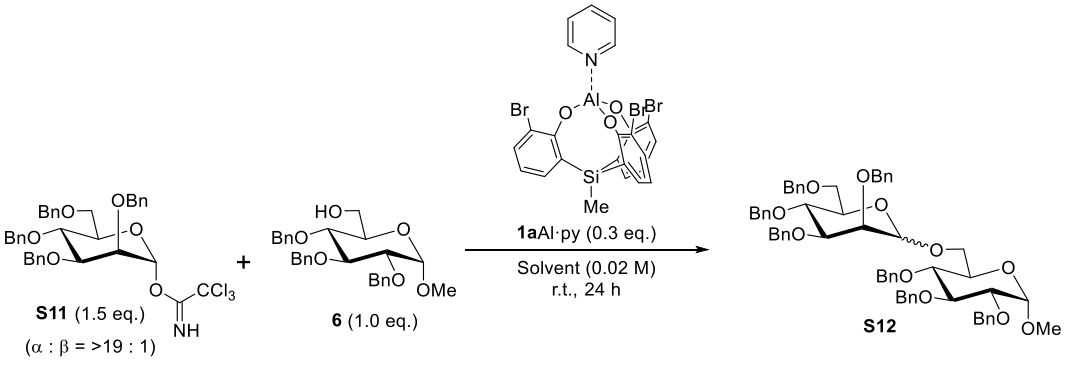

General procedure

In a nitrogen-filled glove box, to a solution of each donor α-**S11** (56.4 mg, 0.082 mmol) and acceptor **6** (25.5 mg, 0.055 mmol) in each solvent (1.1 mL) was added a solution of **1a**Al·py (10.9 mg, 0.017 mmol)

in each solvent (1.6 mL) at room temperature. After stirring for 24 h at room temperature, the mixture was quenched by bubbling of Air. The organic layer was evaporated to give a crude mixture, which was analyzed by ^{1}H NMR with $Cl_2CHCHCl_2$ as an internal standard reagent. Analytical data for **S12** was referenced from a literature.[63]

Table S9. Optimization of 1,6-mannosylation

entry	Solvent	yield of **S12** / %[a]	ratio (α/β)[a]
1	CH_2Cl_2	42	17/1
2	CH_3CN	43	2.6/1
3	Et_2O	40	20/1
4	THF	73	20/1
5	toluene	61	>25/1

[a]Estimated by ^{1}H NMR spectra.

Observation of high-coordinated aluminum complex with Lewis bases via variable temperature ^{27}Al NMR measurements

In a nitrogen-filled glove box, to a solution of Lewis bases (0.05 mmol) in CD_2Cl_2 (1.0 mL) was added **1**Al·py (0.05 mmol) in CD_2Cl_2 (0.4 mL) at room temperature.

Variable temperature ^{27}Al NMR measurements of 1aAl·py with pyridine and 5 in CD_2Cl_2

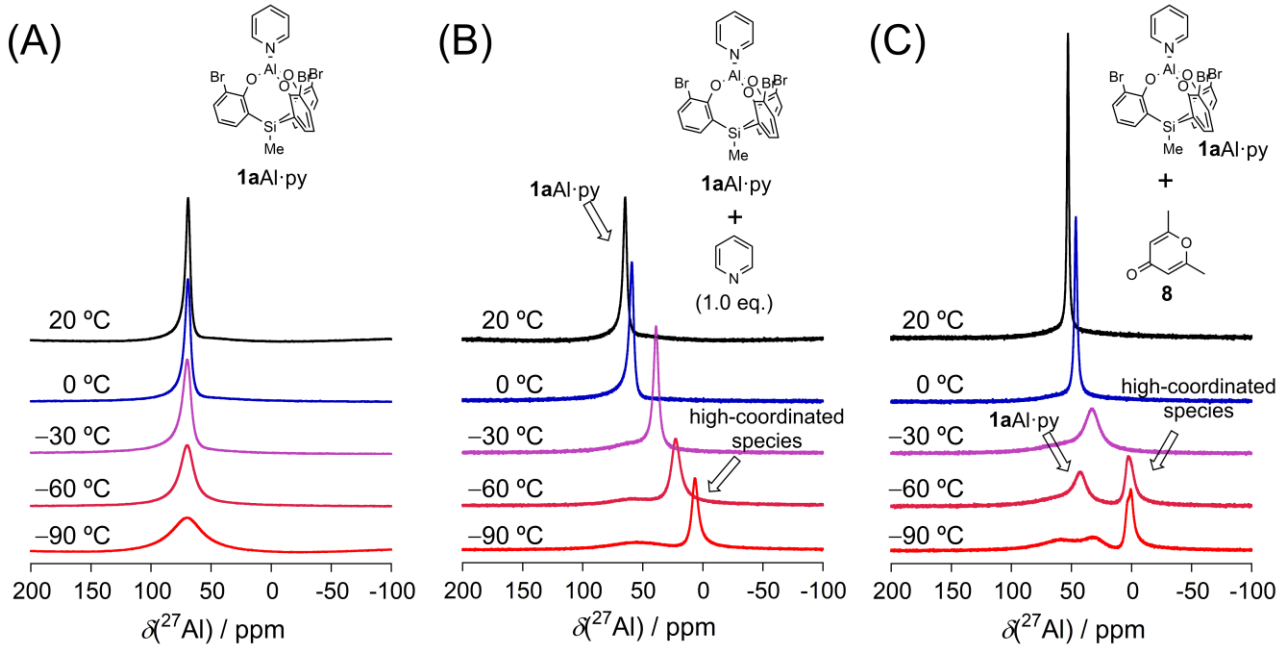

Figure S6. Variable temperature ^{27}Al NMR measurements (103 MHz, $AlCl_3$ in D_2O as an external standard) for (A) **1a**Al·py, (B) **1a**Al·py with pyridine, and (C) **1a**Al·py with **8** in CD_2Cl_2.

Table S10. Summary for NMR data for variable temperature ^{27}Al NMR measurements (103 MHz, $AlCl_3$ in D_2O as an external standard) for **1a**Al·py, **1a**Al·py with pyridine, and **1a**Al·py with **8**.

T/ °C (CD_2Cl_2)	**1a**Al·py $\delta(^{27}Al)$ / ppm	**1a**Al·py+py $\delta(^{27}Al)$ / ppm	**1a**Al·py+**8** $\delta(^{27}Al)$ / ppm
20	71.60	64.76	52.92
0	71.41	59.21	46.32
–30	73.48	39.07	33.51
–60	74.77	22.77	42.54, 2.81
–90	65.06	6.71	31.92, 0.67

Upon cooling, a gradual upfield filed shift of the ^{27}Al signal was observed in the mixture of **1a**Al·py and pyridine or **8**, suggesting the coordination of these Lewis bases to **1a**Al·py (Figures S6B and C).

Variable temperature ^{27}Al NMR measurements of 1aAl·py with α-5 in CD_2Cl_2

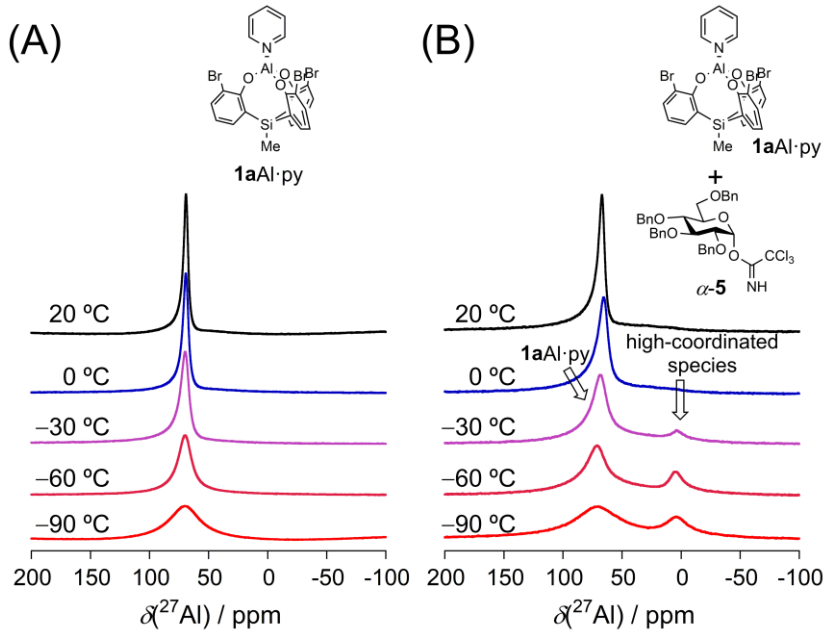

Figure S7. Variable temperature ^{27}Al NMR measurements (103 MHz, $AlCl_3$ in D_2O as an external standard) for (A) **1a**Al·py and (B) **1a**Al·py with α-**5** in CD_2Cl_2.

Table S11. Summary for NMR data for variable temperature ^{27}Al NMR measurements (103 MHz, $AlCl_3$ in D_2O as an external standard) for **1a**Al·py and **1a**Al·py with α-**5**.

T/ °C (CD_2Cl_2)	**1a**Al·py $\delta(^{27}Al)$ / ppm	**1a**Al·py+α-**5** $\delta(^{27}Al)$ / ppm
20	71.60	67.14
0	71.41	65.67
–30	73.48	68.97, 4.15
–60	74.77	71.16, 4.88
–90	65.06	71.35, 4.09

When mixing **1a**Al·py with α-**5**, the similar upfield shift of the ^{27}Al signal was observed at low temperature (Figure S7B). The high-coordinated aluminum species of **1a**Al·py with **5** should be generated at low temperature.

Variable temperature ^{27}Al NMR measurements of 1bAl·py in CD_2Cl_2

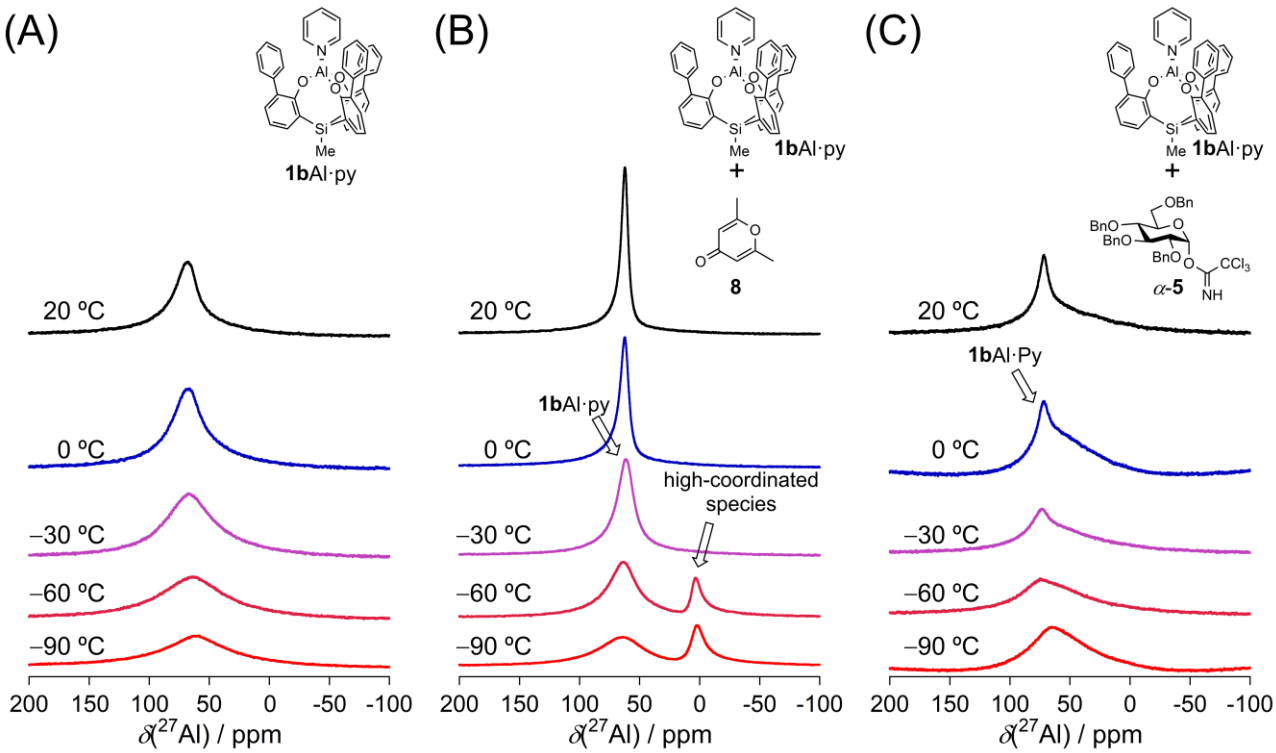

Figure S8. Variable temperature ^{27}Al NMR measurements (103 MHz, $AlCl_3$ in D_2O as an external standard) for (A) **1b**Al·py, (B) **1b**Al·py with **8**, and (C) **1b**Al·py with α-**5** in CD_2Cl_2.

Table S12. Summary for NMR data for variable temperature ^{27}Al NMR measurements (103 MHz, $AlCl_3$ in D_2O as an external standard) for **1b**Al·py, **1b**Al·py with **8**, and **1b**Al·py with α-**5** in CD_2Cl_2.

T/ °C (CD_2Cl_2)	**1b**Al·py δ(^{27}Al) / ppm	**1b**Al·py+**8** δ(^{27}Al) / ppm	**1b**Al·py+α-**5** δ(^{27}Al) / ppm
20	70.19	62.38	1.60
0	70.37	62.38	71.41
–30	70.49	61.58	73.48
–60	71.16	67.32, 3.17	74.77
–90	56.70	64.52, 2.01	65.06

A upfiled shift was observed in the mixture of **1b**Al·py and **8**, suggesting the coordination of **8** to **1b**Al·py (Figure S8B). For **1b**Al·py with α-**5**, however, no significant upfield shift was observed (Figure S8C). The three phenyl groups should inhibit the coordination of α-**5** with the aluminum center, which led to the low catalytic activity of **1b**Al·py in the glycosylation.

Variable temperature ^{27}Al NMR measurements of 1aAl·py in THF-d_8

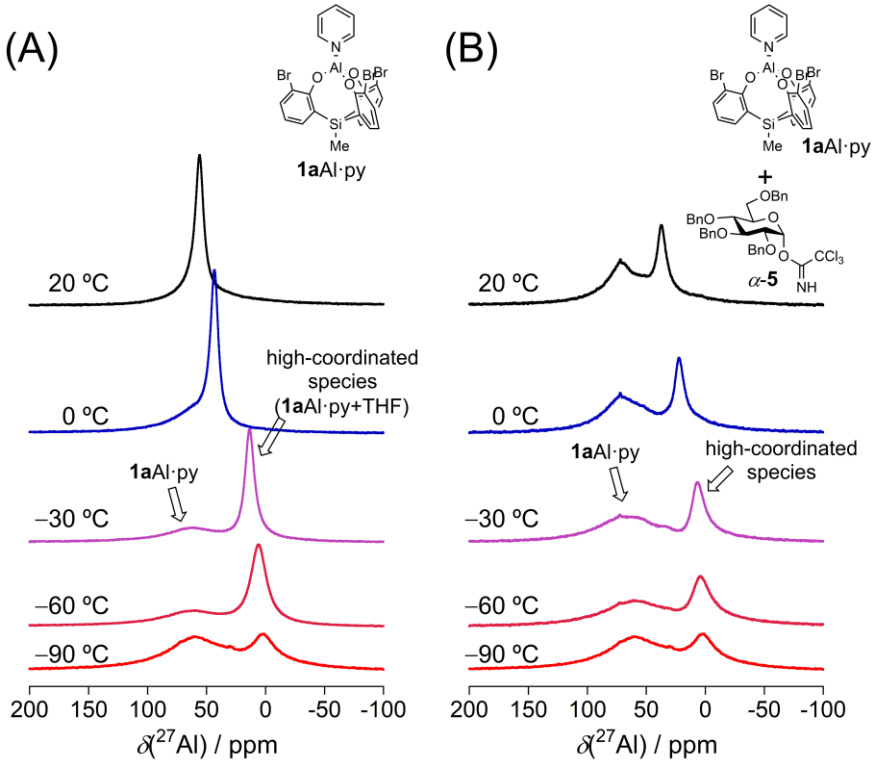

Figure S9. Variable temperature ^{27}Al NMR measurements (103 MHz, $AlCl_3$ in D_2O as an external standard) for (A) **1a**Al·py, and (B) **1a**Al·py with α-**5** in THF-d_8.

Table S13. Summary for NMR data for variable temperature ^{27}Al NMR measurements (103 MHz, $AlCl_3$ in D_2O as an external standard) for **1a**Al·py, and **1a**Al·py with α-**5** in THF-d_8.

T/ °C (THF-d_8)	**1a**Al·py δ(^{27}Al) / ppm	**1a**Al·py+α-**5** δ(^{27}Al) / ppm
20	56.03	71.84, 37.42
0	43.39	71.96, 22.34
–30	13.55	6.53
–60	6.35	3.97
–90	5.92	2.81

Upon cooling, a gradual upfield shift of ^{27}Al signal of **1a**Al·py was observed, suggesting the generation of a high-coordinated species of **1a**Al·py via the coordination of THF (Figure S9A). In the presence of α-**5**, an ^{27}Al signal in the upper field region was observed even at room temperature, strongly suggesting the interaction of **1a**Al·py with α-**5** in preference to THF (Figure S9B). The preferred coordination of **1a**Al·py with α-**5** realized the high catalytic glycosylation with high stereoselectivity in ethereal solvents.

Variable temperature ^{27}Al NMR measurements of 1bAl·py in THF-d_8

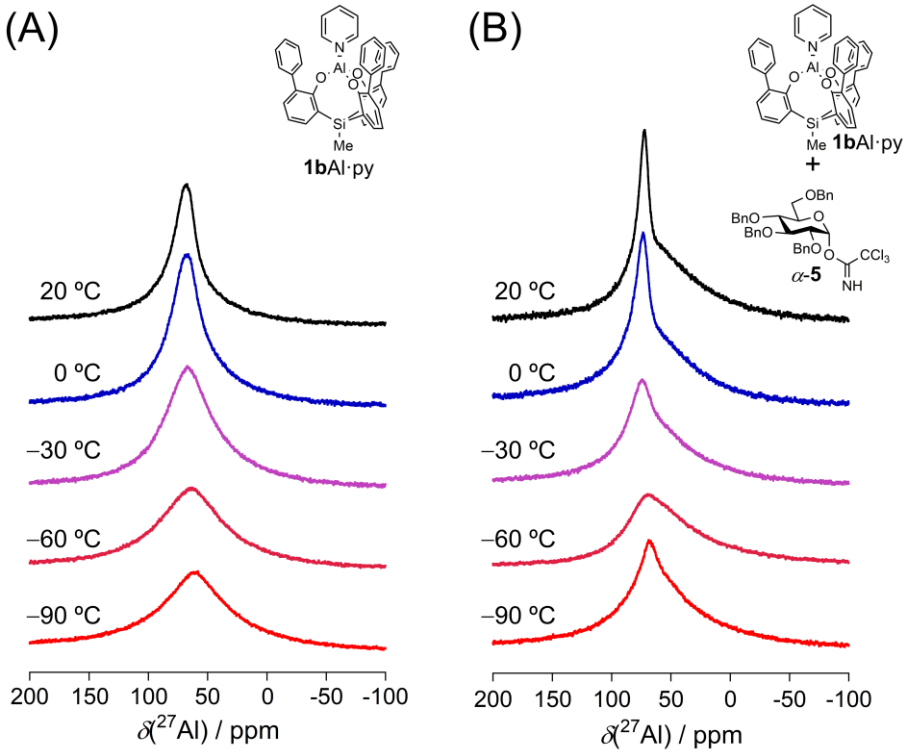

Figure S10. Variable temperature ^{27}Al NMR measurements (103 MHz, $AlCl_3$ in D_2O as an external standard) for (A) **1b**Al·py, and (B) **1b**Al·py with α-**5** in THF-d_8.

Table S14. Summary for NMR data for variable temperature ^{27}Al NMR measurements (103 MHz, $AlCl_3$ in D_2O as an external standard) for **1b**Al·py, and **1b**Al·py with α-**5** in THF-d_8.

T/ °C (THF-d_8)	**1b**Al·py δ(^{27}Al) / ppm	**1b**Al·py+α-**5** δ(^{27}Al) / ppm
20	67.39	72.32
0	66.53	73.48
–30	67.20	74.46
–60	64.33	69.58
–90	58.35	68.24

The steric hindrance around the aluminum center of **1b**Al·py inhibited the coordination of THF or α-**5** even at room temperature (Figure S10B).

Observation of reaction mixture of glycosylation via variable temperature ^{27}Al NMR measurements

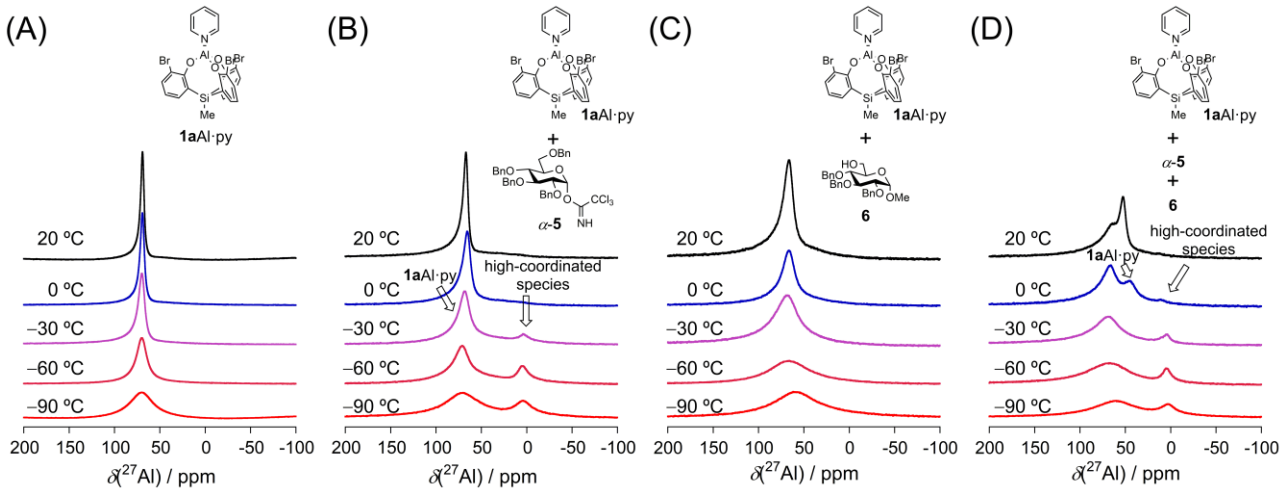

Figure S11. Variable temperature ^{27}Al NMR measurements (103 MHz, $AlCl_3$ in D_2O as an external standard) for (A) **1a**Al·py, (B) **1a**Al·py with α-**5**, (C) **1a**Al·py with **6**, and (D) reaction mixture (**1a**Al·py with α-**5** and **6**) in CD_2Cl_2.

Table S15. Summary for NMR data for variable temperature ^{27}Al NMR measurements (103 MHz, $AlCl_3$ in D_2O as an external standard) for **1a**Al·py, **1a**Al·py with α-**5**, **1a**Al·py with **6**, and reaction mixture (**1a**Al·py with α-**5** and **6**) in CD_2Cl_2.

T/ °C (CD_2Cl_2)	**1a**Al·py $\delta(^{27}Al)$ / ppm	**1a**Al·py+α-**5** $\delta(^{27}Al)$ / ppm	**1a**Al·py+**6** $\delta(^{27}Al)$ / ppm	**1a**Al·py+α-**5**+**6** $\delta(^{27}Al)$ / ppm
20	71.60	67.14	66.47	52.80
0	71.41	65.67	66.65	45.78, 10.44
–30	73.48	68.97, 4.15	68.24	4.15
–60	74.77	71.16, 4.88	66.65	4.40
–90	65.06	71.35, 4.09	59.45	3.17

Monitoring the reaction mixture of the glycosylation of α-**5** with **6** via ^{27}Al NMR measurement clearly indicated the selective activation of donor α-**5** with cage-shaped aluminum complex **1a**Al·py. Upon cooling, a gradual upfield shift of ^{27}Al signal of **1a**Al·py with α-**5** was observed, suggesting the generation of a high-coordinated aluminum species of **1a**Al·py with α-**5** (Figure S11B). However, the mixture of **1a**Al·py with **6** in CD_2Cl_2 gave no signal temperature dependency, indicating that the interaction of aluminum center with acceptor **6** was insignificant (Figure S11C). Furthermore, the reaction mixture including **1a**Al·py, α-**5**, and **6** exhibited the similar signal shift to that of the combination of **1a**Al·py with α-**5** (Figure S11D).

Observation of reaction mixture of glycosylation via ^{1}H NMR measurements

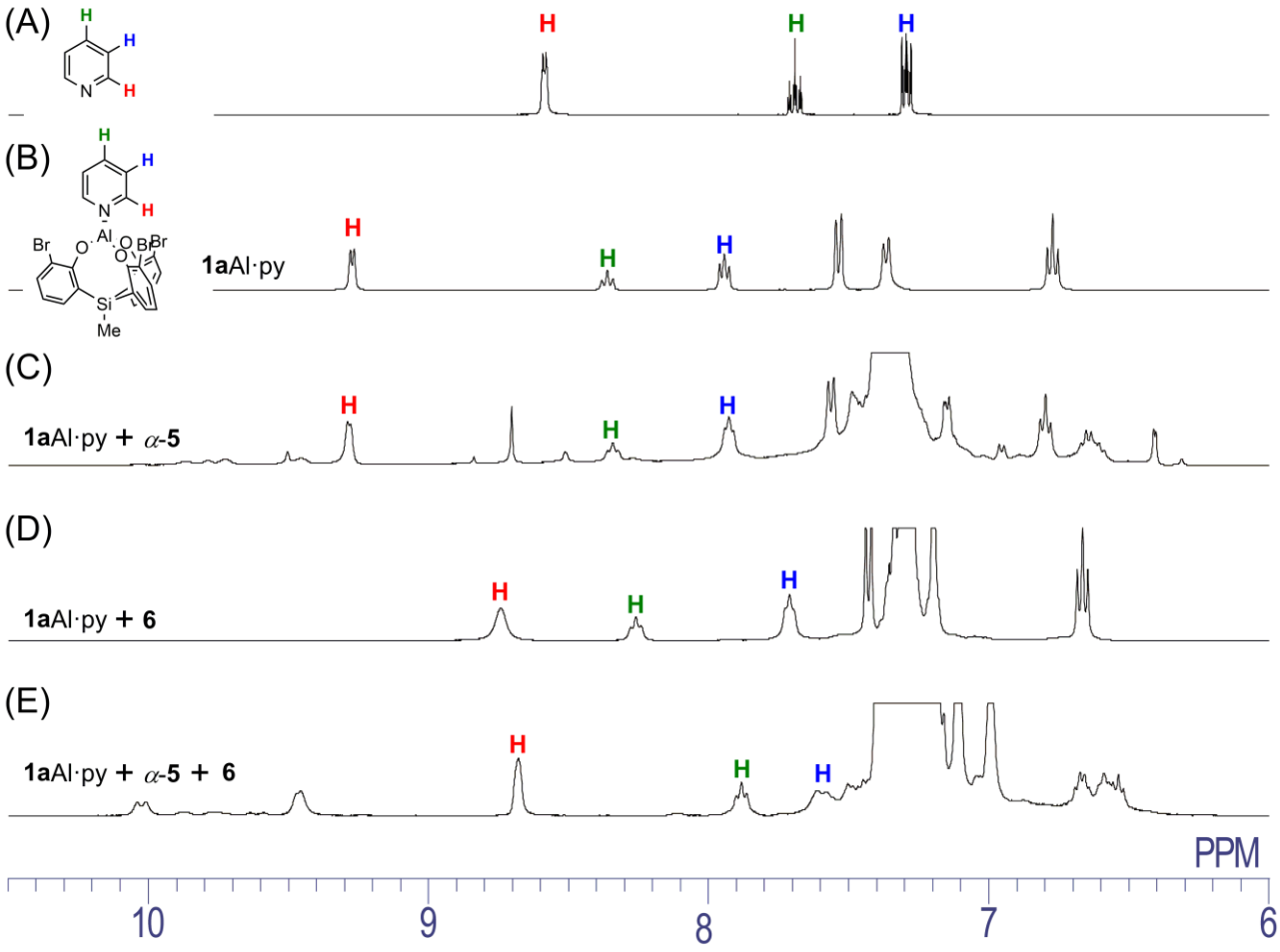

Figure S12. Partial ^{1}H NMR spectra (400 MHz, CD_2Cl_2) for (A) free pyridine (rt), (B) **1a**Al·py (–90 °C), (C) **1a**Al·py with α-**5** (–90 °C), (D) **1a**Al·py with **6** (–90 °C), and (E) reaction mixture (**1a**Al·py with α-**5** and **6**, –90 °C).

The proton signals of pyridine for **1a**Al·py were shifted downfield compared to those of free pyridine under all the conditions examined. These observations illustrate the preservation of coordination of pyridine to the aluminum center irrespective the presence or absence of glycosyl donor α-**5** or acceptor **6**.

Catalytic reactions using 1Al·py

Mukaiyama aldol reaction

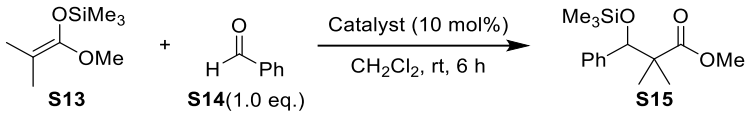

In a nitrogen-filled glove box, to the solution of dimethylketene methyl trimethylsilyl acetal **S13** (0.5 mmol) and benzaldehyde **S14** (0.5 mmol) in CH_2Cl_2 (2 mL) was added the isolated aluminum or borate catalyst (0.05 mmol) at room temperature. After stirring for 6 h at room temperature, $NaHCO_3$ aq (10 mL) was added to the mixture. The products were extracted with dichloromethane (3 x 10 mL). The organic layer was dried with $MgSO_4$ and evaporated to give a crude mixture, which was analyzed by NMR.

Table S16. Mukaiyama aldol reaction catalyzed by **1**Al or **1**B complexes.

entry	catalyst	yield of **S15** / %
1	**1a**Al·py	99
2	**1a**B·py	51
3	**1a**B·THF	99
4	**1b**Al·py	68
5	**1b**B·py	~0
6	**1b**B·THF	91

Addition of allyltributylstannane with benzaldehyde

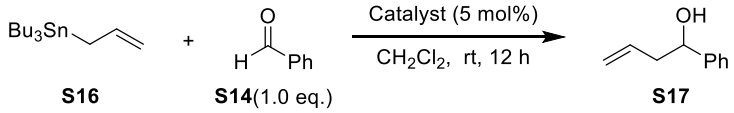

In a nitrogen-filled glove box, to the solution of the isolated aluminum or borate catalyst (0.025 mmol) in CH_2Cl_2 (2 mL) was added allyltributylstannane **S16** (0.5 mmol) and benzaldehyde **S14** (0.5 mmol) at room temperature. After stirring for 12 h at room temperature, NH_4F aq (10 mL) was added to the mixture. The products were extracted with dichloromethane (3 x 10 mL). The organic layer was dried with $MgSO_4$ and evaporated to give a crude mixture, which was analyzed by NMR.

Table S17. Addition of allyltributylstannane with benzaldehyde catalyzed by **1**Al or **1**B complexes.

entry	catalyst	yield of **S17**/ %
1	**1a**Al·py	84
2	**1a**B·py	~0
3	**1a**B·THF	21
4	**1b**Al·py	71
5	**1b**B·py	~0
6	**1b**B·THF	99

Cycloaddition of the Danishefsky's diene with benzaldehydes

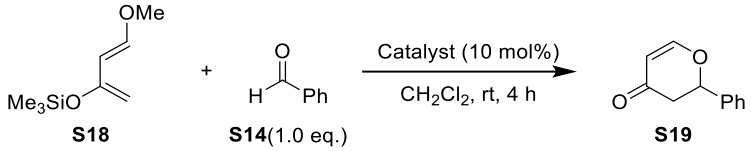

In a nitrogen-filled glove box, to the solution of the isolated aluminum or borate catalyst (0.05 mmol) in CH_2Cl_2 (2 mL) was added Danishefsky's diene **S18** (0.5 mmol) and benzaldehyde **S14** (0.5 mmol) at room temperature. After stirring for 4 h at room temperature, HCl aq (10 mL) was added to the mixture. The products were extracted with dichloromethane (3 x 10 mL). The organic layer was dried with $MgSO_4$ and evaporated to give a crude mixture, which was analyzed by NMR.

Table S18. Cycloaddition of the Danishefsky's diene with benzaldehyde catalyzed by **1**Al or **1**B complexes.

entry	catalyst	yield of **S19** / %
1	**1a**Al·py	62
2	**1a**B·py	39
3	**1a**B·THF	36
4	**1b**Al·py	81
5	**1b**B·py	2
6	**1b**B·THF	58

2-5. References

[1] M. Fujita, O. C. Lightbody, M. J. Ferguson, R. McDonald, J. M. Stryker, *J. Am. Chem. Soc.* **2009**, *131*, 4568–4569.

[2] S. G. Nelson, B.-K. Kim, T. J. Peelen, *J. Am. Chem. Soc.* **2000**, *122*, 9318–9319.

[3] N. Emig, H. Nguyen, H. Krautscheid, R. Réau, J.-B. Cazaux, G. Bertrand, *Organometallics* **1998**, *17*, 3599–3608.

[4] N. Emig, F. P. Gabbaï, H. Krautscheid, R. Réau, G. Bertrand, *Angew. Chem. Int. Ed.* **1998**, *37*, 989–992.

[5] F. Akagi, Y. Ishida, T. Matsuo, H. Kawaguchi, *Dalt. Trans.* **2011**, *40*, 2375.

[6] U. Verkerk, M. Fujita, T. L. Dzwiniel, R. McDonald, J. M. Stryker, *J. Am. Chem. Soc.* **2002**, *124*, 9988–9989.
[7] N. Emig, R. Réau, H. Krautscheid, D. Fenske, G. Bertrand, *J. Am. Chem. Soc.* **1996**, *118*, 5822–5823.
[8] T. Ooi, D. Uraguchi, N. Kagoshima, K. Maruoka, *J. Am. Chem. Soc.* **1998**, *120*, 5327–5328.
[9] T. Ooi, N. Kagoshima, K. Maruoka, *J. Am. Chem. Soc.* **1997**, *119*, 5754–5755.
[10] K. B. Simonsen, N. Svenstrup, M. Roberson, K. A. Jørgensen, *Chem. - A Eur. J.* **2000**, *6*, 123–128.
[11] D. P. Heller, D. R. Goldberg, W. D. Wulff, *J. Am. Chem. Soc.* **1997**, *119*, 10551–10552.
[12] P. O. Adero, H. Amarasekara, P. Wen, L. Bohé, D. Crich, *Chem. Rev.* **2018**, *118*, 8242–8284.
[13] S. van der Vorm, T. Hansen, H. S. Overkleeft, G. A. van der Marel, J. D. C. Codée, *Chem. Sci.* **2017**, *8*, 1867–1875.
[14] K. A. D'Angelo, M. S. Taylor, *J. Am. Chem. Soc.* **2016**, *138*, 11058–11066.
[15] J. C. Kendale, E. M. Valentín, K. A. Woerpel, *Org. Lett.* **2014**, *16*, 3684–3687.
[16] A. C. West, C. Schuerch, *J. Am. Chem. Soc.* **1973**, *95*, 1333–1335.
[17] M. Prévost, O. St-Jean, Y. Guindon, *J. Am. Chem. Soc.* **2010**, *132*, 12433–12439.
[18] D. Crich, S. Sun, *J. Org. Chem.* **1996**, *61*, 4506–4507.
[19] Y. Zhu, B. Yu, *Chem. - A Eur. J.* **2015**, *21*, 8771–8780.
[20] C. Gouliaras, D. Lee, L. Chan, M. S. Taylor, *J. Am. Chem. Soc.* **2011**, *133*, 13926–13929.
[21] J. P. Issa, C. S. Bennett, *J. Am. Chem. Soc.* **2014**, *136*, 5740–5744.
[22] P. Peng, R. R. Schmidt, *J. Am. Chem. Soc.* **2015**, *137*, 12653–12659.
[23] Y. Park, K. C. Harper, N. Kuhl, E. E. Kwan, R. Y. Liu, E. N. Jacobsen, *Science* **2017**, *355*, 162–166.
[24] P. Peng, R. R. Schmidt, *Acc. Chem. Res.* **2017**, *50*, 1171–1183.
[25] H. Yamamoto, Ed. , *Lewis Acids in Organic Synthesis*, Wiley-VCH, Weinheim, **2000**.
[26] M. D. Healy, M. R. Mason, P. W. Gravelle, S. G. Bott, A. R. Barron, *J. Chem. Soc. Dalt. Trans.* **1993**, 441.
[27] M. D. Healy, M. B. Power, A. R. Barron, **1994**, *130*, 63–135.
[28] K. Maruoka, Y. Araki, H. Yamamoto, *J. Am. Chem. Soc.* **1988**, *110*, 2650–2652.
[29] K. Maruoka, S. Saito, A. B. Concepcion, H. Yamamoto, *J. Am. Chem. Soc.* **1993**, *115*, 1183–1184.
[30] J. Pinkas, T. Wang, R. A. Jacobson, J. G. Verkade, *Inorg. Chem.* **1994**, *33*, 4202–4210.
[31] Y. Kim, J. G. Verkade, *Inorg. Chem.* **2003**, *42*, 4804–4806.
[32] W. Su, Y. Kim, A. Ellern, I. A. Guzei, J. G. Verkade, *J. Am. Chem. Soc.* **2006**, *128*, 13727–13735.
[33] S. M. Raders, J. G. Verkade, *J. Org. Chem.* **2009**, *74*, 5417–5428.
[34] J. Weil, R. T. Mathers, Y. D. Y. L. Getzler, *Macromolecules* **2012**, *45*, 1118–1121.
[35] S. H. Reisberg, H. J. Hurley, R. T. Mathers, J. M. Tanski, Y. D. Y. L. Getzler, *Macromolecules* **2013**, *46*, 3273–3279.
[36] T. Matsuo, H. Kawaguchi, *Chem. Lett.* **2004**, *33*, 640–645.
[37] W.-J. Su, L.-C. Liang, *Inorg. Chem.* **2018**, *57*, 553–556.
[38] M. Yasuda, S. Yoshioka, S. Yamasaki, T. Somyo, K. Chiba, A. Baba, *Org. Lett.* **2006**, *8*, 761–764.
[39] M. Yasuda, S. Yoshioka, H. Nakajima, K. Chiba, A. Baba, *Org. Lett.* **2008**, *10*, 929–932.
[40] A. Konishi, K. Nakaoka, H. Nakajima, K. Chiba, A. Baba, M. Yasuda, *Chem. - A Eur. J.* **2017**, *23*, 5219–5223.
[41] M. Yasuda, H. Nakajima, R. Takeda, S. Yoshioka, S. Yamasaki, K. Chiba, A. Baba, *Chem. - A Eur. J.* **2011**, *17*, 3856–3867.
[42] H. Nakajima, M. Yasuda, R. Takeda, A. Baba, *Angew. Chem. Int. Ed.* **2012**, *51*, 3867–3870.
[43] A. Konishi, R. Yasunaga, K. Chiba, M. Yasuda, *Chem. Commun.* **2016**, *52*, 3348–3351.
[44] A. Konishi, K. Nakaoka, H. Maruyama, H. Nakajima, T. Eguchi, A. Baba, M. Yasuda, *Chem. - A Eur. J.* **2017**, *23*, 1273–1277.
[45] A. C. Iii, D. Morales, J. L. Lecuivre, M. J. Scott, *Organometallics* **2002**, *21*, 418–428.
[46] A. Konishi, H. Nakajima, H. Maruyama, S. Yoshioka, A. Baba, M. Yasuda, *Polyhedron* **2017**, *125*, 130–134.
[47] S. Yoon, Y. Kim, J. G. Verkade, *Phosphorus. Sulfur. Silicon Relat. Elem.* **2014**, *189*, 1193–1206.
[48] M. Oishi, Y. Ichinose, N. Nomura, *Eur. J. Inorg. Chem.* **2016**, *2016*, 1596–1603.
[49] K. C. Nicolaou, S. A. Snyder, X. Huang, K. B. Simonsen, A. E. Koumbis, A. Bigot, *J. Am. Chem.*

Soc. **2004**, *126*, 10162–10173.
[50] S. D. Walker, T. E. Barder, J. R. Martinelli, S. L. Buchwald, *Angew. Chem. Int. Ed.* **2004**, *43*, 1871–1876.
[51] S. Toyota, M. Oki, *Bull. Chem. Soc. Jpn.* **1992**, *65*, 1832–1840.
[52] "The substrate scopes were summarized in Tables S3-S5," **n.d.**
[53] S. S. Nigudkar, K. J. Stine, A. V. Demchenko, *J. Am. Chem. Soc.* **2014**, *136*, 921–923.
[54] E. Juaristi, G. Cuevas, *Tetrahedron* **1992**, *48*, 5019–5087.
[55] D. B. G. Williams, S. B. Simelane, H. H. Kinfe, *Org. Biomol. Chem.* **2012**, *10*, 5636.
[56] S.-S. Weng, C.-L. Li, C.-S. Liao, T.-A. Chen, C.-C. Huang, K.-T. Hung, *J. Carbohydr. Chem.* **2010**, *29*, 429–440.
[57] H. Satoh, H. S. Hansen, S. Manabe, W. F. Van Gunsteren, P. H. Hu, C.- Zu, *J. Chem. Theory Comput*. **2010**, *6*, 1783–1797.
[58] R. Benn, E. Janssen, H. Lehmkuhl, A. Rufínska, *J. Organomet. Chem.* **1987**, *333*, 155–168.
[59] *CrystalStructure*, Rigaku Corporation, Tokyo, Japan, **2015**.
[60] B. A. Garcia, D. Y. Gin, *J. Am. Chem. Soc.* **2000**, *122*, 4269–4279.
[61] H. Chiba, S. Funasaka, T. Mukaiyama, *Bull. Chem. Soc. Jpn.* **2003**, *76*, 1629–1644.
[62] M. Koshiba, N. Suzuki, R. Arihara, T. Tsuda, H. Nambu, S. Nakamura, S. Hashimoto, *Chem. - An Asian J.* **2008**, *3*, 1664–1677.
[63] J. Y. Baek, B.-Y. Lee, M. G. Jo, K. S. Kim, *J. Am. Chem. Soc.* **2010**, *132*, 7229–7229.

Chapter 3
Synthesis and Catalytic Activity of Atrane-type Hard and Soft Lewis Superacids with a Silyl, Germyl, or Stannyl Cationic Center

3-1. Introduction

Lewis acids play an important role in all areas of chemistry.[1] Control of Lewis acidity determined by the type of central element and ligand is a central issue in making the most efficient and widespread use of an ideal Lewis acid.[2] Although a wide range of affinity for various substrates, from hard to soft Lewis basic substrates, have been sought, the coexistence of hard and soft Lewis acidities in the same central element is mostly difficult. The recent advances in hard and soft Lewis superacids (LSAs)[3,4] using heavier group 14 elements (Si, Ge, and Sn) have the potential to be a reasonable approach to solve this problem. As the rational design guide for hard and soft LSAs, the values of two ion affinities are frequently employed. Fluoride ion affinity (FIA)[5,6] is an ideal method to measure the scale of the hardness of Lewis acids. Lewis acids that have larger FIA values than monomeric SbF_5 in the gas phase are classified as LSAs.[3] On the other hand, hydride ion affinity (HIA)[7] is used to evaluate soft Lewis acidity. Lewis acids that exceed the HIA of $B(C_6F_5)_3$ are considered to be soft LSAs.[3] Lewis acids that meet these two criteria are categorized into hard and soft LSAs. Significant progress in this field has been achieved in recent years (Figure 1A). The Greb group reported bis(catecholato)silanes as the first neutral silicon-based hard LSAs[8–10] The same group also successfully synthesized bis(perchlorocatecholato)germane as a hard and soft LSA having a germanium center.[11,12] Driess *et al*. demonstrated facile access to pristine LSA, $Si(OTf)_4$, in which the OTf substituents work as excellent leaving groups and modulate reactivity towards hard and soft Lewis bases.[13] In these systems that activated a variety of substrates, the hard and soft Lewis acidities result from the formation of the highly coordinated Si and Ge centers. The importance of the highly coordinated group 14 centers[14–16] in organic synthesis has been extensively investigated, resulting in chemo-,[17] stereo-,[18,19] and regioselective[20] synthetic approaches. Despite the high synthetic utility of highly coordinated states, precise control of the coordination number of LSAs has scarcely been considered. There is still room for the active use of highly coordinated group 14 centers in the investigation of more efficient organic syntheses catalyzed by hard and soft LSAs.

In order to tame the high coordination states in LSAs, we designed atrane-type molecules **1**E^+ having a cationic group 14 center (Figure 1B). The high reactivity of the heavier group 14 cations,[21] which readily cleave various bonds such as C–F[22] and Si–H[23], could serve the potential development of efficient hard and soft LSAs. However, due to their poor stability against external environments, such as temperature and moisture, thermodynamic[24,25] or kinetic[26–29] stabilization is required for sufficient stability, which has hampered the catalytic utility except for silyl cations.[30] Our design employs the

atrane-type framework[31] and brings three benefits for the establishments of heavier group 14 cation-based LSAs: 1) stabilization of the cationic center by the intramolecularly transannular N–E (E = Si, Ge, or Sn) bond, 2) orientation of the coordinated site of the cationic center by blocking one of the two apical vacant orbitals of the N–E bond, and 3) facile tuning of steric and electronic factors by changing the aromatic ligands. Although few works to isolate cationic atrane-type molecules having a group 14 center were reported,[32–34] their use as hard and soft catalytic LSAs remains unexplored. Herein, we report the synthesis and catalytic activity of the atrane-type molecules **1**E^+ (E = Si, Ge, or Sn) with a cationic group 14 center (Figure 1B). The molecules **1**E^+ behave as hard and soft LSAs and display activity in a variety of Lewis acid-catalyzed transformations.

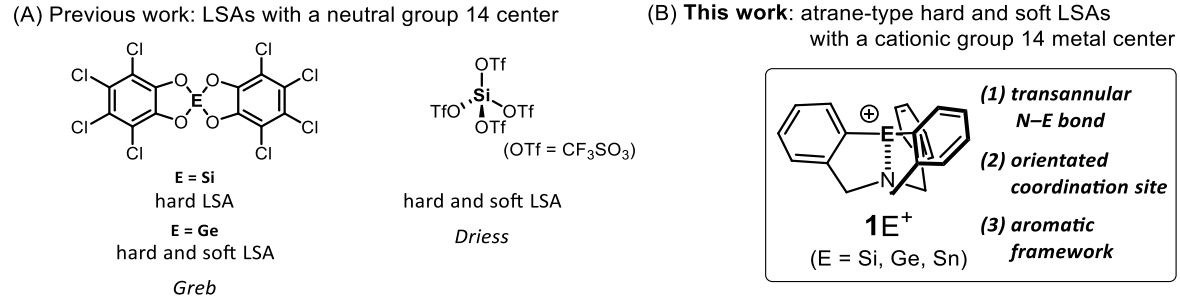

Figure 1. (A) Previously studied hard and soft LSAs having neutral group 14 centers. (B) Molecular structure of atrane-type LSAs having cationic group 14 centers is presented herein.

3-2. Results and Discussion

The synthetic route for **1**E^+ is summarized in Scheme 1. Preparation of tribenzylamine derivative **3** from commercially available *o*-bromobenzyl bromide **2**[35] and subsequent trilithiation followed by treatment with ECl_4 (E = Si, Ge, or Sn) afforded the atrane-type molecules **1**ECl in high yields. The treatment of **1**ECl with $SbCl_5$[36] in CH_3CN gave the desired cationic atrane molecules **1**E^+ as CH_3CN-adducts ([**1**E(CH_3CN)] [$SbCl_6$]). For the synthesis of **1**Si^+, the addition of $AgClO_4$ into **1**SiCl was also applicable, to yield [**1**Si][ClO_4]. The use of $AgClO_4$ was not suitable for the synthesis of **1**Ge^+ and **1**Sn^+, because inseparable side products were generated. When other silver salts, $AgBF_4$, $AgPF_6$, and $AgSbF_6$ were applied to the synthesis of **1**Si^+, the fluorinated atrane-type molecule **1**SiF was quantitatively obtained, indicating that the in situ generated cation **1**Si^+ abstracted a fluoride ion from the counterions because of its high FIA (see below).[8,12] The ^{29}Si NMR signals for **1**Si^+ ([**1**Si(CH_3CN)][$SbCl_6$], –53.9 ppm; [**1**Si(CH_3CN)][ClO_4], –53.8 ppm, in CD_3CN) are close to that of neutral **1**SiCl (–52.3 ppm), implying a strong electron donation from the nitrogen atom via the transannular N–Si bond and the coordination of a CH_3CN (or CD_3CN) molecule. The ^{119}Sn NMR signal of [**1**Sn(CH_3CN)][$SbCl_6$] (–59.3 ppm in CD_3CN) appeared at the range reported for five coordinated stannyl cations (–26.8[37] to –

76.3[25] ppm), indicating that the Sn center of [**1**Sn(CH$_3$CN)][SbCl$_6$] assumes a highly coordinated state in solution.

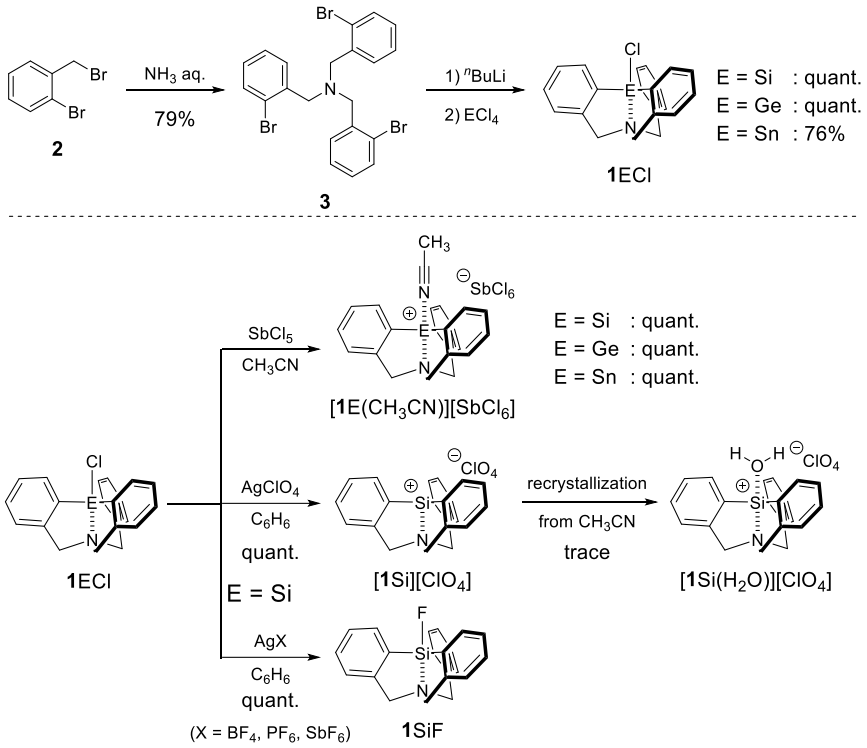

Scheme 1. Synthetic route for atrane-type molecules **1**E$^+$ bearing a cationic group 14 center.

The molecular geometries of [**1**E(solvent)]$^+$ were confirmed by X-ray crystallographic analysis. The ortep drawings are depicted in Figure 2. Recrystallization from a CH$_3$CN solution gave a single crystal of [**1**E][SbCl$_6$] as a CH$_3$CN-adduct ([**1**E(CH$_3$CN)]$^+$ [E = Si, Ge, or Sn]). Through the recrystallization of [**1**Si][ClO$_4$] from a CH$_3$CN solution, we surprisingly obtained a water adduct species ([**1**Si(H$_2$O)][ClO$_4$]) in a crystalline form.[38] When the recrystallization was performed even in a nitrogen-filled glovebox, the water-adduct was obtained. We believe that even trace amounts of moisture in the glovebox may be easily captured by the cationic species. Despite several attempts, the isolation of [**1**Si(H$_2$O)][ClO$_4$] remained in trace amounts, hampering other spectroscopic characterizations except for the X-ray analysis. Some geometric parameters are summarized in Table 1. All cations show an approximate C_3 symmetry and the average of the dihedral L–E–C^1–C^2 angles (φ) are small (~15°). This structural feature indicates that the positive charge communicates with the aromatic skeletons less and strongly localizes on the group 14 center. The group 14 center assumes a nearly trigonal-bipyramidal structure with a five coordination. The relatively short bond length of the N^1–E bond ([**1**Si(CH$_3$CN)][SbCl$_6$], 2.016 Å; [**1**Ge(CH$_3$CN)][SbCl$_6$], 2.091 Å; [**1**Sn(CH$_3$CN)][SbCl$_6$], 2.267 Å; [**1**Si(H$_2$O)][ClO$_4$], 2.110 Å) suggests the efficient transannular interaction at the apical position.

In the structures [**1**E][$SbCl_6$], the average of the C^{ip}–E–C^{ip} angle decreases in order from **1**Si^+ to **1**Ge^+ to **1**Sn^+ ([**1**Si(CH_3CN)][$SbCl_6$], 119.49°; [**1**Ge(CH_3CN)][$SbCl_6$], 119.24°; [**1**Sn(CH_3CN)][$SbCl_6$], 117.59°), which is induced by the difference in the elemental size. The larger elemental center leads to a longer N^1–E bond and lower planarity around the center.

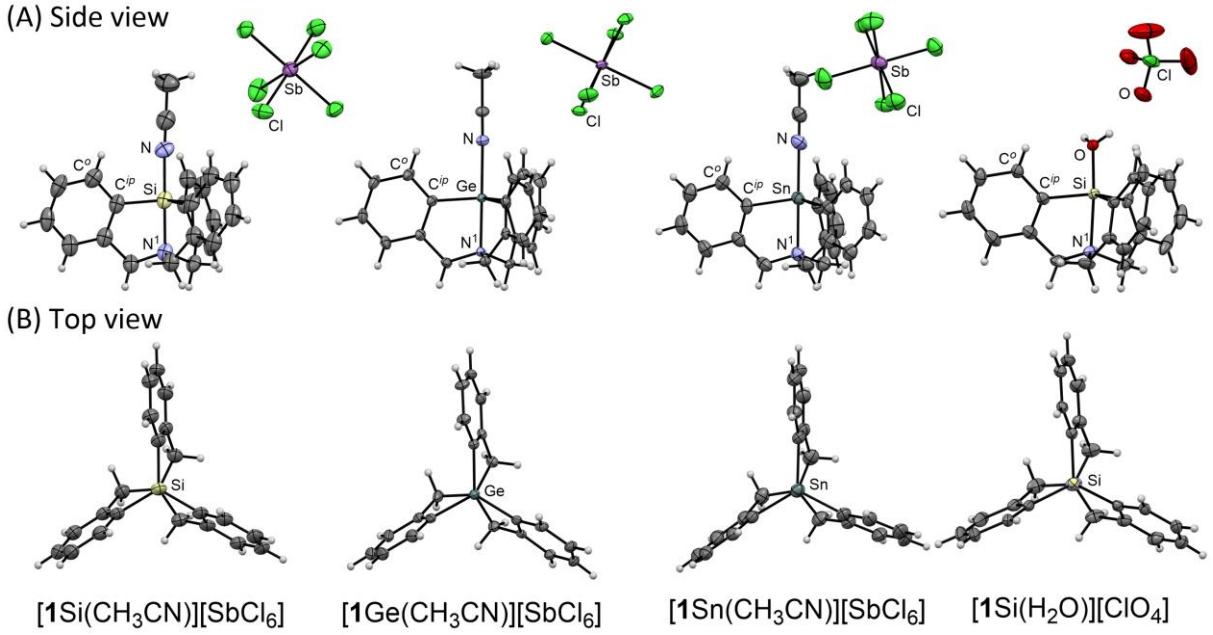

Figure 2. X-ray structures of atrane-type molecules **1**E^+. (A) Side and (B) top views. For top views, an adducted molecule, CH_3CN or H_2O, is omitted for clarity. Thermal ellipsoids are drawn at the 50% probability level.

Table 1. Summary of selected geometric parameters of atrane-type molecules **1**E^+.

	[**1**Si(CH_3CN)][$SbCl_6$]	[**1**Ge(CH_3CN)][$SbCl_6$]	[**1**Sn(CH_3CN)][$SbCl_6$]	[**1**Si(H_2O)][ClO_4]
φ(C^o–C^{ip}–E–L) / °[a]	15.16	14.81	12.06	14.05
N^1–E / Å	2.016(4)	2.091(2)	2.267(4)	2.110(14)
<(C^{ip}–E–C^{ip}) / °[a]	119.49(15)	119.24(11)	117.59(17)	118.43(7)

[a] Mean values.

In order to assess the characters of **1**E^+ with no adducts of solvents, we considered the Lewis acidity of **1**E^+ by quantum chemical calculations. The values of FIA and HIA were estimated according to the

reported method[13] (Table 2 and see Supporting Information). The gas phase FIAs of **1**E^+ were obviously larger than that of SbF_5, meeting the criteria for hard LSAs. Furthermore, the gas phase HIAs of **1**E^+ sharply exceeded the HIA of $B(C_6F_5)_3$, rendering these new compounds also soft LSAs. The orders of FIA (**1**Si^+ > **1**Ge^+ ≈ **1**Sn^+) and HIA (**1**Si^+ < **1**Ge^+ < **1**Sn^+) are reversed, and this is reflected by the difference in atomic sizes (Si < Ge < Sn). Where **1**Si^+, with the smallest elemental center exhibits the largest FIA (hardest Lewis acidity), **1**Sn^+ with the largest elemental center shows the largest HIA values (softest Lewis acidity). Using both criteria, **1**Ge^+ is located between **1**Si^+ and **1**Sn^+. It should be noted that both the gas phase FIAs and HIAs of **1**E^+ are much larger (> 200 kJ/mol) than those of the previously reported neutral Lewis acids. The distinct duality of hardness and softness is derived from the presence of a positive charge on the group 14 center of **1**E^+. The localized positive charge of **1**E^+ should be significantly affected by solvation. The effect of solvation in CH_2Cl_2 on the FIAs/HIAs were also evaluated (parenthesis values in Table 2). The large damping of FIAs/HIAs of **1**E^+ was revealed, and the corrected FIAs/HIAs of **1**E^+ are reduced to a lever comparable to the reported neutral Lewis acids. Similar damping upon solvation was also reported in other hard and soft LSAs.[13]

Table 2. DFT-calculated ion affinities (fluoride: FIA, hydride: HIA) for selected Lewis acids (LA) in $kJmol^{-1}$.[a]

Lewis acid	FIA (FIA_{sol})[b] LA/LA–F^-	HIA (HIA_{sol})[b] LA/LA–H^-
1Si^+	762 (303)	754 (264)
1Ge^+	710 (252)	764 (273)
1Sn^+	713 (255)	783 (289)
$Si(cat^{Cl})_2$	507[8][c] 495 (283)[13]	– 491 (251)[13]
$Si(OTf)_4$[13]	521 (305)	547 (306)
SbF_5[13]	500 (338)	–
$B(C_6F_5)_3$[13]	443 (227)	514 (268)

[a] PW6B95-D3BJ/def2-QZVPP//B3LYP-D3BJ/def2-SVP. [b] B3LYP-D3BJ/def2-SVP, gas phase geometries with CPCM in CH_2Cl_2. [c] DLPNO-CCSD(T)/cc-aug-pVQZ//PW6B95-D3(BJ)/def2-TZVPP.[8]

The experimental evaluation of the Lewis acidity of atrane-type cationic group 14 species was also performed. Subjecting [**1**Si][ClO_4] in $CDCl_3$ to $Et_3P{=}O$ provided an estimate of Lewis acidity (Gutmann-Beckett method).[39,40] After the addition of phosphine oxide to the solution of the silyl cation [**1**Si][ClO_4], the acceptor number (AN) was determined by the ^{31}P NMR chemical shift difference ($\Delta\delta^{31}P$) between the free phosphine oxide and the formed adduct of **1**Si^+ with $Et_3P{=}O$.[41] The estimated AN of [**1**Si][ClO_4] (AN = 85.3) is in the same range as the reported Lewis acids, $B(C_6F_5)_3$ (AN = 81.8)[42], BF_3 (AN = 84.0),[43] and smaller than that of the silyl cation [Et_3Si][$B(C_6F_5)_4$] (AN = 105.2).[44] Unfortunately, the evaluation of Lewis acidity for hexachloro antimonate salts ([**1**Si(CH_3CN)][$SbCl_6$], [**1**Ge(CH_3CN)][$SbCl_6$], and [**1**Sn(CH_3CN)][$SbCl_6$]) was unsuccessful because those cations gradually decomposed after the addition of phosphine oxide. We also attempted to compare the C≡N bond stretching modes of [**1**E(CH_3CN)][$SbCl_6$], but the undesired intermolecular interactions of the coordinated CH_3CN with lattice solvents and/or counterion hampered the quantitative evaluations. Alternatively, the DFT calculation provides insight into the LUMO orbitals of **1**E^+. The calculated LUMOs of **1**E^+ at the B3LYP/6-31G** for C, H, and N and LANL2DZ for Si, Ge, and Sn are shown in Figure 3. The vacant p-type orbital is mainly localized on the group 14 center, correlating with the structural features observed in the crystallographic analysis. The LUMO level decreases (**1**Si^+, –0.15 eV; **1**Ge^+, –0.17 eV; **1**Sn^+, –0.20 eV) with increasing elemental size and N^1–E bond length. This trend can be explained by the strength of the interaction between the group 14 center and the nitrogen atom. For quantitative information on the bonding N^1–E interaction, a natural bond orbital (NBO) analysis was conducted. The NBO charges and Wiberg bond indices (WBI) obtained (Figure 3 and Table S5) reveal that the positive charge mainly localizes on the group 14 center rather than the N^1 atom and the bond length of the N^1–E bond increases in the order from Si to Ge to Sn. These results provide strong support that the cations are readily stabilized by the coordination of solvents as the observation from the NMR and X-ray analyses.

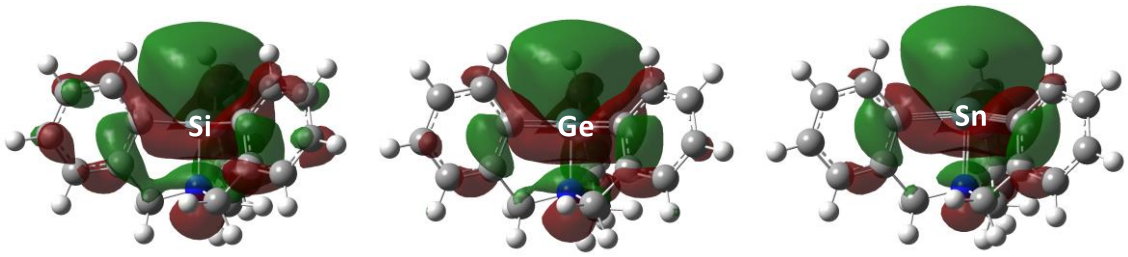

	1Si^+	**1**Ge^+	**1**Sn^+
LUMO [eV]	–0.15	–0.17	–0.20
WBI (N^1-E)	0.416	0.384	0.311

Figure 3. LUMO orbitals and WBIs of **1**E$^+$ calculated by the B3LYP/6-31G** for C, H and N and LANL2DZ for Si, Ge and Sn.

The utility in Lewis acid catalyst for our hard and soft LSAs **1**E$^+$ was probed. The harmony of extreme hardness and softness of **1**E$^+$ readily activates a wide range of substrates as a LSA catalyst. The investigated catalytic activities of the atrane-type cations **1**E$^+$ and **1**E(CH$_3$CN)$^+$ are summarized in Table 3. First, the hydrodefluorination of an aliphatic C–F bond was catalytically achieved for 1-adamantyl fluoride **4** in CH_2Cl_2 (reaction A in Table 3). [**1**Si][ClO_4] afforded the product **5** in the highest yield (92%) compared to the other cation salts of $SbCl_6^-$. When [**1**E(CH$_3$CN)][$SbCl_6$] was employed, GC-MS monitoring indicated the formation of adamantyl chloride as a side product. Under the reaction conditions, $SbCl_6^-$ would work as a chlorination source, which lowers the catalytic activities of [**1**E(CH$_3$CN)][$SbCl_6$]. The fluorination of the solvent or the chlorination of the catalyst were not observed.

In contrast, the Friedel-Crafts dimerization of 1,1-diphenylethylene **6** was catalyzed effectively by [**1**E(CH$_3$CN)][$SbCl_6$], whereas [**1**Si][ClO_4] did not afford the product **7** (reaction B). In the catalytic cycle, [**1**E(CH$_3$CN)][$SbCl_6$] can reproduce the active cationic species **1**E$^+$ more effectively than [**1**Si][ClO_4], presumably because of the weaker coordination of $SbCl_6^-$ compared to that of ClO_4^-. To confirm the affinity toward alkyne substrates, the cyclization of propargylamide **8** was conducted (reaction C). All cations **1**E$^+$ and **1**E(CH$_3$CN)$^+$ gave the cyclic compound **9** even though substrate **8** has a coordinating amide group. Hard Lewis acids are readily coordinated by harder Lewis basic moieties, which inhibits the interaction with softer Lewis basic moieties. Notably, the rigid structures of **1**E$^+$ around the group 14 center given by the atrane framework help to activate the alkyne moiety of **8** without any deactivation by a strong interaction with the amide moiety. [**1**Sn(CH$_3$CN)][$SbCl_6$] exhibited the highest catalytic activity because of the softness of the Sn center in comparison to the Si and Ge centers.[45] Furthermore, all cations were further applicable to the cyclization reaction of the other alkyne **10** for the synthesis of isocoumarin **11** even though substrate **10** has an acidic proton (reaction D). There are no reported heavier group 14 species to catalyze alkyne cyclization reactions. Our results demonstrate the catalytic utility of **1**E$^+$ having a cationic group 14 center stabilized by the atrane framework.

Table 3. Catalytic applications of our atrane-type molecules **1**E^+ and **1**$E(CH_3CN)^+$.

(A) Hydrodefluorination of **4**

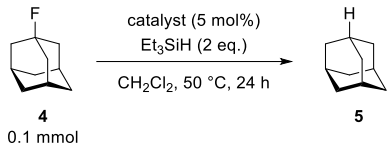

4
0.1 mmol

5

(B) Friedel-Crafts dimerization of **6**

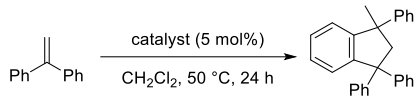

6
0.1 mmol

7

(C) Cyclization reaction of alkyne **8**

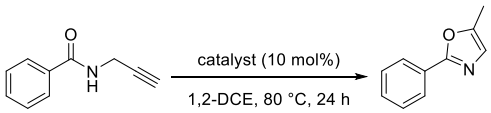

8
0.2 mmol

9

(D) Cyclization reaction of alkyne **10**

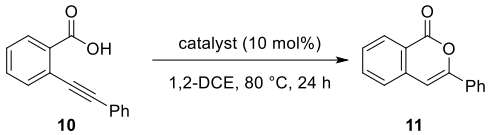

10
0.2 mmol

11

reaction	catalyst			
	[**1**Si(CH_3CN)][$SbCl_6$]	[**1**Ge(CH_3CN)][$SbCl_6$]	[**1**Sn(CH_3CN)][$SbCl_6$]	[**1**Si][ClO_4]
A yield of **5** [%]	44	25	19	92
B yield of **7** [%]	82	59	43	trace
C yield of **9** [%]	46	44	77	85
D yield of **11** [%]	89	91	99	89

The effect of the atrane structure of **1**E$^+$ on its catalytic activity was clearly represented in the carbonyl reduction of 4-(trifluoromethyl)benzaldehyde **12** with triethylsilane (Table 4). In the catalytic system of [**1**Si][ClO_4], product **13** was easily obtained without any cleavage of the C–F bond (entry 1). The other atrane-type cations [**1**E(CH_3CN)][$SbCl_6$] also gave product **13** in high yield (Table S4). On the other hand, the activation of Et_3SiH with [Ph_3C][$B(C_6F_5)_4$][22,46–48], in which some cationic silyl species are in-situ generated but their cationic characters are far from a 'true silyl cation',[49] showed inferior catalytic activity (entry 2). A number of unidentified side products were generated and confirmed by NMR measurement. The atrane framework of **1**E$^+$ dramatically improves the catalytic activities of the cationic group 14 center.

Table 4. Difference of catalytic activity between [**1**Si][ClO_4] and Et_3SiH/[Ph_3C][$B(C_6F_5)_4$].

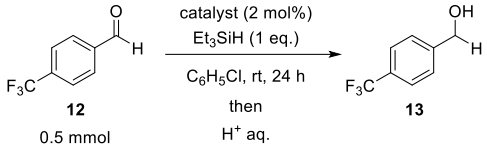

entry	catalyst	yield of **13** [%]
1	[**1**Si][ClO_4]	100
2	[Ph_3C][$B(C_6F_5)_4$]	48

Judging from the features of **1**E$^+$ concerning Lewis acidity and reactivity, [**1**Si][ClO_4], which has a more stable counter anion under the reaction conditions, is the most tolerant salt. Thus, we applied the silyl cation [**1**Si][ClO_4] to a competitive reaction of silyl enol ether **14** with a mixture of benzaldehyde dimethyl acetal **15** and benzaldehyde **16** (Table 5). Interestingly, a significant solvent dependency was observed. In THF, acetal **15** reacted with **14** prior to aldehyde **16** in a highly selective manner (**17**/**18** = 99/1, entry 1). On the other hand, upon changing the solvent to toluene, the selectivity was completely reversed, giving the product **18** (**17**/**18** = 11/89, entry 2). Other Lewis acids were also investigated (entries 3–10). The Si-based Lewis acids, Me_3SiClO_4[50] and Me_3SiOTf, exhibited a similar solvent dependency to that of [**1**Si][ClO_4], but the selectivity towards **17**/**18** was lower (entries 3–6). The B-based Lewis acids, $B(C_6F_5)_3$ and $BF_3{\cdot}OEt_2$, showed no solvent dependence (entries 7–10). The observed selectivity of **1**Si$^+$ would be derived from the difference in the interaction of the Si$^+$ center with the substrate. For the activation of the acetal **15** with **1**Si$^+$, a cationic oxonium-type intermediate is generated by the elimination of one methoxy group. The process, assisted by **1**Si$^+$, would be accelerated in a high polar solvent, resulting in the highly selective formation of **17** in THF. In contrast, in a low polar solvent, the interaction of the carbonyl group of **16** with **1**Si$^+$ would take precedence over the activation of **15**.

In addition to the coexistence of the hardness and softness of Lewis acidity, the localized cationic nature of **1**Si$^+$ allowed for sensitive recognition of the substrates depending on the polarity of the solvent. The observed result is the first example of a switch in the selectivity in the competitive reaction between acetal and aldehyde. Notably, this chemoselectivity is the result of a concentrated effect of the structural and electronic features of our hard and soft LSAs.

Table 5. Competitive reactions of silyl enol ether **14** with a mixture of benzaldehyde dimethyl acetal **15** and benzaldehyde **16** catalyzed by [**1**Si][ClO_4].

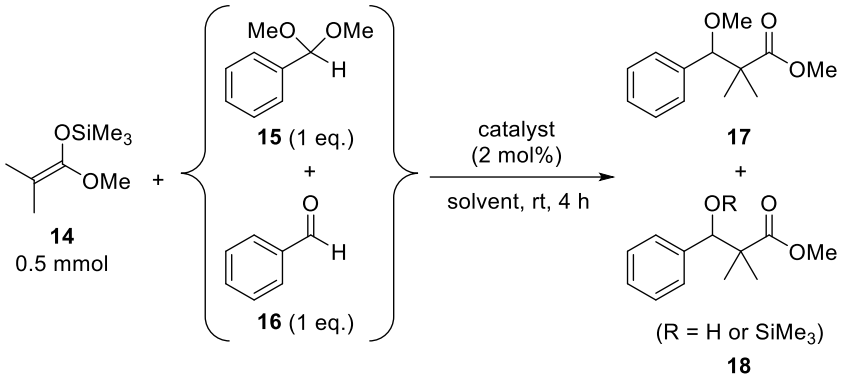

entry	catalyst	solvent	yield of **17** [%]	yield of **18** [%]	Ratio of **17**/**18**
1	[**1**Si][ClO_4]	THF	94	1	99/1
2		toluene	11	89	11/89
3	Me_3SiClO_4	THF	83	4	95/5
4		toluene	21	62	25/75
5	Me_3SiOTf	THF	64	30	68/32
6		toluene	15	77	16/84
7	$B(C_6F_5)_3$	THF	40	59	40/60
8		toluene	6	88	6/94
9	$BF_3{\cdot}OEt_2$	THF	0	11	–
10		toluene	0	18	–

3-3. Conclusion

We successfully synthesized the atrane-type group 14 cations **1**E^+ (E = Si, Ge, or Sn) in only three steps. The atrane structure of **1**E^+ stabilized a localized positive charge on the group 14 center, introducing hard and soft Lewis superacidity. The robustness of **1**E^+ allowed handling under standard experimental conditions, which served as a versatile Lewis acid catalyst. Various reactions, including hydrodefluorination, the Friedel-Crafts reaction, alkyne cyclization, and carbonyl reduction, were efficiently catalyzed by **1**E^+. The rigid atrane framework assisted the formation of the highly coordinated states, resulting in the catalytic activities of **1**E^+. The high sensitivity of the localized positive charge of the **1**Si^+ center to solvent polarity demonstrated unique chemoselectivity.

The design concept that employs the atrane-type framework to stabilize a highly reactive cationic metal provides a new strategy to propose highly reactive species as stable catalysts with hard and soft Lewis superacidities. Further study expanding the catalytic utility of hard and soft LSAs having a cationic metal center are ongoing in our group.

3-4. Experimental Section

General

NMR spectra were recorded on JEOL-AL400 and JEOL-ECS400 spectrometers (400 MHz for ^{1}H, and 100 MHz for ^{13}C) with TMS as an internal standard. ^{1}H and ^{13}C NMR signals of compounds were assigned using HMQC, HSQC, HMBC, COSY, NOESY, and ^{13}C off-resonance techniques. Positive and negative FAB and EI mass spectra were recorded on a JEOL JMS-700 and Shimadzu GCMS-QP2010 Ultra, respectively. High-resolution mass spectra were obtained by magnetic sector type mass spectrometer. The high resolution ESI mass spectra were analyzed by using a JEOL JMS-T100LP. IR spectra were recorded as thin films or as solids in KBr pellets on a JASCO FT/IR 6200 spectrophotometer.

Data collection for X-ray crystal analysis was performed on Rigaku/XtaLAB Synergy-S/Mo (MoK_α λ = 0.71075 Å), and Rigaku/XtaLAB Synergy-S/Cu (CuK_α λ = 1.54187 Å) diffractometers. All calculations were performed with the observed reflections [$I>2\sigma(I)$] by the Olex2 program.[51] All non-hydrogen atoms were refined with anisotropic displacement parameters and hydrogen atoms were placed at calculated positions and refined "riding" on their corresponding carbon atoms.

Materials

Anhydrous dichloromethane, 1,1-dichloroethane, benzene, THF, acetonitrile, diethylether, toluene and hexane were purchased and used as obtained. All reagents were obtained from commercial suppliers and used as received. All reactions were carried out under nitrogen. Tris(2-bromobenzyl)amine **3**[35] was prepared by the reported procedures. The products of the reactions, **7**, **9**,[52] **11**,[53] **13**,[54][55] **17**[56] and

18[57] were known in literatures.

Synthetic procedures

Synthesis of atrane-type derivatives 1ECl (E = Si, Ge, Sn)

*General procedure for the synthesis of atrane-type derivatives **1**ECl (E = Si or Sn)*

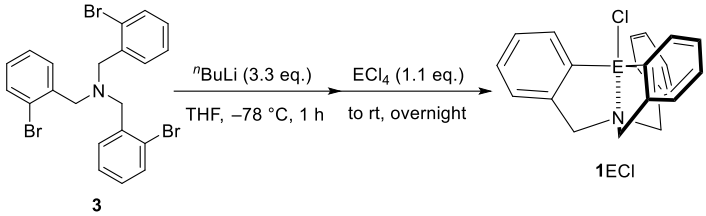

Under N_2 atmosphere, ^{n}BuLi (1.6 M in hexane, 41.3 mL, 66.0 mmol) was titrated to a solution of tris(2-bromobenzyl)amine **3**[35] (10.5 g, 20.0 mmol) in THF (120 mL) at –78 °C and stirred for 1 hour. After dropwisely adding ECl_4 (22.0 mmol) into the reaction mixture, the reaction temperature was allowed to warm up to room temperature. The reaction mixture was quenched by methanol and the solvents were removed under vacuum to give the crude product. Washing the product with methanol afforded the pure product **1**ECl as a colorless solid.

12-chloro-7,12-dihydro-5*H*-12,6-([1,2]benzenomethano)dibenzo[*c*,*f*][1,5]azasilocine 1SiCl

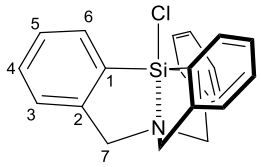

yield quant.; mp >300 °C; IR (KBr) ν = 3060 (m), 2922 (m), 1592 (m), 1441 (s), 1353 (s), 1234 (s), 1127 (s), 1067 (s), 968 (s), 828 (s), 726 (s) cm^{-1}; ^{1}H NMR (400 MHz, $CDCl_3$) 8.39 (dd, J = 7.4, 1.6 Hz, 3H, 6-H), 7.37 (td, J = 7.4, 1.2 Hz, 3H, 5-H), 7.33 (td, J = 7.8, 1.6 Hz, 3H, 4-H), 7.11 (d, J = 6.8 Hz, 3H, 3-H), 4.02 (s, 6H, 7-H); ^{13}C NMR (100 MHz, $CDCl_3$) 143.29 (s, C-2), 138.13 (d, C-6), 134.25 (s, C-1), 130.13 (d, C-4), 128.22 (d, C-5), 124.18 (d, C-3), 57.88 (t, C-7); ^{29}Si{^{1}H} NMR (78.5 MHz, $CDCl_3$, Me_4Si in $CDCl_3$ as an external standard) –52.3; MS (EI$^+$, 70 eV) m/z 349 ([M+2]$^+$, 10), 347 (M$^+$, 27), 312 (17), 256 (100), 229 (11), 165 (17); HRMS (EI$^+$, 70 eV) Calculated ($C_{21}H_{18}ClNSi$): 347.0897 (M$^+$), Found: 347.0890 (M$^+$); Analysis $C_{21}H_{18}ClNSi$ (347.9170), Calculated: C, 72.50; H, 5.22; Cl, 10.19; N, 4.03; Si, 8.07, Found: C, 72.59; H, 5.17; N 4.11.

12-chloro-7,12-dihydro-5*H*-12,6-([1,2]benzenomethano)dibenzo[*c*,*f*][1,5]azastannocine 1SnCl

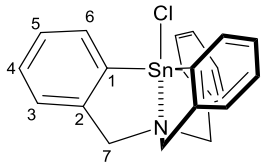

yield 76%; mp 226.0–226.2 °C; IR (KBr) ν = 3058 (m), 2909 (m), 1436 (s), 1354 (w), 1261 (w), 1193 (m), 1099 (m), 964 (m), 819 (w), 753 (s) cm^{-1}; ^1H NMR (400 MHz, $CDCl_3$) 7.98 (dd, J = 7.2, 1.6 Hz, 3H, 6-H), 7.37 (td, J = 7.4, 1.2 Hz, 3H, 5-H), 7.30 (td, J = 7.4, 1.6 Hz, 3H, 4-H), 7.14 (d, J = 8.0 Hz, 3H, 3-H), 4.03 (s, 6H, 7-H); ^{13}C NMR (100 MHz, $CDCl_3$) 142.61 (s, C-2), 137.07 (s, C-1), 136.17 (d, C-6), 129.58 (d, C-4), 128.64 (d, C-5), 126.08 (d, C-3), 58.24 (t, C-7); $^{119}Sn\{^1H\}$ NMR (147.5 MHz, $CDCl_3$, Me_4Sn in $CDCl_3$ as an external standard) –81.7; MS (EI^+, 70 eV) m/z 441 ($[M+2]^+$, 6), 439 (M^+, 16), 437 ($[M–2]^+$, 14), 404 (18), 348 (100), 284 (85), 178 (68); HRMS (EI^+, 70 eV) Calculated ($C_{21}H_{18}ClNSn$): 439.0150 (M^+), Found: 439.0145 (M^+).

12-chloro-7,12-dihydro-5*H*-12,6-([1,2]benzenomethano)dibenzo[*c*,*f*][1,5]azagermocine 1GeCl

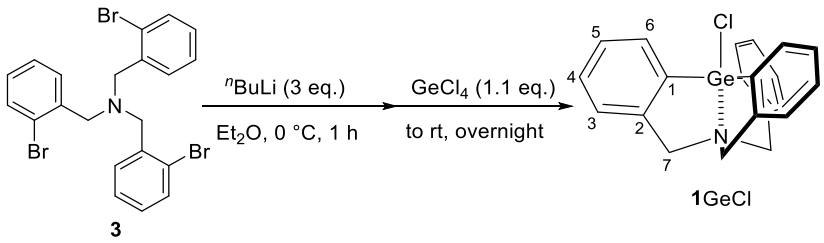

Under N_2 atmosphere, ^{n}BuLi (1.6 M in hexane, 3.75 mL, 6.0 mmol) was titrated to a solution of tris(2-bromobenzyl)amine **3**[35] (1.05 g, 2.0 mmol) in Et_2O (35 mL) at 0 °C and stirred for 1 hour. After dropwisely adding tetrachlorogermane (0.43 g, 2.0 mmol) into the reaction mixture, the reaction temperature was allowed to warm up to room temperature. The reaction mixture was quenched by methanol and the solvents were removed under vacuum to give the crude product. Washing the product with methanol afforded the pure product **1**GeCl as a colorless solid quantitatively (0.79 g, quant.).

mp 239.2–239.8 °C; IR (KBr) ν = 3056 (w), 2913 (w), 1440 (s), 1353 (w), 1259 (w), 1107 (w), 969 (w), 823 (w), 754 (s) cm^{-1}; ^1H NMR (400 MHz, $CDCl_3$) 8.31 (d, J = 7.2 Hz, 3H, 6-H), 7.39 (t, J = 7.4 Hz, 3H, 5-H), 7.33 (td, J = 7.4, 1.6 Hz, 3H, 4-H), 7.14 (d, J = 7.6 Hz, 3H, 3-H), 4.04 (s, 6H, 7-H); ^{13}C NMR (100 MHz, $CDCl_3$) 141.69 (s, C-2), 135.30 (d, C-6), 135.26 (s, C-1), 129.86 (d, C-4), 128.55 (d, C-5), 125.12 (d, C-3), 57.20 (t, C-7); MS (EI^+, 70 eV) m/z 395 ($[M+2]^+$, 11), 393 (M^+, 25), 358 (33), 302 (100), 265 (10), 178 (15), 165 (25); HRMS (EI^+, 70 eV) Calculated ($C_{21}H_{18}ClNGe$): 393.0340 (M^+), Found: 393.0337 (M^+).

*General procedure for the synthesis of atrane-type derivative [**1**E(CH₃CN)][SbCl₆]*

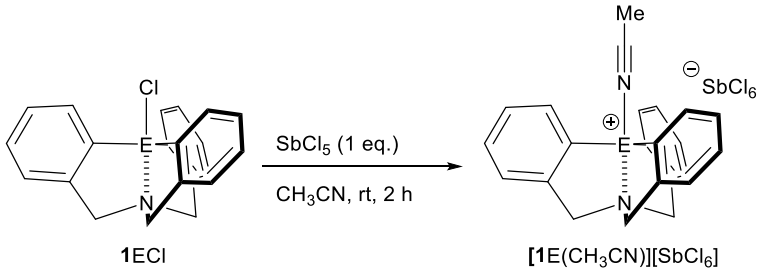

1ECl [**1**E(CH₃CN)][SbCl₆]

In a glove box, to a solution of **1**ECl (0.50 mmol) in acetnitrile (6 mL) was added pentachloroantimony (164.5 mg, 0.50 mmol) at room temperature. The reaction mixture was stirred at room temperature for 2 h. After stirring, the volatiles were evaporated and the residue was washed with hexane (3 x 5 mL). The obtained residue was dried under reduced pressure to quantitatively give the product [**1**E(CH₃CN)][SbCl₆] as a white solid. For X-ray analysis, recrystallization from a CH₃CN solution afforded a single crystal of [**1**E(CH₃CN)][SbCl₆] as a CH₃CN adduct.

5*H*-12,6-([1,2]benzenomethano)dibenzo[*c*,*f*][1,5]azasilocin-12(7*H*)-ylium hexachlorostibate(V)

[**1**Si(CH₃CN)][SbCl₆]

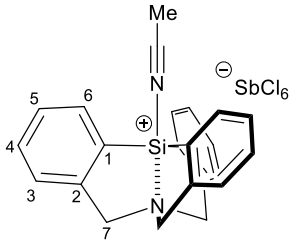

yield quant.; mp 225.2–225.5 °C; IR (KBr) ν = 3059 (w), 2925 (m), 2316 (s), 2288 (s), 1594 (m), 1442 (s), 1369 (w), 1240 (m), 1135 (m), 1073 (m), 964 (m), 829 (w), 759 (s) cm^{-1}; ^{1}H NMR (400 MHz, CD₃CN) 7.99 (d, J = 8.0 Hz, 3H, 6-H), 7.52 (td, J = 7.2, 1.6 Hz, 3H, 4-H), 7.46 (t, J = 8.0 Hz, 3H, 5-H), 7.32 (d, J = 7.2 Hz, 3H, 3-H), 4.24 (s, 6H, 7-H); ^{13}C NMR: (100 MHz, CD₃CN) 145.17 (s, C-2), 135.66 (d, C-6), 132.75 (d, C-4), 129.62 (d, C-5), 128.45 (s, C-1), 126.36 (d, C-3), 59.35 (t, C-7); ^{29}Si{^{1}H} NMR (78.5 MHz, CD₃CN, Me₄Si in CDCl₃ as an external standard) –53.9; HRMS (ESI) Calculated ($C_{23}H_{21}N_2Si$): 353.14685 ([M(CH₃CN)]$^+$), ($C_{21}H_{18}NSi$): 312.12030 (M$^+$), Found: 353.14518, 312.11896.

5*H*-12,6-([1,2]benzenomethano)dibenzo[*c*,*f*][1,5]azagermocin-12(7*H*)-ylium hexachlorostibate(V)

[**1**Ge(CH_3CN)][$SbCl_6$]

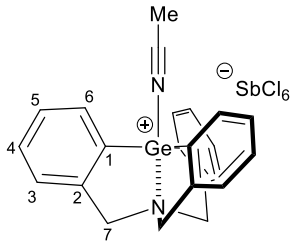

yield quant.; mp 185.2–185.5 °C; IR (KBr) ν = 3057 (m), 2927 (m), 2305 (m), 2277 (m), 1610 (m), 1442 (s), 1297 (w), 1199 (w), 965 (w), 824 (w), 758 (s) cm^{-1}; ^1H NMR (400 MHz, CD_3CN) 7.97 (dd, J = 7.0, 1.6 Hz, 3H, 6-H), 7.51 (td, J = 7.6, 1.6Hz, 3H, 4-H), 7.48 (td, J = 7.6, 1.6 Hz, 3H, 5-H), 7.35 (dd, J = 7.2, 1.6 Hz, 3H, 3-H), 4.28 (s, 6H, 7-H); ^{13}C NMR: (100 MHz, CD_3CN) 143.24 (s, C-2), 133.72 (d, C-6), 132.36 (d, C-4), 130.26 (s, C-1), 130.05 (d, C-5), 127.11 (d, C-3), 59.19 (t, C-7); HRMS (ESI) Calculated ($C_{23}H_{21}N_2Ge$): 399.09110 ([M(CH_3CN)]$^+$), ($C_{21}H_{18}NGe$): 358.06455 (M^+), Found: 399.09151, 358.06517.

5*H*-12,6-([1,2]benzenomethano)dibenzo[*c*,*f*][1,5]azastannocin-12(7*H*)-ylium hexachlorostibate(V)

[**1**Sn(CH_3CN)][$SbCl_6$]

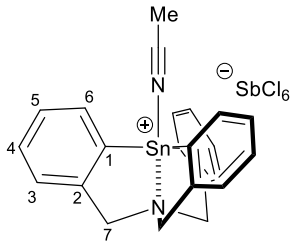

yield quant.; mp 111.8–112.2 °C; IR (KBr) ν = 3055 (w), 2931 (w), 2257 (w), 1612 (m), 1439 (s), 1353 (w), 1258 (w), 1197 (w), 966 (w), 851 (w), 756 (s) cm^{-1}; ^1H NMR (400 MHz, CD_3CN) 7.86–7.84 (m, 3H, 6-H), 7.47–7.44 (m, 6H, 5-H, 4-H), 7.35–7.31 (m, 3H, 3-H), 4.19 (s, 6H, 7-H); ^{13}C NMR (100 MHz, CD_3CN) 144.47 (s, C-1), 135.94 (d, C-6), 133.47 (s, C-2), 131.64 (d, C-4), 129.95 (d, C-5), 128.04 (d, C-3), 59.30 (t, C-7); $^{119}Sn\{^1H\}$ NMR (147.5 MHz, CD_3CN, Me_4Sn in $CDCl_3$ as an external standard) –59.3; HRMS (ESI) Calculated ($C_{23}H_{21}N_2Sn$): 445.07212 ([M(CH_3CN)]$^+$), ($C_{21}H_{18}NSn$): 404.04557 (M^+), Found: 445.07171, 404.04681.

5*H*-12,6-([1,2]benzenomethano)dibenzo[*c*,*f*][1,5]azasilocin-12(7*H*)-ylium perchlorate [**1**Si][ClO_4]

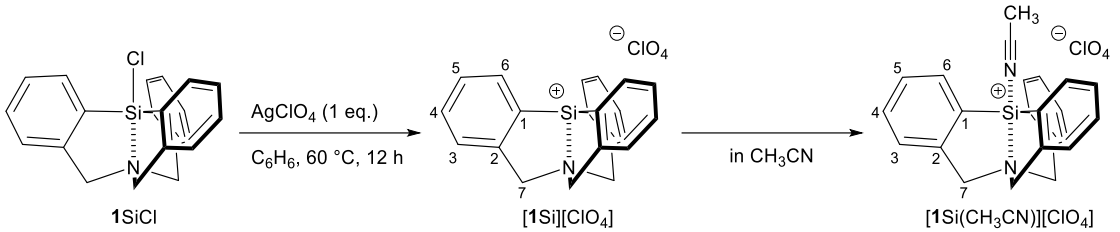

In a glove box, to a solution of **1**SiCl (69.6 mg, 0.20 mmol) in benzene (6 mL) was added silver perchlorate (41.5 mg, 0.20 mmol) at room temperature in a sealed vessel. The reaction mixture was stirred at 60 °C for 12 h. After stirring, the reaction mixture was extracted with chloroform (3 x 5 mL) and silver salts were removed through filtration. The collected organic layers were evaporated to give the product [**1**Si][ClO_4] as a white solid quantitatively (1.04 g, quant.). For recording the melting point and the IR spectrum, the fresh solids were used as a no solvent-adduct form. The solubility of [**1**Si][ClO_4] in $CDCl_3$ was not enough and the only ^{1}H NMR spectrum was recorded. The NMR spectra, including ^{13}C and ^{29}Si NMR were collected in CD_3CN, in which [**1**Si][ClO_4] existed as a CD_3CN-adduct [**1**Si(CD_3CN)][ClO_4].

[**1**Si][ClO_4]; mp 276.8–277.2 °C; IR (KBr) ν = 3055 (w), 2925 (w), 1595 (w), 1444 (m), 1196 (s), 1133 (m), 1020 (s), 968 (m), 821 (m), 728 (m) cm^{-1}; ^{1}H NMR (400 MHz, $CDCl_3$) 8.84 (d, J = 7.2 Hz, 3H), 7.14 (t, J = 7.2 Hz, 3H), 7.03 (td, J = 7.5, 1.2 Hz, 3H), 6.57(d, J = 7.2 Hz, 3H), 2.94 (s, 6H, 7-H).

[**1**Si(CD_3CN)][ClO_4]; ^{1}H NMR (400 MHz, CD_3CN) 8.00 (d, J = 6.8 Hz, 3H, 6-H), 7.50 (td, J = 7.6, 1.6 Hz, 3H, 4-H), 7.46 (t, J = 7.0 Hz, 3H, 5-H), 7.30 (d, J = 7.6 Hz, 3H, 3-H), 4.20 (s, 6H, 7-H); ^{13}C NMR (100 MHz, CD_3CN) 145.11 (s, C-2), 135.66 (d, C-6), 132.67 (d, C-4), 129.59 (d, C-5), 128.45 (s, C-1), 126.27 (d, C-3), 59.25 (t, C-7); ^{29}Si{^{1}H} NMR (78.5 MHz, CD_3CN, Me_4Si in $CDCl_3$ as an external standard) –53.8; HRMS (ESI) Calculated ($C_{23}H_{21}N_2Si$): 353.14685 ([M(CH_3CN)]$^+$), ($C_{21}H_{18}NSi$): 312.12030 (M$^+$), Found: 353.14640, 312.12001

*General procedure for the reaction of **1**SiCl with silver salt*

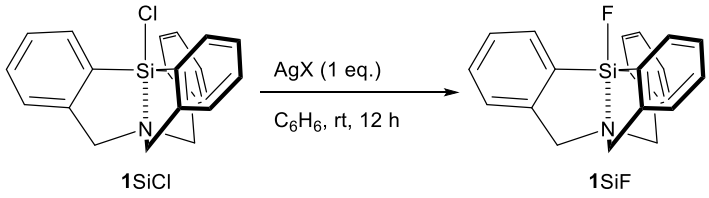

In a glove box, to a solution of **1**SiCl (17.4 mg, 0.05 mmol) in benzene (2 mL) was added silver perchlorate (0.05 mmol) at room temperature in a sealed vessel. The reaction mixture was stirred at rt for 12 h. After stirring, the reaction mixture was extracted with chloroform (3 x 5 mL) and silver salts were removed through filtration. The collected organic layers were evaporated to give the product **1**SiF as a white solid quantitatively (16.6 mg, qunat.).

12-fluoro-7,12-dihydro-5*H*-12,6-([1,2]benzenomethano)dibenzo[*c*,*f*][1,5]azasilocine 1SiF

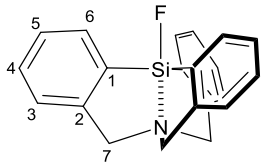

mp 276.1–276.3 °C; IR (KBr) ν = 3010 (w), 2855 (w), 1591 (w), 1442 (m), 1349 (w), 1236 (m), 1132 (m), 1072 (m), 973 (m), 832 (w), 720 (s) cm^{-1}; ^{1}H NMR (400 MHz, $CDCl_3$) 8.03 (d, J = 6.8 Hz, 3H, 6-H), 7.38–7.33 (m, 3H, 5-H), 7.32–7.29 (m, 3H, 4-H), 7.13 (d, J = 6.4 Hz, 3H, 3-H), 4.01 (s, 6H, 7-H); ^{13}C NMR (100 MHsz, $CDCl_3$) 144.19 (s, $^{3}J_{C\text{-}F}$ = 3.3 Hz, C-2), 136.49 (d, C-6), 134.59 (s, $^{2}J_{C\text{-}F}$ = 29.6 Hz, C-1), 129.72 (d, C-4), 127.93 (d, C-5), 124.15 (d, $^{4}J_{C\text{-}F}$ = 1.7 Hz, C-3), 58.37 (t, C-7); $^{29}Si\{^{1}H\}$ NMR (78.5 MHz, $CDCl_3$, Me_4Si in $CDCl_3$ as an external standard) –56.4 (d, $^{1}J_{Si\text{-}F}$ = 274 Hz); ^{19}F NMR (372.4 MHz, $CDCl_3$, CF_3COOH in $CDCl_3$ as external standard) –149.2 (s), –149.2 (d, $^{1}J_{F\text{-}29Si}$ = 274 Hz); MS (EI^+, 70 eV) m/z 331 (M^+, 17), 240 (100), 213 (9), 165 (18); HRMS (EI^+, 70 eV) Calculated ($C_{21}H_{18}FNSi$): 331.1193 (M^+): Found: 331.1191 (M^+); Analysis $C_{21}H_{18}FNSi$ (331.4654), Calculated: C, 76.10; H, 5.47; F, 5.73; N, 4.23; Si, 8.47, Found: C, 75.83; H, 5.40; N, 4.26.

X-ray crystallographic data

Arane-type molecule 1 SiCl (CCDC: 2093562)

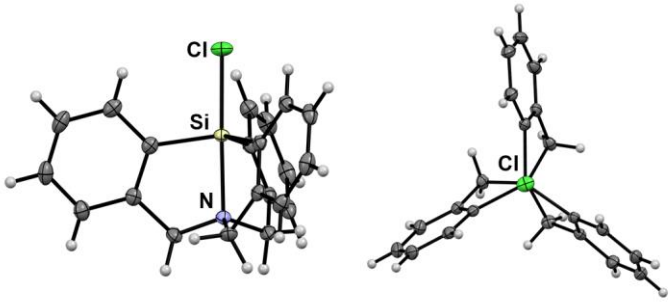

Figure S1. ORTEP drawings of **1**SiCl at the 50% probability level.

Empirical Formula	$C_{21}H_{18}ClNSi$	Z value	4
Formula Weight	347.90	D_{calc}	1.362 g/cm^3
Crystal Color, Habit	colorless, block	F_{000}	728.0
Crystal Dimensions	0.159×0.113×0.078 mm	μ(MoK$_\alpha$)	2.659 mm^{-1}
Crystal System	monoclinic	Temperature	123 K
Lattice Type	Primitive	Data/restraints/parameters	3435/0/217
Lattice Parameters	a = 10.3135(2) Å	Residuals: R_1 ($I > 2.00\sigma(I)$)	0.0305
	b = 13.5330(2) Å	Residuals: wR_2 (all data)	0.0804
	c = 12.6094(2) Å	Goodness of Fit Indicator	1.070
	β = 105.357(2) °		
	V = 1697.09(5) Å^3		
Space Group	$P2_1/c$ (#14)		

Arane-type molecule 1 GeCl (CCDC: 2093563)

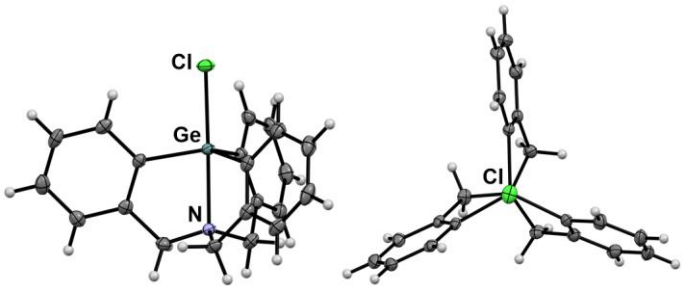

Figure S2. ORTEP drawings of **1**GeCl at the 50% probability level.

Empirical Formula	$C_{21}H_{18}ClGeN$	*Z* value	4
Formula Weight	392.40	D_{calc}	1.519 g/cm^3
Crystal Color, Habit	colorless, block	F_{000}	800.0
Crystal Dimensions	0.109×0.07×0.04 mm	μ(MoK$_\alpha$)	1.942 mm^{-1}
Crystal System	monoclinic	Temperature	123 K
Lattice Type	Primitive	Data/restraints/parameters	4340/0/217
Lattice Parameters	a = 10.3385(4) Å	Residuals: R_1 ($I > 2.00\sigma(I)$)	0.0315
	b = 13.6424(6) Å	Residuals: wR_2 (all data)	0.0730
	c = 12.6364(5) Å	Goodness of Fit Indicator	1.065
	β = 105.666(4) °		
	V = 1716.05(13) Å^3		
Space Group	$P2_1/c$ (#14)		

Arane-type molecule 1 SnCl (CCDC: 2093564)

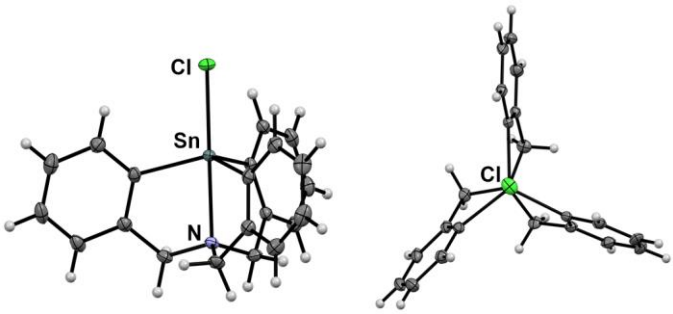

Figure S3. ORTEP drawings of **1**SnCl at the 50% probability level.

Empirical Formula	$C_{21}H_{18}ClNSn$	*Z* value	4
Formula Weight	438.50	D_{calc}	1.626 g/cm^3
Crystal Color, Habit	colorless, block	F_{000}	872.0
Crystal Dimensions	0.164×0.137×0.104 mm	μ(CuK$_\alpha$)	12.706 mm^{-1}
Crystal System	monoclinic	Temperature	123 K
Lattice Type	Primitive	Data/restraints/parameters	3624/0/217
Lattice Parameters	a = 10.3784(2) Å	Residuals: R_1 ($I > 2.00\sigma(I)$)	0.0248
	b = 14.1635(2) Å	Residuals: wR_2 (all data)	0.0636
	c = 12.6571(2) Å	Goodness of Fit Indicator	1.078
	β = 105.633(2) °		
	V = 1791.70(5) Å^3		
Space Group	$P2_1/c$ (#14)		

Arane-type molecule [**1**Si(CH_3CN)][$SbCl_6$] (CCDC: 2093565)

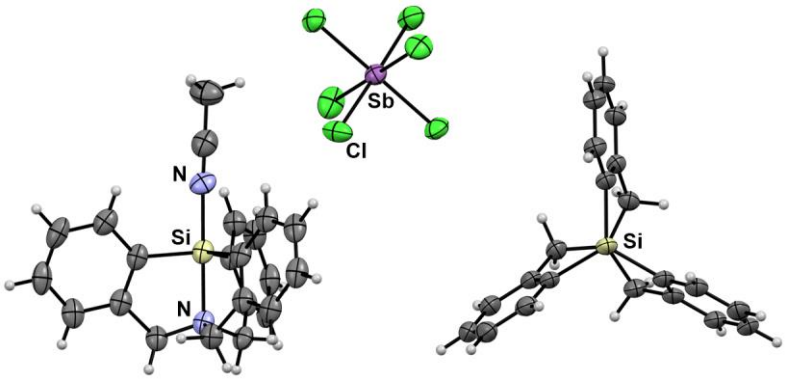

Figure S4. ORTEP drawings of [**1**Si(CH_3CN)][$SbCl_6$] at the 50% probability level.

Empirical Formula	$C_{25.5}H_{25}Cl_7N_3SbSi$	*Z* value	2
Formula Weight	771.47	D_{calc}	1.556 g/cm^3
Crystal Color, Habit	colorless, plate	F_{000}	766.0
Crystal Dimensions	0.09×0.064×0.044 mm	μ(CuK_α)	12.383 mm^{-1}
Crystal System	triclinic	Temperature	123 K
Lattice Type	Primitive	Data/restraints/parameters	6669/0/418
Lattice Parameters	a = 12.6355 (3) Å	Residuals: R_1 ($I > 2.00\sigma(I)$)	0.0549
	b = 12.6590 (2) Å	Residuals: wR_2 (all data)	0.1649
	c = 12.6726 (2) Å	Goodness of Fit Indicator	1.053
	α = 119.216 (2) °		
	β = 96.855 (2) °		
	γ = 104.050 (2) °		
	V = 1647.11(6) Å^3		
Space Group	*P*-1 (#2)		

Arane-type molecule [**1**Ge(CH_3CN)][$SbCl_6$] (CCDC: 2093566)

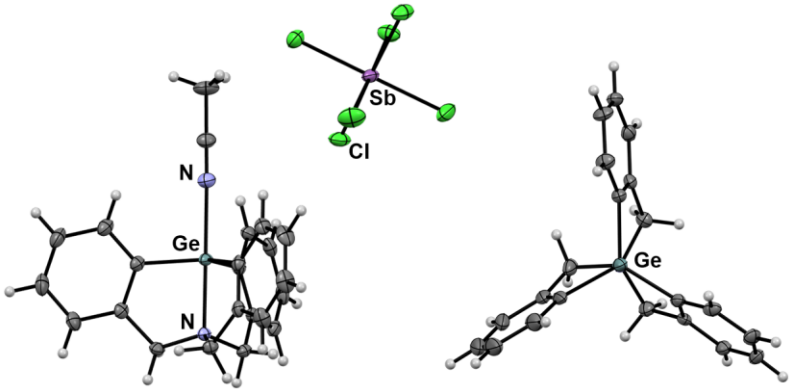

Figure S5. ORTEP drawings of [**1**Ge(CH_3CN)][$SbCl_6$] at the 50% probability level.

Empirical Formula	$C_{25}H_{24}Cl_6GeN_3Sb$	*Z* value	4
Formula Weight	773.51	D_{calc}	1.700 g/cm^3
Crystal Color, Habit	colorless, plate	F_{000}	1520.0
Crystal Dimensions	0.2×0.142×0.079 mm	μ(MoK_α)	2.440 mm^{-1}
Crystal System	triclinic	Temperature	123 K
Lattice Type	Primitive	Data/restraints/parameters	15554/0/653
Lattice Parameters	a = 12.8774(3) Å	Residuals: R_1 ($I > 2.00\sigma(I)$)	0.0362
	b = 13.1471(3) Å	Residuals: wR_2 (all data)	0.0903
	c = 21.0849(4) Å	Goodness of Fit Indicator	1.071
	α = 76.106(2) °		
	β = 84.698(2) °		
	γ = 60.738(2) °		
	V = 3021.74(13) Å^3		
Space Group	*P*-1 (#2)		

Arane-type molecule [**1**Sn(CH_3CN)][$SbCl_6$] (CCDC: 2093567)

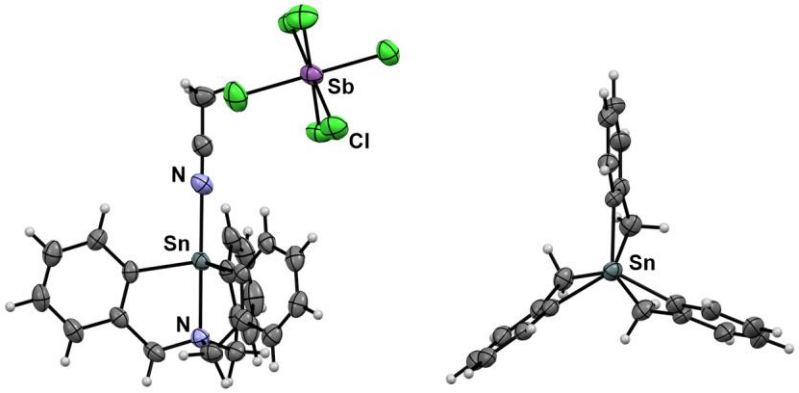

Figure S6. ORTEP drawings of [**1**Sn(CH_3CN)][$SbCl_6$] at the 50% probability level.

Empirical Formula	$C_{28}H_{27}Cl_6N_{4.25}SbSn$	*Z* value	2
Formula Weight	876.18	D_{calc}	1.687 g/cm^3
Crystal Color, Habit	colorless, plate	F_{000}	856.0
Crystal Dimensions	0.073×0.061×0.048 mm	μ(CuK_α)	16.447 mm^{-1}
Crystal System	triclinic	Temperature	123 K
Lattice Type	Primitive	Data/restraints/parameters	6981/0/364
Lattice Parameters	a = 11.3423(2) Å	Residuals: R_1 ($I > 2.00\sigma(I)$)	0.0456
	b = 12.7969(3) Å	Residuals: wR_2 (all data)	0.1244
	c = 12.8354(3) Å	Goodness of Fit Indicator	1.039
	α = 70.513(2) °		
	β = 80.349(2) °		
	γ = 81.999(2) °		
	V = 1724.47(7) Å^3		
Space Group	*P*-1 (#2)		

Arane-type molecule [**1**Si(H_2O)][ClO_4] (CCDC: 2093568)

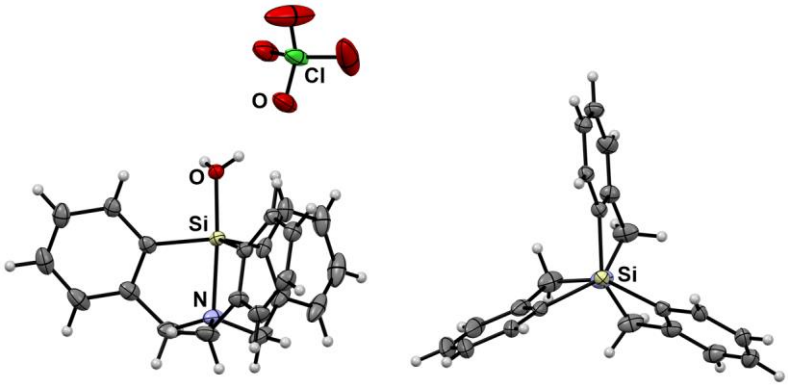

Figure S7. ORTEP drawings of [**1**Si(H_2O)][ClO_4] at the 50% probability level.

Empirical Formula	$C_{21}H_{20}Cl_{0.5}NO_3Si$	*Z* value	8
Formula Weight	760.39	D_{calc}	1.370 g/cm^3
Crystal Color, Habit	colorless, block	F_{000}	1596.0
Crystal Dimensions	0.244×0.19×0.12 mm	μ(MoK_α)	1.969 mm^{-1}
Crystal System	monoclinic	Temperature	123 K
Lattice Type	Centered	Data/restraints/parameters	3766/0/245
Lattice Parameters	a = 17.4804(2) Å	Residuals: R_1 ($I > 2.00\sigma(I)$)	0.0422
	b = 12.38840(10) Å	Residuals: wR_2 (all data)	0.1120
	c = 18.1542(2) Å	Goodness of Fit Indicator	1.062
	β = 110.2740(10) °		
	V = 3687.80(7) Å^3		
Space Group	*C*2/*c* (#15)		

Arane-type molecule 1 SiF (CCDC: 2093569)

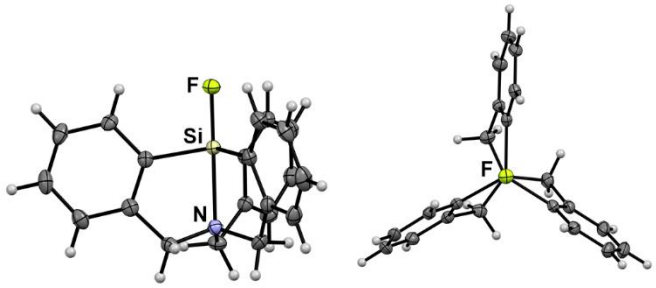

Figure S8. ORTEP drawings of **1**SiF at the 50% probability level.

Empirical Formula	$C_{21}H_{18}NFSi$	*Z* value	4
Formula Weight	331.45	D_{calc}	1.323 g/cm^3
Crystal Color, Habit	colorless, prism	F_{000}	696.0
Crystal Dimensions	0.174×0.153×0.1 mm	μ(MoK$_\alpha$)	0.152 mm^{-1}
Crystal System	orthombic	Temperature	123 K
Lattice Type	Primitive	Data/restraints/parameters	4004/0/217
Lattice Parameters	*a* = 8.4221(3) Å	Residuals: R_1 ($I > 2.00\sigma(I)$)	0.0347
	b = 8.6878(3) Å	Residuals: wR_2 (all data)	0.0796
	c = 22.7411(8) Å	Goodness of Fit Indicator	1.046
	V = 1663.96(10) Å^3		
Space Group	$P2_12_12_1$ (#19)		

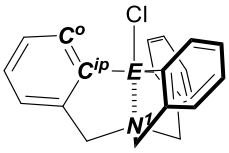

Table S1. Summary of geometrical parameters of atrane-type molecules **1**ECl.

	1SiCl	**1**GeCl	**1**SnCl
φ(C^o–C^{ip}–E–L) / °[a]	15.8	15.17	14.86
N^1–E/ Å[a]	2.1090(11)	2.2221(16)	2.3576(18)
<(C^{ip}–E–C^{ip}) / °[a]	118.43(6)	117.71(8)	115.83(8)
<(CH$_2$–N^1–CH$_2$) / °[a]	112.03(10)	113.07(15)	112.88(18)

[a] Mean values.

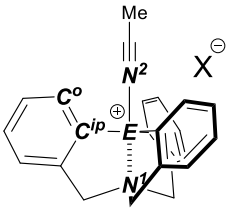

Table S2. Summary of geometrical parameters of atrane-type molecules [**1**E][X].

	[**1**Si(CH$_3$CN)] [SbCl$_6$]	[**1**Ge(CH$_3$CN)] [SbCl$_6$]	[**1**Sn(CH$_3$CN)] [SbCl$_6$]	[**1**Si(H$_2$O)] [ClO$_4$]
φ(C^o–C^{ip}–E–L) / °[a]	15.16	14.81	12.06	14.05
N^1–E/ Å[a]	2.016(4)	2.091(2)	2.267(4)	2.110(14)

<(C^{ip}–E–C^{ip}) / °[a]	119.49(15)	119.24(11)	117.59(17)	118.42(7)
<(CH_2–N^1–CH_2) / °[a]	111.93(3)	112.67(2)	112.63(4)	112.06(14)
–C≡N^2 (in CH_3CN) / Å	1.142(6)	1.131(5)	1.137(7)	–

[a] Mean values.

Gutmann-Beckett method

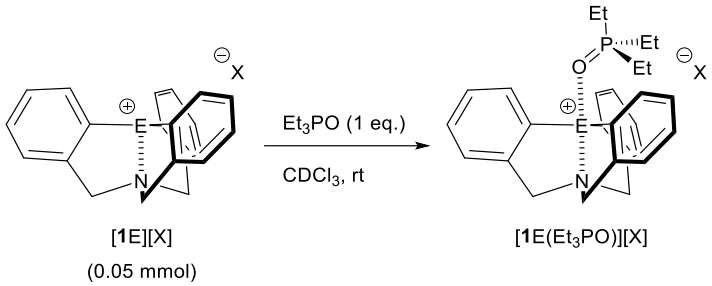

In a nitrogen-filled glove box, to a solution of atrane-type cation [**1**E][X] (0.05 mmol) in $CDCl_3$ (1 mL) was added triethylphosphine oxide (6.7 mg, 0.05 mmol) at room temperature in a sealed tube. For [**1**Si][ClO_4], the desired adduct [**1**Si(Et_3PO)][ClO_4] was isolated in a crystal form and characterized by X-ray analysis (Figure S9). From the ^{31}P NMR measurement of [**1**Si(Et_3PO)][ClO_4] in $CDCl_3$, the acceptor number (AN) of [**1**Si][ClO_4] was estimated to be 85.3.

Characterization of [1Si(Et_3PO)][ClO_4]

mp 152.3–152.5 °C; IR (KBr) ν = 3050 (w), 2918 (w), 1595 (w), 1443 (m), 1349 (w), 1232 (w), 1092 (s), 969 (w), 729 (m) cm^{-1}; ^1H NMR (400 MHz, $CDCl_3$) 7.65–7.61 (m, 3H), 7.47–7.40 (m, 6H), 7.26–7.22 (m, 3H), 4.05(s, 6H), 2.69 (dq, J = 10.4, 7.8 Hz, 6H), 1.39 (dq, J = 18.7, 7.8 Hz, 9H); ^{13}C NMR: (100 MHz, $CDCl_3$) 144.46, 134.62, 131.06, 128.49, 128.32, 125.46, 57.53, 19.45 (d, $^1J_{CP}$ = 66.1 Hz), 6.03 (d, $^2J_{CP}$ =5.8 Hz); ^{31}P NMR (160.1 MHz, $CDCl_3$, D_3PO_4 in D_2O as an external standard) 79.6.

AN was estimated by using the following equation. AN = 2.21 × ($\delta(^{31}P)_{LA–Et3PO}$ – 41)[41]

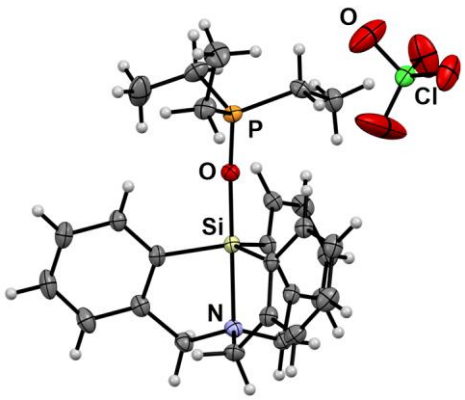

Figure S9. ORTEP drawings of [**1**Si(Et$_3$PO)][ClO$_4$] at the 50% probability level. (CCDC: 2093570)

Empirical Formula	$C_{27}H_{33}ClNO_5PSi$	*Z* value	4
Formula Weight	546.05	D_{calc}	1.357 g/cm^3
Crystal Color, Habit	colorless, block	F_{000}	1152.0
Crystal Dimensions	0.246 × 0.077 × 0.068 mm	μ(CuK$_\alpha$)	2.579 mm^{-1}
Crystal System	orthorhombic	Temperature	123 K
Lattice Type	Primitive	Data/restraints/parameters	4265/1/338
Lattice Parameters	*a* = 19.9184(3) Å	Residuals: R_1 ($I > 2.00\sigma(I)$)	0.0377
	b = 9.05410(10) Å	Residuals: wR_2 (all data)	0.0982
	c = 14.8192(2) Å	Goodness of Fit Indicator	1.036
	V = 2672.54(6) Å^3		
Space Group	*Pna*2$_1$ (#33)		

Hydrodefluorination of 1-adamantyl fluoride 4

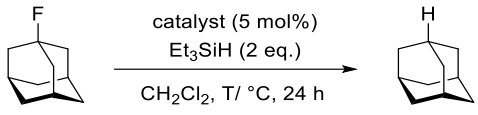

4
0.1 mmol

5

In a nitrogen-filled glove box, to a solution of 1-adamantylfluoride **4** (15.4 mg, 0.1 mmol) and Et$_3$SiH (23.2 mg, 0.2 mmol) in dichloromethane (0.5 mL) was added cation [**1**E][X] (5 mol%, 0.02 mmol) at rt in a sealed vessel. After stirring for 24 h at 50 °C, ethyl acetate was added to the mixture. The residues were analyzed by GC to obtain the yield using dodecane as an internal standard.

Table S3. Summary of hydrodefluorination of 1-adamantylfluoride **4**.

entry	catalyst	T [°C]	Yield of **5** [%]	Recovery of **4** [%]
1	[**1**Si][SbCl$_6$]	rt	22	34
2	[**1**Si][SbCl$_6$]	50	44	0
3	[**1**Ge][SbCl$_6$]	rt	6	52
4	[**1**Ge][SbCl$_6$]	50	25	0
5	[**1**Sn][SbCl$_6$]	rt	5	43
6	[**1**Sn][SbCl$_6$]	50	19	0
7	[**1**Si][ClO$_4$]	rt	100	0
8	[**1**Si][ClO$_4$]	50	92	0

Friedel-Crafts type dimerization of 1,1-diphenylethylene 6

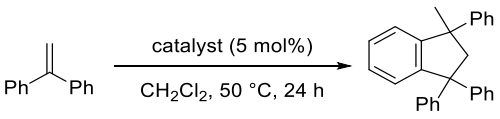

6
0.1 mmol

7

In a nitrogen-filled glove box, to a solution of 1,1-diphenylethylene **6** (18.0 mg, 0.1 mmol) in dichloromethane (0.5 mL) was added cation [**1**E][X] (5 mol%, 0.005 mmol) at room temperature in a sealed vessel. After stirring for 24 h at 50 °C, ethyl acetate was added to the mixture. The residues were evaporated to give a crude mixture, which was analyzed by NMR to obtain the yield using 1,1,2,2-tetrachloroethane as an internal standard.

General procedure of cyclization reaction of alkynes 8 or 10

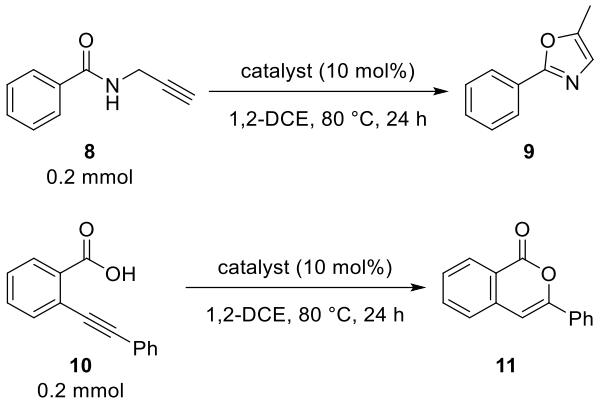

In a nitrogen-filled glove box, to a solution of alkyne (**8**[58] or **10**,[59] 0.2 mmol) in 1,2-dichloroethene (2 mL) was added cation [**1**E][X] (10 mol%, 0.02 mmol) at room temperature in a sealed vessel. After stirring for 24 h at 80 ˚C, ethyl acetate was added to the mixture. The residues were evaporated to give a crude mixture, which was analyzed by NMR to obtain the yield using 1,1,2,2-tetrachloroethane as an internal standard.

Hydrosilylation of 4-(trifluoromethyl)benzaldehyde 12

In a nitrogen-filled glove box, to a solution of 4-(trifluoromethyl)benzaldehyde **12** (87.1 mg, 0.5 mmol) and Et_3SiH (58.1 mg, 0.5 mmol) in acetnitrile (2 mL) was added cation [**1**E][X] (2 mol%, 0.01 mmol) at room temperature in a sealed vessel. After stirring for 13 h at 80 °C, ethyl acetate was added to the mixture. The residues were evaporated to give a crude mixture, which was analyzed by NMR to obtain the yield using 1,1,2,2-tetrachloroethane as an internal standard.

Table S4. Difference of Catalytic Activity between atrane-type cation **1**E^+ and $[Et_3Si][B(C_6F_5)_4]$.

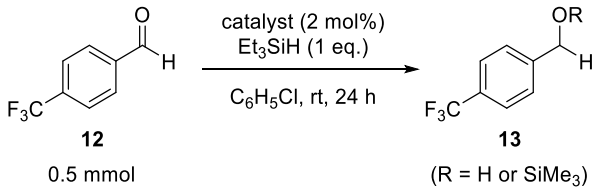

entry	catalyst	Yield of **13** [%]
1	[**1**Si][$SbCl_6$]	0
2[a]	[**1**Si][$SbCl_6$]	86

3[a]	[**1**Ge][$SbCl_6$]	94
4[a]	[**1**Sn][$SbCl_6$]	92
5	[**1**Si][ClO_4]	100
6[a]	[**1**Si][ClO_4]	100
7	[Ph_3C][$B(C_6F_5)_4$]	48
8[a]	[Ph_3C][$B(C_6F_5)_4$]	90

[a] catalyst (10 mol%), CH_3CN, 80 ˚C, 13 h

Competitive reaction of silyl ketene acetal 14 with the mixture of benzaldehyde dimethylacetal 15 and aldehyde 16

In a nitrogen-filled glove box, to a solution of silyl ketene acetal **14** (87.2 mg, 0.5 mmol), benzaldehyde dimethylacetal **15** (76.1 mg, 0.5 mmol) and benzaldehyde **16** (53.1 mg, 0.5 mmol) in solvent (2 mL) was added Lewis acid (2 mol%, 0.01 mmol) at rt in a sealed vessel. After stirring for 4 h at room temperature, ethyl acetate was added to the mixture. The residues were evaporated to give a crude mixture, which was analyzed by NMR to obtain the yield using 1,1,2,2-tetrachloroethane as an internal standard.

Table S5. Summary of Chemoselectivity in competitive reactions between acetal **15** and aldehyde **16** with various Lewis acids.

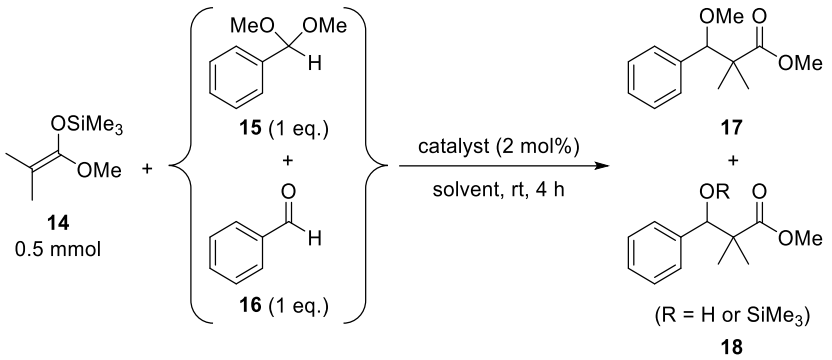

entry	catalyst	solvent	Yield of **17** [%]	Yield of **18** [%]	Ratio of **17**/**18**
1	[**1**Si][ClO_4]	THF	94	1	99/1
2		toluene	11	89	11/89
3	Me_3SiClO_4	THF	83	4	95/5
4		toluene	21	62	25/75
5	Me_3SiOTf	THF	64	30	68/32
6		toluene	15	77	16/84
7	$B(C_6F_5)_3$	THF	40	59	40/60
8		toluene	6	88	6/94
9	$BF_3{\cdot}OEt_2$	THF	0	11	–
10		toluene	0	18	–

Computational Details

All calculations for **1**Si^+, **1**Ge^+ and **1**Sn^+ were conducted using the Gaussian 16 Rev. C. 01 program.[60] For the estimations of the LUMO level, the optimizations of **1**Si^+, **1**Ge^+ and **1**Sn^+ were performed with the B3LYP functional and 6-31G** for C, H, N and LANL2DZ for Si, Ge, Sn basis set. The obtained optimized structures are local minimum structures with all positive vibrational frequencies. The details of the evaluations of FIA and HIA values are summarized in below.

LUMOs of 1E$^+$

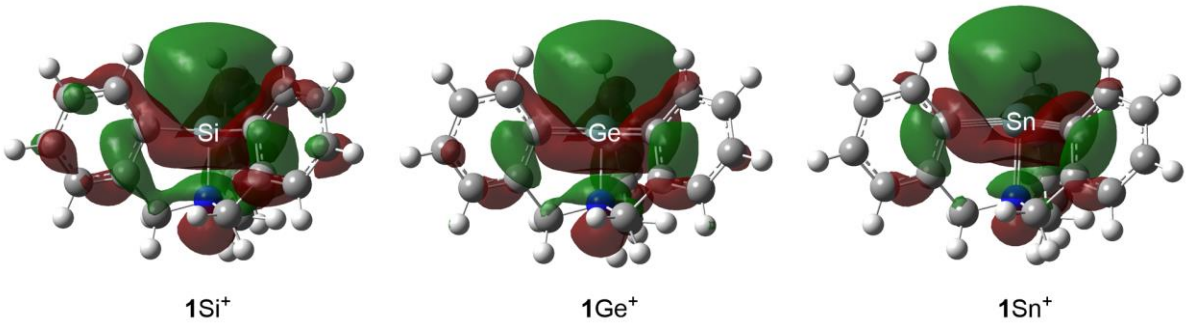

Figures S11. The molecular orbital of the LUMO concerning the Lewis acidity calculated at the B3LYP/6-31G** for C, H, N and LANL2DZ for Si, Ge, Sn level (the contour level of 0.02 / Å^3)

Table S6. Calculated characteristic parameters for the E-N linkage in cations **1**Si$^+$, **1**Ge$^+$, **1**Sn$^+$.

	1Si$^+$	**1**Ge$^+$	**1**Sn$^+$
LUMO [eV]	–0.15	–0.17	–0.20
N^1–E [Å]	1.921	2.014	2.174
ρ(E)	1.966	1.951	2.054
ρ(N^1)	–0.607	–0.598	–0.608
WBI (N^1–E)	0.416	0.384	0.311

WBI: Wiberg bond index, ρ: natural charge according to the NBO analysis.

Fluoride and Hydride Ion Affinities (FIA, HIA)

The computations were performed using the Gaussian 16 program.[60] Fluoride ion affinities were determined with respect to the procedure suggested by Greb and Krossing.[61] Herein, we adopted the same level of the theory and methodology recently reported by Driess.[13]

Accordingly, we chose the Me_3SiF/Me_3Si^+ reference system for the calculation of absolute FIA values ($\Delta_{ref}H$ (FIA(Me_3Si^+)) = 952.5 kJmol^{-1})[61] and HIA values ($\Delta_{ref}H$ (HIA(Me_3Si^+)) = 959 kJmol^{-1}).[7] In a first step, geometry optimizations were performed at the B3LYP[62][63][64][65]-D3BJ[66] level with def2-SVP[67] basis set for all atoms. Stationary points were confirmed as true minima by vibrational frequency analysis (no negative imaginary value). Thermal corrections at 298.15 K were obtained from the same level of theory. In a second step, single point calculations at the PW6B95[68]-D3BJ[66]/def2-QZVPP[67][69] level of theory were conducted. The obtained electronic energies were combined with the thermal correction from the 1st step in order to obtain the total energies of the Lewis acid (LA and Me_3Si^+) and its fluoride/hydride adduct ([LA–X]$^-$ and Me_3Si–X). With the obtained values, the reaction enthalpy of equation 1 (Δ_1H) was determined and subtraction of the FIA (X = F)/HIA (X = H) of Me_3Si^+ (equation

3: $\Delta_{ref}H - \Delta_1H$) gave the final gas phase FIAs/HIAs.

Equation 1: LA + $Me_3Si–X$ → $[LA–X]^-$ + Me_3Si^+	Δ_1H
Equation 2: $Me_3Si–X \rightarrow Me_3Si^+ + X^-$	$\Delta_{ref}H$ X = F: 952.5 $kJmol^{-1}$ (CCSD(T)/CBS) X = H: 959 $Jmol^{-1}$ (G3)
Equation 3: $LA + X^- \rightarrow [LA–X]^-$	FIA or HIA = $\Delta_{ref}H - \Delta_1H$

In order to evaluate the damping of the FIAs/HIAs upon solvation, we approximated the enthalpies of solvation (ΔH_{solv}) for the fluoride anion/hydride anion, the Lewis acids and their fluoride/hydride adducts in dichloromethane. For this purpose, single point calculations (B3LYP/def2-SVP) with vibrational frequency analysis were conducted based on the gas phase geometries (B3LYP/def2-SVP) using the CPCM[70][71] model as implemented in Gaussian 16. The respective ΔH_{solv} were obtained by subtraction of the thus obtained enthalpies from the gas phase enthalpies. Combination of ΔH_{solv} with the gas phase FIA provided the FIA_{solv}/HIA_{solv} data, which is not intended to be an absolute value.

Table S7. Details of the calculation of FIA for **1**E^+.

compound	ElectronicEnergy _SPcalculation PW6B95(D3BJ)/def2QZVPP	ThermalCorrelation_295.15K _B3LYP(D3BJ)/def2SVP	Toltal_energy /hartree	Total_energy /$kJmol^{-1}$		Δ_1H /$kJmol^{-1}$	FIA /$kJmol^{-1}$
Me_3Si-F	-509.8216745	0.121059	-509.70062	-1338218.966			
Me_3Si^+	-409.4641393	0.116076	-409.3480633	-1074743.34			
1Si^+	-1156.928107	0.353731	-1156.574376	-3036586.023			
1SiF	-1257.211322	0.356886	-1256.854436	-3299871.322		190.3264332	762.173567
1Ge^+	-2945.178219	0.352602	-2944.825617	-7731639.658			
1GeF	-3045.441107	0.355469	-3045.085638	-7994872.343		242.9411907	709.558809
1Sn^+	-1081.536047	0.351483	-1081.184564	-2838650.073			
1SnF	-1181.800297	0.354312	-1181.445985	-3101886.435		239.2636528	713.236347

Table S8. Details of the calculation of FIA for **1**E^+ including solvation correlation (CH_2Cl_2).

compound	Enthalpy_gasphase_298.15K _Spcalculation _B3LYP(D3BJ)/def2SVP	Enthalpy_DCM_298.15K _Spcalculation _B3LYP(D3BJ)/def2SVP	H_{solv} /hartree	H_{solv} /kJmol^{-1}	ΔH_{solv} /kJ/mol^{-1}	Δ_1H(sol) /kJmol^{-1}	FIA(sol) /kJmol^{-1}
F-_anion	-99.686473	-99.813335	-0.1269	-333.076181			
				Δ_2H(sol)	619.423819		
1Si^+	-1154.206765	-1154.263446	-0.0567	-148.815966	126.2261635		
1SiF	-1254.255245	-1254.263849	-0.0086	-22.589802		316.5526	302.8712
1Ge^+	-2941.553009	-2941.609798	-0.0568	-149.099519	124.821521		
1GeF	-3041.584067	-3041.593314	-0.0092	-24.2779985		367.7627	251.6611
1Sn^+	-1079.103509	-1079.16164	-0.0581	-152.622941	124.8609035		
1SnF	-1179.131068	-1179.141642	-0.0106	-27.762037		364.1246	255.2993

Table S9. Details of the calculation of HIA for **1**E^+.

compound	ElectronicEnergy _SPcalculation PW6B95(D3BJ)/def2QZVPP	ThermalCorrection_295.15K _B3LYP(D3BJ)/def2SVP	Toltal_energy /hartree	Total_energy /kJmol^{-1}		Δ_1H /kJmol^{-1}	HIA /kJmol^{-1}
Me_3Si-H	-410.3474628	0.12653	-410.22093	-1077035.059			
Me_3Si^+	-409.4641393	0.116076	-409.3480633	-1074743.34			
1Si^+	-1156.928107	0.353731	-1156.574376	-3036586.023			
1SiH	-1157.730248	0.361138	-1157.36911	-3038672.598		205.1439676	753.856032
1Ge^+	-2945.178219	0.352602	-2944.825617	-7731639.658			
1GeH	-2945.983911	0.359523	-2945.624388	-7733736.83		194.546662	764.453338
1Sn^+	-1081.536047	0.351483	-1081.184564	-2838650.073			
1SnH	-1082.347778	0.357542	-1081.990236	-2840765.364		176.4278239	782.572176

Table S10. Details of the calculation of HIA for **1**E^+ including solvation correlation (CH_2Cl_2).

compound	Enthalpy_gasphase_298.15K _Spcalculation _B3LYP(D3BJ)/def2SVP	Enthalpy_DCM_298.15K _Spcalculation _B3LYP(D3BJ)/def2SVP	H_{solv} /hartree	H_{solv} /kJmol^{-1}	ΔH_{solv} /kJ/mol^{-1}	Δ_1H(sol) /kJmol^{-1}	HIA(sol) /kJmol^{-1}
H-_anion	-0.486369	-0.622545	-0.1362	-357.530088			
				Δ_2H(sol)	601.469912		
1Si^+	-1154.206765	-1154.263446	-0.0567	-148.815966	131.936626		
1SiH	-1155.007215	-1155.013644	-0.0064	-16.8793395		337.0806	264.3893
1Ge^+	-2941.553009	-2941.609798	-0.0568	-149.099519	133.496173		
1GeH	-2942.357202	-2942.363145	-0.0059	-15.6033465		328.0428	273.4271
1Sn^+	-1079.103509	-1079.16164	-0.0581	-152.622941	136.3710955		
1SnH	-1079.912857	-1079.919047	-0.0062	-16.251845		312.7989	288.671

3-5. References

[1] A. Corma, H. García, *Chem. Rev.* **2003**, *103*, 4307–4366.
[2] H. Yamamoto, Ed. , *Lewis Acids in Organic Synthesis*, Wiley-VCH, Weinheim, **2000**.
[3] L. Greb, *Chem. – A Eur. J.* **2018**, *24*, 17881–17896.
[4] L. O. Müller, D. Himmel, J. Stauffer, G. Steinfeld, J. Slattery, G. Santiso-Quiñones, V. Brecht, I. Krossing, *Angew. Chem. Int. Ed.* **2008**, *47*, 7659–7663.
[5] T. E. Mallouk, G. L. Rosenthal, G. Mueller, R. Brusasco, N. Bartlett, *Inorg. Chem.* **1984**, *23*,

3167–3173.
[6] K. O. Christe, D. A. Dixon, D. McLemore, W. W. Wilson, J. A. Sheehy, J. A. Boatz, *J. Fluor. Chem.* **2000**, *101*, 151–153.
[7] H. Böhrer, N. Trapp, D. Himmel, M. Schleep, I. Krossing, *Dalt. Trans.* **2015**, *44*, 7489–7499.
[8] R. Maskey, M. Schädler, C. Legler, L. Greb, *Angew. Chem. Int. Ed.* **2018**, *57*, 1717–1720.
[9] A. L. Liberman-Martin, R. G. Bergman, T. D. Tilley, *J. Am. Chem. Soc.* **2015**, *137*, 5328–5331.
[10] D. Hartmann, M. Schädler, L. Greb, *Chem. Sci.* **2019**, *10*, 7379–7388.
[11] D. Roth, H. Wadepohl, L. Greb, *Angew. Chem. Int. Ed.* **2020**, *59*, 20930–20934.
[12] T. Thorwart, D. Roth, L. Greb, *Chem. – A Eur. J.* **2021**, chem.202101138.
[13] A. Hermannsdorfer, M. Driess, *Angew. Chem. Int. Ed.* **2021**, *60*, 13656–13660.
[14] A. Konishi, Y. Minami, T. Hosoi, K. Chiba, M. Yasuda, *Chem. - A Eur. J.* **2016**, *22*, 12688–12691.
[15] M. Kira, M. Kobayashi, H. Sakurai, *Tetrahedron Lett.* **1987**, *28*, 4081–4084.
[16] M. Braun, *Modern Enolate Chemistry: From Preparation to Applications in Asymmertric Synthesis*, Wiley-VCH, **2016**.
[17] M. Yasuda, K. Hayashi, Y. Katoh, I. Shibata, A. Baba, *J. Am. Chem. Soc.* **1998**, *120*, 715–721.
[18] S. E. Denmark, T. Wynn, *J. Am. Chem. Soc.* **2001**, *123*, 6199–6200.
[19] Y. Minami, K. Nishida, A. Konishi, M. Yasuda, *Chem. – An Asian J.* **2020**, *15*, 1852–1857.
[20] M. Yasuda, T. Oh-Hata, I. Shibata, A. Baba, H. Matsuda, *J. Chem. Soc., Perkin Trans. 1* **1993**, 859–865.
[21] H. F. T. Klare, L. Albers, L. Süsse, S. Keess, T. Müller, M. Oestreich, *Chem. Rev.* **2021**, *121*, 5889–5985.
[22] V. J. Scott, R. Çelenligil-Çetin, O. V Ozerov, *J. Am. Chem. Soc.* **2005**, *127*, 2852–2853.
[23] R. Panisch, M. Bolte, T. Müller, *J. Am. Chem. Soc.* **2006**, *128*, 9676–9682.
[24] H. Schmidt, S. Keitemeyer, B. Neumann, H.-G. Stammler, W. W. Schoeller, P. Jutzi, *Organometallics* **1998**, *17*, 2149–2151.
[25] A. Růžička, R. Jambor, I. Císařová, J. Holeček, *Chem. - A Eur. J.* **2003**, *9*, 2411–2418.
[26] K.-C. Kim, C. A. Reed, D. W. Elliott, L. J. Mueller, F. Tham, L. Lin, J. B. Lambert, *Science* **2002**, *297*, 825–827.
[27] C. Schenk, C. Drost, A. Schnepf, *Dalt. Trans.* **2009**, *2*, 773–776.
[28] A. Sekiguchi, T. Fukawa, V. Y. Lee, M. Nakamoto, M. Ichinohe, *Angew. Chem. Int. Ed.* **2003**, *42*, 1143–1145.
[29] A. Sekiguchi, T. Fukawa, V. Y. Lee, M. Nakamoto, *J. Am. Chem. Soc.* **2003**, *125*, 9250–9251.
[30] J. C. L. Walker, H. F. T. Klare, M. Oestreich, *Nat. Rev. Chem.* **2020**, *4*, 54–62.
[31] J. G. Verkade, *Coord. Chem. Rev.* **1994**, *137*, 233–295.
[32] A. Tzschach, K. Jurkschat, *Pure Appl. Chem.* **1986**, *58*, 639–646.
[33] A. Kavoosi, E. Fillion, *Angew. Chem. Int. Ed.* **2015**, *54*, 5488–5492.
[34] E. Fillion, A. Kavoosi, K. Nguyen, C. Ieritano, *Chem. Commun.* **2016**, *52*, 12813–12816.
[35] Q. Chen, C. E. Buss, V. G. Young, S. Fox, *J. Chem. Crystallogr.* **2005**, *35*, 177–181.
[36] P. N. Billinger, P. P. K. Claire, H. Collins, G. R. Willey, *Inorganica Chim. Acta* **1988**, *149*, 63–67.
[37] B. Kašná, R. Jambor, L. Dostál, A. Růžička, I. Císařová, J. Holeček, *Organometallics* **2004**, *23*, 5300–5307.
[38] Z. Xie, R. Bau, C. A. Reed, *J. Chem. Soc. Chem. Commun.* **1994**, 2519.
[39] U. Mayer, V. Gutmann, W. Gerger, *Monatshefte für Chemie* **1975**, *106*, 1235–1257.
[40] M. A. Beckett, G. C. Strickland, J. R. Holland, K. Sukumar Varma, *Polymer (Guildf).* **1996**, *37*, 4629–4631.
[41] I. B. Sivaev, V. I. Bregadze, *Coord. Chem. Rev.* **2014**, *270–271*, 75–88.
[42] M. A. Beckett, D. S. Brassington, S. J. Coles, M. B. Hursthouse, *Inorg. Chem. Commun.* **2000**, *3*, 530–533.
[43] E. L. Myers, C. P. Butts, V. K. Aggarwal, *Chem. Commun.* **2006**, 4434–4436.
[44] H. Großekappenberg, M. Reißmann, M. Schmidtmann, T. Müller, *Organometallics* **2015**, *34*, 4952–4958.
[45] R. Vivas-Reyes, A. Aria, *Eclética Química* **2008**, *33*, 69–76.
[46] J. B. Lambert, Y. Zhao, H. Wu, *J. Org. Chem.* **1999**, *64*, 2729–2736.
[47] K. Hara, R. Akiyama, M. Sawamura, *Org. Lett.* **2005**, *7*, 5621–5623.
[48] M. Kira, T. Hino, H. Sakurai, *Chem. Lett.* **1992**, *21*, 555–558.

[49] M. Nava, C. A. Reed, *Organometallics* **2011**, *30*, 4798–4800.
[50] T. Saitoh, S. Yoshida, J. Ichikawa, *J. Org. Chem.* **2006**, *71*, 6414–6419.
[51] O. V Dolomanov, L. J. Bourhis, R. J. Gildea, J. A. K. Howard, H. Puschmann, *J. Appl. Crystallogr.* **2009**, *42*, 339–341.
[52] A. Herrera, R. Martínez-Alvarez, P. Ramiro, D. Molero, J. Almy, *J. Org. Chem.* **2006**, *71*, 3026–3032.
[53] A. Tyagi, N. U. D. Reshi, P. Daw, J. K. Bera, *Dalt. Trans.* **2020**, *49*, 15238–15248.
[54] A. P. Dieskau, J. M. Begouin, B. Plietker, *European J. Org. Chem.* **2011**, *3*, 5291–5296.
[55] M. Teci, N. Lentz, E. Brenner, D. Matt, L. Toupet, *Dalt. Trans.* **2015**, *44*, 13991–13998.
[56] N. Li, J. Wang, X. Zhang, R. Qiu, X. Wang, J. Chen, S.-F. Yin, X. Xu, *Dalt. Trans.* **2014**, *43*, 11696–11708.
[57] T. Nakagawa, H. Fujisawa, Y. Nagata, T. Mukaiyama, *Bull. Chem. Soc. Jpn.* **2004**, *77*, 1555–1567.
[58] P. Wipf, Y. Aoyama, T. E. Benedum, *Org. Lett.* **2004**, *6*, 3593–3595.
[59] V. K. Rawat, K. Higashida, M. Sawamura, *Adv. Synth. Catal.* **2021**, *363*, 1631–1637.
[60] M. J. Frisch, G. W. Trucks, H. B. Schlegel, G. E. Scuseria, M. A. Robb, J. R. Cheeseman, G. Scalmani, V. Barone, G. A. Petersson, H. Nakatsuji, X. Li, M. Caricato, A. V. Marenich, J. Bloino, B. G. Janesko, R. Gomperts, B. Mennucci, H. P. Hratchian, J. V. Ortiz, A. F. Izmaylov, J. L. Sonnenberg, D. Williams-Young, F. Ding, F. Lipparini, F. Egidi, J. Goings, B. Peng, A. Petrone, T. Henderson, D. Ranasinghe, V. G. Zakrzewski, J. Gao, N. Rega, G. Zheng, W. Liang, M. Hada, M. Ehara, K. Toyota, R. Fukuda, J. Hasegawa, M. Ishida, T. Nakajima, Y. Honda, O. Kitao, H. Nakai, T. Vreven, K. Throssell, J. J. A. Montgomery, J. E. Peralta, F. Ogliaro, M. J. Bearpark, J. J. Heyd, E. N. Brothers, K. N. Kudin, V. N. Staroverov, T. A. Keith, R. Kobayashi, J. Normand, K. Raghavachari, A. P. Rendell, J. C. Burant, S. S. Iyengar, J. Tomasi, M. Cossi, J. M. Millam, M. Klene, C. Adamo, R. Cammi, J. W. Ochterski, R. L. Martin, K. Morokuma, O. Farkas, J. B. Foresman, D. J. Fox, *Gaussian 16*, Gaussian, Inc., Wallingford CT, **2016**.
[61] P. Erdmann, J. Leitner, J. Schwarz, L. Greb, *ChemPhysChem* **2020**, *21*, 987–994.
[62] S. H. Vosko, L. Wilk, M. Nusair, *Can. J. Phys.* **1980**, *58*, 1200–1211.
[63] A. D. Becke, *J. Chem. Phys.* **1993**, *98*, 1372–1377.
[64] C. Lee, W. Yang, R. G. Parr, *Phys. Rev. B* **1988**, *37*, 785–789.
[65] P. J. Stephens, F. J. Devlin, C. F. Chabalowski, M. J. Frisch, *J. Phys. Chem.* **1994**, *98*, 11623–11627.
[66] S. Grimme, S. Ehrlich, L. Goerigk, *J. Comput. Chem.* **2011**, *32*, 1456–1465.
[67] F. Weigend, R. Ahlrichs, *Phys. Chem. Chem. Phys.* **2005**, *7*, 3297.
[68] Y. Zhao, D. G. Truhlar, *J. Phys. Chem. A* **2005**, *109*, 5656–5667.
[69] F. Weigend, *Phys. Chem. Chem. Phys.* **2006**, *8*, 1057.
[70] V. Barone, M. Cossi, *J. Phys. Chem. A* **1998**, *102*, 1995–2001.
[71] M. Cossi, N. Rega, G. Scalmani, V. Barone, *J. Comput. Chem.* **2003**, *24*, 669–681.

Conclusions

The synthesis and properties of cage-shaped compounds with a group 13/14center were investigated in this research. The Lewis acidity of a boron or an aluminum center can be modulated by the cage-shaped ligand. Moreover, the coordination environment controlled by the rigid structure showed unique chemo- and stereoselectivities. The cage-shaped structure was also effective to control the coordination number of heavier group 14 cations and utilize them as hard and soft Lewis superacid catalysts.

In chapter 1, the origin of the selectivity for aromatic compounds from π-pocket was investigated. In the competitive hetero Diels-Alder reaction, three aryl groups around the boron center were found to be essential for the selectivity. Moreover, the electronic state of the π-pocket had great influence on the selectivity. The electron rich or π-expanded π-pocket showed high selectivities for broad aromatic aldehydes, indicating the existence of π-electron interactions between π-pocket and aromatic aldehydes. From the kinetic study and the theoretical calculation, it was revealed that noncovalent interactions between π-pocket and aromatic aldehydes played an important role for the selectivity. Furthermore, the more difficult intramolecular recognition of carbon frameworks was achieved with the flow system.

In chapter 2, the rigid and bulky triphenoxy ligand gave the monomeric cage-shaped aluminum complex preventing the formation of the multinuclear aluminum complex. The aluminum complex showed a moderate Lewis acidity and catalytic activities in many reactions. In ^{27}Al NMR, the highly coordinated state of the aluminum center was observed. Mechanisms to activate Lewis bases were found to be different from the cage-shaped boron and aluminum complexes. The property of the highly coordinated state was effective to control the stereoselectivity in glycosylation reactions. The aluminum complex showed a high β selectivity in the reaction derived from the highly coordinated state while the boron complex did an α selectivity.

In chapter 3, the atrane-type heavier group 14 cations were synthesized. The atrane framework stabilized the cations thermodynamically by the intramolecular electron donation from the nitrogen atom and kinetically from the rigidity of the atrane structure where phenyl groups were introduced. The electron donation from the nitrogen atom was also important to enable them to work as Lewis acid catalysts. From FIA and HIA evaluations, they turned out to have hard and soft Lewis superacidities. The cations were applicable to many transformations with hard or soft substrates. Furthermore, the atrane-type cations showed interesting selectivities depending on solvents in the competitive reaction of silyl enol ether with acetal and aldehyde. The cations showed the highest selectivities compared to other typical silicon and boron catalysts. The catalytic use and precise controls of heavier group 14 cations were achieved by the atrane structure.

A knowledge obtained from chapter 1 and 2 is that structural controls by triphenoxy ligands enables us to precisely control their Lewis acidities and their coordination environment to give high chemo- and stereoselectivities. Chapter 3 showed the cage-shaped control can be applied to the heavier group 14 cations.

The knowledge gives us strategies to design the coordination environment of Lewis acids with organic ligands, which show high chemoselectivities. Furthermore, the cage-shaped ligand control is promising to stabilize and utilize highly reactive species as catalysts.